DEVELOPMENT AND CHARACTERIZATION OF HIGH-PERFORMANCE TiC AND TiN CERMETS

by

Marciel Gaier

Submitted in partial fulfilment of the requirements
for the degree of Doctor of Philosophy

at

Dalhousie University
Halifax, Nova Scotia
December 2019

DEDICATION

This thesis is dedicated to my wife Nathieli Beltran Schiavi, my mother Tatiane Delbrucke, Eliseu Vieira de Lima and my brother Michel Gaier and Julia Beltrami.

Also, this thesis is dedicated to my supervisors Dr. Kevin Plucknett and Dr. Zoheir Farhat. Also, my friends Chuhong Wang, Zhila Memarrashidi, Tahrim Alam Rusho which help me in the research.

TABLE OF CONTENTS

LIST OF TABLES

LIST OF FIGURES

ABSTRACT

'Cermets' are engineered composites that combine ceramic and metallic phases to generate materials that, typically, exhibit both high hardness and toughness. Because of this combination of constituents, cermets can exhibit a moderately low coefficient of friction combined with good wear resistance. In addition, through careful selection of the actual cermets phase compositions, they can also possess high oxidation resistance and good thermal stability. The development and synthesis of TiC/TiN with novel binder alloys such as stainless steel 316L and PH17-4PH, Ni_3Al and additions such as graphene nanoplatelets (GNPs) and Mo_2C were developed for applications under extreme wear resistance environments.

The effects of incorporating Mo_2C additions into TiN-Ni_3Al cermets, in terms of their densification response and microstructural development have also been studied. It is demonstrated that an increase in the Mo_2C content reduces both the melting and solidification temperature of the Ni_3Al-based component of the system, which is initially formed via reaction sintering. The wettability of the Ni_3Al binder was improved through additions of Mo_2C, enhancing the densification process.

The influence of series of post-sinter heat treatments, between 600 and 1340 °C, on atomic ordering of the Ni_3Al on the TiC-30Ni_3Al were also studied. An increase in Vickers hardness, from 1400 to 1530 HV, is observed as a result of heat treatment at 1200 ºC. Furthermore, the scratch hardness value was improved from 11.89 to 18.12 GPa, with the main wear mechanisms being identified as TiC grain pull out and brittle fracture. Other heat treatments were performed on the TiC-PH 17-4 stainless steel based cermets, evaluating the effects of heat treatments on precipitation hardening steels in comparison with non-heat treatable steel, when used in combination with TiC. Martensitic Cu rich precipitates were identified by X-ray diffraction analysis when TiC-17-4 precipitation hardening steel was heat treated. An increase in Vickers hardness from 1160 to 2342 HV is as a result of a 1150 ºC heat treatment. Moreover, the scratch resistance was significantly improved, dropping from 1.74 to 0.8 μm in scratch depth, when performed at a load of 30N.

LIST OF ABBREVIATIONS AND SYMBOLS USED

°C	Degree Celsius
°F	Degree Fahrenheit
a	Half Diagonal Length Of A Vickers Indentation
A	Area In Contact
c	Total Distance From A Vickers Indentation Centre To Crack Tip
d	Average Diagonal Length Of A Vickers Indentation
E	Young's Modulus
ε	Strain
h	Distance
l	Crack Length Of A Vickers Indents
µm	Micrometre
AISI	American Iron And Steel Institute
ASTM	American Society For Testing And Materials
BCC	Body-Centered Cubic
CAPES	Coordenação De Aperfeiçoamento De Pessoal De Nível Superior
CIP	Cold Isostatic Pressing
COF	Coefficient Of Friction
CVD	Chemical Vapour Deposition
DSC	Differential Scanning Calorimetry
TG	Thermogravimetric
EDS	Energy Dispersive X-Ray Spectroscopy
eV	Electronvolt
Å	Angstrom
F	Force
FCC	Face Centered Cubic
FE-SEM	Field Emission Scanning Electron Microscopes
FWHM	Full Width At Half Maximum
g	Gram
g/cm^3	Gram Per Cubic Centimetre
GNPs	Graphene Nanoplatelets
GPa	Gigapascal
H1150	Heat Treatment At 1150 °F
H925	Heat Treatment At 925 °F
HSp	Scratch Hardness Number
PDF	Powder Diffraction File
LPS	Liquid Phase Sintering
HV	Vickers Hardness
HVOF	High Velocity Oxygen Fuel Spraying
ICDD	The International Centre For Diffraction Data
IFR	Indentation Fracture Resistance
ICP-OES	Inductively Coupled Plasma Optical Emission Spectrometry
k	Specific Wear Rate
K	Bulk Modulus

N	Total Number
kgf	Kilogram Force
K_{IC}	Critical Stress Intensity Factor Under Mode I
kJ/mol	Kilojoule Per Mole
kV	Kilovolt
L_c	Mean Height Of The Crystallite
LRO	Long Range Ordering
m	Meter
s	Second
mbar	Millibar Pressure Unit
mm	Millimetre
mm^3	Millimetre Cubic
N	Newtons
MPa	Megapascal
MW	Megawatts
nm	Nanometer
PM	Powder Metallurgy
Pm3m	Hermann–Mauguin Notation
psi	Pound-Force Per Square Inch
PVB	Polyvinyl Butyral
PVD	Physical Vapor Deposition
R_a	Mean Roughness
RPM	Revolutions Per Minute
SAE	Society Of Automotive Engineers
SEM	Scanning Electron Microscopy
SQS	Special Quasirandom Structures
UMT	Universal Micro Tribometer
ν	Poisson's Ratio
DFT	Density Functional Theory
PAW	Projector-Augmented Wave
GGA	Generalized Gradient Approximation
PBE	Perdew-Burke Ernzerhof
VASP	Vienna Ab Initio Simulation Package
PVB	Polyvinyl Butyral
Wt.%	Weight Percent
XRD	X Ray Diffraction
C	Stiffness Coefficient

CHAPTER 1 INTRODUCTION

Transition metal carbonitrides, in particular titanium carbonitride (Ti(C,N)), have been shown increase interest due to a combination of unique properties such as high melting temperature, high hardness, wear resistance and, high thermal conductivities [1]. Titanium carbide (TiC) and titanium nitride (TiN) are isomorphous, therefore a continuous solid solution can be prepared selecting the right ratio of Ti/C and N [2]. Ti(C,N) has high hardness (2000HV), but its toughness is limited for most applications [3]. Therefore, the toughness is usually improved by addition of a metallic binder. The most common binders are nickel (Ni) alloys, due to their improved corrosion resistance. However, metallic binders such as iron (Fe), chromium (Cr), cobalt (Co), molybdenum (Mo) were also successfully introduced [4]. An intermetallic phase, stoichiometric (and non-stoichiometric) nickel aluminide (Ni_3Al) has been receiving special attention due the its elevated strength and oxidation resistance at high temperatures (~1100°C) because the formation of passive alumina (Al_2O_3) layer [5]. However, while these materials have been studied substantially in the last three decades, the most used '*hardmetal*' in the industry is still tungsten carbide cobalt (WC-Co), with higher molecular weight and a significant negative impact environmentally [6].

The properties mentioned above make TiC and TiN good candidates to be used in the ceramic-metal composite (or cermets) family of materials, particularly when coupled with a metallic binder phase such as stainless steels or Ni_3Al to improve some specific characteristics [3]. Ni_3Al has been also studied and used in many aerospace applications (i.e. coatings for gas turbines and jet engines) due its high temperature performance [7]. Therefore, Ti(C/N)-Ni_3Al based cermets have attractive properties that can potentially give large advances in lightweight applications compared to WC, with a very good combination of high hardness, corrosion and wear resistance [8]. In addition to that, WC-Co has high rate of deterioration at high temperatures due to its poor oxidation resistance and plastic deformation [9].

In comparison to TiC, TiN also shows relevant interest due to its physical and chemical properties, with a high melting point (2927ºC), excellent oxidation properties, and a lower friction coefficient compared to most cermets [10]. TiN is also used as a coating on a variety of machining tools, and also in many other applications due to its high wear resistance combined with a low coefficient of friction [11]. The addition of nitrogen in the cermets also is known to decrease the wettability by

molten metallic binders. Pure titanium carbide has good wettability, however as the amount of nitrogen increases, it is necessary to use secondary agents to improve wettability [4].

In this research, a new class of TiC and TiN cermets were produced using a simple *"press and sinter"* methodology. These materials were prepared using Ni_3Al and two different types of stainless steel as binder phases, namely austenitic 316L and a grade of (martensitic) precipitation hardened steel 17-4 PH.

Further modifications/additions were also examined in order to increase chemical and tribo-mechanical performance. To increase the wettability and further densification of TiN- Ni_3Al based cermets, Mo_2C was added as secondary phase. Other components were also tested, including the use of graphene nanoplatelets (GNP), coupled with TiC-Ni_3Al, and aiming to increase wear resistance and create self-lubricating properties. A series of heat treatment techniques were also examinated, including long range ordering (LRO) heat treatments on TiC-Ni_3Al, and precipitation hardening heat treatments on TiC-17-4 PH with the goal of increasing the wear resistance of cermets.

To access the performance and life cycle of this material, several techniques were used to characterize and test the properties of the manufactured cermets. A common use for such ceramic-metal composites is as wear resistant parts in the automotive, aerospace, mining, mineral processing, and oil and gas industries. Due to the extreme environment that these materials are subjected to in many applications, severe testing conditions were applied when developing the cermets.

This work uses optical and scanning electron microscopy to characterise the resultant microstructures of the different compositions. The mechanical properties such as hardness and indentation fracture resistance, combined with tribological measurements are also tested. The harness measurements were conducted by an indentation technique using a *sharp* Vickers indenter, with the application of low and high loads. These approaches use low loads (i.e. 1kgf) to avoid crack formation and collect the *real* hardness without dispersing energy through the formation of cracks. The higher indentation loads, such as 30 or 50kgf are then used to calculate the indentation fracture resistance of the material, which is related to the toughness.

The sintering behaviour of the materials are then measured through using thermal analysis characterisation methods, including differential scanning calorimetry (DSC), thermogravimetric analysis (TGA), and dilatometry, while the related microstructural and phase characterisation was performed using scanning electron microscopy (SEM) and X-ray diffraction (XRD). Using these systems, it is possible to obtain specific melting and solidification temperatures, shrinkage and expansion profile(s) and, finally, the densification response during liquid phase sintering. The melting and solidification of specific phases are related to the phases analysed by SEM identified with energy dispersive X-ray spectroscopy (EDS), and confirmed with XRD.

This thesis will be subsequently divided into nine chapters, which combines all the goals and objectives of the research. In Chapter 2, a literature review is presented showing major results on cermet materials to date, used of advanced binder phases, the materials that are used and their limitations, synthesis methodologies, industrial applications and an overview of the characterization techniques that are used in this field of research, with the focus on wear performance. Chapter 3 presents the main experimental methodologies and types of analysis used in this research. Chapter 4 then presents a study on the thermal properties, sintering behaviour and densification mechanisms of TiN-N_3Al cermets using Mo_2C to improve the wettability of Ni_3Al on TiN grains. The main densification mechanisms were observed and described, improving then further the mechanical performance of such materials. Chapters 5 and 6 are related to further improvements of the wear performance of TiC-N_3Al cermets using two strategies. GNPs were added, substituting for the binder phase, in order to increase toughness and reduce friction, therefore increasing wear performance. The investigation focused on how the GNPs additions influence the processing and densification response of TiC-Ni_3Al cermets, their fundamental mechanical properties and, most importantly, the tribological behaviour of the resultant GNP-containing cermets is studied. Chapter 6 shows the effects of post-sinter heat treatments (between 600 and 1340 °C) on atomic ordering of the Ni_3Al. These materials have been assessed using chemical, mechanical and tribological techniques. The main wear mechanisms were identified, as well as the influence of the heat treatments on the overall performance of the material. Also, the ordering transitions were subsequently related to the structural changes predicted through *ab-initio* modelling approaches by a research collaboration with Dr. Tsanka Z. Todorova in the Department of Chemistry department at Dalhousie University.

Chapter 7 explain the first principles and experimental validation studies of fundamental mechanical (elastic moduli, Poisson ratio and hardness) and thermal (expansion coefficient) properties were compared to assess the responses in fully dense (99% theoretical density) of TiC-30vol-% Ni_3Al using a liquid phase sintering process. The experimental elastic moduli were determined using a pulse-echo method, while hardness was assessed using the Vickers indentation test. The volumetric thermal expansion of the sample was studied using dilatometry. This work also involved Dr. Tsanka Z. Todorova who was responsible for the *first principles* calculations.

Chapter 8 is related to a novel processing approach using cermets with stainless steel-based binders. A 17-4 precipitation hardenable steel was used in order to study the overall mechanical and tribological performance, following heat treatments on the steel containing cermets. All of the results and experiments, data analysis and manuscript preparation of this thesis were performed by the thesis author with the guidance of the PhD supervisors (Dr. Kevin Paul Plucknett and Dr. Zoheir Farhat), with the exception of the *ab-initio and first principles* modelling approaches in Chapter 7 and 8. Chapter 9 provides a summary of these research findings and accomplishments, as well as future recommendations for work related to this research topic.

The overall objectives of this work are to improve the mechanical and wear performance of cermets by using diverse approaches that includes heat treatments, incorporation of novel particles or by changing the chemistry of the cermets. The specific objectives of this work are outlined bellow:

- Improve the densification and study the sintering response of TiN-Ni_3Al based cermets with Mo_2C additions;
- Study the mechanical and tribological properties of TiC-Ni_3Al based cermets with GNPs additions;
- Investigate the influence of atomic ordering heat treatments of the Ni_3Al on TiC- Ni_3Al based cermets;
- Study mechanical and thermal properties of TiC- Ni_3Al using experimental and *first-principles* calculations;
- Study the mechanical and tribological property of TiC-steel based cermets.

CHAPTER 2 LITERATURE REVIEW

The literature review explores all the concepts and principles necessaries to understand the following chapters. It gives an overview of the types of materials being synthesised and developed in this research, as well as including topics related to understanding of basic characterization methodologies for the cermets. An overview and history of cermets, TiC and TiN power fabrication methods, the synthesis of cermets, as well as several recent binder phases such as Ni_3Al, stainless steels are provided, along with the effects of incremental additions such as GNPs. An in-depth study on the characterization of cermets, such as mechanical properties including Vickers indentation hardness and fracture resistance, overall chemical and microstructures obtained, and several approaches of wear testing a material (such as reciprocating sliding wear, scratch testing and the "pin on disc" approach, with its specific uses and mechanisms) have also been covered. An overview relating to wear properties and wear rates and the latest achieved results in the literature are also shown. A review of the limitations and possible ways to further improve mechanical properties, using additives such as GNPs or using heat treatments, is presented.

2.1 Introduction to Cermets

Cermets are defined as composite materials with ceramic and metallic components. Cermets are specifically engineered to have the optimal properties that are in between both ceramics, such as high hardness and elevated temperature performance, and those of metallic materials, such as ability to undergo some degree of plastic deformation. Cermets and cemented carbides are one of the most used materials in terms of powder metallurgy products worldwide [12]. The reasoning is related to its outstanding performance in extreme environments together with a cost-benefit when compared to materials such as diamonds and high speed steels [13]. Cemented carbides cover a large range of materials and applications in many important industries, i.e. tool materials (milling, drilling turning,) for machining metal components in the automotive and aerospace industry, as well as several components for tools and drill bits, wire drying dies and punch tools [14].

The first cemented carbide was invented in 1927 by the German company Friedrich Krupp, as was composed of tungsten carbide and cobalt (WC-Co) under the name WIDIA (an acronym for the

German words WIe DIAmant=like diamond) [14]. The first use of this material was related to wire drawing and wear resistant parts. In recent years after this invention, the additions of other carbides (such as TiC) were made to improve properties of basic WC-Co compositions for specific machining operations. Subsequently, additions of nitrogen in the form of TiN and Ti(C,N) to TiC-Mo_2C-Ni created the first "advanced" cermet with increased performance for high cutting speeds and better finishing outputs [13].

During the decade of the 1980s, with the introduction of aluminum oxide (Al_2O_3) and other refractory metals, a dramatic increase in cutting tool performance was obtained. In terms of coatings, processes such as chemical vapour deposition (CVD) or physical vapour deposition (PVD), using hard materials such as TiC, TiN and Ti(C,N) on the surface of cemented carbides allowed a significant improvement in the wear resistance of tools. In the last decade, the focus has changed to high performance multilayer CVD coatings containing Al_2O_3, Ti(C,N), Zr(C,N) and (Ti,Al)N, where high resistance against oxidation and wear, combined with a low coefficient of friction, were obtained. Other types of coatings have shown significant progress, such as high velocity oxyfuel (HVOF) surface protection that demonstrated minimal porosity and excellent bond strength. The process of HVOF thermal spraying coatings was also originally developed in the early 1980's by Browning Engineering Co in the U.S.A. and marketed as the Jet Kote HVOF spray system. During the spraying, a carrier gas with hypersonic velocities of about 1800 $m.s^{-1}$ and combustion temperatures in the order of about 3,000 °C spray the particles onto the surface, creating a protective coating layer. Depending on particle size and density, and the ceramic/binder chemistry the coating can achieve outstanding properties. In addition, high spray distances allow to produce coatings with porosity levels of less than 1% with the right application conditions [15].

By selecting the right combination of the ceramic, metallic binder and process parameters, a wide variety of chemical, mechanical, tribological and microstructures can be achieved. Some international classification system has been created with the scope of standardizing cermets. The most relevant ones are the ISO-committee TC (29 April 1958), the US-Industrial code and the DIN 4990 (1948)[14]. These materials are then divided into four categorizations according to the microstructure and chemical properties, as shown in Figure 2.1. These include WC morphology and chemistry, cubic carbide containing cemented carbide and cermets, functionally graded cemented carbides, and binder design of cemented carbides.

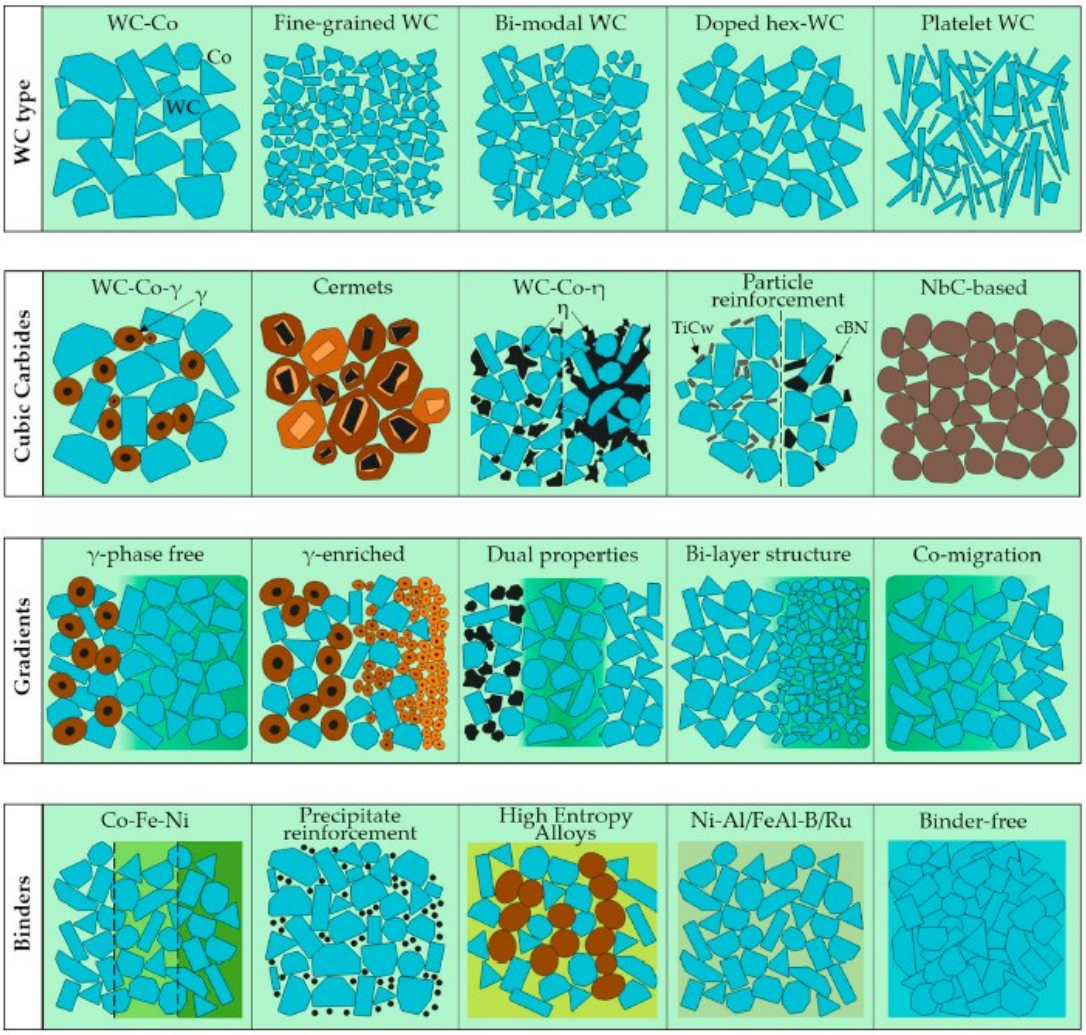

Figure 2.1 Categorisation of cemented carbide according to their microstructures and chemical properties [3].

Cermets usually consist of approximately 50-95% of the ceramic phase by volume, embedded in a continuous matrix of an elemental metal or alloyed binder. The combination of metal and non-metal in cermets occurs on a microscale, with fine ceramic particles ranging usually from 1-25μm. These materials have desirable qualities, depending upon physical characteristics such as densification and wetting behaviour. For instance, the wetting response of the molten metal on the ceramic is a critical factor that determines the final strength and wear resistance. For instance, a cermet that has 3% porosity, *due to poor wetting*, could have a wear rate 2 orders of magnitude larger than a fully dense one [3].

Figure 2.2 shows a typical cermet microstructure and chemical composition of a sample imaged in a scanning electronic microscope (SEM), coupled energy dispersive X-ray spectroscopy (EDS), in this instance a TiC based composition sintered by the liquid phase sintering methodology. The formation of a core-rim structure and its composition is shown in Figures 2.2 and 2.3. The dark gray grains represent the ceramic phase, which in this case shows a core-rim structure, with W and Zirconia (Zr) present in the rim. The light gray phase represents the metallic binder phase, composed of Ni_3Al.

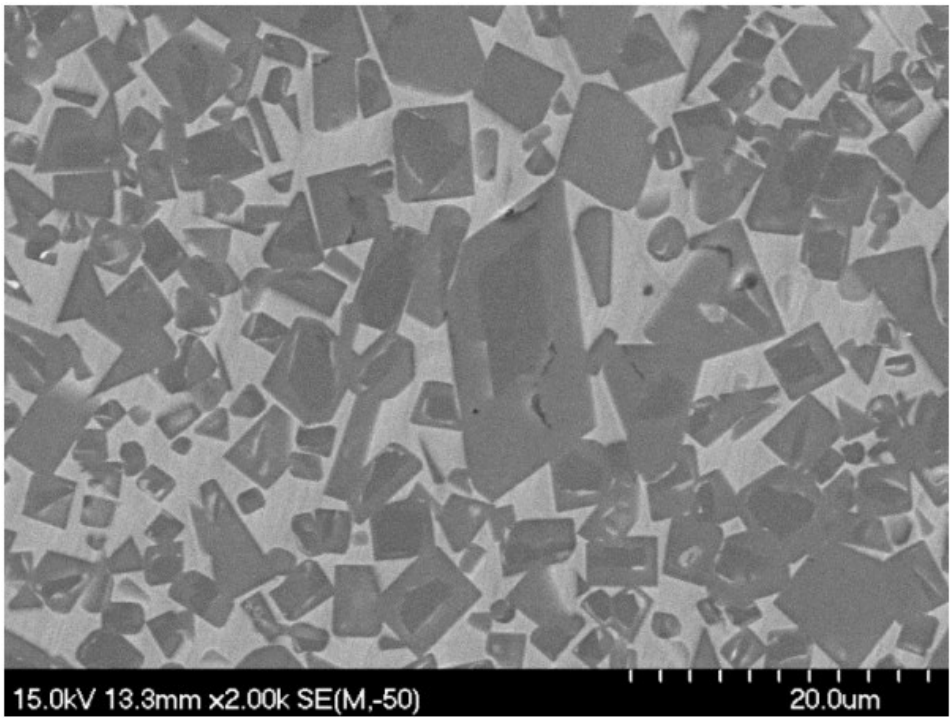

Figure 2.2 Scanning electron microscopy of TiC with Ni_3Al as metallic phase and W and Zr as impurities [1].

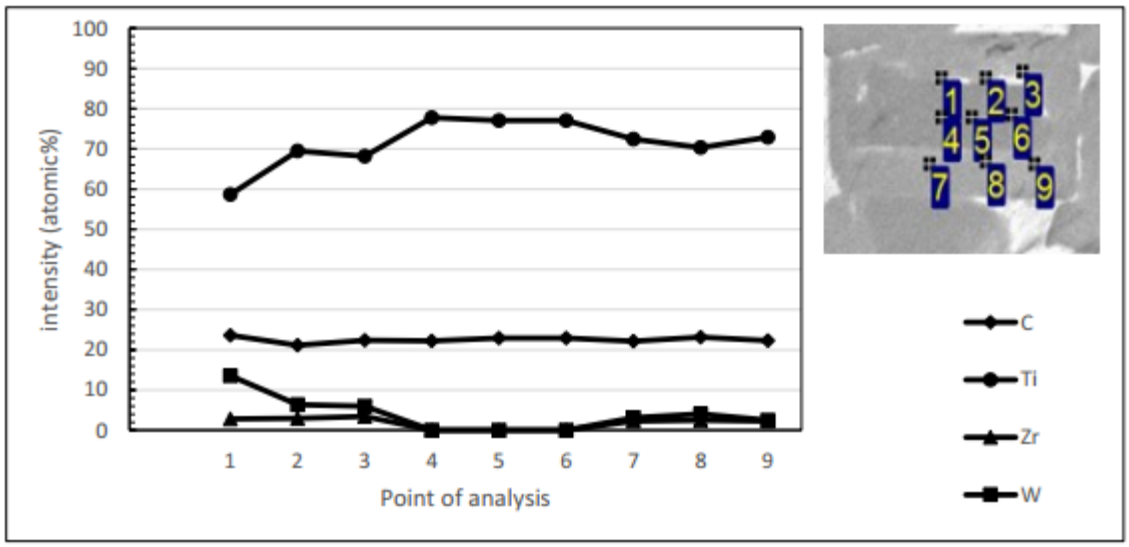

Figure 2.3 EDS of the TiC grains with showing the core-rim structure [1].

The overall market for cermets has grown fast in the past 30 years. The total production in 1993 was around 20,000 tons and increased to 30,000 tons (2000), with almost 60,000 tons being produced in 2008, with significant contribution from the Chinese in the market more recently. The production of these materials in China raised from 7,000 tons in 2001 to 20,000 tons in 2011, and 28,000 tons in 2017. In the same time that China is also responsible for 60% of the world consumption reaching 55,000 tons in 2017 [3]. The market shows that as of today, 35% of the cermets are recycled. The processing industry consider tungsten and titanium containing scrap high value in comparison to ore, due to its price as raw material. In terms of applications, around 65% of the total cemented carbide production is applied to metal cutting tools. The oil and mining industry also take a significantly large piece of the market, with about 15% market share, whereas wood and construction industries account for 10% [3].

2.2 Titanium Carbide and Titanium Nitride

TiC and TiN are two of the most important compounds amoung the transition metal carbides, due to their excellent combination of physical and chemical properties. TiC has a high melting point (3067°C), Vickers hardness (2855 – 3569 HV), Young's modulus (410-450 GPA), a good flexure strength (240-400MPa) and low density (4.93 g/cm^3), combined with a good thermal conductivity

(21 W/m^2 K) [16]. Due to its properties, TiC-based cermets are used in several wear resistant applications. TiN also has a high melting point (2930°C), Vickers hardness (1800-2100HV), Young's modulus (251 GPA), flexure strength(210-350MPa) and a low density (5.22 g/cm$^{3)}$, combined with a good thermal conductivity (19.2 W/m^2 K) [17]. Both TiC and TiN can be used as substitutes for WC due to their elevated hardness and therefore, high wear resistance. Ni is also added as a alternative binder for TiC, being more environmental friendly and economical than Co [18,19].

2.2.1 Crystal structure of TiC and TiN

TiC and TiN have a sodium chloride crystal structure like many carbides, which is the face-centered cubic (FCC) crystal structure. The Ti atoms are localized at the edge of the crystal cell, with C atoms in the interstitial sites[2,20]. The carbon atoms on the TiC superlattice can be replaced by nitrogen atoms in any proportions, that means C for TiC or N for TiN-filled edges of face-centered cubic, while Ti atoms occupied (0.5, 0,0) position of the superlattice, as shown schematically in Figure 2.4. Therefore, it is possible to form Ti(C,N) in solid solution. It is important to outline that the physical–mechanical properties would vary with the amount of nitrogen and carbon [20].

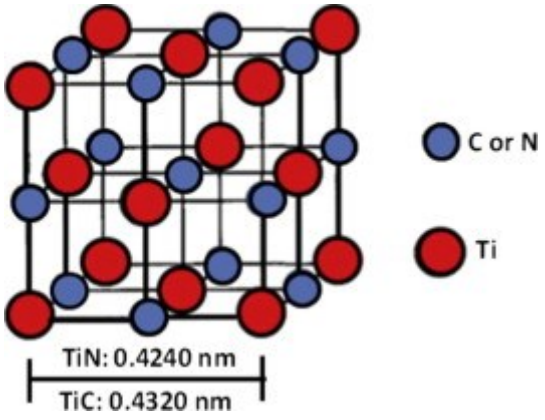

Figure 2.4 Crystal cell TiC and TiN [20].

2.2.2 Production of TiC, TiN and Ti(C,N) powders

TiC, TiN and Ti(C,N) can be produced by several techniques, including direct carbonization or nitridation of elemental titanium metal or titanium hydride. The reaction takes place using titanium oxide (TiO_2) in excess of carbon or nitrogen, slowly generating the final product [12,21]. The process to produce this powder requires unusually high temperatures and relatively large periods of time, i.e. 2000°C for up 20 hours. The reactions [22] to produce TiC, TiN and Ti(C,N) are represented bellow:

$TiO_2(s) + 3C(s) = TiC(s) + 2CO(g)$ **Equation 2.1**

$TiO_2(s) + 2C(s) + 0.5N_2(g) = TiN(s) + 2CO(g)$ **Equation 2.2**

$TiO_2(s) + 3C(s) + 0.5N_2(g) = + Ti(C,N)(s) + 2CO(g)$ **Equation 2.3**

After these steps, the reaction produces agglomerated powders that must be further milled and chemically purified. Oxygen from the starting powders and contamination from WC-Co milling media are common on industrial grade powders. Other less relevant methodologies are also used in order to produce TiC and TiN, such as the reaction of Ti with carbon and the chemical reaction using titanium halide ($TiCl_4$) in carbon and hydrogen atmosphere [12].

2.3 Nickel Aluminide Binders

Nickel aluminide intermetallic based alloys have been developed for use in high temperatures, where stainless steel use is limited. Because of that, the aerospace industry is one of the early adopters of this material. The Ni-Al binary phase diagram in Figure 2.5 shows the following intermetallic compounds (Al_3Ni, Al_3Ni_2, Al_3Ni_5, NiAl, Ni_3Al) of those Ni_3Al is the most used due to its high temperature properties. Ni_3Al presents the one of the highest melting point (lower than Ni/Al only) according to the phase diagram shown in Figure 5, as well as, good strength and high temperature corrosion resistance.

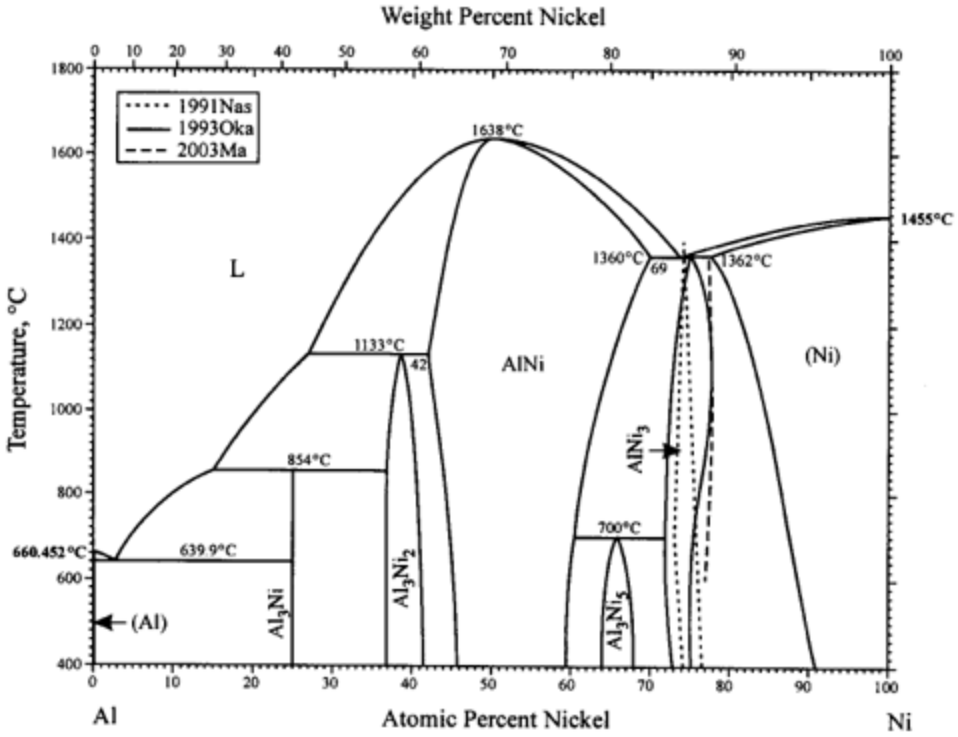

Figure 2.5 The Ni-Al phase diagram adapted from [23].

An intermetallic compound is formed as ordered phases of two or more metallic elements that have created an new alloy, with multiple lattices that described its atomic structure [24]. The degree of ordering within the structure drives the physical properties of the alloy and are usually dictated by the processing methodology. When they achieve a long range ordering superlattice, this mechanism restricts the dislocation movement maintaining physical properties at high temperature [24].

Between all intermetallic forms, the NiAl compound has the higher melting point (1638°C) when compared with Ni_3Al (peritectic, 1385 °C). On the other hand, it suffers from low temperature brittleness and poor strength at high temperatures [25]. Some improvements have been made in terms of the brittleness though grain refinement and incorporation of a second phase. This material has attracted significant interest in substituting for Ni-based superalloys.

2.3.1 Crystal structure of Ni_3Al

Ni_3Al has a cubic crystal structure with a space group Pm3m and a Strukturbericht structure L12 [26]. Figure 2.6 shows the unit cell of Ni_3Al, with Al atoms occupying the corners of the cube and Ni atoms located at the cube faces in the lattice. The NiAl crystal structure is classified as primitive cubic CsCl structure. The Strukturbericht designation for this structure is B2. It can be described in terms of two inter penetrating cubic cells where Al atoms occupy one sublattice and the Ni atoms occupy the second sublattice [27].

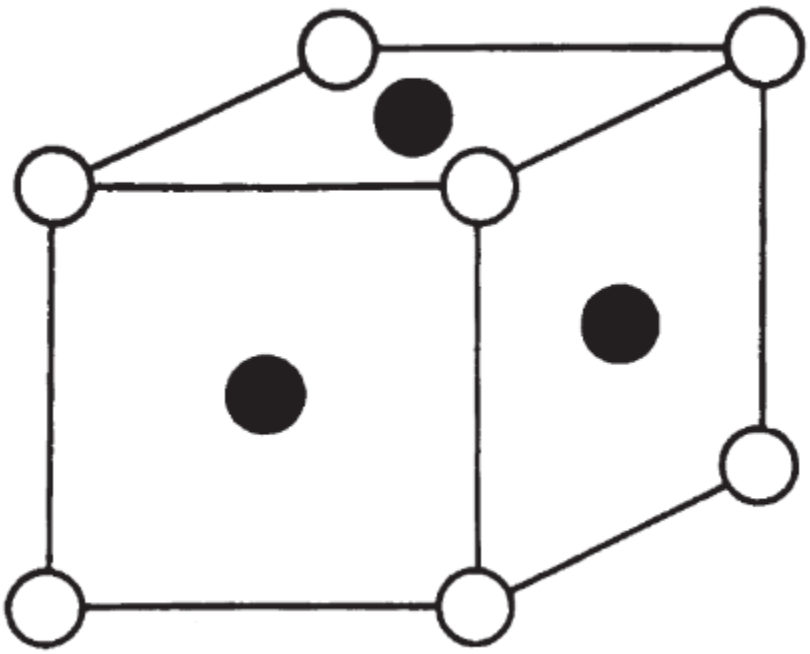

Figure 2.6 Unit cell of Ni_3Al. Ni atoms (filled circles) are on face centres and Al atoms (open circles) at corners [27].

2.4 Stainless Steel Binders

Stainless steels are a class of iron-based alloys that contain ≥10.5% chromium (Cr). The main function of the Cr is to form a passive layer of chromium oxide (Cr_2O_3). Other elements that may

be added to the steel are Ni and Mo, with the function to increase the corrosion resistance. There are a significant number of stainless-steel grades, with the most common being the 300 series. These alloys have 18% of Cr, with specifically 316 also having 8% of Ni and 2% Mo, and being particularly recommended for applications against corrosion in marine environments due to salt and pitting corrosion resistance. All these properties made them particularly appropriated for use as binder in cermets.

2.4.1 Classification of Stainless steel

A system to catalog and classify different types of stainless steel according to their compositions and characteristics have been developed by the American Iron and Steel Institute (AISI) and as well the Society of Automotive Engineers (SAE). The following table shows the series that were developed to classify stainless steel:

Table 2.1 Series of stainless steel and its composition

Series name	**Characteristics**
AISI 200 series	austenitic chromium-nickel-manganese alloys
AISI 300 series	austenitic chromium-nickel alloys
AISI 400 series	ferritic and martensitic chromium alloys
AISI 500 series	heat-resisting chromium alloys
AISI 600 series	special alloys that are not included in the above

The austenitic class of stainless steel have the best corrosion resistance among the different grades. On its alloying elements, Cr and Ni further increase the resistance of the passive films in the surface against acidic atmospheres. Characteristics of this family of stainless steels include an FCC crystal structure, good corrosion resistance and high toughness at ambient temperature.

This class of steel presents work hardening properties, being able to be cold worked. The 300 series are extensively used in the piping and marine industry, as well for heat exchange applications. The most common types include 304, 316 and 317. Slight variations on the compositions are suitable

for specific applications, depending on the environment, for i.e. high Cr and Mo contents are used for superior corrosion resistance and nitrogen (N) for applications where there it is a required high strength.

Martensitic steels have a body centred cubic structure (BCC) and are usually heat treated for different notable applications that require high strength and hardness. The most common martensitic stainless steels are the 400 series. While the corrosion resistance of these steels is lower than the other series, they are applied in mild environments due to being susceptible to hydrogen embrittlement and cracking.

Precipitation hardening heat treatments are also applied for a range of martensitic steels. These alloys combine very high strength, hardness and corrosion resistance, with a yield strength up to 1300 MPa. These properties are achieved by additions of Cu and Nb. A large series of heat treatments are possible, due to the small additions of precipitates that work as secondary phase. These particles impede the movement of dislocations, causing the material to increase strength. One example of this type of steels is grade 17-4PH, which is a 630 series alloy. The corrosion resistance of alloy 17-4PH is comparable to the 300 series and superior than the 400 series stainless steels. This alloy is used in applications where the combination of moderate corrosion resistance and high strength are required.

2.5 Novel Particle Additions

Several secondary particles have been examined to further increase the wear resistance of cermets. For instance, industrial diamonds and graphene particles can be added to these composite materials with the functionality of increasing hardness, toughness or decreasing the coefficient of friction. The addition of fine industrial diamonds particles substituting the TiC offers the potential to significantly increase the composite elastic modulus, hardness and, potentially, the wear resistance and fracture toughness of the final composition [28]. The toughness in this case would be increased due to greater crack deflection around the ultra-high hardness diamond particles. Similarly, the addition of graphene or graphene nanoplatelets (GNPs) would increase the yield stress of the binder alloy [29].

Graphene is defined as a single layer of carbon atoms that are bonded by covalent bonds in hexagonal honeycomb lattice and van der Waals forces in between layers. Graphene is an allotropic form of carbon, effectively a plane of sp2-bonded atoms with a molecular bond length of 0.142 nanometers. Graphene particles have a great potential to increase the hardness of the cermets, but also to reduce the coefficient of friction of the surface. Several layers of graphene stacked on top of each other form graphite. Graphene is defined by the ISO/TS 80004-13:2017 according to the number of layers as follows[30]:

- Single layer graphene: single layer of carbon atoms arranged in a hexagonal lattice. Must have a flake thickness <0.335 nm;
- Few layers graphene: 2-5 layers of graphene.
- Graphene nanoplatelets: stacks of graphene that are 1 to 15 nanometers thick, with diameters ranging from sub-micrometre to 100 micrometres.

2.6 Production of Cermets

2.6.1 Powders Selection and Processing

Cermets are essentially manufactured by powder metallurgy (PM) processes. The production starts with micron-sized powders and the understanding of basic properties to achieve a homogenous and controlled process [31]. The powder attributes such as size, distribution of size, particle agglomeration, surface area, particle friction, flow and packing, internal structure and composition play very important roles to control the output of parts from a PM process [31].

Usually, most of the particles used in the PM process are in the range from 0.5 – 40 μm. However, particles size is not as important as the size distribution for packing density, green strength and final densification of the parts [32]. Particles sizes and shapes are important in order to obtain a good flow by gravity force (free flowing in the Hall flow meter), which simulate the "feed shoe" used by the PM industry. The particles should flow from a hopper to the "feed shoe" naturally, and then fill the whole format of the produced part. The size of particles is very important for green strength as well, for i.e. for iron particles, they need to be smaller than 54 μm. in diameter to have enough green strength to be sintered [32].

Fine particles produces a better surface finish, because of the small pores and fast sintering due to the high surface area, usually generating a denser part when compared to large particles [31]. On the other hand, fast sintering may result in rapid shrinkage, that can lead to problems with dimensional control and cracks in the surface of the material. Small particles are also expensive to produce, hard to flow, and tend to have irregular shape resulting in final low green strength [31]. For this reason, binders tend to use additives in the composition to improve particle flow and green strength. These additives, usually organic are further eliminated in the sintering process [31].

2.6.2 Mixing, Milling and Sieving Procedures

To obtain a uniform mixture, dry powders are subjected to a series of processes that includes mixing, milling and sieving. The constituent powders are typically mixed in batches using ball mill methodology, usually in solutions containing solvents. The recommended mixture uses a ratio of 10:1 media to powder in mass ratio. These variables are selected to improve the total energy that the ZrO or WC-Co milling media have to reduce the particles size and homogenize the powders. After being completely homogenized, the powders are dried and sieved through a mesh to remove agglomerated particles.

2.6.3 Compaction Methodologies

Several techniques can be applied in order to compact powders in specific shapes. This process is crucial in order to produce powder metallurgy components. The two main approaches applied by the industry are uniaxial and isostatic pressing. For simple and rapid shape formation, die compaction is used with fast formation of objects with accurate dimensions. An organic binder may be added in the composition to reduce die wall friction. Also, a combination of coarse particles and small particles can be made to achieve high green strength and densities [12].

Green strength is one of the most important factors for powder compaction. To obtain a good green strength it is necessary to have a good powder compressibility and interlocking between particles and with binders and lubricants. Another important variable of green strength is powder shape. Irregular powders tend to result in a poor packing condition, on the other hand allows the green part to obtain a better green strength due the particle interlocking mechanisms [12].

When using uniaxial pressing, the pressure is applied in one direction in a hardened die. The final part takes the shape of the die and compress though the pressure. This methodology is applied to simple shapes, that allows compaction and densification through one plane. The advantage of uniaxial pressing is high speed, which is preferred by industry due its simplicity [12]. Uniaxial die compression has many benefits; however, it also has problems. There are limitations on the component size and density, density gradient can form within the sample, and complications such as high die wear arise. Compressibility plays an important rule for hard feedstock powders, being more challenging to obtain a part with a suitable density due to low compaction ability [12].

Another common methodology used to compact powders is isostatic pressing. This method involves the application of pressure in all directions and no longer require the use of a die. This fact gives a lot more flexibility to the process in terms of shape, and no longer requires use of a lubricant to reduce the die wall friction effect. Two methodologies are used in this process, wet-bag processing and dry-bag processing. Wet bag process requires that the part is already in shape before pressing and can cause slight shape changes in parts with high angles. In the wet bag method, the object must be sealed in a plastic bag, which is pressed by a hydraulic fluid in all directions. The dry-bag processing uses a plastic rubber in the shape of the final part, where the powder is poured into and submersed in the hydraulic fluid, which is pressurized in the shape of the bag [32]. This methodology has more flexibility in terms of parts with high angles and complex shapes, however it is not widely used by industry due to its low production yield.

Other parameters must be observed when pressing powders. When a new part is being designed, a homogeneous microstructure in terms of density and composition must be obtained to avoid problems related to the development of cracks, deformation in shape, and potentially failures in the final sintered body. When in the green condition, and while is being ejected from the die, the die wall friction can generate density gradients in the microstructure which can cause flaws in the compact. One way to minimize this problem is by levelling and uniformly filling the die before compaction. Also, lubricant can be used to reduce particle inter-friction and friction between the die and part to obtain a more uniform densification. Another important relation that can be engineered for a successful pressing, is the use of the lowest length to diameter ratio as possible, with a maximum value of r=0.5 for a single press [1,23]. Once the part has enough green density and green strength, the heat treatment is performed.

2.6.4 Sintering

In order to increase the mechanical properties of the compacted part, it is necessary to thermally induce the particles to fuse to each other, a process that is called sintering. The bonding and mass transfer between particles are accelerate by an increase in the temperature of the compound. Microstructural changes and chemical reactions that promote the total decrease in free energy of the system, by reduction of the porosity, surface area, while promoting densification of the material, are consequences of the sintering process [33]. After compaction, particles touch each other and create contact between the particles. During the different stages of sintering, many diffusion processes occur, filling the porosity between these particles. As thermal energy and time increases, the particles create a bond between each other by the formation of a neck, and eventually the particles form an isolated pore in the grain boundary region. This isolated pore is indicative of an intermediate/final stage of sintering. As the time increases, the porosity gets smaller and more spherical, and sometimes they can break the retention of the grain boundaries and mover through to the core of the grains, which is a indicative of final stage sintering, as highlighted by the Figure 2.7 and Figure 2.8 [12].

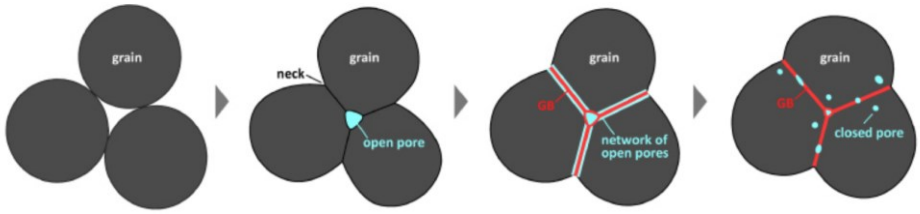

Figure 2.7 Stages of sintering. Diagram showing grains, pores and grain boundaries. Originally from [34].

When these sintering stages happens below the melting temperature of the constituents, the sintering is achieved by atomic diffusion, from the bulk region of the particles in direction to the grain boundary and neck of the particles. Some of the small particles, that have a higher surface area are diffused into larger grains, resulting in coarsening of the microstructure as time is increased. As a result, the number of grains is proportionally reduced over the sintering time. In addition to the bulk transport phenomena mentioned above, there are a few mass transport processes that happen at/in the surface region of the particles at relative low temperatures. The

surface mass diffusion does not promote densification; however, they promote growth of the neck radius between the particles. Essentially, there are three kinds of surface diffusion mechanisms that are outlined in the following schematic: evaporation-condensation, surface diffusion and volume diffusion as shown in Figure 8 [35].

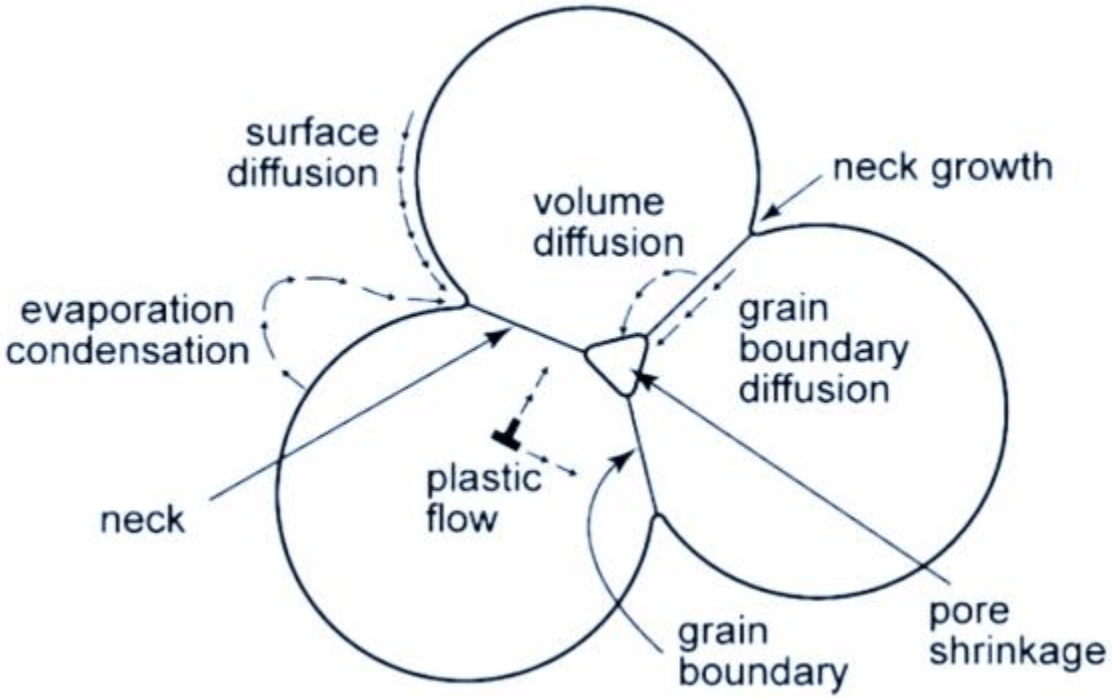

Figure 2.8 Mechanism of sintering. Adapted from [32].

Bulk mass transport mechanisms are prevalent at high temperatures and promote atomic transportation from the bulk of the particles to the pores and to the surface [12]. The major mass transport mechanism is the movement of vacancies in a direction to the bulk of the particles and atoms going to the surface in the opposite direction, resulting in *"neck"* growth between particles [32].

2.6.4.1 Liquid Phase Sintering

Liquid phase sintering is a methodology that uses a phase with lower melting point, in order to obtain a molten liquid phase between the solid grains to accelerate diffusion. Due the presence of a liquid phase, the kinetics of the reactions can speed up by tenfolds when compared to solid state sintering. This methodology is specially used for materials with high melting point, that cannot by

sintered efficiently otherwise. A few requirements are necessary on this type of sintering, such as: the liquid must not be soluble within the matrix, to allow high diffusion rates. In addition, a minimum solubility of the solid phase into the molten phase is necessary [33]. The liquid phase must have some degree of wettability on the solid grains, allowing low contact angles and therefore allowing the molten phase spread over the solid grains [12]. Once the melting temperature is achieved, the liquid wet and spreads between the solid particles, giving freedom for particle rearrangements [36]. The solid phase can then diffuse through the liquid by *Ostwald ripening* (solution-reprecipitation process), increasing the dissolution of small grains and reprecipitation onto larger grains, and the associated larger grains into even bigger ones. This process is responsible for the coarsening of the microstructure [32] and allows the changes in shapes, *i.e.* grains change shape to spherical and fill the porosity with a better packing factor. This methodology is used in large scale by industry with the advantages of using lower temperatures and shorter sintering times than solid state sintering. The main mechanisms are sketched in Figure 2.9 as follows.

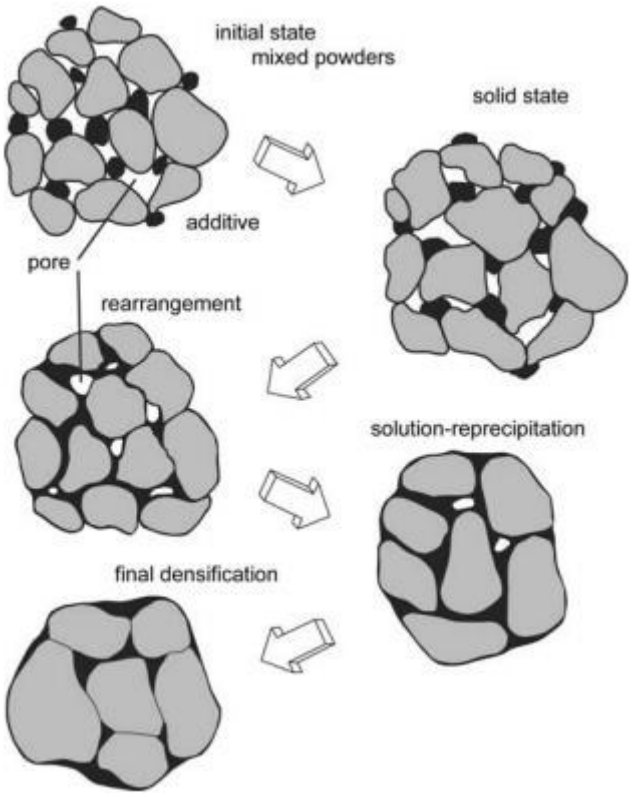

Figure 2.9 Mechanisms of liquid phase sintering [36].

The contact angle between the liquid and solid phases plays a very important role in liquid phase sintering. The contact angle represents a metastable equilibrium measurement of the interfacial energy balance, represented in Figure 2.10. In order for a liquid to wet a solid, the total interfacial energy must be minimised [4]. The contact angle characterizes the degree of wetting of the liquid into the solid phase. The contact angle changes with the balance of the three-surfaces energies. A poor wetting of the liquid phase results in sweating of the liquid from the sample, resulting in a large amount of porosity [4,12]. With successful wetting, the liquid phase creates a capillary force witch drives densification between the liquid and solid phases.

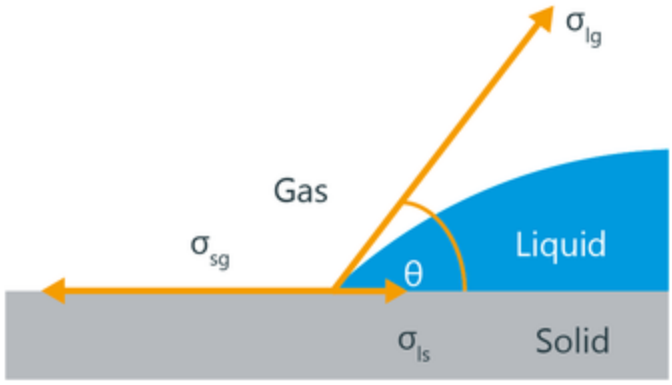

Figure 2.10 Schematic diagram of contact angle [37].

Residual pores can be the source of internal cracking and frequently result in poor mechanical resistance, or negative effects on the strength of the sintered part [38].

In order to promote low angle contacts, usually in the range of < 30 °, the addition of active elements is sometimes required. These additives promote a thin interfacial phase that increase the wettability of the liquid compound onto the solid. For example, in the case of cermets, one of the common additions is Ti which forms an intermediate cluster of TiO or TiN (depending upon local atmosphere) on nitride ceramics [39]. This additive must satisfy the free energy conditions (liquid metal must have lower surface free energy than solid) and react with the base ceramic. It's has

been suggested that a metallic character in the ceramic is necessary to promote a good wetting by liquid metals [30,31]

The literature shows that the wetting behavior of TiC systems is strongly related with the presence of oxygen in the sintering environment. The carbon content of TiC phase alters the wetting by metals. As the carbon content increases towards stoichiometry, the dissolution of the metals decreases [40]. Additions of Ti can increase the metallic character of the compound, and therefore decrease the wetting angle [37,40].

Other common additions to cermets are Mo or Mo_2C. In small amounts, Mo shows a tendency to envelope the solid particles of TiN creating an interfacial layer that speeds up diffusion and reduce the wetting angles to lower than $\theta < 4\ ^\circ\theta$ [8]. The wettability of TiC, TiN, and TiO by metals tends to increase with decreasing C, N, or O concentrations, and with the increase of the metallic bond content on the solution [37,41].

2.7 Thermal Analysis

Thermal analysis involves a broad spectrum of analytical techniques that determine the behaviour of a material according to the temperature. Some types of analysis focus on quantifying the thermal effects in terms of released substances, for example mass spectroscopy and other evolved gas analysis (EGA) coupling methods. In the field of powder metallurgy, the three most used measurements categories include calorimetry changes (differential scanning calorimetry, DSC), mass change (thermogravimetric) and length change (dilatometry) during sintering and heat treatments.

2.7.1 Differential Scanning Calorimetry and Thermogravimetric analysis (DSC/TG)

The differential scanning calorimetry and thermogravimetric (DSC/TG) analyses are techniques where it is possible to study the reactions, sintering development and microstructure evaluation of materials in terms of changes in mass and thermal flow during melting and solidification events.

All materials have a unique amount of heat that is absorbed to undergo a physical transformation. This physical transformation, for metallic elements characterize phase transitions that will show as an exothermic or endothermic peak according to its phase diagram. The working principle of a DSC is that each material has a unique specific heat, so they require a well know amount of heat to increase the temperature of a determined weight. In order for comparison, a reference material with a known heat capacity is used. For DSC, the often-chosen material as a reference is alumina (Al_2O_3 – 99.9999% purity), which allows measurement of the heat flow with very high precision.

Thermogravimetric (TG) analysis is a technique that measures the changes in mass as a function of working temperature and time. For cermets characterization, it is important to understand the level of oxidation of the components, which is important for the metallic binder. Mass loss due to phenomena such as vaporization, sublimation, absorption, adsorption and/or desorption are also measured. Information regarding phase transitions may be also be observed, however the DSC traces must be analysed for confirmation. The thermal degradation of constituents within a specific time and temperature can also be obtained, i.e. water content and lubricant evaporation temperature.

Other factors such as oxidation behaviour as a function of temperature, in different atmospheres, can generate information about necessary sintering and heat treatment conditions for commercial applications. One of the main advantages of thermogravimetric analysis is the very small amount of sample (mass) required by the test. Also, the possibility to observe kinetics of reactions and run, in most of the cases, differential scanning calorimetry analysis simultaneously.

2.7.2 Dilatometry analysis

Dilatometry analysis is one of the main instruments used to obtain thermal properties of materials. The change in length temperature and time are measured with a nanometric precision. The dilatometry analyses use a pushrod "*arm*" which is coupled to the sample in order to detect dimensional changes. Normally, a force of at least 5 mN is applied to the tested specimen to guarantee the contact between the tested material and the instrument. For this test, the sample must be solid in shape, being either fully dense or pressed to a suitable strength to be tested. The dynamic and static coefficient of thermal expansion is then obtained using the variation of length as a

function of temperature. If the sample is isotropic, it is possible to obtain the volume expansion coefficient as well. For powder metallurgy, when the material is being submitted to a sintering condition, it is expected to shrink due to the reduction of porosity. The volumetric size reduction allows then the geometric calculation of the density. In the same way, for liquid phase sintering, the diffusion is enhanced by the presence of the molten phase, increasing the reduction of length by fast diffusion rates a liquid phase formation temperature. Shrinkage or expansion measured by dilatometry is also used to determine phase transitions events if there are associated volume changes.

2.8 Hardness and Wear Performance

2.8.1 Vickers Hardness

The hardness and wear resistance of a material is often related in a direct proportion. To a certain extent, as the hardness increases the wear resistance also increases. One of the most used methodologies to measure the hardness of cermets is by Vickers indentation. The test is performed by applying a fixed load using a predetermined indenter geometry. In the case of Vickers hardness, the geometry is a diamond pyramid where the hardness is evaluated by the ratio between applied load versus penetration depth of a specific contact area. The Vickers scale present a continuous value when compared with Rockwell hardness, that present different scales [42].

Other properties and mechanical characteristics of the tested materials can be calculated from hardness measurements, such as the indentation fracture resistance. It is previously presented in the literature that as the hardness increases, the indentation fracture toughness decreases [35]. As a "*generic rule*", brittle materials tend to form larger cracks more easily when compared with ductile materials [42]. In result of that, for cermets, as the concentration of the metallic phase is increased, the higher the fracture resistance will be expected. The toughness of cermets also vary according to factors such as the binder mean free path and ceramic grain sizes[43].

The Vickers hardness indenter is a square-based pyramid, with an angle of 136°. The indenter tip is a sharp diamond typically with the ability to apply loads of 1, 5, 10, 20, 30, 50, 100, and/or 120 kg. For most applications, 50 kg is the maximum used load while 1 or 5 kg are used to brittle

materials. When subjected to this test, an "*imprint*" of the indenter geometry is created in the surface of the material, and the hardness value is then calculated using the following equation:

$$\boldsymbol{HV = \frac{F}{A} = \frac{1.8544F}{d^2}} \qquad \textbf{Equation 2.1}$$

where F is the force in kilograms, A is the surface area of the resulting indentation in square millimeters, and d is the distance between the corner of the indent *imprint* in mm.

2.8.2 Indentation fracture resistance

The indentation fracture resistance is related to the toughness of the material, or the crack resistance. Materials properties such as grain size, presence of defects and porosity, or the presence of hard particles within the microstructure can define the crack pattern within the microstructure of a composite or an alloy. The concept that relates the length of the indentation cracks to the toughness of a material was first proposed by Palmqvist, while working with metal carbides and performing a Vickers indentation experiment. Two types of crack where observed, including one named after "*Palmqvist*" itself, and half-penny (also called medial cracks), that are shown in Figure 2.11.

Half penny cracks are a type of fracture seen in brittle materials, while Palmqvist cracks form predominantly in more ductile systems [44]. The crack formation has first been studied by Niihara et al [45], where several ceramic materials were used to determine the types of cracks, using the crack ratio between *length(l): indentation size(a)*; if the ratio is below 2.5 the material is believed to be more ductile in nature, however if the ratio is above 2.5 it is predominantly brittle.

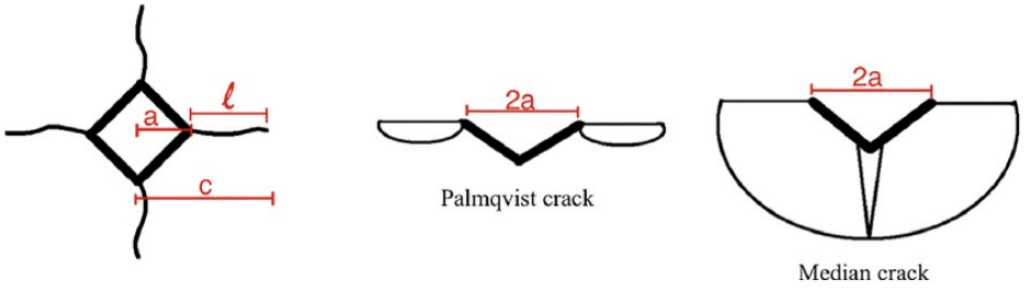

Figure 2.11 Types of cracks developed by Vickers indentation hardness. (a)Top view of Vickers indenter print (b) Palmqvist type crack and (c) Median or half-penny type crack [46].

Further development of more wear resistant and hard materials is a challenge in the development of novel cermets. Increasing hardness without the reduction of indentation fracture resistance is a challenge yet to be overcome. In this instance, flake-like materials such as graphene have been used, due to its properties related to increased hardness and as a crack barrier between grain boundaries, increasing the fracture resistance simultaneously.

2.8.3 Wear Damage

Wear is defined as damage in a surface caused by one or two surfaces in contact, and in relative motion. All materials have imperfections on the surface, that create a surface profile with a specific waviness and roughness. The “peaks” of contact between two surfaces are called asperities, defined as an unevenness of the surface. The scale of this roughness can be in km (for example a mountain) to nanometers (electropolished material) depending on the surface history of the material. During the wear process, there is transference of material from one surface to another or to the ambient environment, altering the physical and chemical properties, and generating loss of material. When the material removed from one of the surfaces is transferred to the counter face, a type of wear named adhesion wear is occuring [47]. Also, the removed material could potentially become loose, and stay in between the two surfaces as a third body, generating a three-body abrasion wear mechanism. Abrasive wear is caused by the interaction of a surface though abrasive particles, fluids, chemicals or heat [42]. Wear can also be combined with chemical reactions that

can either benefit the exposed surface or cause more damage [42]. In some cases, the resultant oxide layer can be protective against corrosion or be more wear resistant than the substrate bulk material.

The most common type of wear is mechanical. This can be classified as adhesion, erosion, impact and/or surface fatigue. Also, there is fretting wear, when adhesive and abrasive wear is combined. When the affected surface reacts with the ambient environment or the other surface, corrosion or oxidation of the surface generates a phenomenon defined as tribocorrosion. The adhesive type of wear is caused by fusion of face and counter surface contact area, which leads to fracture of the least strong surface. Fatigue wear is related to a cyclic force applied over the same surface area, which eventually leads to failure [48]. From a practical perspective, all wear processes are failure or damage of engineering surfaces.

To avoid excessive costs with failure of materials, several ways have been researched to control problems with wear and friction. A popular way of reducing wear is by the addition of a third body in between the two contact surfaces. The most used material is defined as "*lubricant*", most commonly making use of polymers with a long carbon chain, which creates a thin layer between the two moving surfaces, reducing the friction between the contacts [42]. Alternatives solutions add lubricants directly into the base material, which leads to a self-lubricated material that slowly release this substance over time when subjected to wear degradation. The used of a lubricant is one extra step during production or use of an engineer part, which can add significant cost for the final product [42]. In the next sections, each types of wear will be further explained in order of importance, starting from adhesive wear. Wear mechanisms tend to not happen in isolation; however, a separation must be made in order to study wear mechanisms more deeply.

2.8.3.1 Adhesive Wear

Adhesive wear is related to the contact between two asperities, which causes a high-pressure contact area due a low surface in contact with the applied load. This localized force eventually will cause a catastrophic failure and detach part of the material from one surface to the other, with material transfer to this new surface. Adhesive wear is characterized by high material removal rates and an unstable coefficient of friction [42]. The transfer of material occurs in both directions,

and eventually will result in the formation of a layer of loose material in between the contacts. This loose material can create further damage to the surfaces, increasing the wear rates or can help prevent surface damage by lubricating the sliding bodies, thus supressing wear of the surfaces. One of the most common types of failure due to adhesive wear is an absence of lubricant when needed, generating dry contact, adhesion of asperities and aggressive damage [49].

Adhesion wear of composites and engineering materials has a different mechanism when compared to classic materials. The adhesion wear is mainly controlled by the resistance against local plastic strain, which represents the resistance of the binder phase to hold the matrix of the composite. The stress caused by the load can cause the binder to be extruded from the surface and compress the composite matrix. The main factor that influences the wear rate by adhesion wear in these types of materials involve the resistance to the plastic strain [47].

Figure 2.12 shows the adhesion mechanism of a single asperity, where the exposed surface surffers adhesion, then is further removed by a counter surface with the higher yield strength. The removed particle then left a high angle asperity surface, that will be subsequently removed by similar mechanism. Studies that were conducted using SEM shows that the removed asperity may form a true wear particle that is removed or forms a third body that is transformed into a tribofilm between the two surfaces [50].

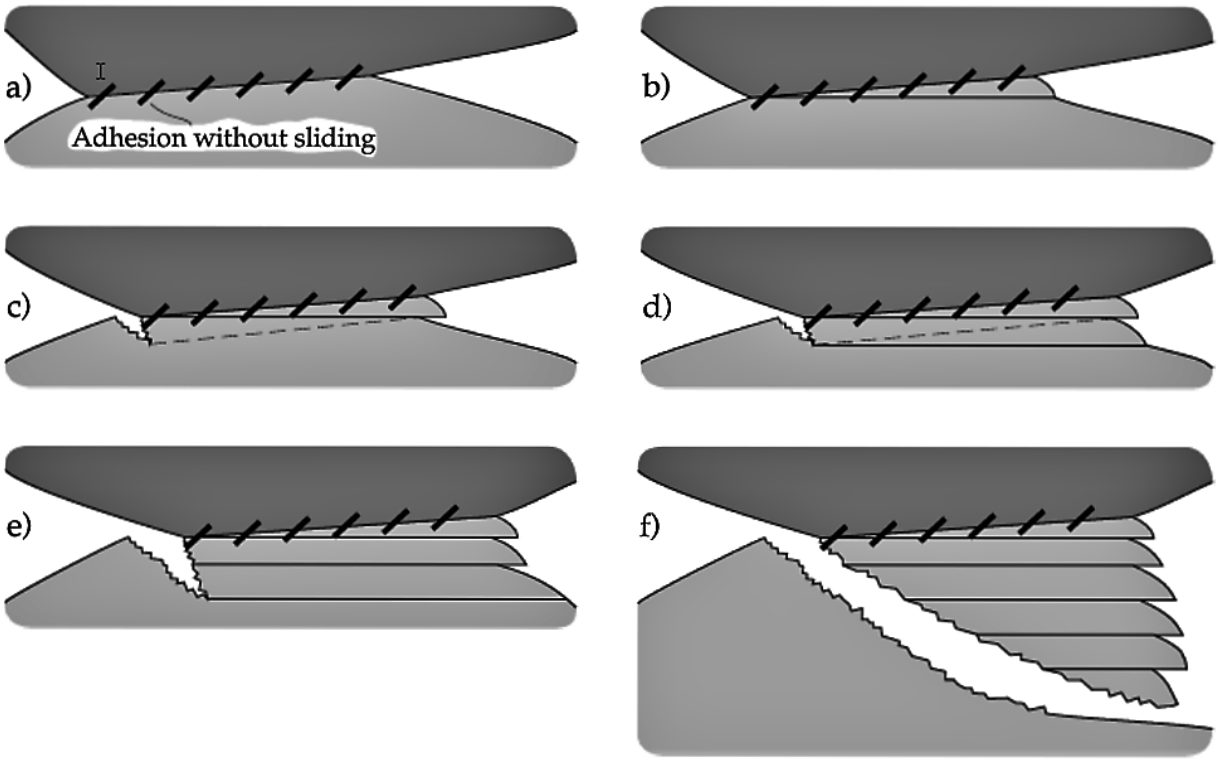

Figure 2.12 Mechanism of debris formation during adhesive wear [33].

2.8.3.2 Abrasive Wear

Abrasive wear is one of the most aggressive and common types of wear mechanisms that generate catastrophic failure. It most commonly occurs when fragments, particles or fluids, usually including brittle and high angle constituents, act as a third body in between two surfaces.

The solid object(s) that have equal or higher hardness tends to wear the one with lower hardness. Because of the small surface area in contact, the asperities are fractured in between the surfaces leaving a fingerprint, or a simple defect on the surface. Many of these phenomena cause abrasive wear. This process can be also initiated because of the asperities present in the surface of the material, when in contact with another surface cause plastic deformation and final displacement of material. For surfaces with very high hardness, the removed particle can be generated by catastrophic fracture, which generates micro-cracks in the materials and results in high wear rates [42].

The nature of abrasive wear is well identified by the macrostructure and groves in the surface of the worn material. In the literature, it is possible to identify two modes of abrasive wear: two- body and three-body abrasive wear. The main difference between the two modes is that in a two-body abrasive wear the asperities are rigidly attached to the surface of one body, on the other hand, for a three-body abrasive wear the abrasive particles are free to roll and slide under the two surfaces. The differences are demonstrated in Figure 2.13.

Previous reports show that there are significant differences between these two types of abrasive wear. Two-body wear could cause wear rates up to ten times larger than three body wear, due to the combination with other types of aggressive wear mechanisms [51]. Also, the hardness of the bulk material plays a significant role in three-body abrasive wear, but not as significant in the two-body type wear. Two-body wear has similarities with the cutting mechanism (to be discussed in a following section). Its suggested also that for the three body model, the debris is removed in successive layers in contact with the abrasive particles [52].

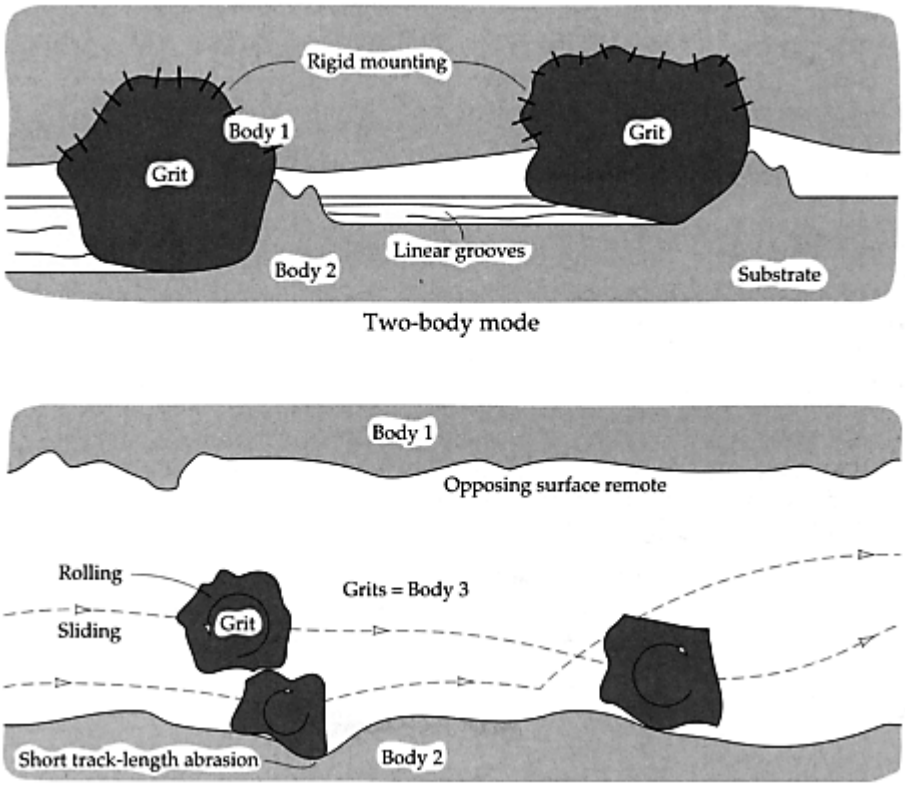

Figure 2.13 Two and Three body abrasive wear [54].

2.8.3.3 Erosive Wear

Erosive wear is caused when a solid and fluid impact a solid surface. Erosive wear happens frequently in particular types of industries that use particles or liquids moving in contact with a surface. Typical examples of erosive attack are in turbine blades in gas pumps and airplane turbines, oil gas pipes, mineral slurry systems and propellers of vessels [52,53]. The main variable of this type of wear are the properties of the eroding particles and the fluid.

2.8.3.3.1 Mechanisms of Erosive Wear

Erosive wear depends on several variables that are mainly defined by the material, size, velocity, and angle of impingement of particles onto the eroded surface. If the particle is harder than the worn surface, it is possible erosive wear will occur. When fluid and particles are present, there is a combination of fatigue and erosion wear [52]. As can be observed in Figure 2.14, the incident angle of the particle has a large influence on the type(s) of wear mechanism. At low angles, the particles tend to travel along the surface of the material. At high angles, the particles tend to break and damage the surface. High speeds are also responsible for higher abrasive wear rates.

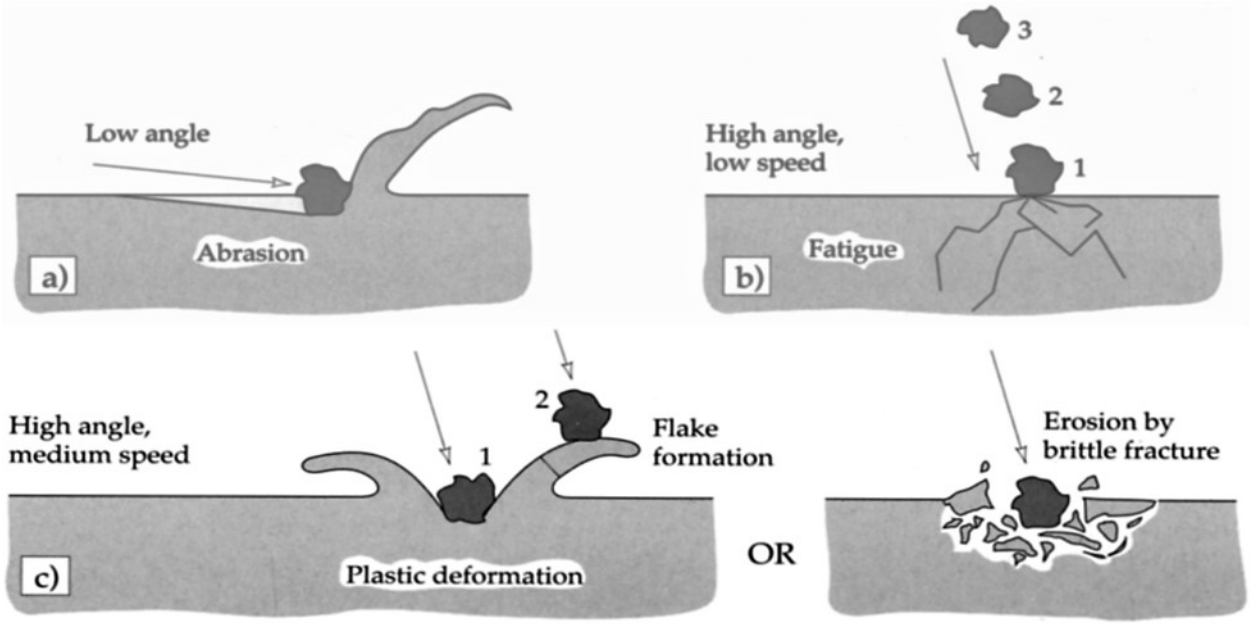

Figure 2.14 (a) erosive wear at low angles, (b) erosive wear at high angles and (c) plastic deformation and brittle fracture by multiple particle impact at medium velocities [54].

2.8.3.4 Corrosive and Oxidative Wear

The main characteristic of corrosive and oxidative wear is the chemical reaction between the worn material and atmosphere. The atmosphere could be in the form of humidity in the air, salt water from the sea, a chemical reagent or even a lubricant on/in the surface[55]. It is important consider that corrosive wear is a complex mechanism when compared to adhesive or erosive types for example, due to its relationship with other kinds of mechanical wear. This combination of wear mechanisms is called "*tribocorosion*". For some applications, the formation of a corrosive layer is used in favour of maintaining the surface integrity against other types of failure mechanisms. The surface oxide layer may reduce the coefficient of friction, which consequently tends to decrease the wear rates.

2.8.3.4.1 Corrosive Wear

The chemical reaction on the surface of the solids usually leads to a considerable loss of material underneath. If the surface is subjected to sliding motion, one of the following process may occurs: 1) a lubricating film may form, which inhibits corrosion and wear; 2) a passive *weak* film is formed and subsequently removed from the surface, repeating the process multiple times and causing high

wear rates; 3) a protective film is formed and may be worn by galvanic/pitting corrosion, where mechanical and corrosive wear will act independently removing material from the surface. The forms of interaction are illustrating in Figure 2.15.

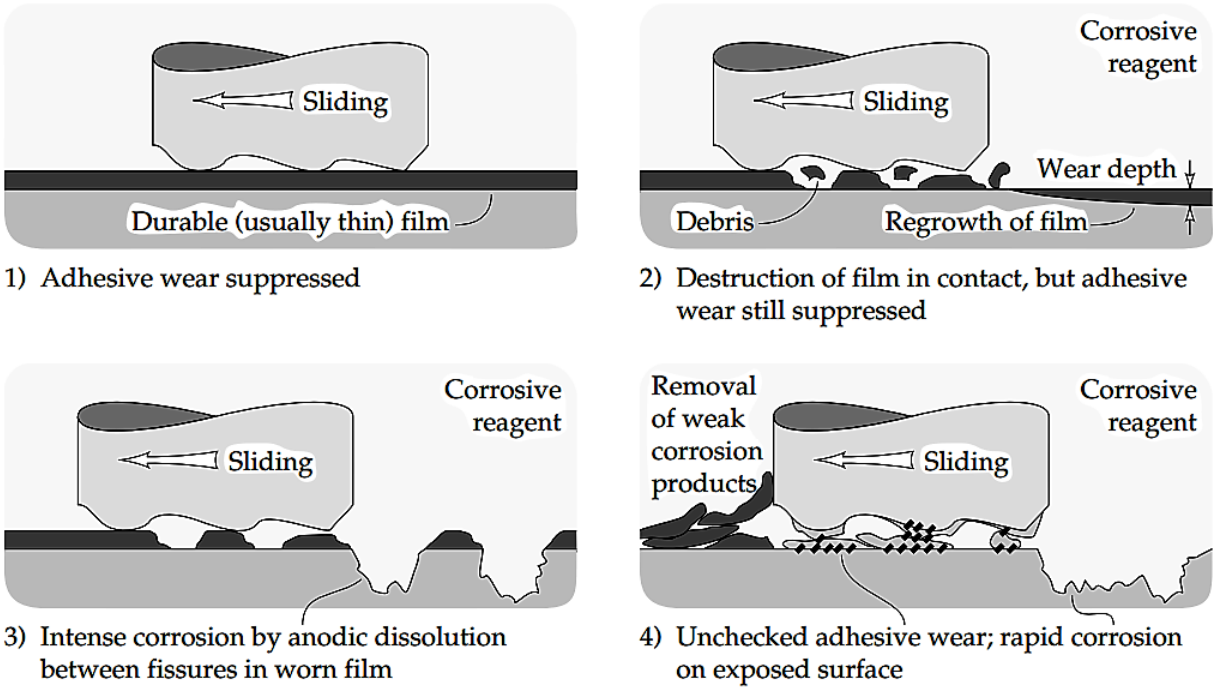

Figure 2.15 Methods of corrosion and sliding wear [56].

In the first case, a protective film is formed on the surface and further wear is supressed. This film prevents the material from suffering high wear rates in the first instance. In the ideal case, this films may protect the surface against wear in the case of high loads[57]. The second process in the Figure 2.15 is characterized by high corrosion rates, which results from the formation of a film with low mechanical strength that is constantly removed by wear, and at the same time a new corroded film is formed on the surface. This is the most common type of tribocorrosion mechanism. It is important to observe that most parts of corroded films are extremely brittle and protect the surface only while there is no mechanical stress [58]. The third process shows that wear mainly caused by highly reactive environments, where localized corrosion occurs on active areas and interfaces. The last process in the Figure 2.15 happens in situations when the surface is subjected to extremely corrosive environments, where corrosion products are very weak and

soluble in the liquid media. It is important to emphasize that corrosive-mechanical wear is mainly due to the short life time of the passive films formed on the surface [42].

In scenarios where the lubricant reactivity is low, adhesive wear can be predominant because of the lack of protective surface films. However, if the lubricant reactivity is too high, there is a wear rate associated with corrosive wear. Figure 2.16 shows that at specific sliding speed it is possible to obtain an *"engineering point"*, where the wear rate can be optimized at its minimum [59].

.

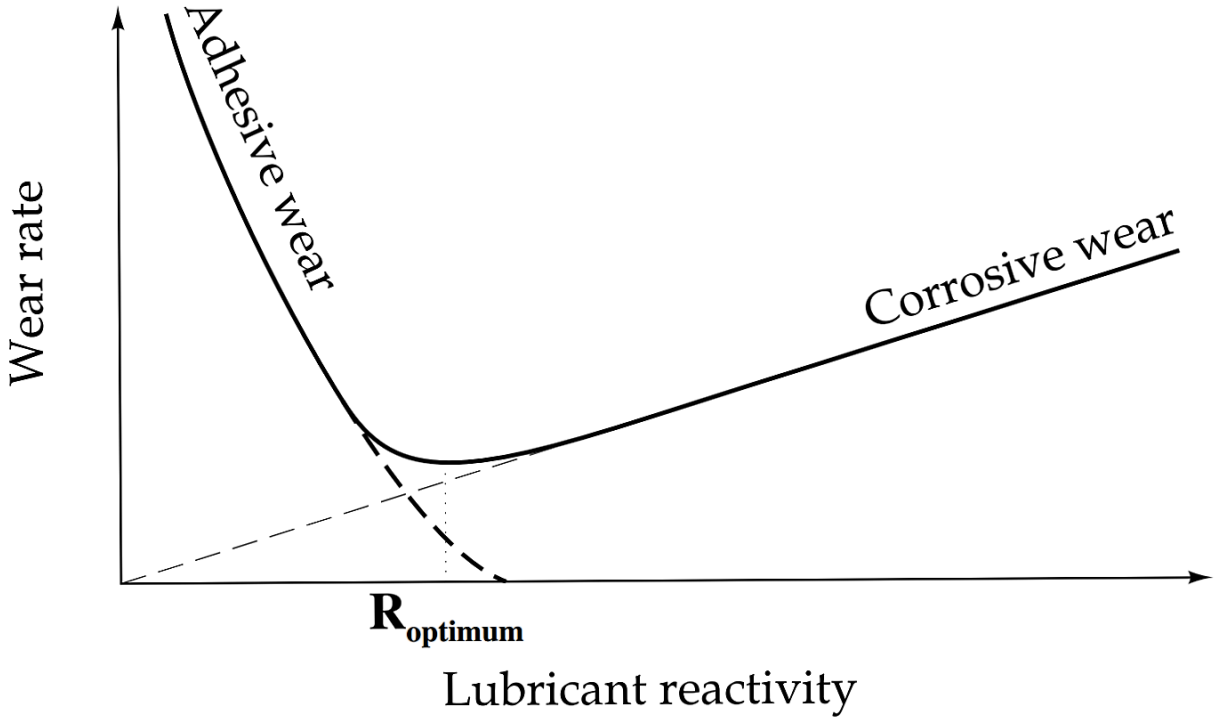

Figure 2.16 Wear rate associated with adhesive and corrosive wear based on lubricant reactivity [60].

Abrasion and erosion wear combined with corrosion due the repeated removal of passive (semi-)protective layers is one of the most aggressive types of wear reported in the literature. The synergism between corrosive and erosive/abrasive wear could potentially be important in applications such as oil pipes and in the mining industries due the extensive use of slurry-like materials. These fluids contain chemically active materials in a mixture of hard and brittle particles.

Lubricants contaminated with grits from mechanical wear, i.e. engines can also cause failure. The first model, where thin superficial layers of passive films are removed was proposed by Zelders [61] and is shown in Figure 2.25.

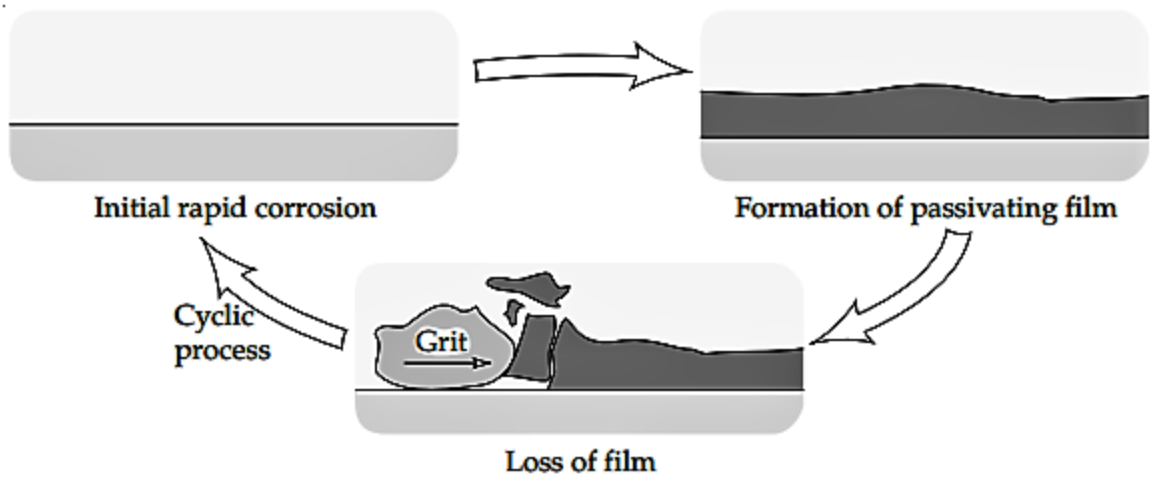

Figure 2.17 Cyclic wear mechanism by erosive/abrasive and corrosive wear [62].

This mechanism is prevalent when the corrosive mechanism alone results in wear rates higher than mechanical wear itself. In the other cases, the surface will wear due to abrasive/erosive mechanism(s) and the oxidation of the surface will be irrelevant [63].

2.8.4 Wear of Cermets

Cermets generally exhibit good resistance against oxidation and build up edge formation due to better chemical stability and high temperature hardness when compared to non-engineered materials [18]. WC-Co based hardmetals are tough and hard, however, they tend to have a high wear rate when applied in high temperature situations due to their lack of oxidation resistance and high levels of plastic deformation [18,64]. Several studies show that TiC-based cermets can be applied in such scenarios for high temperature abrasive wear resistance performance, high temperature hardness, good thermal chemical stability and thermal deformation resistance. These cermets can be particularly brittle, however significant toughness improvement could be achieved

by addition of selective binders such as Fe, Cr, Ni, Mo and special alloys, depending on the applications [18,65,66].

Some wear mechanisms such as binder extrusion, ceramic grain fracture and grain pull out are more frequently observed on cermets due to the presence of a ductile binder and a hard phase. When this material is subjected to high stress abrasive environments, limited plastic deformation of the carbide phases and a more significant deformation is seen in the binder. When a less intensive form of wear occurs, the material is removed by abrasion, leading to binder extrusion, ceramic grain fracture and/or pull out, and cracking by fatigue [67,68].

Fe-based alloys are a good choice among the chosen binders due to their low cost and good mechanical properties. For instance, WC-10wt.%Co, WC-10wt.%Ni, and WC-10 wt.% Fe all present very similar hardness and fracture toughness properties [69]. Studies have indicated that Co binders can be further substituted by Fe-alloys, however some challenges remain due to problems with hydrogen embrittlement, lower corrosion resistance and the high cost of sintering [70,71].

Ni based binders are one of the most widely used by industry. Ni-alloys and elemental Ni are responsible for significant increase in the toughness and ductility of the cermets. Other parameters such as easier densification and better corrosion resistance, coupled with lower cost and environmental impact are benefits of using Ni-based binders when compared to Co. Cardinal et al [3] have observed the wear resistance of TiC and Ti(C_xN_x) related to their friction coefficient. These materials have obtained high wear resistance, as shown in Figure 2.17, with wear observed rates values as low as $1.8x10^{-7}$ $mm^3/N.m^{-1}$. Other properties such as a reduction of the coefficient of friction are promising to further increase the wear resistance of these materials.

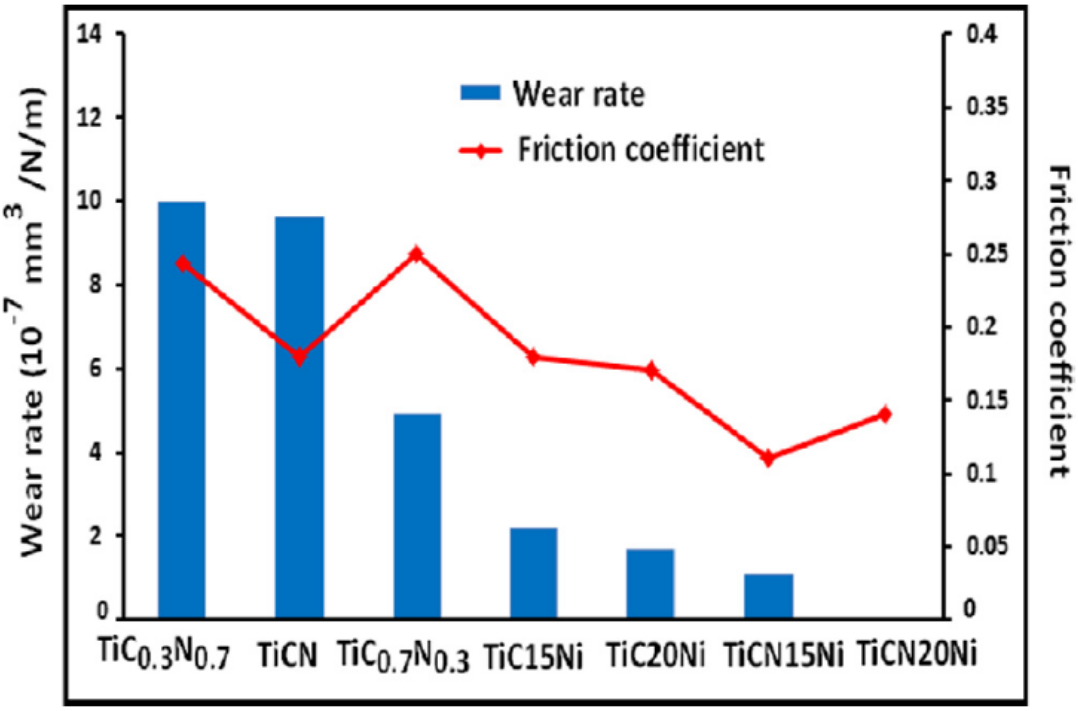

Figure 2.18 Wear rates and coefficient of friction for TiC-TiN based cermets [3].

CHAPTER 3 EXPERIMENT METHODOLOGIES AND ANALYSIS

This chapter gives the details relating to the methodologies used in this study. This includes characterization of the raw materials such as dry powders, including TiC, Ni, NiAl, Fe-316L, Fe-17-4 PH and graphene nanoplatelets, as well processing conditions and the final properties of the specimens after being sintered.

Properties related to the chemical composition, size and shape of the powders were analysed using SEM with EDS. In terms of the overall materials processing and characterization, the powder metallurgy process was used to produce the samples, while microstructure, and mechanical and wear properties were assessed using optical microscopy, SEM/EDS, Vickers hardness and universal mechanical testing (UMT) system. The crystallographic structure of the samples and raw materials were analysed by X-ray diffraction.

3.1 Raw Materials Characterization and Tested Compositions

The cermets in the current study have been prepared using commercially available powders. The following table outlines the powders used in these experiments, with their respective lot number, particle size and supplier information. The Ni_3Al intermetallic binder phase was produced using a reaction sintering approach, based on a Ni and Ni/Al powder blend [22–24,27].

Table 3.1 Powders used in the experiments and their respective size and manufacturer information.

Powder	**Lot or batch number**	**Particle size(μm)**	**Manufacturer**
TiN	L52737	1-2	Treibacher Industrie AG
TiC	45693	1-2	Treibacher Industrie AG
Ni	L10W013	2.2-3	Alfa Aesar
NiAl	D28X029	<150	Alfa Aesar
Mo_2C	PL71887718	1-2	Pacific Particulate Materials
GNPs	B#003	5-10	GIT Inc.
316L	18D0775	1-6	Sandvik Osprey Powders
17-4 PH	18D0788	1-6	Sandvik Osprey Powders

The microstructure and size of the individual powders and tested blends can be observed in Figures 3.1 – 3.7.

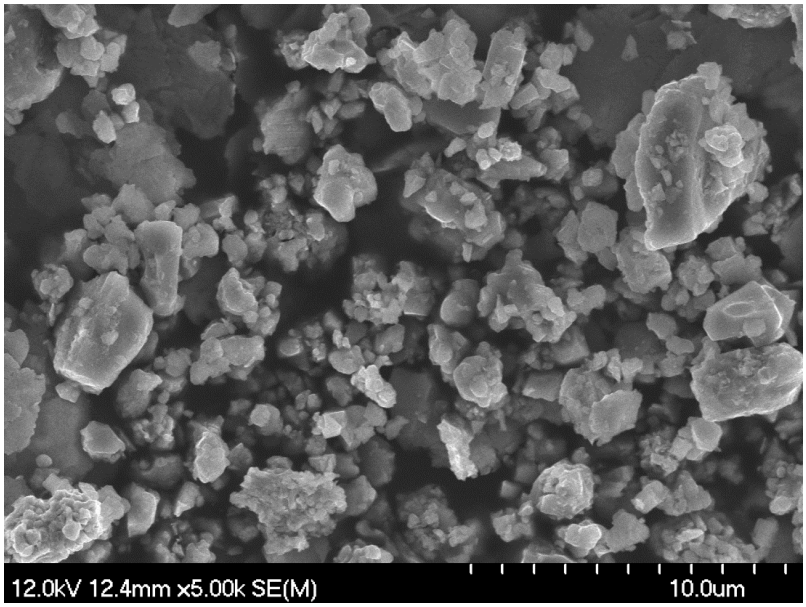

Figure 3.1 Representative SEM image of the as-received TiC ceramic powders.

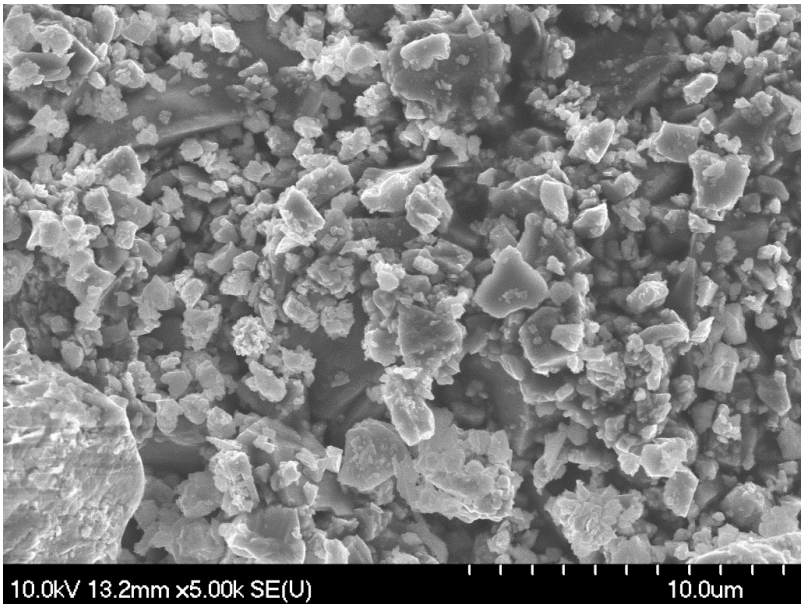

Figure 3.2 Representative SEM image of the as-received TiN ceramic powders.

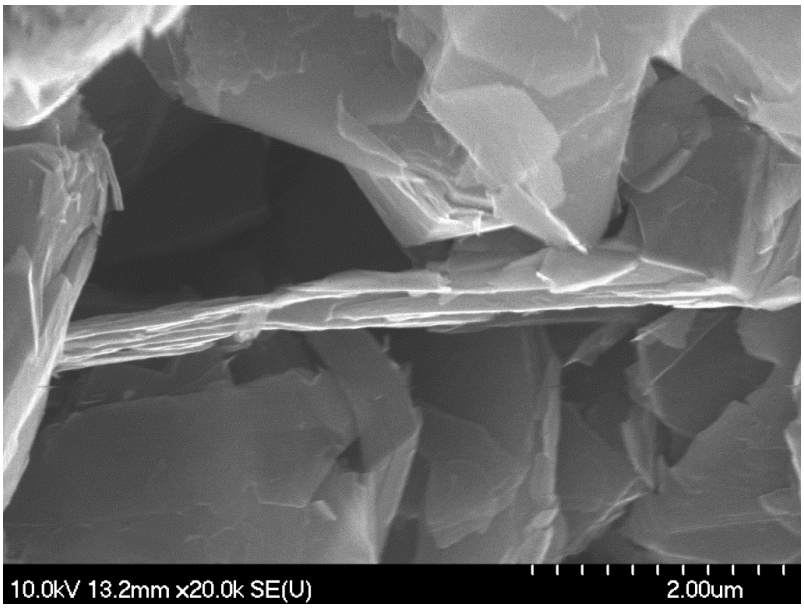

Figure 3.3 Representative SEM image of the as-received Graphene nanoplatelets.

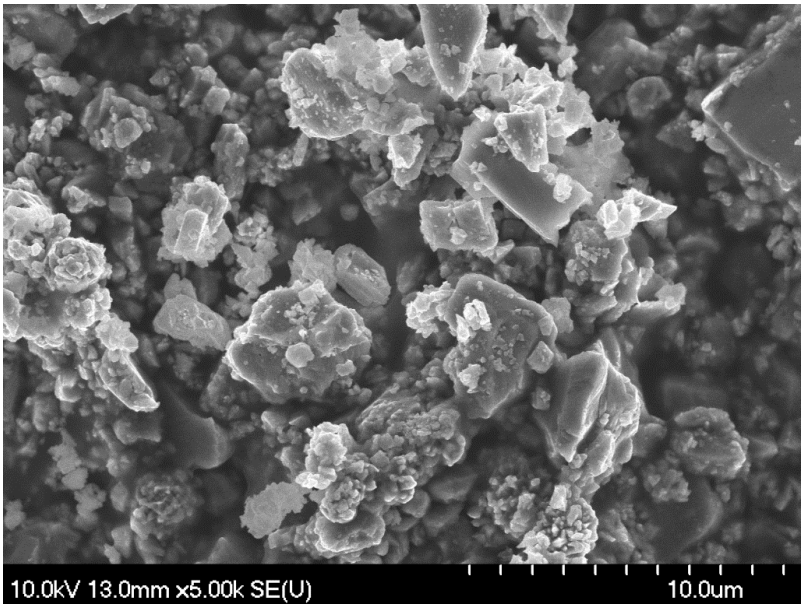

Figure 3.4 Representative SEM image of the powder mixture of TiN – 30 vol.% non-stoichiometric NiAl-Ni-10 vol% Mo_2C powders mixture.

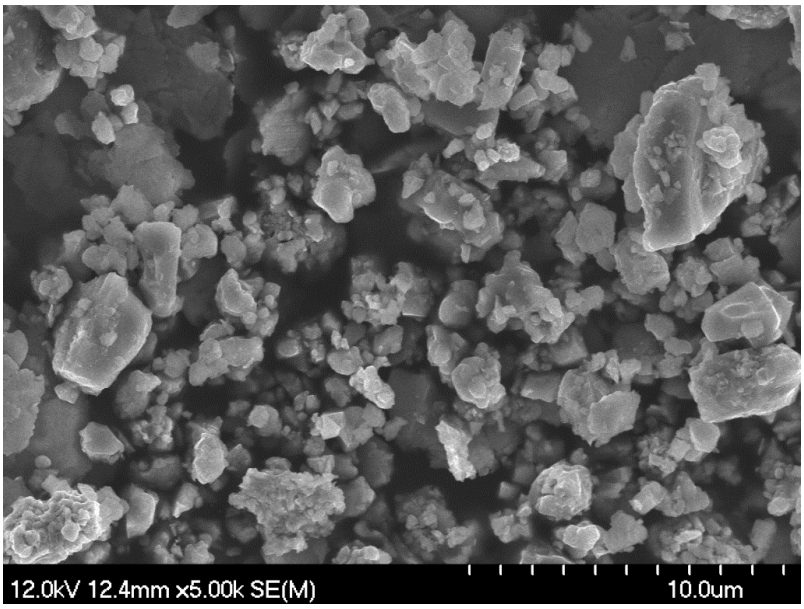

Figure 3.5 Representative SEM image of the powder mixture of TiN – 30 vol.% Ni_XAl-Ni powders.

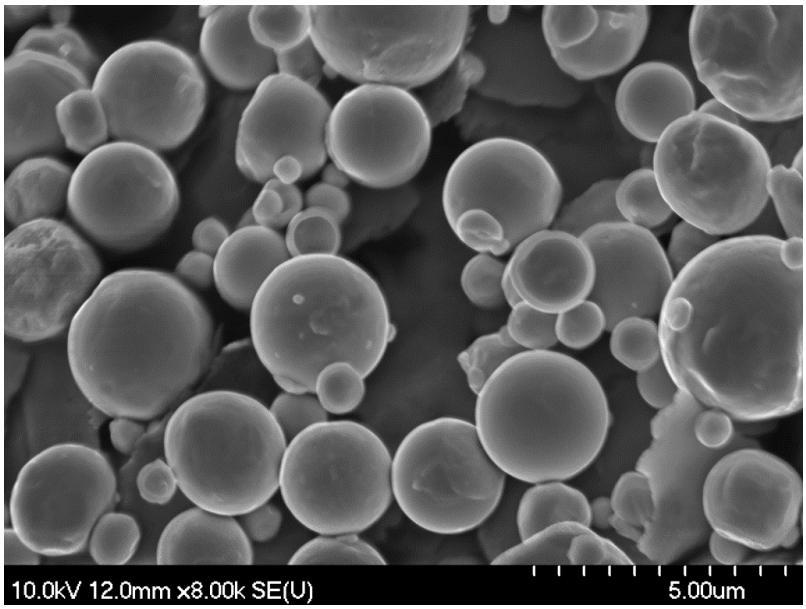

Figure 3.6 Representative SEM image of the as received pre-alloyed 316L powders, sized from 1-6 μm.

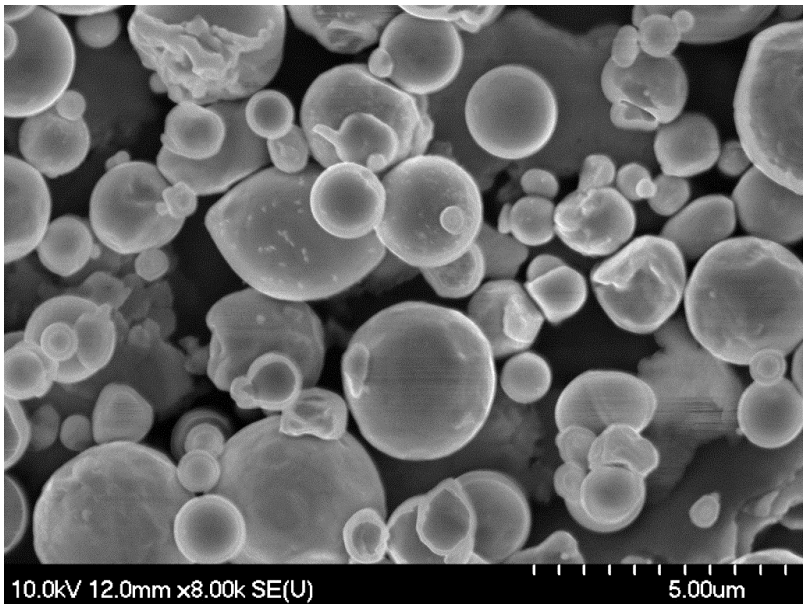

Figure 3.7 Representative SEM image of the as received pre-alloyed 17-4 precipitation hardening powders, sized from 1-6 μm.

The powder blends tested in this work are shown in Table 3.2, classified based on their category: ceramic phase, binder phase and noble particles additions.

Table 3.2 List of powder blends and their volume fraction of the experimented tested compositions.

Composition ID	**Ceramic phase**		**Binder phase**				**Particles addition**
Vol.%	TiC	TiN	Ni_3Al	Mo_2C	316L	17-4 PH	GNP
TiC- Ni_3Al	70		30				
TiC - 316LSS	70				10		
TiC - 316LSS	80				20		
TiC - 316LSS	90				30		

TiC - 17-4 PH SS	70			10	
TiC - 17-4 PH SS	80			20	
TiC - 17-4 PH SS	90			30	
TiC - Ni_3Al - GNP	70	29.75			0.25
TiC - Ni_3Al - GNP	70	29.50			0.5
TiC - Ni_3Al - GNP	70	28.75			1.25
TiC - Ni_3Al - GNP	70	27.50			2.5
TiN - Ni_3Al - Mo_2C	70	30			
TiN - Ni_3Al - Mo_2C	69.5	30	0.5		
TiN - Ni_3Al - Mo_2C	68.75	30	1.25		
TiN - Ni_3Al - Mo_2C	67.5	30	2.5		
TiN - Ni_3Al - Mo_2C	65	30	5		
TiN - Ni_3Al - Mo_2C	62.5	30	7.5		
TiN - Ni_3Al - Mo_2C	60	30	10		

3.2 Cermet Fabrication and Characterization

The next sections show in detail the methodology applied to produce and characterize the tested cermet compositions outlined in Table 3.2. The flow chart in Figure 3.8 shows the main steps involved in the fabrication of the cermets for this work.

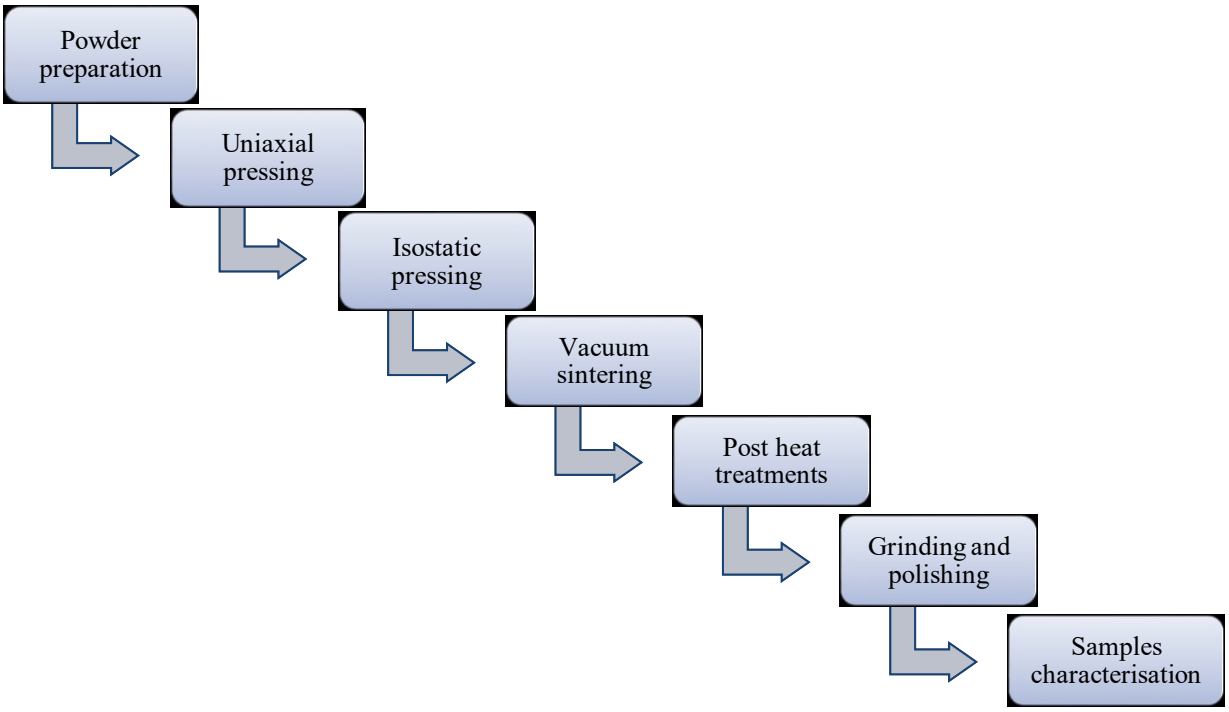

Figure 3.8 Flow diagram of the steps to produce the samples.

3.2.1 Cermet Sample Preparation

The powders blends listened in Table 3.2 were mixed in 50 g batches, with an addition of 0.5 wt.% polyvinyl butyral (PVB) wax in order to increase green strength and particle rearrangement during compaction. The powder blends were ball milled in acetone for 24 hours at 60 RPM, using yttria stabilized zirconia milling media (Ø = 10 mm), with a 10:1 ratio of mass media/powder. The samples were then dried in a fume hood for 24 hours and sieved through a 75 μm mesh to eliminate large particles and promote uniformity in the sintering process. The processed ratio between the ceramic, binder and additions typically had always a constant factor, to study the effect of either the binder phase, the ceramic phase or a specific post heat treatment to achieve the most desirable wear properties according to previous publications [72,73]. The exception to this was when GNPs were added to the TiC-Ni_3Al composition (Table 3.1). The dried and sieved powders were subsequently compacted in a uniaxial press (Model S/N 41000-102, Carver Inc., Wabash, IN, USA) with an applied load of 69 MPa (10,000 psi) into disc-shaped pellets with geometry and

dimensions of 20 mm diameter and ~5 mm thick or 31.75 mm diameter with a ~6 mm thick samples. For assessment of sliding wear behaviour, cylindrical-shaped test specimens (~4.24 mm diameter × ~10.56 mm length) were used. The pellets were then compacted in a cold isostatic press (CIP) (Model S/N-101462-1, Avure Technologies Inc., Franklin, TN, USA) at 207 MPa (30,000 psi), held for 30 seconds to achieve a green density of 60 % ± 5 % of theoretical and enough green strength to be transfered to the vacuum sintering chamber.

The sintering and post heat treatments were performed in a R.D. Webb Red Devil® vacuum furnace (Materials Research Furnaces, Suncook, NH, USA) under a maximum of 5 x10^{-4} Torr dynamic vacuum atmosphere. Heating and cooling rates of 20 °C/min were used. Below ~800 °C the furnace naturally cools down.

After sintering, the immersion densities of the specimens were determined using Archimedes' principle, in water (at 24 °C); a minimum of three samples were produced and measured for each compositional variant to assess reproducibility, with each sample density determined three times. The specimens were then ground and polished down to a surface profile of about 1 µm using a 0.25 µm using diamond paste. The Archimedes' principle equation is shown in the following:

$$p = \frac{p_w}{1-(w_w/w_a)} \qquad \textbf{Equation 3.1}$$

where p is the density, p_w is the density of water, w_w is the weight of the object in water and w_a is the weight of the object in air.

3.2.2 Sintered Microstructure

Figures 3.9 and 3.10 present examples of the sintered samples using two of the experimented binders, namely Ni_3Al and 316L stainless steel. The light gray phase represents the metallic binder additions and the dark gray phase represent the TiC grains. A highly spherical ceramic phase is characteristic of the stainless-steel binder, rather than an angular TiC microstructure when Ni_3Al binder is used, where the grains retain the angular shape of the particles. This suggest that the TiC-316L system has a higher relative associated surface energy, being more reactive [1,2].

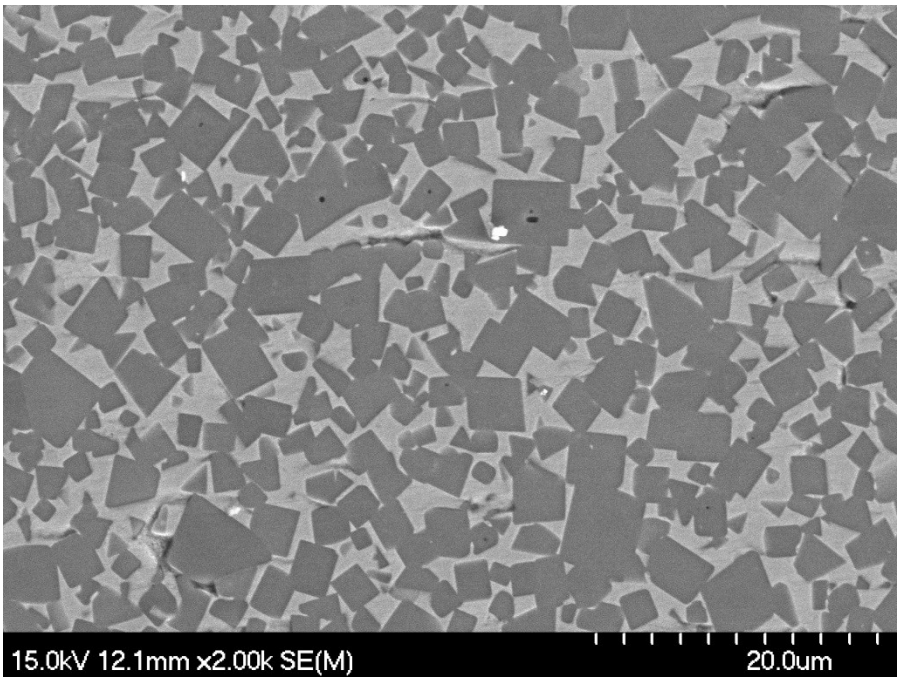

Figure 3.9 Typical TiC 30vol.% Ni_3Al sintered microstructure.

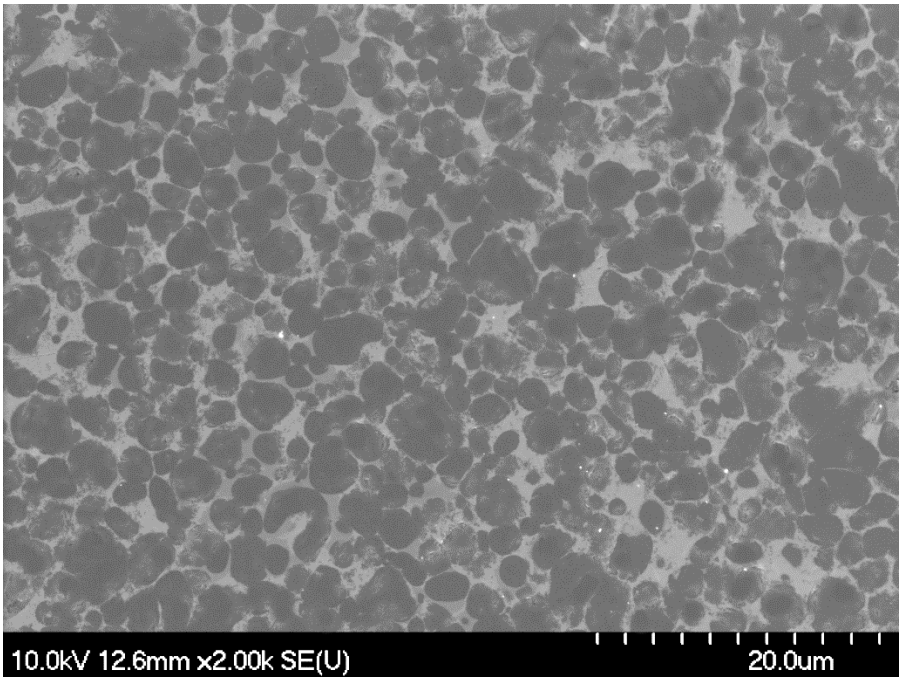

Figure 3.10 Typical TiC 30 vol.% stainless steel (316L) sintered microstructure.

3.2.3 Hardness and Fracture Resistance

The Vickers hardness of the polished cermets was determined by applying a load of 1 kg, following ASTM 1327-15. The low applied indenter load helps to avoid significant cracking around the indent corners, with the sample subsequently analysed using optical microscopy for precise indentation size measurement.

The indentation fracture resistance (IFR) was also assessed using the Vickers indentation method, with an applied load from 30 to 50 kg. The IFR was determined by using both the approach proposed by Anstis et al. [74] and also that of Niihara [45]. The two approaches were used to fully assess the crack behaviour of the cermets in order to know the transition from brittle median cracking (i.e. c:a >2.5), expected at lower binder content, to more ductile Palmqvist cracking (i.e. c:a< 2.5), expected at higher binder contents (here c is the indentation crack length and a is the indent diagonal). The following diagram (Figure 3.11) shows the types of cracks observed. A representative of the hardness measurement and characteristic cracks on the edge of the Vickers indenter is shown on Figure 3.12

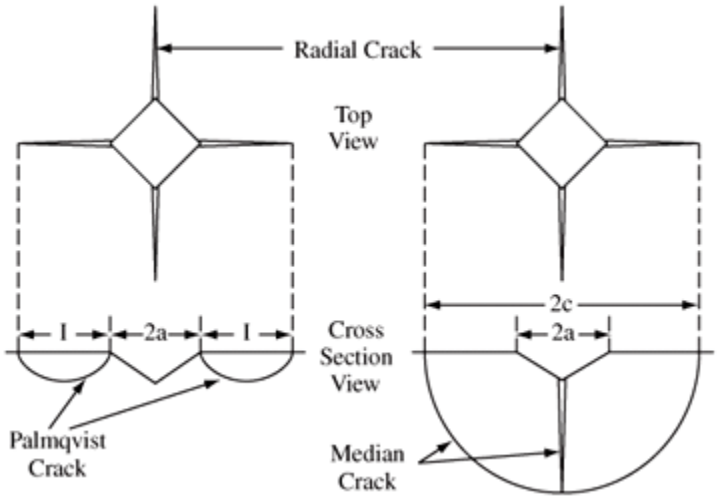

Figure 3.11 Crack formation by Vickers hardness indentation [3].

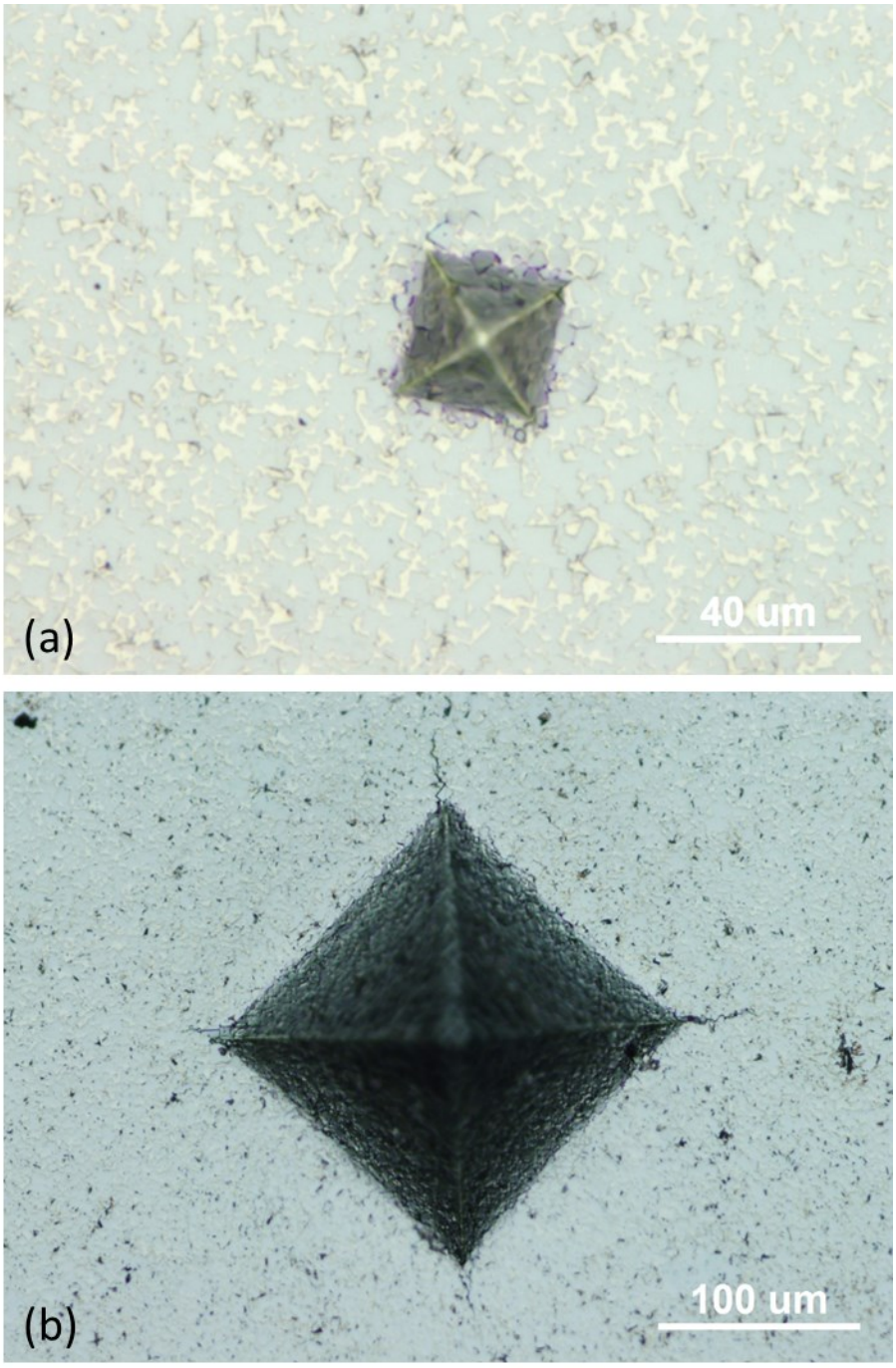

Figure 3.12 Vickers indentation representation for (a) 1 kg and (b) 50 kg on the surface of a TiC-Ni_3Al sample. Note the cracks on the edge of the indenter imprint.

3.2.4 Wear Testing and Analysis

Assessment of the wear performance of the synthesised composites was performed using a Universal Micro Tribometer (UMT; Bruker Corporation, Campbell, CA, USA), specifically with the scratch module using a Rockwell diamond indenter (with a tip radius of 200 μm). The schematic of the equipment setup is shown in Figure 3.13.

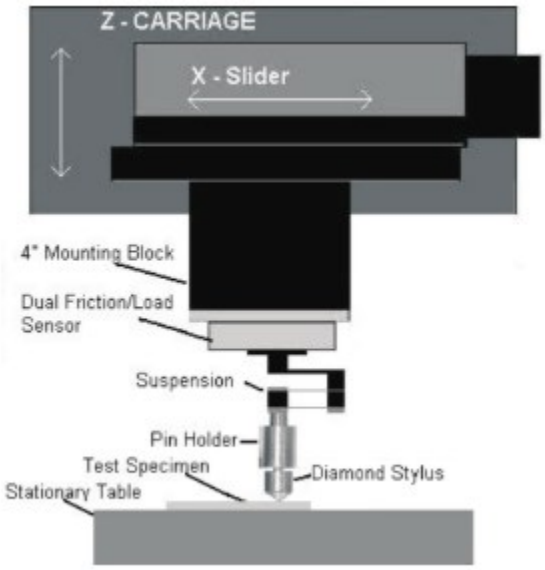

Figure 3.13 Schematic of the UMT instrument when used for scratch testing (Image source from: ASTM G171-03 Scratch hardness G171-03 Scratch Test Method for Scratch Hardness of Materials Using a Diamond Stylus on the Micro-Tribometer).

Using the scratch module, a single pass of 5 mm length was performed, with a sliding speed of 0.166 mm/s, under operating conditions of room temperature and relative humidity from 40-50% in all the experiments. The applied loads were varied from 10 up to 100 N, to generate the scratch tracks. Related data was obtained from the associated UMT software, providing dynamic numerical values for the depth of the indenter versus the applied force nominally continuously during each test. Moreover, the coefficient of friction, dynamic load and scratch depth were subsequently extracted through the digital data-acquisition system obtained from the UMT test equipment.

For assessment of sliding wear behaviour, cylindrical-shaped test specimens (~4.24 mm diameter × ~10.56 mm length), were placed into the sample holder of an 'in-house' designed and constructed block-on-ring system. A counter-face ring (grade WC-6Co) was obtained as a "standard" tribo-pairing system against the specimen, with the WC-6Co rings obtained from Endurance Carbide Inc.

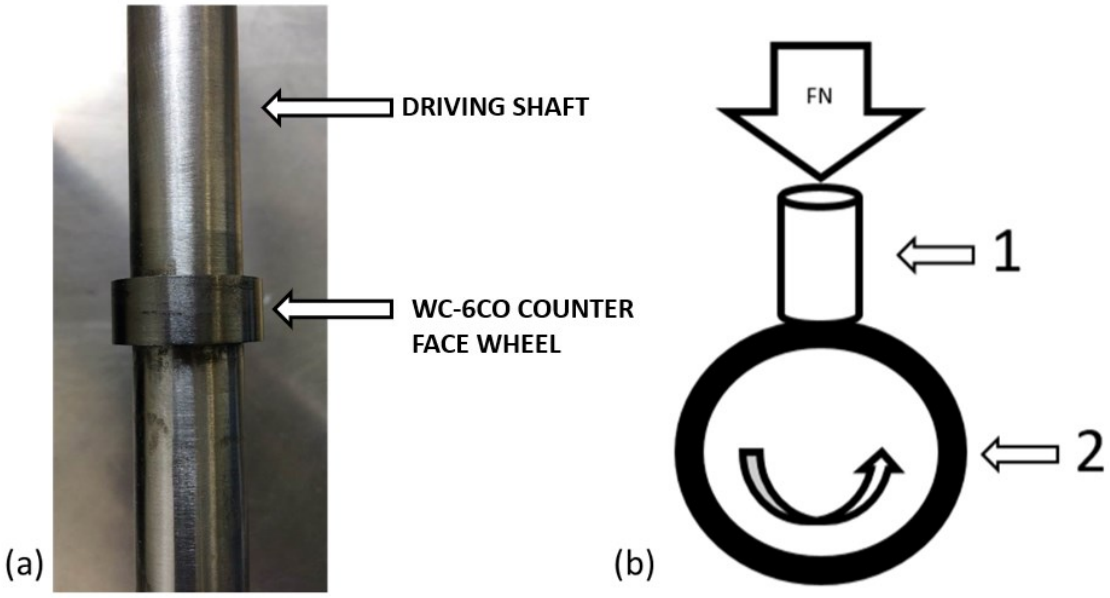

Figure 3.14 (a) Block-on-ring (grad) attached to the driving shaft of sliding wear system. (b) Schematic representation of the block-on-ring wear tester used in the experiment. 1 test specimen and 2 counter-face ring.

To access the wear rate of the samples the following procedure was undertaken. Both the samples and the counter-face ring were ground to a mean surface roughness of ~5 μm prior to the test. The initial weight and weight of the sample was then measured at 5 min intervals for up to 45 minutes total test duration, with a precision of 0.0001g. The measured weight loss is then converted into a material volume loss (V) by dividing by the material density (p), and then further used to calculated with specific wear rate using the Lancaster equation.

$$k = \frac{V}{PS} \qquad \textbf{Equation 3.2}$$

where k is specific wear rate in $mm^3 N^{-1} m^{-1}$, P is the applied load and S is the total sliding distance. For all tests, the rotation speed of the WC-Co counter-face wheel was maintained constant at 210 rpm, with an applied load of 100 N. The full test duration of 45 min corresponds to a total sliding distance of 540 m.

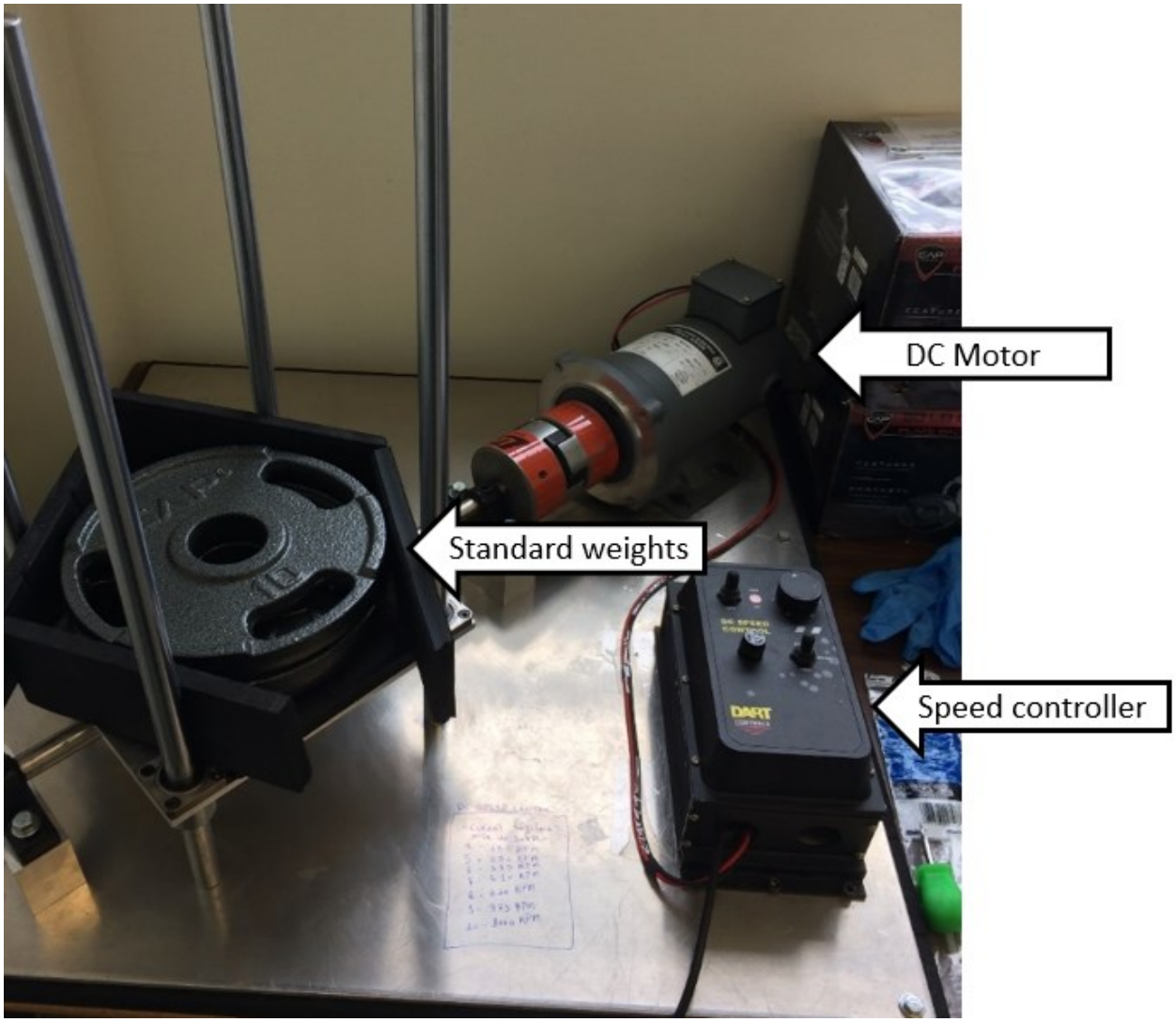

Figure 3.15 'In-house' designed block-on-ring sliding wear system. Note the sample and driving shaft are shown in Figure 3.14.

The wear performance was then evaluated using SEM to observe the damaged area and wear mechanisms. The depth and surface characteristics were measured using a three-dimensional confocal laser scanning microscope (CLSM; Keyence VK-X100K; Keyence Company, Osaka, Japan). The regions of interest was ~0.705 × 3.3 mm (i.e., 2.32 mm^2). The resolutions of the

measurements were 0.05 µm in x- and y-dimensions and 0.02 µm in the z-dimension (vertical direction). For each selected region of interest, the upper and lower limits of the laser scan were focused to the highest and the lowest elevation levels within the selected area.

The average width of the scratch track is measured using FE-SEM, and the scratch hardness number, *HSp*, was then determined using the relationship:

$$HS_p = \frac{8P}{\pi W^2} \qquad \textbf{Equation 3.3}$$

where P is the applied normal load and W is the scratch width.

The various damage mechanisms were then examined at higher magnifications within the SEM, inside the area of the scratch track, where it is possible to gather information about the main wear mechanism(s) of the evaluated cermet material. Mechanisms such as grain pull out, intra-granular grain cracks, binder extrusion and others are quantified and described.

3.2.5 X-Ray Diffraction Analysis

The crystallographic phase evaluation of the polished cermet surfaces and powders used in this work were conducted using X-ray diffraction (XRD; Bruker D-8 Advance Bruker Corp., Billerica, MA, USA), under CuKα radiation, operating at 40 kV and 40 mA, with a scanning range (2θ) from 20 to 80º.

For the GNP particles, an estimation of the average thickness of the flakes was calculated by the mean height of the crystallite (L_c) in the direction of the c-axis according to the Scherrer equation [26]:

$$L_c = \frac{0.89\lambda}{\beta \cos(\theta)} \qquad \text{Equation 3.4}$$

where λ is the X-ray wavelength (i.e., 1.5406 Å for CuKα), β is the full width at half maximum (FWHM) height of the peak (in radians), and θ is the Bragg angle.

3.2.6 Thermal analysis

3.2.6.1 Differential Scanning Calorimetry (DSC) and Thermogravimetric analysis (TGA)

To evaluate the sintering phase evolution, selected compacted samples were sintered in the DSC/TGA system (Model Q600 SDT, TA Instruments Ltd., New Castle, DE, USA). The chamber was kept under an Ar (99.99%) atmosphere, with a constant flow rate of 100 ml/min. The DSC chamber was purged at least twice before each run to avoid sample oxygen contamination from the atmosphere. The samples were normally heated up to 50 ˚C for 20 minutes to equilibrate heat flow measurements, then heated up to 1500 ˚C at a heating rate of 20˚C/min, kept for 1 minute at maximum temperature, and cooled down to room temperature at 20˚C/min according to the Figure 3.16. A minimum of three samples were studied to ensure reproducibility.

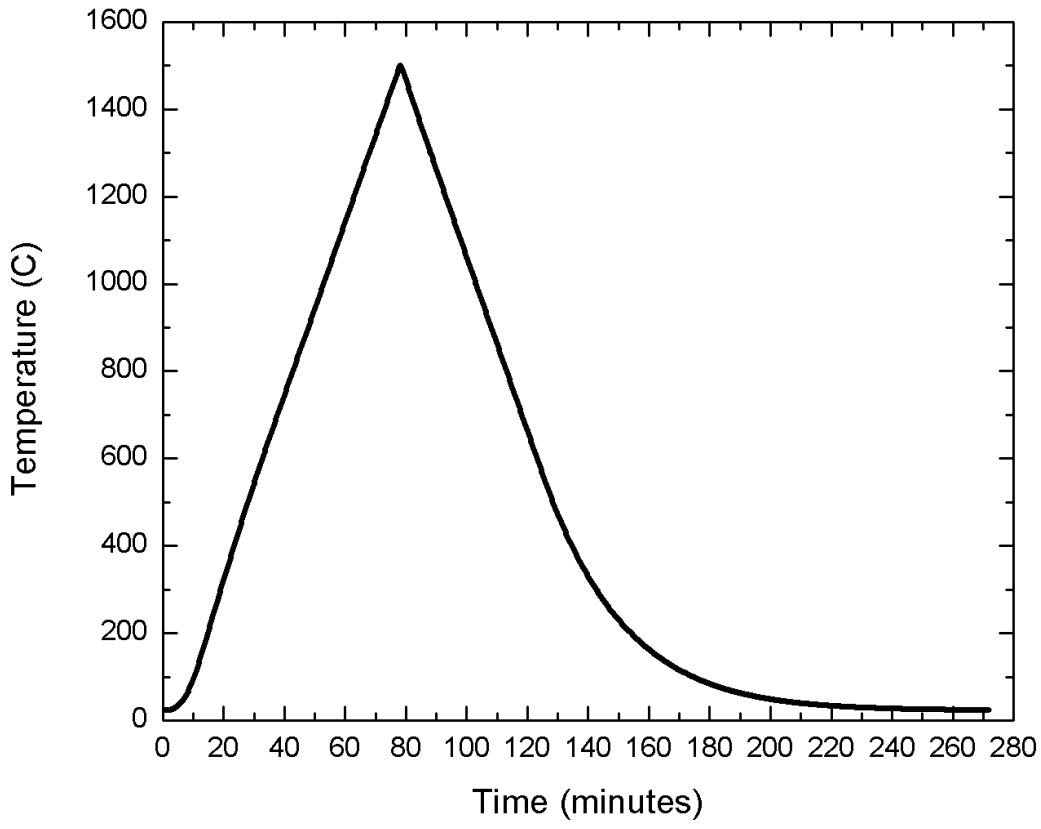

Figure 3.16 DSC temperature profile used on the experiments.

3.2.6.2 Dilatometry

The expansion/shrinkage response of the various cermet compositions during sintering was assessed by dilatometry (Model 401C, Netzsch Instruments, Germany). The dilatometer samples were compacted in a uniaxial single action press using a 6.38 mm diameter hardened steel die, at a compaction pressure of ~100 MPa. The lengths of the dilatometer samples were 10 mm. Sintering was conducted under a dynamic vacuum ($< 1\times 10^{-3}$ mbar), with the samples heated at a rate of 20 °C/min to 1500 °C. Cooling was conducted at a nominal rate of 20 °C/min. During sintering samples were supported in the dilatometer on an Al_2O_3 cradle, with two Al_2O_3 discs in contact with the Al_2O_3 pushrods of the dilatometer, as shown in Figure 3.17. The cradle and plates were coated with a protective yttria (Y_2O_3) layer to prevent any bonding with the samples. A minimum of three samples of each cermet composition were sintered in the dilatometer to ensure test reproducibility. All the experiments were performed using alumina (aluminum oxide) coated with yttria (yttrium oxide) on both sides of the samples to reduce possible adhesion between the samples and the crucible.

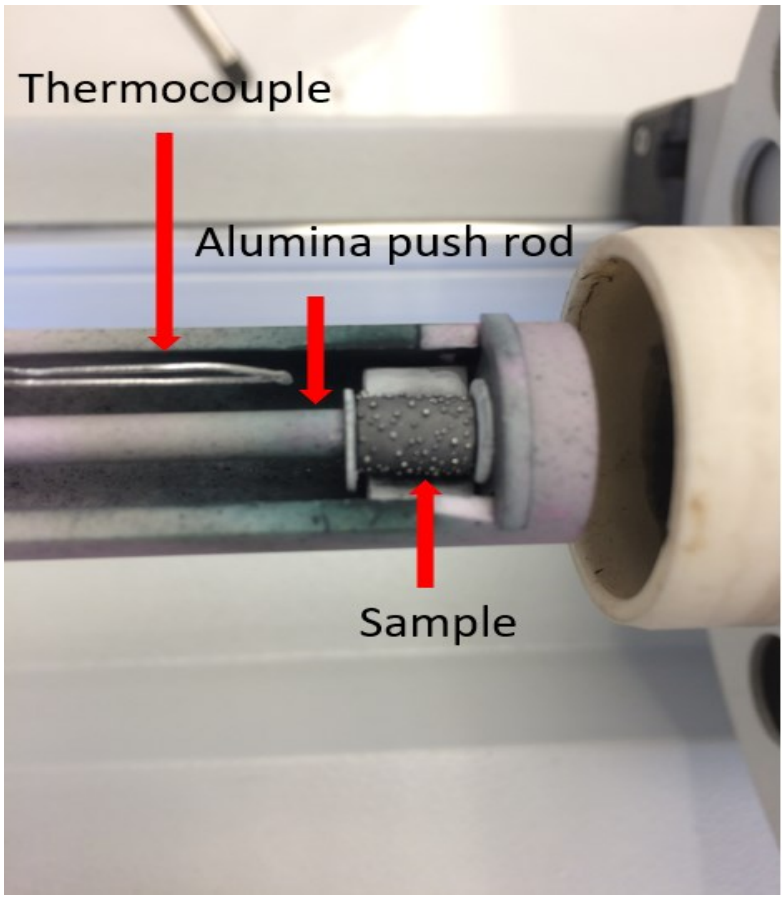

Figure 3.17 Schematic showing sample arrangement inside the dilatometer furnace.

3.2.7 Raman spectroscopy

Raman spectroscopy was performed with the goal to confirm the quality and number of layers of the GNPs used in the cermet compositions. For that, T64000 Raman spectrometer (Horiba Scientific Jobin Yvon, Edison, NJ, USA) instrument was selected to run the experiment. A 632.8 nm HeNe laser (JDS Uniphase Corp., Nepean, Ontario, Canada), with a power of 1.6W and incident through a 100x objective lens, was used to analyse the GNP spectra and estimate the number of layers. Five scans were averaged over 20 s for each measurement.

CHAPTER 4 THE INFLUENCE OF Mo_2C ADDITIONS ON THE MICROSTRUCTURAL DEVELOPMENT AND SINTERING RESPONSE OF TiN-Ni_3Al CERMETS

Status: *Published:* International Journal of Refractory Metals and Hard Materials, 71(2018) 262-272.

Abstract

The objectives of this work were to assess the effects of incorporating Mo_2C additions into TiN-Ni_3Al cermets, in terms of their densification response and microstructural development. The individual powder components, together with the milled/compacted powder blends were characterised using differential scanning calorimetry and thermogravimetric analysis. Dilatometry was used to determine the densification and sintering response. It is demonstrated that an increase in the Mo_2C content reduces both the melting and solidification temperature of the Ni_3Al-based component of the system, which is initially formed via reaction sintering. Crystalline phases were identified using X-ray diffraction, which demonstrated that TiN and Mo_2C are retained following sintering, and confirmed the formation of Ni_3Al. The wettability of the Ni_3Al binder was improved through additions of Mo_2C, enhancing the densification process. A simple microstructural development model has been outlined, proposing that the Mo_2C dissolves during liquid phase sintering, and re-precipitates as a shell on TiN grains either during sintering or solidification, which improves the wetting response between the nitride phase and intermetallic binder.

Keywords: liquid phase sintering; wetting; differential scanning calorimetry; dilatometry;

4. 1 Introduction

Ceramic-metal composites, or cermets, are widely used in industrial applications requiring high hardness and wear resistance [75], including their use as coatings on a wide variety of metallic substrates [76]. These applications include implementation as cutting or machining tools, bearings, wear resistant coatings, etc. However, many factors can impact the performance characteristics of advanced cermets, including their phase composition, the ceramic grain size and shape, and the

metallic binder content and composition [32]. The extent of densification of the final component is particularly important in terms of mechanical strength and tribological performance, and processing approaches are invariably designed to achieve near theoretical densities wherever possible [31].

The ultimate physical characteristics are determined by the constituents used to comprise the cermet, with the ceramic phase often based on high elastic modulus compounds such as carbides, borides or nitrides [13]. Similarly, the interactions between the ceramic and metallic phases are extremely significant for the successful production of fully densified cermets, which are typically processed by liquid phase sintering [33]. Consequently, the relative wettability and solubility between the phases are important factors to consider during the sintering stage [32,40]. With the right conditions, it is possible to obtain a cermet with essentially full density, and therefore the potential for use in high wear resistance applications. As an example, tungsten carbide-cobalt (WC-Co) cemented carbides have been widely developed for structural wear resistance [77]. WC-Co materials have been used in bulk form, and as coatings, typically deposited using high velocity oxyfuel (HVOF) thermal spraying [78,79]. These cemented carbides are invariably processed using liquid phase sintering, with the Co phase having some solubility for W and C [80]. However, WC-Co has a high density (typically ~13 g/cm^3), together with relatively poor corrosion and oxidation resistance, and elevated temperature strength [81]. Consequently, alternative cermet systems are being continuously developed and evaluated.

Titanium nitride (TiN) is one example of a relatively light weight, high hardness ceramic phase that can be envisioned for use in cermet applications due to its characteristics [82]. However, the classical powder metallurgy fabrication process is relatively rarely used for TiN on its own, as the resulting ceramic is quite brittle and low mechanical strength bodies result [83]. As an alternative, it is potentially desirable to synthesise high performance TiN-based materials that have desirable mechanical properties through development of TiN-metal composites [83,84]. To demonstrate the potential of TiN as a structural material, TiN-based coatings have also been successfully deposited using a variety of techniques, including physical vapour deposition [85], reactive plasma spraying [86], and HVOF [87] techniques. In terms of cermet development, one potential issue with the use of TiN is that it is not wet particularly well by molten metals [4]. It is important that the metallic phase must have low contact angle with the ceramic particles during sintering (i.e. the system wets well when molten). However, it has been reported that a variety of molten metals and alloys have

high contact angles with TiN substrates [37,40]. For the TiN-Ni system, it has been demonstrated that this problem can be largely alleviated through additions of molybdenum carbide (Mo_2C), which can decrease the contact angle to values close to 0º [80]. Beyond the wettability, it is also necessary to maintain only limited solubility of the ceramic phase in the molten metal, to achieve successful liquid phase sintering [32]. If the solubility is too high, then shape distortion is likely during liquid formation.

In the present study, the processing of TiN-based cermets has been evaluated using a ductile intermetallic binder based on stoichiometric nickel aluminide (Ni_3Al). The use of Ni_3Al-based intermetallics in TiC and Ti(C,N) cermets has been previously shown to result in materials exhibiting an excellent combination of corrosion and wear resistance, together with high temperature strength retention [1,8]. The influence of Mo_2C additions has also been examined in the current work, in terms of improving the sintering response and phase evolution of TiN-Ni_3Al cermets. The cermet densification behaviour has been assessed using a variety of thermal analysis methods, including differential scanning calorimetry (DSC), thermogravimetric analysis (TGA), and dilatometry, while the related microstructural and phase characterisation was performed using scanning electron microscopy (SEM) and X-ray diffraction (XRD).

4.2 Materials and methods

4.2.1 Bulk Sample Preparation

The cermets in the current study have been prepared using commercially available TiN powder (lot: L52737 TiN-1.8/15; Treibacher Industrie AG, Althofen, Austria), with a manufacturer specified particle size of 1-2 μm. The Ni_3Al intermetallic binder phase was produced using a reaction sintering approach [1,88], from a mixture of fine Ni powder (lot no. NAD71; particle size <45 μm) and a pre-alloyed 50/50 wt% Ni/Al powder (lot no. D28X029; particle size <150 μm); both precursor powders were obtained from Alfa Aesar (Ward Hill, MA, USA). The Mo_2C powder (lot no. PL71887718; Pacific Particulate Materials, Vancouver, BC, Canada) had a similar manufacturer specified particle size range to the TiN (i.e. 1-2 μm). The blending of Ni and Ni/Al powders was designed with the aim of producing a stoichiometric Ni_3Al final composition following high temperature sintering. All powder compositions were mixed in 50g batches, with

the addition of 0.5 wt% polyvinyl butyral (PVB) wax to aid in compaction and increase sample integrity. For the present work, the cermet compositions were produced with 30 vol% of Ni_3Al, and with Mo_2C additions varied from 0-10 vol%, substituting in-part for the TiN content; the examined compositions are summarised in Table 4.1. In order to prepare powder blends, the mixtures were first ball milled for 24 hours at 60 RPM in high density polypropylene bottles, using acetone as the suspension medium and with yttria stabilized zirconia milling media (Ø = 10 mm), charged at a 10:1 mass ratio of media: powder.

Table 4.1 Composition of sintered samples.

Element/Blend	**TiN (vol.%)**	**Ni_3Al (vol.%)**	**Mo_2C (vol.%)**
1	70	30	0
2	69.5	30	0.5
3	68.75	30	1.25
4	67.5	30	2.5
5	65	30	5
6	62.5	30	7.5
7	60	30	10

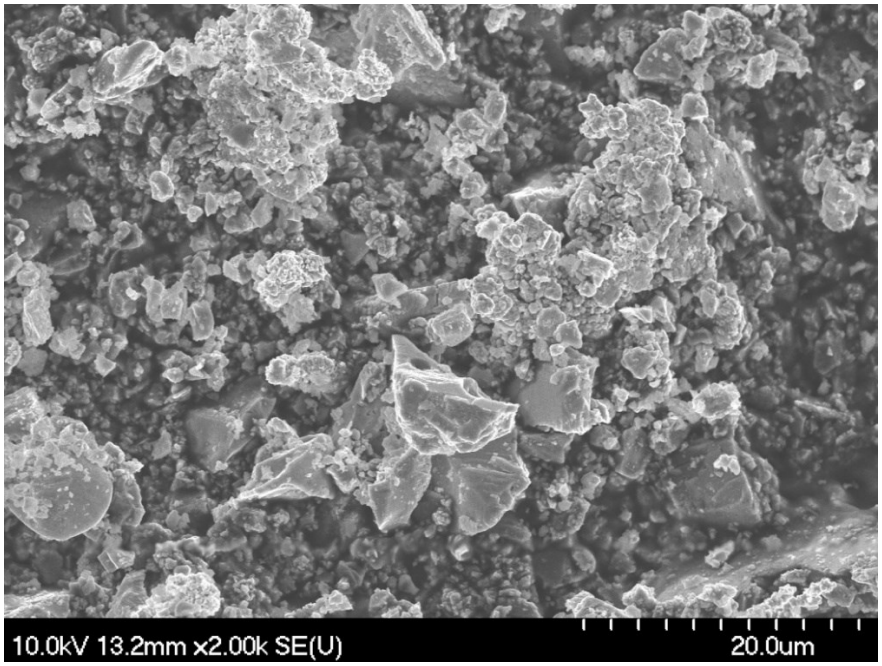

Figure 4.1 Representative SEM image of a dried powder mixture after milling (TiN-Ni_3Al prepared with 10 vol% Mo_2C).

After the milling stage, the suspensions were dried in a fume hood for 24 hours, and then sieved through a -75 μm mesh stainless steel to eliminate any large agglomerates. For bulk cermet samples, the sieved powder was then uniaxially pressed in a hardened steel die (31.75 mm in diameter) at a compaction pressure of ~69 MPa, to give discs approximately 6 mm thick; ~0.2 ml of hexane was dripped onto the loose powder in the die, just prior to compaction, to aid particle rearrangement and hence further improve green strength. Following uniaxial pressing, the samples were sealed in polyethylene bags and further compacted in a cold isostatic press at a pressure of 207 MPa. This second stage helps to eliminate any effects from die wall friction, removing any green density gradients that might form, and helps to achieve higher green densities. Cermet sintering was performed using a vacuum furnace (Red Devil®, R.D. Webb Co., Natick, MA, USA), with samples held at 1550°C for 120 minutes, under a dynamic vacuum of better than 5 x 10^{-4} Torr. During sintering the programmed heating and cooling rates were 20°C/min, with the furnace cooling at a slower, natural rate below ~800°C.

4.2.2 Thermal Analysis Procedures

The various thermal analysis procedures required the preparation of different samples to the 'bulk' materials described in the previous section. DSC/TGA samples were compacted from the milled powders using a uniaxial hydraulic press within a 4.76 mm diameter, hardened steel die. The internal die walls were lubricated with Licowax® C prior to filling with powder. The samples, weighing ~50 mg each, were subsequently compacted to approximately 50 MPa. The DSC and TGA tests were conducted using a simultaneous differential thermal analysis system (Model Q600 SDT, TA Instruments Ltd., New Castle, DE, USA). For the DSC/TGA tests, the compacted cermet samples were held within alumina (Al_2O_3) crucibles, with high purity (>99.999 %) argon flowing through the furnace at a rate of 100 mL/min for the entire heating and cooling cycle. For all tests, the DSC/TGA furnace was initially heated to 50°C, with a short equilibration hold (20 min.), to equilibrate the heat flow measurement. After this equilibrating hold, the cermet samples were heated to 1500°C, and then cooled back to room temperature. The DSC/TGA peaks were resolved at heating/cooling rates of 20°C/min. A minimum of three samples for each powder composition were then studied in the DSC/TGA system, to ensure reproducibility.

The expansion/shrinkage response of the various cermet compositions during sintering was assessed by dilatometry (Modal 401 C, Netzsch Instruments, Germany). The dilatometer samples were compacted in a uniaxial single action press, in an equivalent manner to those prepared for DSC/TGA analysis, using a 6.38 mm diameter hardened steel die, at a compaction pressure of ~100 MPa. The lengths of the dilatometer samples were 10 mm. Sintering was conducted under a dynamic vacuum (< 1 x 10^{-3} mbar), with the samples heated at a rate of 20°C/min to 1500°C. Cooling was conducted at a nominal rate of 20°C/min. During sintering samples were supported in the dilatometer on an Al_2O_3 cradle, with two Al_2O_3 discs in contact with the Al_2O_3 pushrods of the dilatometer. The cradle and plates were coated with a protective yttria (Y_2O_3) layer to prevent any bonding with the samples. A minimum of three samples of each cermet composition were sintered in the dilatometer in order to ensure test reproducibility.

4.2.3 Microstructure and Phase Characterisation

Crystallographic analyses of the various powdered and sintered samples were performed using XRD (Model D-8 Advance, Bruker Corp., Billerica, MA, USA), with CuKα radiation, at 40 kV

and 40 mA. Phase identification was then conducted, following XRD, using the ICCD's PDF-4 database for inorganic materials. For microscopy analysis, the sintered samples were ground and polished using successively finer grades of abrasive diamond, finishing with 0.25 μm diamond paste. The resultant polished microstructures, along with selected powder samples (i.e. prior to sintering), were then analysed using SEM (Model S-4700, Hitachi High Technologies, Inc., Tokyo, Japan). Chemical compositions were analysed within the SEM using energy dispersive X-ray spectroscopy (EDS; Inca X-max, Oxford Instruments, Concord, MA, USA).

4.3. Results and Discussion

4.3.1 Vacuum Sintering Response

TiN-based cermets were prepared with 30 vol.% Ni_3Al, and varying amounts of Mo_2C addition, as a method to investigate and modify the wetting characteristics of the molten intermetallic binder in contact with the nitride phase. Figure 4.1 demonstrates the extent of homogenisation and size refinement that is achieved in the dried powder blends following the initial ball milling stage, in this instance for a sample prepared with 10 vol.% Mo_2C addition. The various constituents are well blended, although visually there is not a significant degree of size reduction. Irregularly-shaped particles, ranging from <1 to 5 μm are observed. The mean sizes of the initial raw powders are typically in the range of 1-3 μm, excluding the pre-alloyed Ni/Al powder, which is initially <150 μm. There is a general reduction in particle size arising with the mixing and milling process, and there is no evidence of the large Ni/Al powder particles after milling and drying. The predominant morphology is one of angular particles being present in the mixture, which is a result of attrition processes during milling. The overall reduced particle size can be expected to enhance densification during the sintering process. Also, there is a broad range of particles from a few microns up to 15 μm, what favours the rearrangement of solid mass to improve packing and green density [32].

Figure 4.2 (a) Macro-photographic images of sintered samples of TiN-Ni_3Al cermets, prepared with various Mo_2C additions. Top row, from left to right, compositions 1 to 4. Bottom row, from left to right, compositions 5 to 7. Samples sintered at 1550 °C for 120 min. (b) Macro-photographic images of the dilatometer sintered samples of TiN-Ni_3Al cermets, prepared with various Mo_2C additions. Top row, from left to right, compositions 1 to 4. Bottom row, from left to right, compositions 5 to 7. Samples were heated to 1500 °C, and then cooled (no hold).

Macro photographic images of various samples after vacuum sintering are presented in Figure 4.2 (with increasing Mo_2C content samples shown from left to right). Without Mo_2C addition (upper row, left hand sample), or with very low additions (upper row), there is a clear inhomogeneity in terms of the 'as-sintered' surface appearance of the samples. These examples show some evidence

of macro-segregation of components within the composite, at least on the exposed surface. As the Mo_2C content is increased above 1.25 vol%, the surface of the materials appears more homogeneous. It has previously been reported that, with an addition of 5 wt% Mo, the wetting angle of Ni_3Al on TiC can be reduced to ~11º [40,89]. In the present work, with a low Mo_2C content it is clear there is still a high degree of segregation. This result can be anticipated from previously reported wetting experiments with Mo_2C presented in the open literature [11]. It was also recently shown, for high nitrogen content Ti(C,N)-Ni_3Al cermets (in this instance with a C:N ratio of 0.3:0.7) [8,90], that Mo_2C can significantly improve melt wetting and densification, even when present in low concentrations (i.e. 1.25 vol%). It was for this reason that Mo_2C was also chosen as a wetting agent in the present work. As noted earlier, for effective liquid phase sintering to occur, it is desirable to obtain the lowest contact angle of the molten phase on the ceramic constituent as is possible [36]. There are several methodologies that can be employed to improve wetting in cermet systems, such as additions of elemental Mo or its carbide, Mo_2C [8,40]. The processing strategy that is presently proposed is that the Mo or Mo_2C may envelope the ceramic grains, creating a thin layer which will decrease the free energy of liquid-solid interfaces, lowering the contact angle, and promoting wetting during sintering; a generally similar behaviour was seen in prior work [91].

The crystallographic stability of the sintered TiN-Ni_3Al-Mo_2C cermets was examined using XRD, with representative sample traces of samples after sintering at 1550°C for 120 minutes shown in Figure 4.3. It is apparent that the Mo_2C peak increases in intensity as a greater amount is added to the composition, as might expected if no deleterious reactions occur. The presence of a very small amount of retained NiAl is apparent for the smallest Mo_2C content, indicating that the Ni_3Al precursors have not fully reacted within the sintering cycle time. For a higher content of Mo_2C (i.e. >1.25 vol.% Mo_2C), the NiAl peak has disappeared, and only the Ni_3Al intermetallic phase is detected in terms of the reacted binder constituents, indicating there is a minimum content of Mo_2C that effectively assists in reactive homogenisation of the pre-alloying Ni and Ni/Al mixture. A broadly similar type of behaviour was seen previously [92], where Ni and Ni/Al peaks lose intensity, while the Ni_3Al intensity rises until the reaction was observed to be complete at 1200°C. This behaviour suggests that Mo_2C act as an homogenizer and participate in the mechanism to improve densification and wetting during sintering, what will be show further at the SEM-EDS chemical composition analysis.

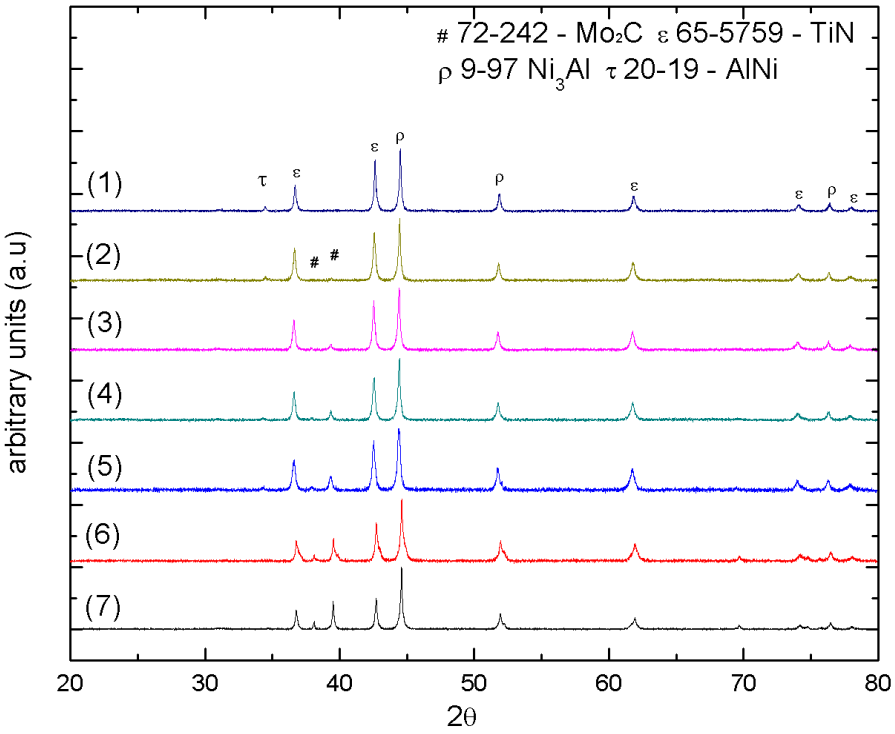

Figure 4.3 Representative XRD traces for the sintered TiN-Ni_3Al cermets, compositions from 1-7. Samples sintered at 1550°C for 120 minutes.

4.3.2 DSC and TGA Evolution

A representative example of the DSC/TGA analyses for the TiC-30 vol% Ni_3Al samples prepared with 5 vol% Mo_2C is shown in Figure 4.4. As would be expected, an endothermic peak was observed during melting, with a related exothermic peak recorded on cooling during solidification. These two peaks correspond quite closely with the melting and solidification temperature of Ni_3Al (1360-1362ºC), following the Ni-Al phase diagram of Okamoto [93].

An initial moderate weight loss (~0.5 wt%) is confirmed by TGA analysis (Figure 4.4), occurring between 200 and 600ºC. This can be primarily attributed to decomposition of the polyvinyl butyral (PVB) wax and Licowax® C lubricants, which are used to aid compaction of the green bodies prior to sintering; potentially small amounts of adsorbed surface moisture may also be lost during this stage. In the TGA trace, it is possible to observe that the final sample weight corresponds to ~99.5 % of the full initial mass. Above 600ºC a very small mass gain is noted (~0.15 %). This is

potentially due to limited oxidation of the samples during heating, which likely arises from the design of the TGA system, as it is not optimised to be vacuum tight. Above ~1200ºC, a rapid weight loss again arises. As similar response was previously reported in the literature for Ti(C,N)-Ni_3Al cermets [90], which was attributed to the volatilisation of MoO_3 present in the surface of the samples. At this temperature, the sample begins to experience rapid mass loss and an endothermic response is observed [90].

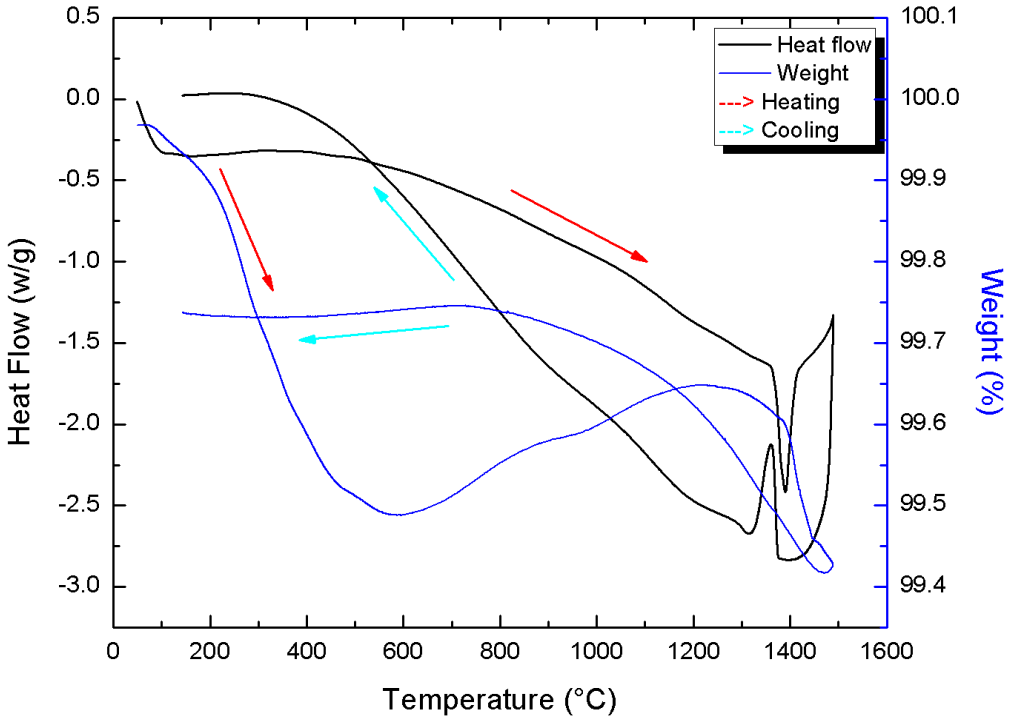

Figure 4.4 Representative combined DSC/TGA traces for the TiN-Ni_3Al cermet composition prepared with 5 vol% Mo_2C. Samples heated/cooled to 1500°C at a rate of 20°C/min.

Representative DSC heating segment data, obtained between 1300 and 1500ºC, is shown in Figure 4.5 for each of the TiN-30 vol% Ni_3Al cermet compositions, prepared with 0 to 10 vol% Mo_2C. These results demonstrate that, as the amount of Mo_2C was increased in the cermet composition, the apparent melting temperature of the Ni_3Al alloy is reduced (by roughly 20ºC). The multiple melting peaks for the compositions from 0-5 vol% Mo_2C additions are also proposed to be related

to the presence of non-equilibrium phases, such as NiAl. For Mo_2C concentrations higher than 5 vol%, the peak gets sharper and is better defined, indicating that the liquid phase is more homogeneous.

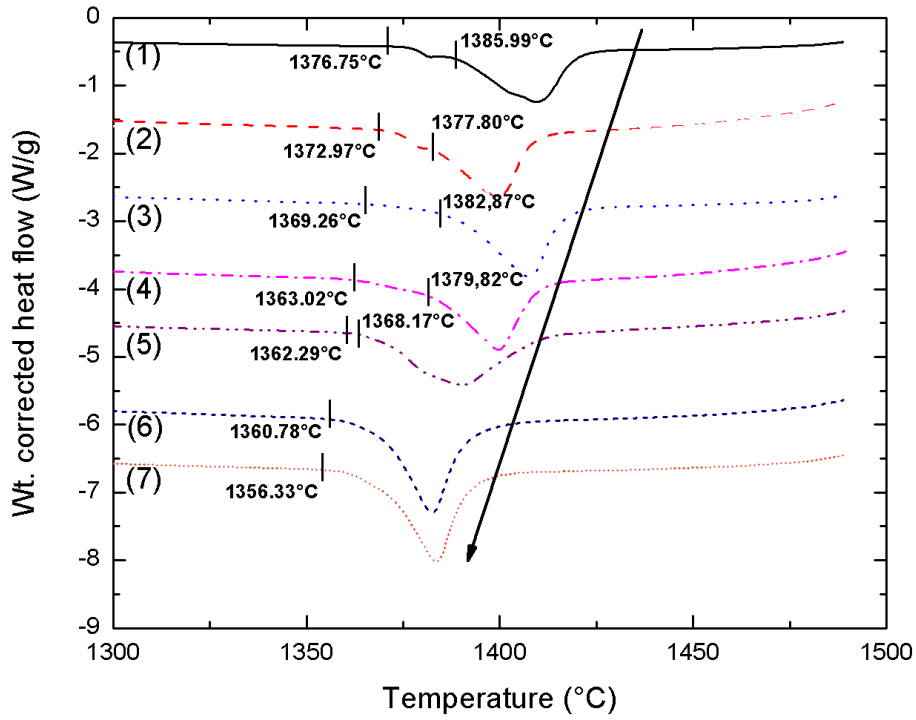

Figure 4.5 Representative segments of the DSC heating curves for TiN-30 vol% Ni_3Al compositions prepared with varying amounts of Mo_2C. Examples show the overall melting peak shifts as the amount of Mo_2C is increased; an exothermic response is shown as the 'up' orientation for each graph. Samples heated/cooled to 1500°C at a rate of 20°C/min.

The DSC solidification peaks for these cermet compositions are presented in Figure 4.6. Similar results were obtained when compared with the melting peaks, which showed that the addition of Mo_2C can reduce the melting temperature of the Ni_3Al alloy. It has been noted that the wettability of a molten metal is partially determined by its thermodynamic stability, and that a small heat of formation is associated with the lower wetting angle is achieved by the solid/liquid interfaces [94]. Mo_2C has the best wettability with liquid metals when compared to related carbides from the groups IVb, Vb and VIb (American notation) of the Periodic Table of the elements, due to it having

the lowest heat of formation. It is anticipated that this assists with the wetting and sinterability of the TiN in the present cermets, through the creation of a thin layer of Mo_2C , which surrounds each ceramic grain and results in a homogeneous melt, as observed in prior work with similar compositions [95].

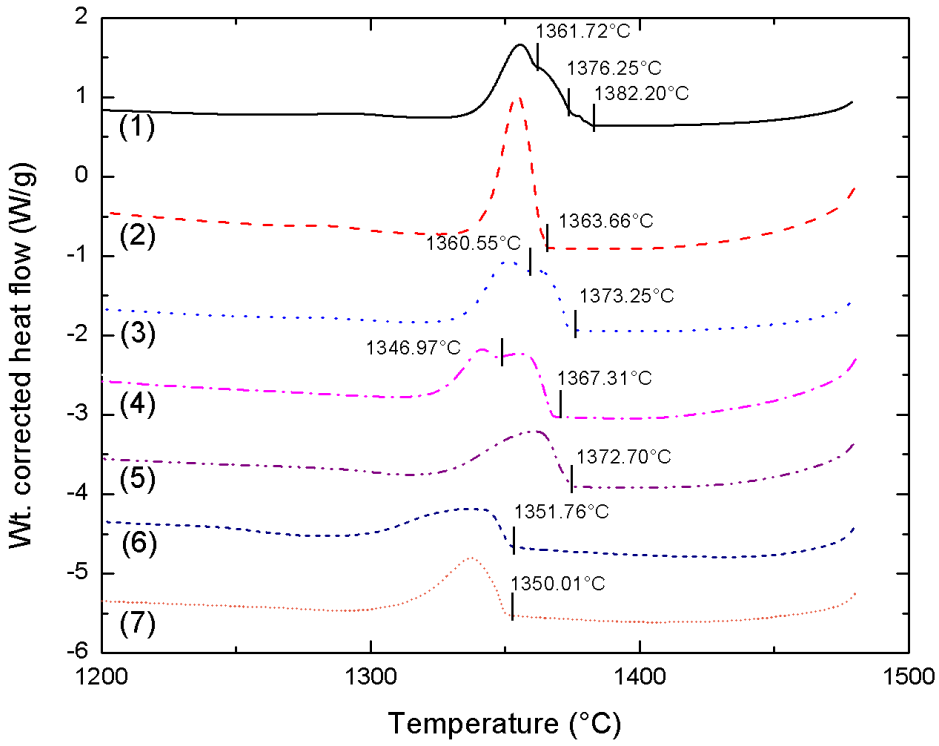

Figure 4.6 Representative segments of the DSC cooling curves for TiN-30 vol% Ni_3Al compositions prepared with varying amounts of Mo_2C. The examples show the overall solidification peak shift as the amount of Mo_2C is increased; an exothermic response is shown as the 'up' orientation for each graph. Samples heated/cooled to 1500°C at a rate of 20°C/min.

Figure 4.7 shows representative TGA curves obtained for each of the compositions within the same temperature range. Each of the samples contains 0.5 vol.% of PVB binder, which volatilises within the temperature range of 300-500°C, corresponding to the observed mass loss at these temperatures. As noted in prior work [90], a mass loss at 800°C occurs due the oxidation of Mo_2C, forming MoO_3, which further reacts with Al to form Al_2O_3, which was proposed to be responsible for a subsequent measurable increase in mass upon solidification. Some mass gain is shown during

solidification in the present work, predominantly for the TiN-Ni_3Al composition, which indicates that residual oxygen reacts with the Ni and Al present in system, since it wants to physically de-wet from the TiN phase[11]. De-nitridation of TiN and subsequent oxidation are possible mechanisms that occur at higher temperatures (e.g. 1500°C), which show as mass loss/gain in all compositions [9,90,96] .

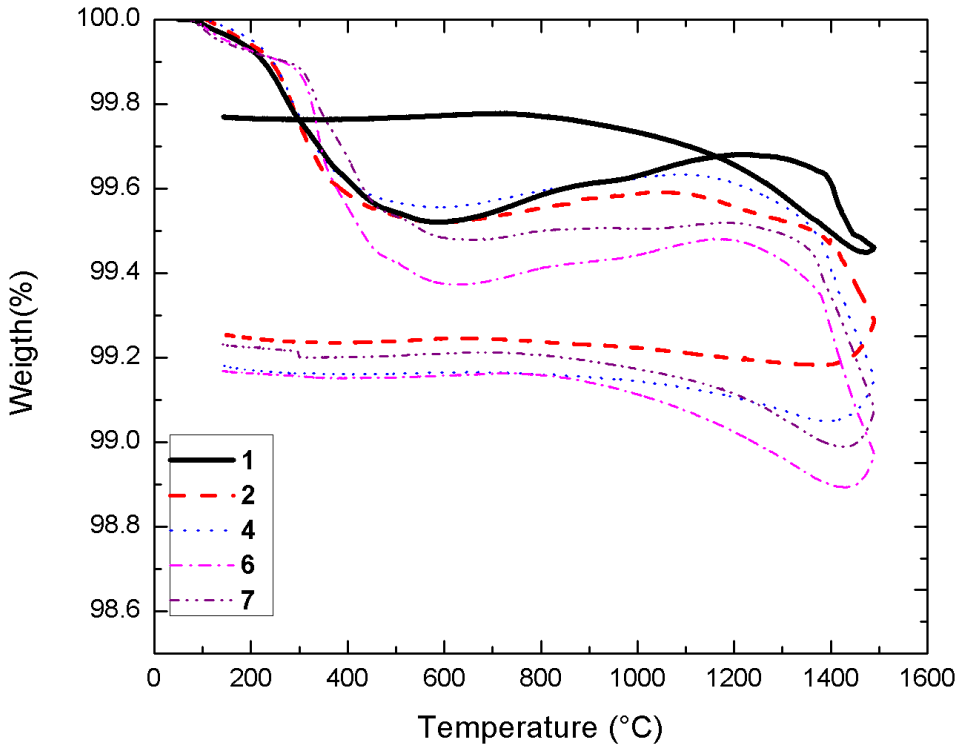

Figure 4.7 Representative TGA traces for selected TiN-30 vol% Ni_3Al-Mo_2C compositions, showing the changes in weight as a function of temperature; additional compositions were omitted for clarity only. Samples heated/cooled to 1500°C at a rate of 20°C/min.

4.3.3 Dilatometry Analysis

The results of dilatometric analysis were used to examine the shrinkage of each composition from room temperature up to 1500ºC (Figure 4.8). The main peak temperature occurs ~78 minutes into the cycle (corresponding to a temperature of ~1500ºC), which relates to a transition between

expansion and shrinkage. On heating, an expansion of ~1 % occurs at ~71 minutes (at ~1361ºC), which corresponds to the melting of Ni_3Al. Samples with less than 5 vol% of Mo_2C exhibited a maximum shrinkage of 8 %. This moderate shrinkage has been attributed to some loss of the intermetallic binder through a de-wetting process, which is visible at the bottom of the samples shown in Figure 4.8. The physical segregation of the metallic phase at the bottom of the sintered specimen is a result of melt de-wetting, together with the combined action of gravity (the metal has a higher density than the TiN).

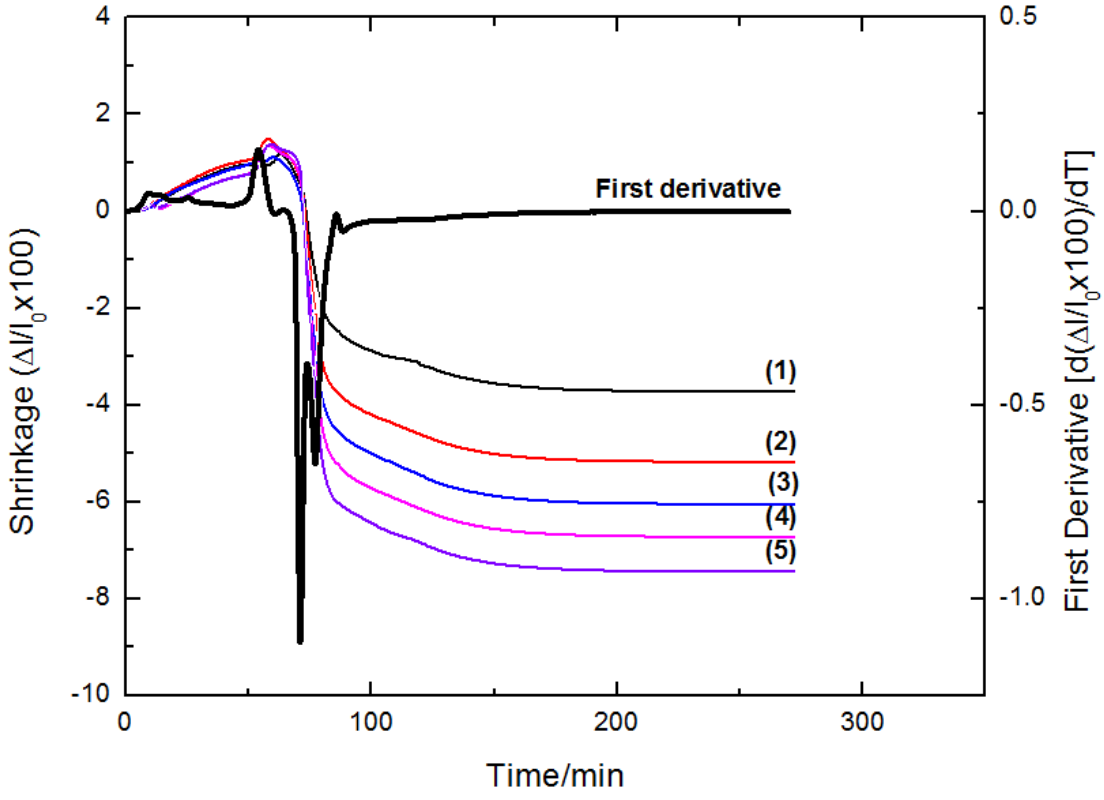

Figure 4.8 Representative dilatometry curves for TiN-30 vol% Ni_3Al cermets with 0 to 5 vol% Mo_2C, showing the extent of densification as a function of temperature. Samples heated/cooled to 1500°C at a rate of 20°C/min.

Samples with Mo_2C concentrations higher than 5 vol% exhibited ~6 % shrinkage, which was purely attributed to liquid phase sintering of the cermet, as little to no segregation/de-wetting was observed (Figure 4.9). Dilatometry traces showed a significant expansion at ~71 minutes

(~1361ºC), which can again be interpreted as the initial melting of the Ni_3Al. A significant reduction in the shrinkage rate was observed at ~85 minutes (~1363ºC), which corresponds to solidification of the melt phase, after which only solid-state sintering takes place for any subsequent densification.

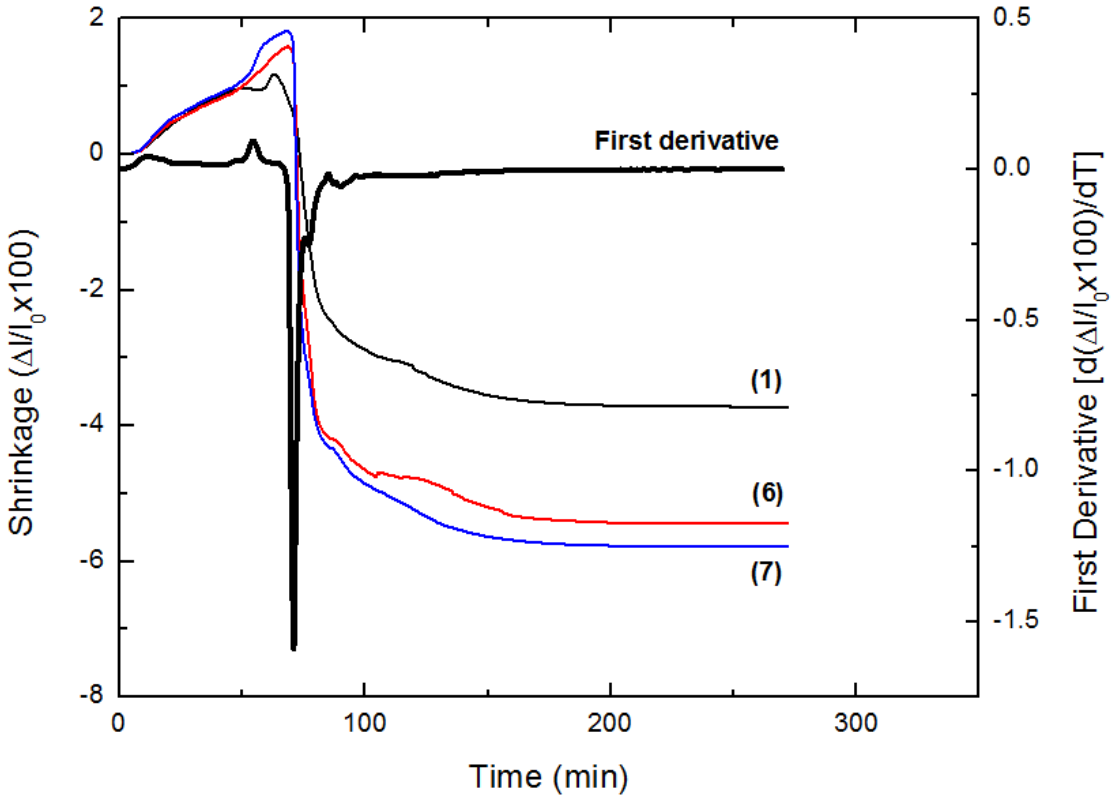

Figure 4.9 Representative dilatometry curves for TiN-30 vol%Ni_3Al with 0, 7.5, and 10 vol% Mo_2C, showing the extent of densification as a function of temperature. Samples heated/cooled to 1500°C at a rate of 20°C/min.

4.3.4 Microstructural Development

It has previously been noted that the sintering behavior of TiN particles can be enhanced through the formation of a Mo-rich shell, which was reported to be less soluble in the binder phase than in the TiN; this increases dissolution into the TiN phase, leaving small cores [91]. It is notable that the addition of Mo_2C into the cermet mixture creates a Mo carbide 'shell' that is invariably located between the TiN and the Ni_3Al-based binder, effectively isolating these phases from each other (at

least partially). In some respects this behaviour is similar to the TiC ‘clustering’ that was observed when large Al_2O_3 particles were added into a TiC-Ni_3Al cermet [97]. In that instance, the Ni_3Al did not wet the Al_2O_3, and a structural re-arganisation occurred with TiC particles both segregating to the Al_2O_3-Ni_3Al interface and showing shape accomodation during liquid phase sintering, in order to better pack and isolate the interface [97]. In the present case it appears that both the TiN and Mo_2C undergo dissolution and re-precipitation, with the Mo carbide phase preferentially re-precipitating at the interface between the TiN and Ni_3Al. This response favours dissolution-reprecipitation during sintering instead of segregation of phases [80]. During this stage of liquid phase sintering, TiN and Mo_2C dissolve in the Ni_3Al binder, and there appears to be a preferential re-precipitation of the Mo carbide on TiN cores when the dissolved concentration reaches saturation. In the subsequent cooling stage any remaining Mo and C present in the melt (above the room temperature solubility limit) also precipitate out, forming outer Mo-rich shells, as shown in Figure 4.10. Further cooling then results in solidification of the intermetallic binder phase.

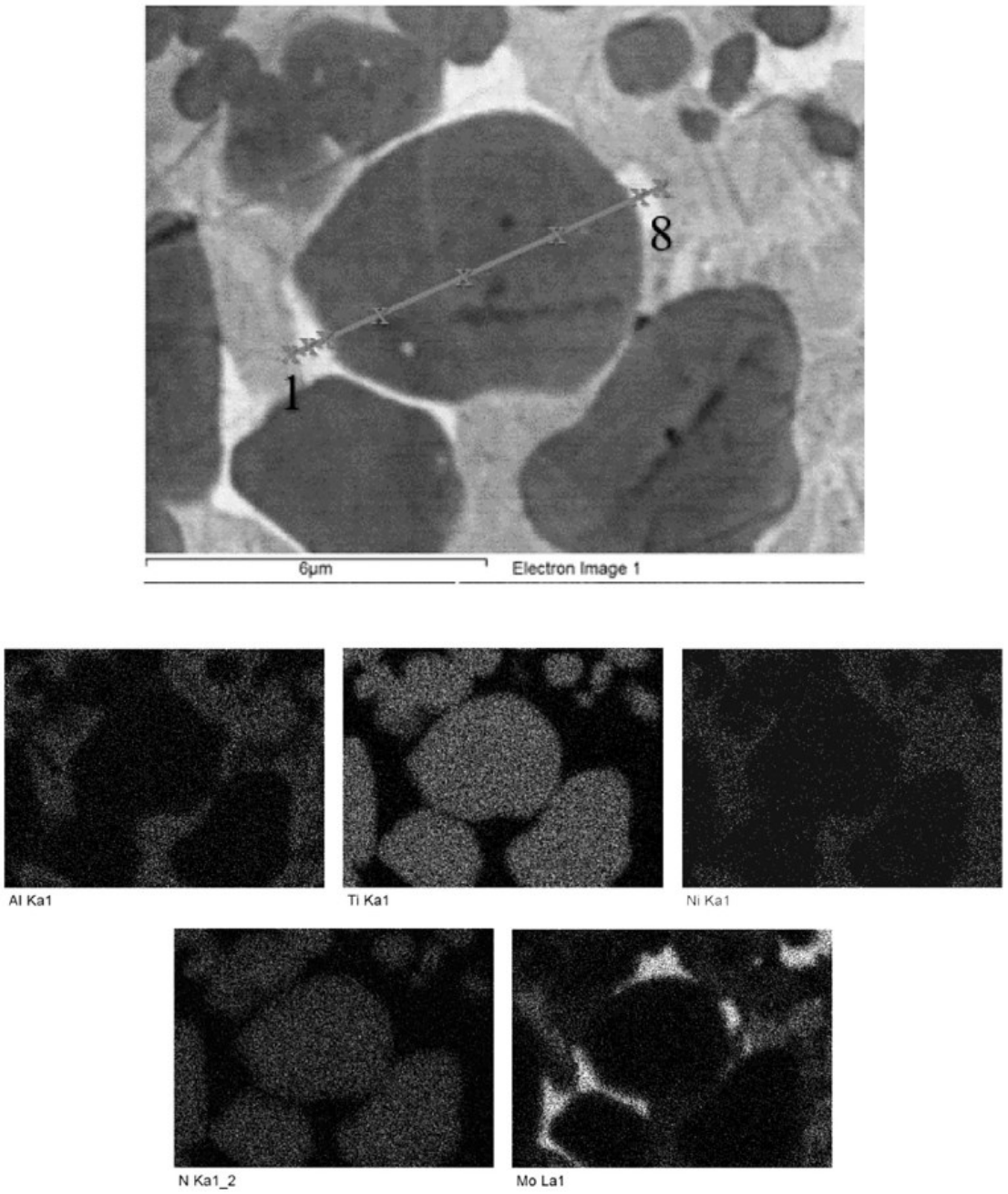

Figure 4.10 Representative SEM EDS image and associated elemental maps for the TiN-30 vol% Ni_3Al composition, prepared with 10 vol% Mo_2C.

Figure 4.10 also presents typical examples of EDS maps for this region, while a related linescan (for points 1 to 8 in Figure 4.10) is presented in Figure 4.11. Mo carbide is observed in between the nitride and binder phase. Up to 2 wt% of oxygen is determined within the binder phase. There is an apparent gradient of composition from the binder to the core of the nitride grain, with up to

5 wt% of Ni and Al recorded in the Mo_2C inner shell; significant caution should be taken in this interpretation, as the electron beam interaction volume (of the order of 1 μm^3) is likely to extend slightly into the surounding binder regions. No significant binder constituents were found to be dissolved into the nitride phase, while up to 4 wt% of residual Ti and N were measured in the binder phase.

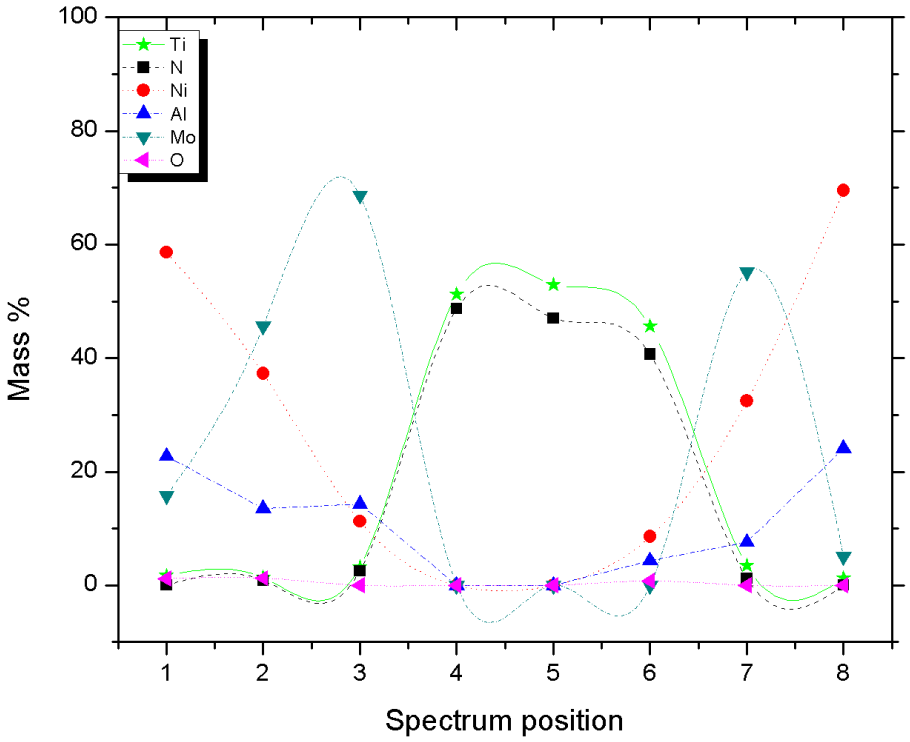

Figure 4.11 Typical EDS compositional profile for a TiN-30 vol% Ni_3Al sample with 10 vol% Mo_2C, which matches Figure 4.10. Samples sintered at 1550°C for 120 minutes.

The SEM images and associated EDS maps presented in Figure 4.12 demonstrate the elemental segregation observed in the composition with 10 vol% Mo_2C. It is apparent that the TiN phase is largely physically separated from the intermetallic Ni_3Al phase after sintering, through the presence of a molybdenum carbide 'shell' covering much of the TiN surface.

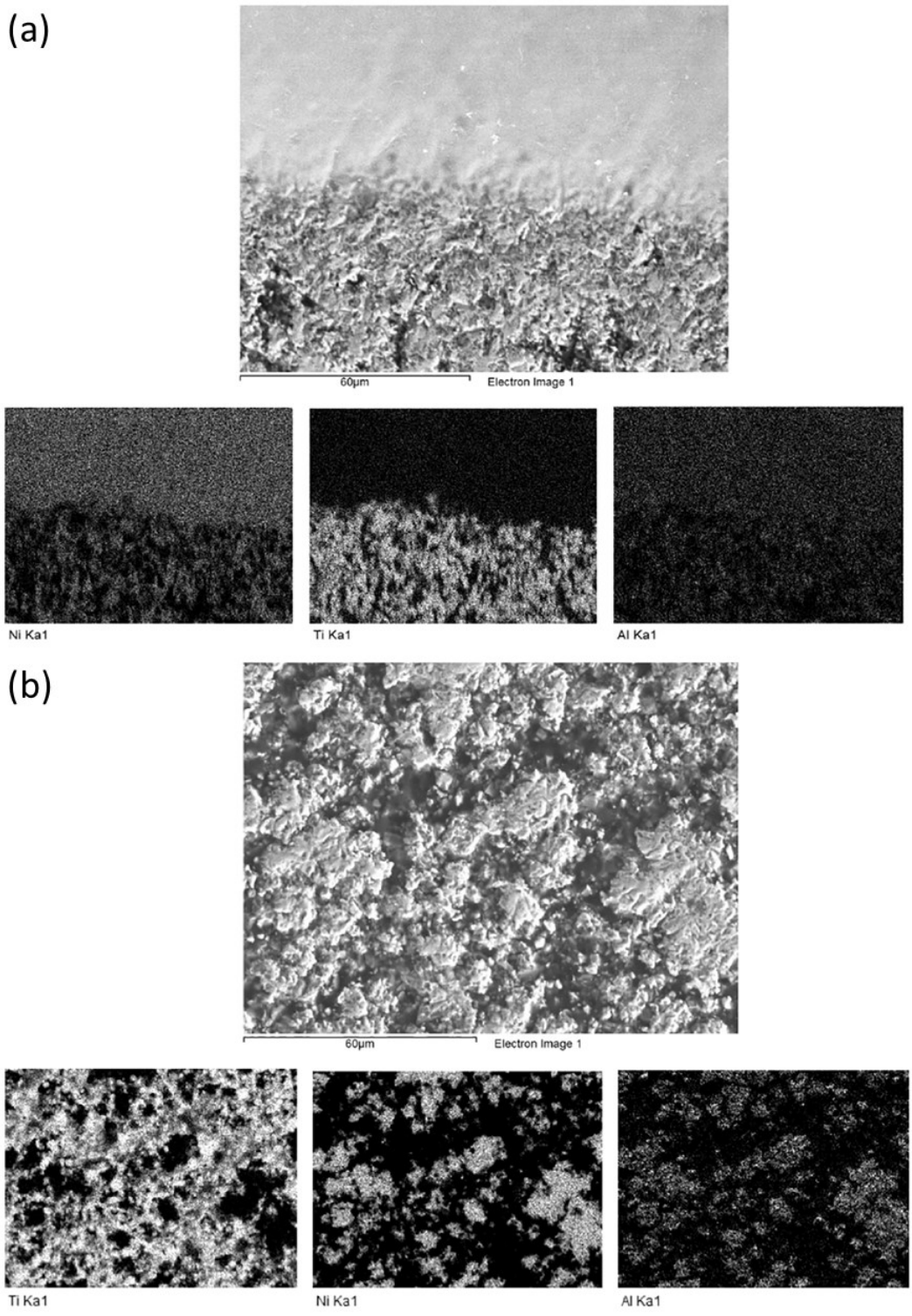

Figure 4.12 Representative EDS elemental maps showing the macro- and micro-segregation in the compositions of: (a) TiN-30 vol% Ni_3Al, and (b) TiN-30 vol% Ni_3Al-10 vol% Mo_2C. Samples sintered at 1550°C for 120 minutes.

The EDS maps in Figure 4.10 demonstrate the elemental segregation observed in the composition with 10 vol% Mo_2C. It is clear that the TiN phase is largely physically separated from the intermetallic Ni_3Al phase after sintering. As increasing Mo_2C is incorporated, the structural interaction is further developed, leading to micro-segregation within the microstructure. For the present work, a simple microstructural model has been developed, based on the SEM-EDS mapping observations, to explain the liquid phase sintering response and associated microstructure formation.

Evaluation of the effects of Mo_2C on the final microstructure development are presented in Figure 4.13. The main differences between the samples without and with Mo_2C during liquid phase sintering relate to the pore sizes and distributions. Large, irregularly-shaped pores are observed in Figure 4.13(a), in the absence of Mo_2C additions. In this instance the Ni_3al binder tries to de-wet from the TiN ceramic phase, so instead of the capillary force driving liquid phase sintering and densification, effectively there a repulsion between the TiN and molten intermetallic phase. Dense, Ni_3Al-rich areas are apparent, with minimal TiN present in these regions. This segregation likely happens as soon the sample reaches the melting temperature of Ni and NiAl mixture. Incorporation of Mo_2C starts to reduce these effects, as highlighted in Figures 4.13(b) and, to a lesser extent, 4.13(c). Addition of 10 vol% Mo_2C further reduces this segregation, and regions of Mo carbide (light contrast) can be seen around many of the TiN grains aiding the liquid phase sintering process. At this level of Mo_2C addition porosity is largely reduced. In addition to this reduction of porosity, it is also possible to observe some limited coarsening within the microstructure of the TiN phase (dark contrast), which is arises through Ostwald ripening due to enhanced mass transfer during the dissolution/re-precipitation sintering stages. A more uniform phase distribution is also clearly observed as the Mo_2C content is increased to 10 vol%.

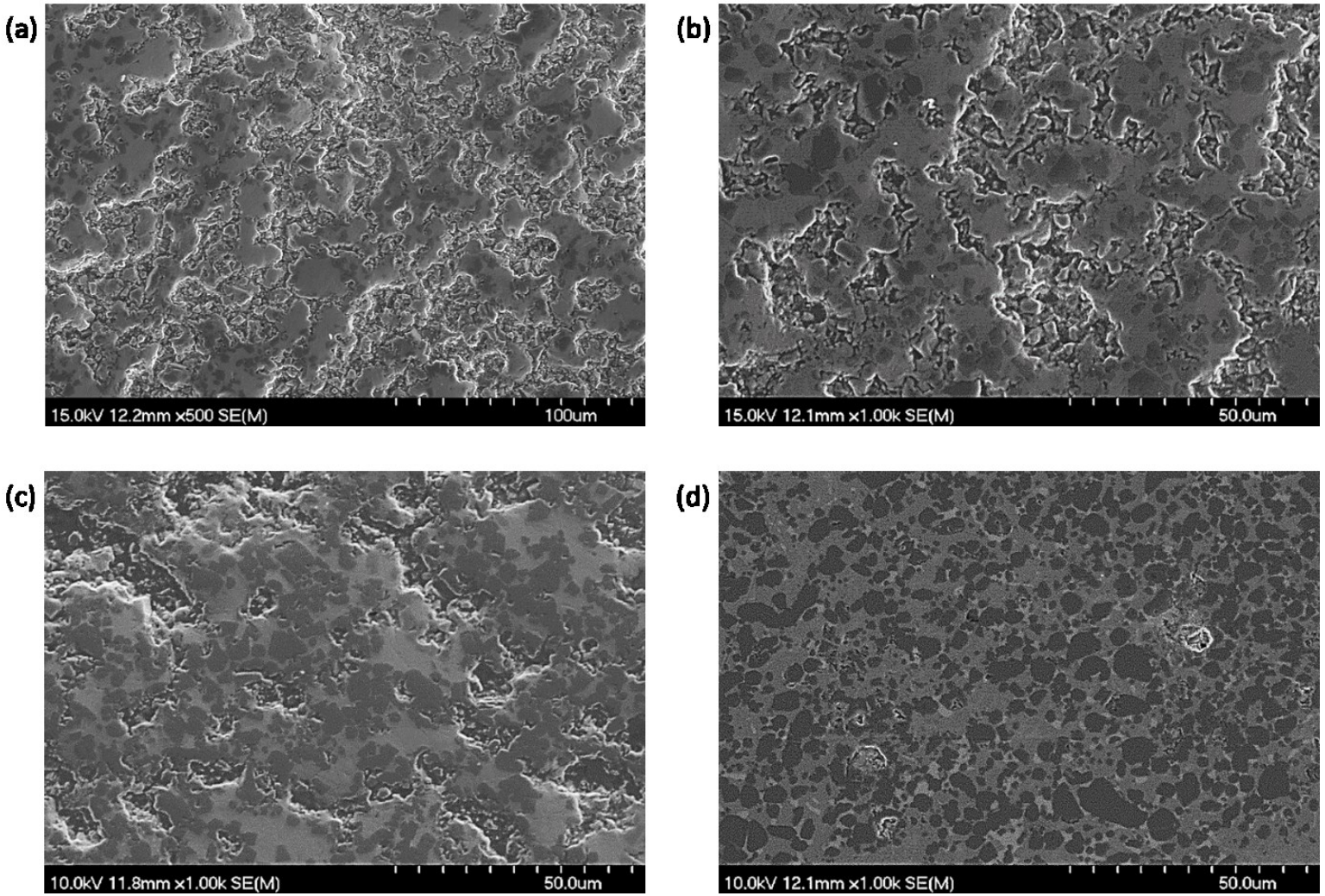

Figure 4.13 Typical SEM images of TiN-30 vol% Ni_3Al samples liquid phase sintered with Mo_2C contents of: (a) 0 vol%, (b) 2.5 vol%, (c) 5 vol% and (d) 10 vol%. Samples sintered at 1550°C for 120 minutes.

For the present work, it is possible to propose a simple microstructural evolution model (Figure 4.14), based on the SEM-EDS mapping observations, that helps to explain the liquid phase sintering response and associated microstructure development. In the absence of Mo_2C, the TiN is not wet very well by the intermetallic melt, segregating from the TiN and even fully de-wetting (Fig. 4.14(a)). As increasing Mo_2C is incorporated, the structural evolution becomes more complex, as both TiN and Mo_2C are dissolved into the melt. However, here it can be anticipated that dissolution of Mo_2C dominates; in a prior study, it was demonstrated that for a solely Mo_2C-Ni_3Al cermet composition, significant Mo_2C coarsening occurs, indicating a high solubility and diffusion rate [30]. Only minimal TiN coarsening is noted in the current study, while the Mo_2C is selectively re-precipitated directly on to TiN grains (as shown in Figure 4.14(b)); effectively this changes an entirely TiNNi_3Al melt interface to a predominantly Mo_2C-Ni_3Al melt interface. Further elucidation of the densification mechanism(s) may be achieved through isothermal sintering studies [39], in addition to constant heating rate dilatometry, which will provide the focus for future studies on the TiN-Mo_2C-Ni_3Al compositions; such studies can provide detailed information regarding both densification and grain growth exponents.

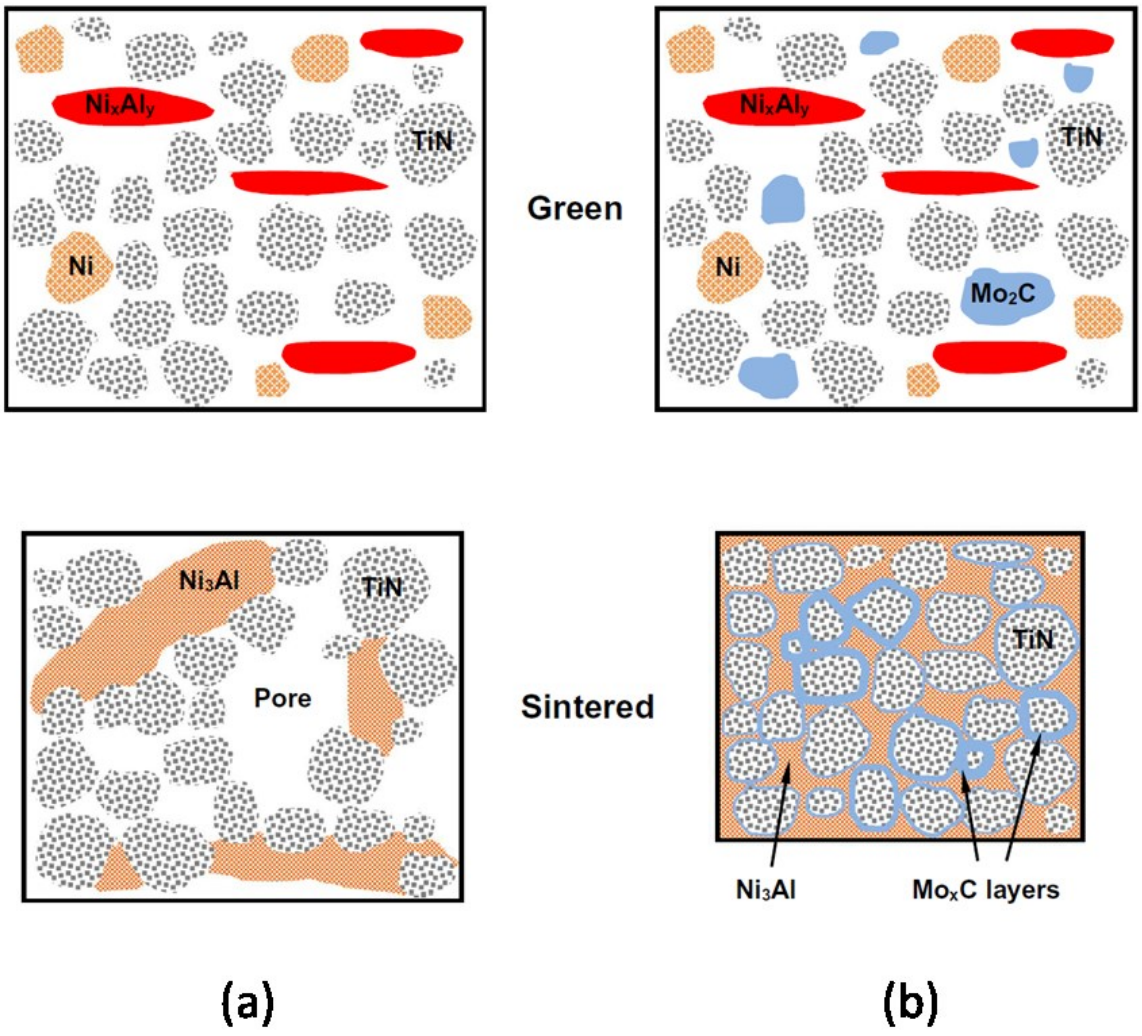

Figure 4.14 A simple schematic representation of the effect of Mo_2C additions on the sintering behaviour of TiN-Ni_3Al cermets. (a) In the absence of Mo_2C, the liquid formation is accompanied by de-wetting, and the subsequent segregation of the molten Ni_3Al phase. (b) Mo_2C additions result in the formation of a thin molybdenum carbide layer on the surface of the TiN grains, leading to significantly improved wetting and densification behaviour.

4.4 Conclusions

In the present work, TiN-based cermets have been prepared with a stoichiometric Ni_3Al, and varying amounts of Mo_2C addition. Macro- and micro-segregation phenomena were observed in the basic TiN-Ni_3Al system, resulting in high porosity. The incorporation of up to 10 vol% of Mo_2C into the hard phase was shown to significantly improve wettability within the system,

thereby reducing porosity in the final sintered microstructure. The addition of Mo_2C also resulted in some limited coarsening of the microstructure, by improving material transport and promoting Ostwald ripening during liquid phase sintering. A simple microstructural model was developed, based on the use of EDS chemical mapping. It demonstrates that that during sintering/cooling a Mo carbide phase precipitates directly onto TiN, creating an enveloping shell structure, which can be anticipated to lead to a reduction of contact angle between the TiN and intermetallic binder phase. This study highlights the beneficial effects of Mo_2C additions in processing TiN cermets.

Acknowledgements

Technical discussions and support provided by Marc Froning and Stephen Gaydos at Boeing Research & Technology, through the course of this work, are gratefully acknowledged. The Canada Foundation for Innovation, the Atlantic Innovation Fund, and other partners who helped fund the Facilities for Materials Characterisation, managed by the Dalhousie University Clean Technologies Research Institute, are also thanked. I would like to acknowledge W.A. Sparling, Z. Memarrashidi for their support on the experimental part of this work, as well my PhD supervisors Z.N. Farhat and K.P. Plucknett for their guidance.

Funding

The authors would like to acknowledge the financial support provided by Boeing Research and Technology (research contract 11-6392). The present work was realized with support of CAPES, Coordination for the Improvement of Higher Level -or Education- Personnel – Brazil.

CHAPTER 5 THE EFFECTS OF GRAPHENE NANO-PLATELET ADDITIONS ON THE SLIDING WEAR OF TiC-Ni_3Al CERMETS

Status: *Published: Tribology International*, 130(2019) 119-132.

Abstract

TiC-Ni_3Al cermets show considerable promise as replacement materials for WC-based hardmetals when component mass, corrosion resistance or higher temperature strength are of importance. The current study investigates potential improvements to selected mechanical and tribological properties of these cermets through addition of graphene nano-platelets (GNPs) to a baseline TiC cermet with 30 vol.% Ni_3Al binder. GNP contents of up to 2.5 vol.% were assessed, replacing Ni_3Al in the overall composition, with samples vacuum sintered at 1550 ºC for 2 hours. The resultant sintered densities all exceeded 99% of theoretical. From initial assessment of the mechanical and tribological responses, it is demonstrated that GNP additions up to 2.5 vol.% can increase the Vickers hardness (from ~1060 to ~1220 HV1) and indentation fracture resistance (from ~14.2 to ~16.7 $MPa•m^{0.5}$). At the same time, GNP additions significantly lower both the coefficient of friction, from ~0.53 to ~0.15, and the specific wear rate, from ~15.5 to ~1.7 x 10^{-6} mm^3/Nm, when assessed with a block-on-ring wear test geometry.

Keywords: cermet, graphene nano-platelets, scratch testing, hardness

5.1 Introduction

'Cermets' are engineered composites that combine ceramic and metallic phases to generate materials that, typically, exhibit both high hardness and toughness [98]. Because of this combination of constituents, cermets can exhibit a moderately low coefficient of friction combined with good wear resistance [99]. In addition, through careful selection of the actual cermets phase compositions, they can also possess high oxidation resistance and good thermal stability [2,100].

As a consequence, the use of cermet materials as thermal spray coatings is also widely studied, with targeted applications in aggressive corrosive and/or erosive environments [101,102]. A common use for such ceramic-metal composites is as wear resistant materials in the mining, mineral processing, and oil and gas industries [103].

One of the most important characteristics of cermets, as well as tungsten carbide-cobalt (WC-Co) based hardmetals, is their capacity to be tailored, in terms of their properties, by changing the chemical phase compositions and the volume (or weight) ratios between the ceramic and metallic phases. This approach can potentially be applied to increase the cermet wear resistance, by increasing the ceramic phase content, which is typically between 70-90 vol.%. However, this can cause the material to become more brittle, and consequently increase erosion wear [13]. An alternative approach to increasing the wear resistance is through addition of a phase with an extraordinary high hardness, such as industrial diamonds, although this can result in an excessive cost increase.

Perhaps unsurprisingly, it has also been shown that the wear resistance of ceramic/ceramic tribo-pairs can be increased under oil lubrication [104]. However, the use of such lubrication is generally unfavourable, due to potential associated environmental issues, as well the limitations the lubricant might impart on the working conditions (*e.g.*, temperature). For this reason, self-lubricating materials have been utilized in composites and cermets as a potential solution [105], as well as in powder metallurgy systems [106]. These previous studies have demonstrated the potential to process graphite-containing cermets at temperatures of ~1440 °C, with nearly fully dense composite materials obtained [107]. Additions of up to 5 vol.% of graphite and/or a decrease in the graphite flake size significantly decreased the wear rates of self-mated wear pairs. A transition from particle extrusion to a plastic deformation wear mechanism occurs, when compared to the baseline cermet compositions [108,109].

As an alternative to graphite, closely related graphene nano-platelets (GNPs) are a relatively cheap material solution, which have been reported to improve mechanical properties in a number of composite systems, such that they present an interesting choice for the manufacture of self-lubricating cermets [110,111]. In the present work additions of GNP particles up to 2.5 vol.% were examined for titanium carbide-nickel aluminide (TiC-Ni_3Al) cermets, whereby the GNP is added specifically into the Ni_3Al intermetallic binder phase using powder metallurgy-based processing

routes. TiC-Ni_3Al cermets, along with WC-Ni_3Al, have been widely studied in recent years [98,112], and have been shown to possess comparable wear resistance to WC-Co [112], while exhibiting superior aqueous corrosion resistance [113]. Furthermore, the TiC-based materials are less than half the density of WC-Co. For the present work, the main objectives are to investigate how the graphene additions, in this case in the form of GNPs, influence the processing and densification response of TiC-Ni_3Al cermets, their fundamental mechanical properties and, most importantly, the tribological behaviour of the resultant GNP-containing cermets.

5.2 Experimental Procedures

5.2.1 Materials Preparation

The following raw materials were used in the present study for the fabrication of TiC-Ni_3Al cermets with GNP additions (summarised in Table 1): TiC powder (lot no. 45693; particle size = 1-2 μm) supplied by Treibacher Industrie AG (Althofen, Austria), elemental Ni (lot no. L10W013; particle size 2.2-3.0 μm), and Ni/Al 50:50 at. % (lot no. D28X029; particle size <150 μm), both obtained from Alfa Aesar (Ward Hill, MA, USA). The GNPs (30-50 layers thick; flake size = 5-10 μm) were obtained from Graphite Innovation and Technologies Inc. (Halifax, Nova Scotia, Canada). Prior to incorporation into the cermet blends, the GNP particles were evaluated to confirm their characteristics, using a T64000 Raman spectrometer (Horiba Scientific Jobin Yvon, Edison, NJ, USA). A 632.8 nm HeNe laser (JDS Uniphase Corp., Nepean, Ontario, Canada), with a power of 1.6 watts and incident through a 100x objective lens, was used to analyse the GNP spectra and estimate the number of layers. Five scans were averaged over 20 s for each measurement.

Table 5.1 Characteristics of starting powders.

Powders	**Particle size(μm)**	**Shape**	**Supplier**
TiC	1-2	Angular	Treibacher Industrie
Ni	2.2–3.0	spiky dendritic	Alfa Aesar
NiAl	150	Irregular	Alfa Aesar
GNP	5-10 (~15nm thick)	Flake	GIT Inc

The final compositions of the TiC-Ni_3Al cermets, both without and with GNP additions, were produced by using an *in-situ* reaction sintering process to form the Ni_3Al binder phase [114]. To achieve this, mixtures based on a blend of Ni and Ni/Al powders were produced with the intent to form a nominally stoichiometric Ni_3Al intermetallic composition in the final cermet. For each of the examined cermet formulations, the TiC, Ni, Ni/Al and GNP powders were milled simultaneously in ~50 g batches, with 0.5 wt.% polyvinyl butyral (PVB) wax added to aid compaction; blends were milled in acetone for 24 hours at 60 rpm, using yttria stabilized zirconia milling media (Ø = 10 mm), with a 10:1 ratio of mass media/powder. The powder mixtures were subsequently dried in a fume hood for 24 hours, and then sieved through a -45 μm mesh stainless steel screen to eliminate any hard agglomerates. All of the cermet compositions were prepared with a fixed 30 vol.% Ni_3Al and GNP combined content, as the baseline 30 vol.% Ni_3Al composition has been shown to exhibit the best wear response in prior studies [1]. In this instance, the GNP additions specifically replace Ni_3Al in the overall composition on a volume basis (up to 2.5 vol.% GNPs), with a baseline cermet of TiC with 30 vol.% Ni_3Al binder (no GNP addition) also prepared. The resultant cermet compositions are summarised in Table 5.2.

Table 5.2 Compositions of the cermets studied in the experiments.

Cermet	**TiC (vol.%)**	**Ni_3Al (vol.%)**	**GNP (vol.%)**
1	70	30	0
2	70	29.75	0.25
3	70	29.50	0.5
4	70	28.75	1.25
5	70	27.50	2.5

The resultant powder was then compacted at ~70 MPa in a hardened steel die (4.76 mm diameter); ~0.2 ml of hexane was added to the powder mixture during die loading as a volatile 'binder' to improve green strength during compaction and die ejection. The samples were then vacuum bagged and cold isostatically pressed (CIPed) at ~207 MPa to further improve the green density and handling strength. Vacuum sintering was subsequently performed at 1550 °C for 120 minutes, under a dynamic vacuum better than $5x10^{-4}$ Torr. Nominal heating and cooling rates of 20 °C/min

were utilised during sintering, while on cooling below ~800 °C the furnace follows a natural cooling rate that is less than 20°C/min.

5.2.2 Cermet Characterisation

After sintering, the immersion densities of the specimens were determined using Archimedes' principle, in water (at 24 °C). The specimens were then ground and polished down to 0.25 μm diamond paste. Subsequent crystallographic phase evaluation of the polished cermet surfaces was conducted using X-ray diffraction (XRD; Bruker D-8 Advance Bruker Corp., Billerica, MA, USA), under CuKα radiation, operating at 40 kV and 40 mA. The sintered microstructures were examined using both optical microscopy (Olympus BX-51, Olympus Corporation, Tokyo, Japan) and field emission scanning electron microscopy (FE-SEM; Hitachi S-4700, Hitachi High Technologies, Tokyo, Japan), with energy dispersive X-ray spectroscopy (EDS; Inca X-max, Oxford Instruments, Concord, MA, USA) available on the FE-SEM for compositional analysis.

The Vickers hardness of the polished cermets was determined applying a load of 1 kg, following ASTM 1327-15. The low applied indenter load helps to avoid significant cracking around the indents, with the sample subsequently analysed using optical microscopy for precise indentation size measurement. The indentation fracture resistance (IFR) was also assessed using the Vickers indentation method, with a 30 kg applied load. In the current indented samples (for a 30 kg load), only Palmqvist-type cracks were observed, so that the IFR values were determined using the Shetty equation [115]:

$$K_{IC} = \frac{0.0319P}{[al^{0.5}]} \qquad \textbf{Equation 5.1}$$

where P is the applied load, a is the crack length distance from the center of the indent and l is the indentation crack length. To ensure the repeatability of the measurements for both the hardness and IFR values, a minimum of 10 indentations was made for each of the test procedures and materials.

The wear performance was evaluated using both scratch and sliding wear tests. For scratch testing, a Universal Micro Tribometer (UMT-1; CETR, Campbell, CA, USA) was used with a diamond indenter sliding in linear motion across the flat surface. This is achieved using a single pass of 5

mm length, with a scratch speed of 0.166 mm/s. Tests were conducted at room temperature (22 ± 2 °C), and with a relative humidity of 40-50 %. In the scratch test, the load is applied downward against the surface of the sample with a Rockwell diamond indenter (with a tip radius of 200 μm). Loads of 50 or 100N were applied to generate the scratch tracks, although data is only presented for 100 N tests as the lower loads did not provide good reproducibility. Data was obtained using the UMT software, which allowed determination of the coefficient of friction (COF) of the surface. The average width of the scratch track was subsequently measured using FE-SEM, and the scratch hardness number, HS_p, was then determined using the relationship [116]:

$$HS_p = \frac{8P}{\pi W^2} \qquad \textbf{Equation 5.2}$$

where P is the normal load and W is the scratch width.

For assessment of sliding wear behaviour, cylindrical-shaped TiC-Ni_3Al test specimens (~4.24 mm diameter × ~10.56 mm length), both without and with GNP additions, were installed into the sample holder of an 'in-house' designed and constructed block-on-ring system; the testing arrangement is shown schematically in Figure 5.1, along an example of the actual cylindrical cermet test sample and also a WC-Co counter-face sample. The annular cross-section WC-Co counter-face ring (grade WC-6Co) of the tribo-pairing was obtained from Endurance Carbide Inc. (Saginaw, MI, USA), with physical dimensions of 18.0 mm outside diameter x 10.0 mm internal diameter x 10.0 mm overall length. The TiC-Ni_3Al based test samples and the WC-Co counter-face wheel were both ground to a surface roughness (R_a) of ~5 μm prior to testing.

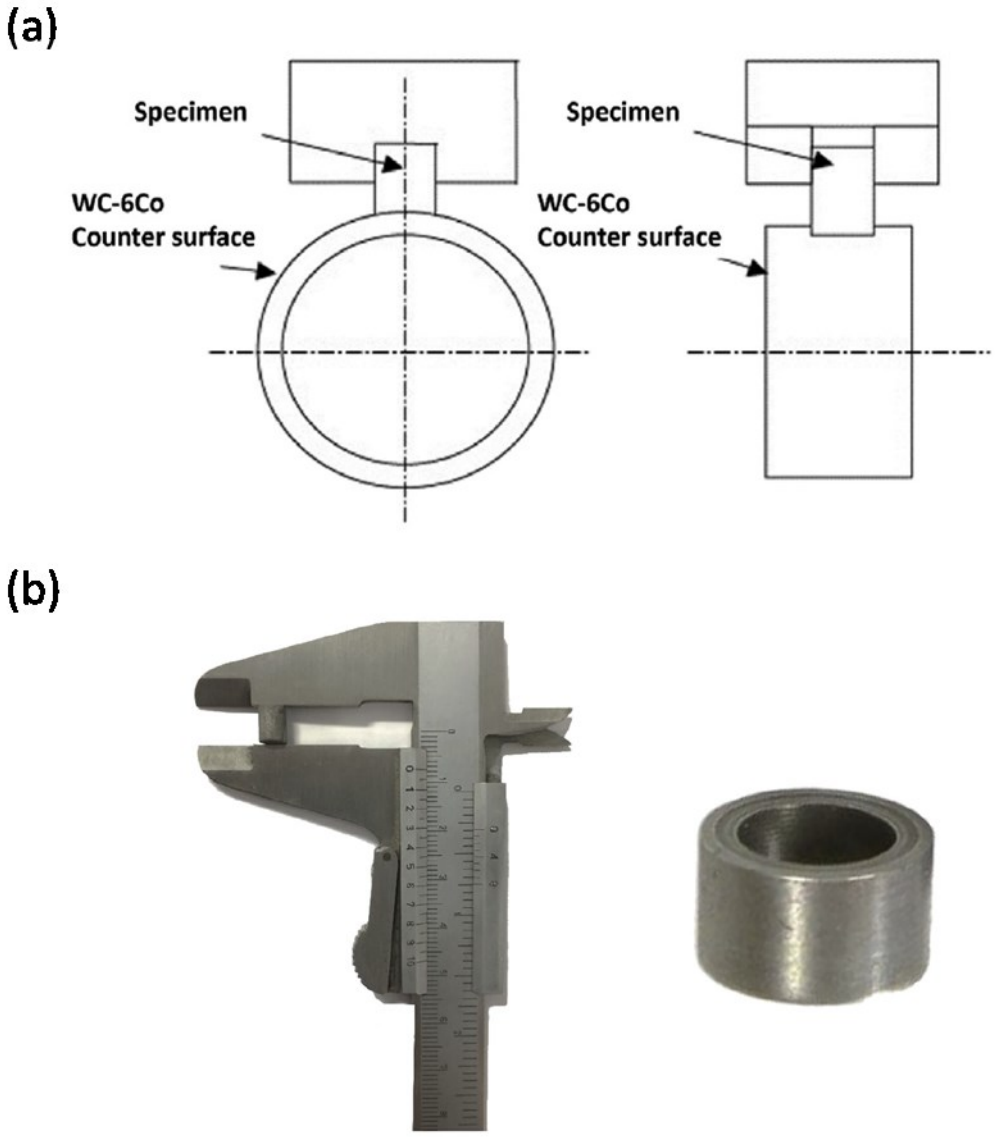

Figure 5.1 (a) A schematic representation of the block-on-ring wear test geometry used in the present work, showing the specimen being evaluated and the WC- 6Co counter surface. (b) Representative images of the test sample, held in a pair of caliper jaws (left), and the WC-Co counter face cylinder (right).

Before each wear test, and then at 5 minute intervals up to 45 minutes total test duration, the weight of the samples was measured (with a precision of 0.0001g). The resultant weight loss is then converted into a material volume loss, V, for each sample [77], with the specific wear rate, k (in units of $mm^3\ N^{-1}\ m^{-1}$), determined for the 45-minute test duration using the Lancaster equation [117]:

$$k = \frac{V}{PS}$$ **Equation 5.3**

where P is the applied load (in N) and S is the total sliding distance (in m). The rotation speed of the WC-Co counter-face wheel was maintained constant at 210 rpm for all tests, with an applied load of 100 N. The full test duration of 45 minutes corresponds to a total sliding distance of 540 m. The tribo-pair interfacial temperature profile during the sliding wear test was measured with a thermal imaging camera. Due to potential fluctuations in the wear response, each of the tests were repeated three times under identical conditions, with both the resultant mean and standard deviation values determined. After testing, the wear damage was evaluated using FE-SEM, with any compositional changes determined using EDS analysis.

5.3 Results and Discussion

5.3.1 GNP and Cermet Microstructure Characterization

In the present work, graphite-derived GNP additions are employed with the aim of improving the wear resistance of TiC-Ni_3Al cermets. An initial aspect of this study is therefore characterisation of the GNPs. Figure 5.2 presents XRD spectra of the supplied GNPs compared with the original graphite feedstock used for GNP production; Miller indices for the respective peaks are also indicated in the graph. It can be seen that there are significant decreases in intensity of the (002) and (004) peaks for the GNP when compared with the raw graphite feedstock material [118]; note that the data has been normalised, based on the relative intensities of the (002) peaks. The inset in this figure highlights the significant reduction in the intensity of the (002) peak, for data presented without normalisation (*i.e.*, the raw data).

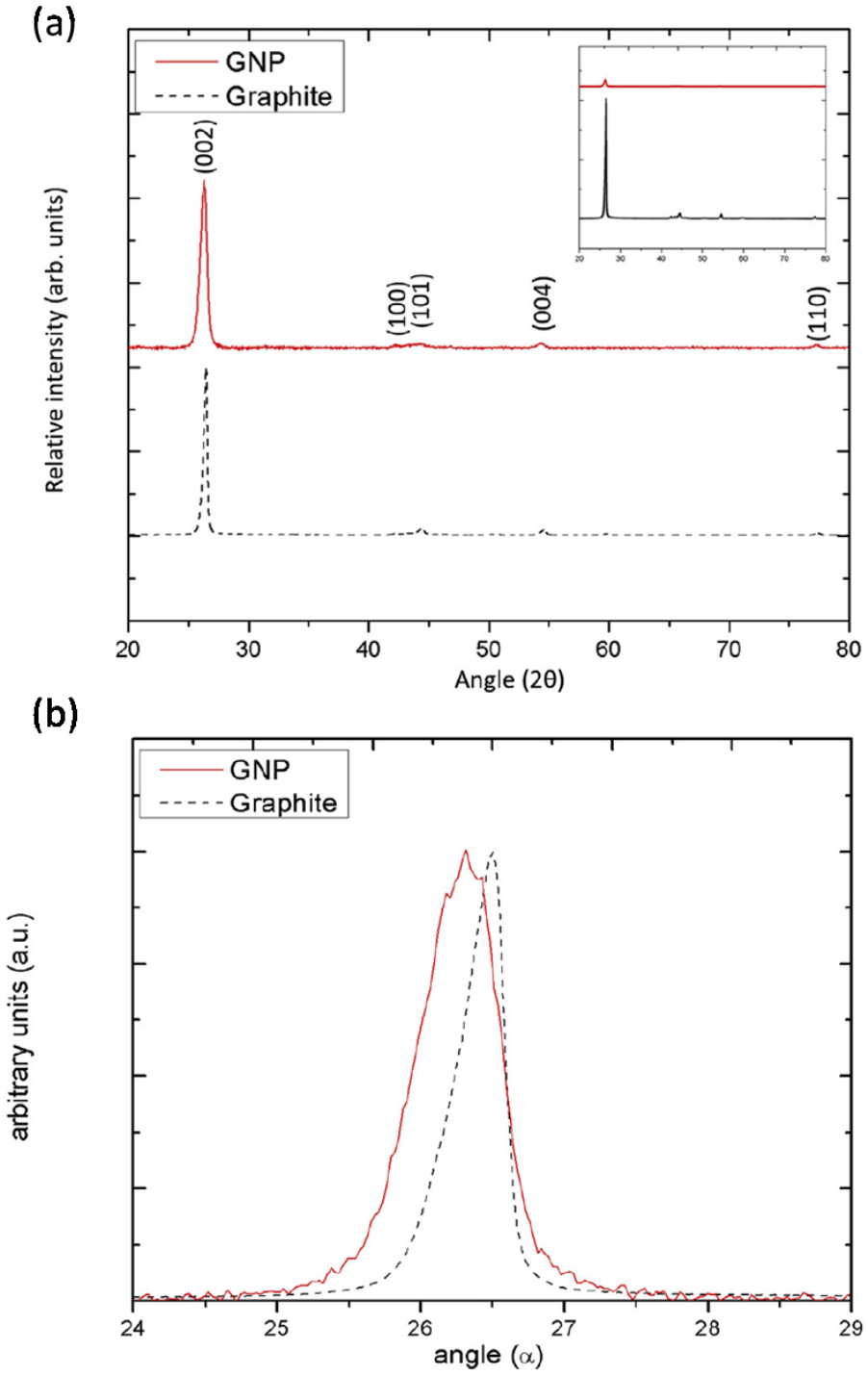

Figure 5.2 (a) X ray diffraction traces obtained for the GNP particles and graphite, for comparison (note that the data is normalised, based on the (002) peak intensity). The inset figure shows the raw data without normalisation. (b) Overlayed data from (a) highlighting the peak broadening that arises for the GNPs.

The mean height of the crystallite (L_c) in the direction of the c-axis, which represents the average thickness of the GNP particles, was then estimated from the Miller indices (002) using the Scherrer equation [119]:

$$L_c = \frac{0.89\lambda}{\beta\cos(\theta)} \qquad \textbf{Equation 5.4}$$

where λ is the X-ray wavelength (*i.e.*, 1.5406 Å for CuKα), β is the full width at half maximum (FWHM) of the peak (in radians) and θ is the Bragg angle. A clear reduction in L_C demonstrated that the number of layers has been decreased during the GNP synthesis process, in this case corresponding to a mean value reduced from ~129 to ~19 layers. As shown in Figure 5.3, when compared to graphite, for Raman analysis there is a change in the shape of the bands D, G and 2D, with the most significant changes observed in the 2D bands [120]. Previous studies have also reported comparable differences in the 2D bands for graphite and graphene [121], showing that the graphite 2D bands consist of two integrals $2D_1/2D_2$ that overlap inside the 2D band, while the GNPs have an increase in the second part of the 2D band.

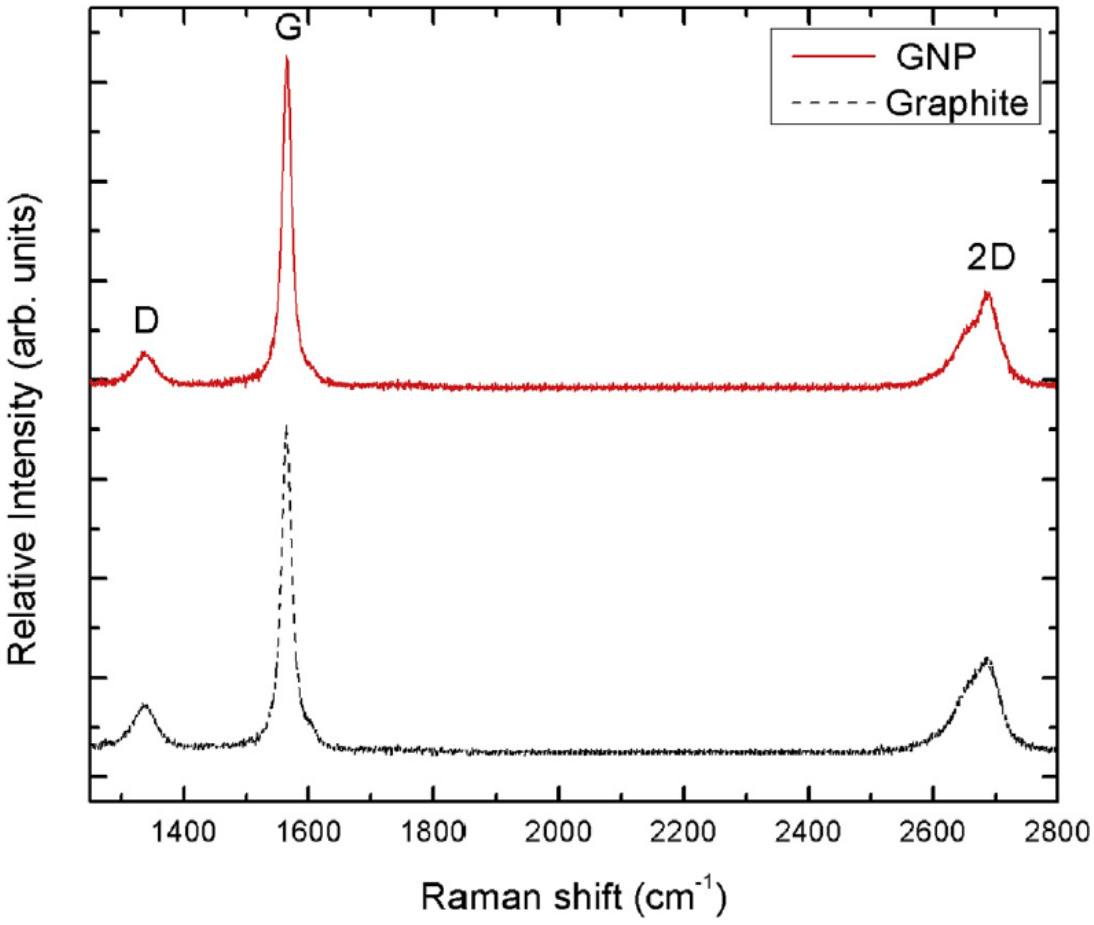

Figure 5.3 Raman mapping comparing the spectra between 1250 and 2800 cm−1 for GNP particles and the original graphite feedstock material (532 nm excitation).

Figure 5.4 shows a typical FE-SEM image of an as-milled powder mixture, used in the subsequent preparation of the green preforms. The extent of homogenisation and size refinement that is achieved following the initial ball milling stage is demonstrated; in this instance the baseline composition, with TiC-30 wt.% Ni_3Al, is shown. The fine, angular particles within the size range of 1-2 microns correspond to the TiC, although visually there is not a significant degree of size reduction. The irregularly-shaped particles ranging from 4-8 microns are agglomerates of small TiC grains and milled particles of Ni/Al and/or Ni; particle compositions were confirmed through EDS analysis. The fine particle distribution improves the potential for production of fully dense samples during the subsequent sintering process, due to the high densification that can be achieved during stage 1 of the liquid phase sintering process [32]. The predominantly irregular morphology,

with angular particles in the powder mixture, results in high attrition during the milling process. The overall moderately broad size range and shape of the powder particles can be expected to improve the green density, through better particle packing during cold compaction, which is further improved by the addition of the PVB lubricant during milling.

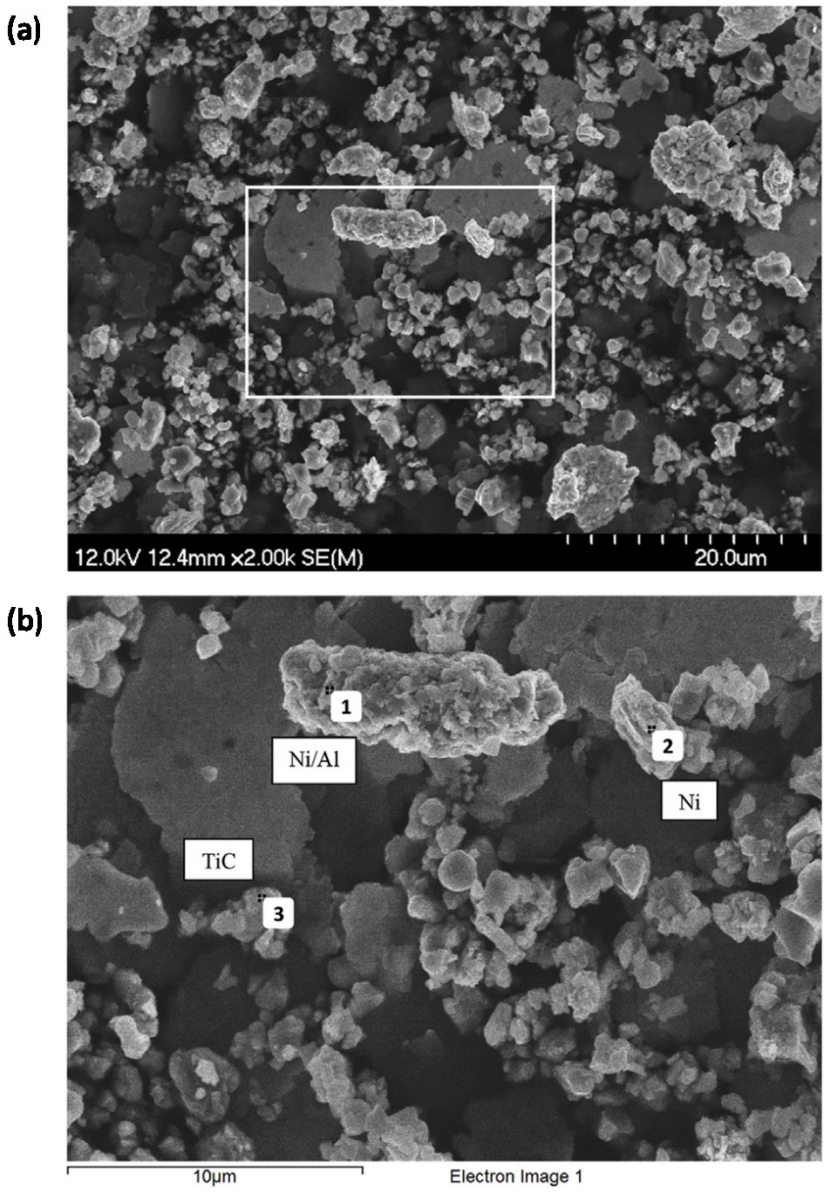

Figure 5.4 (a) Representative FE-SEM image of the blended/milled powder mixture. (b) Inset shows region where EDS analysis was conducted, and the resultant phases.

After sintering, it is clearly important to achieve high density cermets, so the influence of GNP additions on densification was assessed. Figure 5.5 demonstrates that the GNP additions, up to a

maximum of 2.5 vol.% in the present work, do not have any significantly deleterious effects on the densification response, with each of the cermets sintered to greater than 99 % of theoretical density. Figure 5.5 shows a small density decrease is noted with the GNP additions, but it is less than 0.5 % reduction of the theoretical density. Ultimately, if the GNP content is increased past 2.5 vol.% it is likely that some drop-off in final sintered density will be observed, which warrants further study.

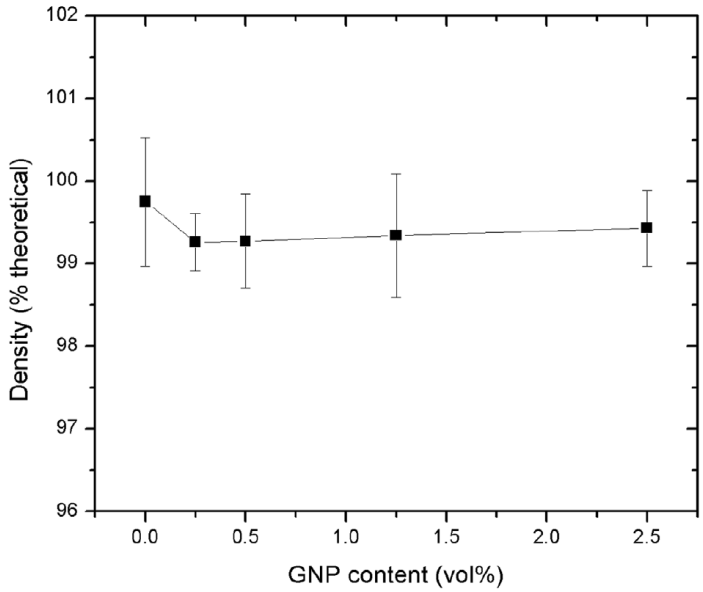

Figure 5.5 The sintered densities for the TiC-30 vol.% Ni_3Al cermets as a function of GNP content; values were determined by Archimedes immersion in distilled water.

The high degree of densification is further confirmed through optical and scanning electron microscopy examination of the GNP containing cermets (Figures 6 and 7). Here the small, dark contrast regions are GNP particles and occasional clusters of particles. It is apparent that the GNPs are relatively well dispersed through the TiC-Ni_3Al cermet structure, which is desirable from a predictive property perspective.

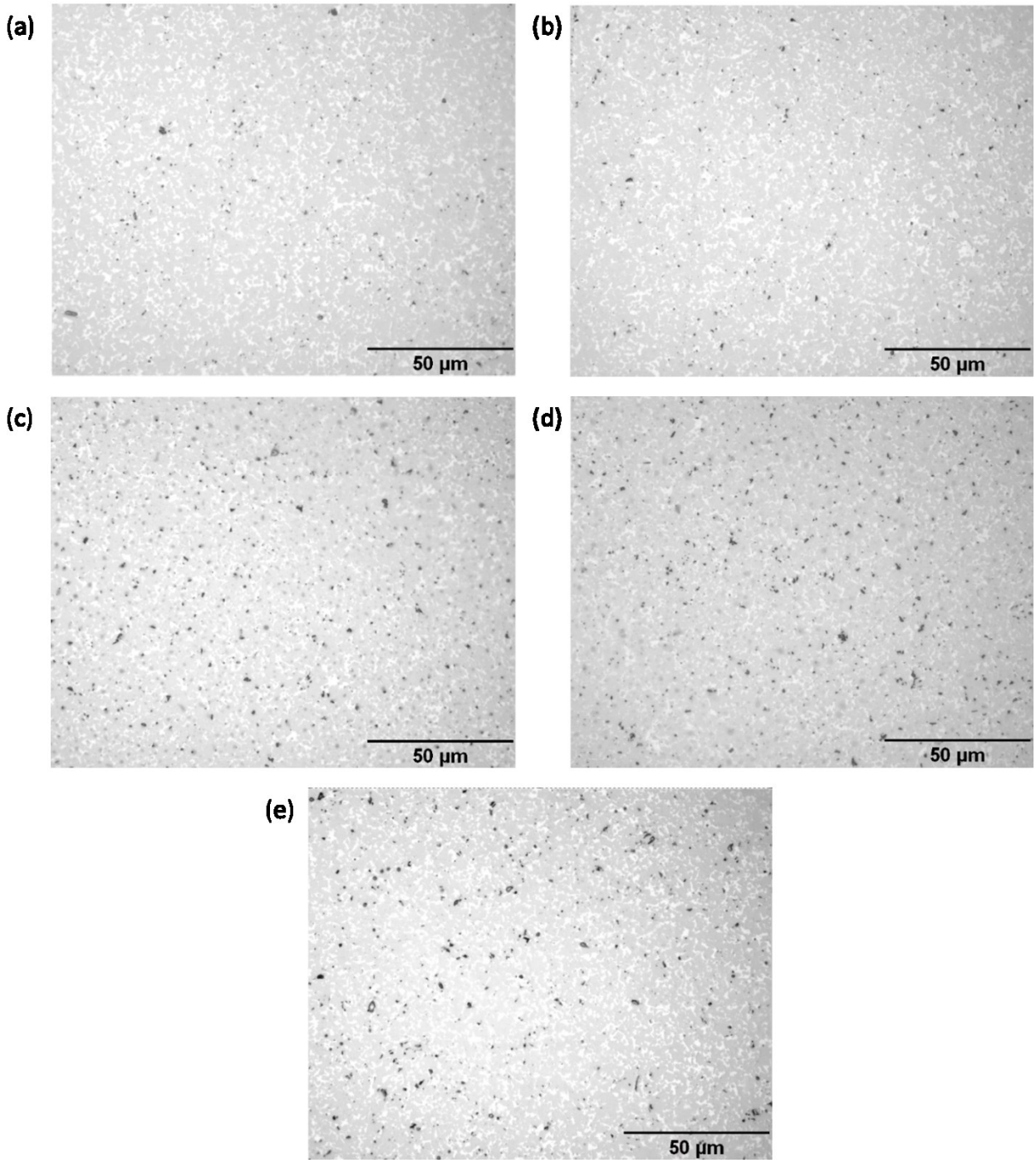

Figure 5.6 The effects of GNP additions on the TiC-Ni_3Al cermets, examined using optical microscopy: (a) 0 vol % GNPs, (b) 0.25 vol.% GNPs, (c) 0.5 vol.% GNPs, (d) 1.25 vol.% GNPs, and (e) 2.5 vol.% GNPs.

Qualitatively, there also appears to be a small degree of refinement of the TiC ceramic grains with increasing GNP contents. In a recent study, graphite particles were added to Ti(C,N)-Ni based

cermets [107]. They indicated that a dissolution/re-precipitation can occur with the graphite additions, such that it dissolves into the Ni-based liquid during sintering and then re-precipitates during cooling [107]. In that instance, the addition was termed “dissociative graphite” [12], due to the proposed dissolution/re-precipitation mechanism, although there was no confirmation in the article that it was retained in a graphitic form if it was dissolved and then re-precipitated. It was indicated that increasing the graphite particle size subsequently retards their dissolution [12], as might be expected in such a scenario. This difference in dissolution response was suggested to result in the observed transition from an aggregated morphology to isolated graphite with increasing initial particle size.

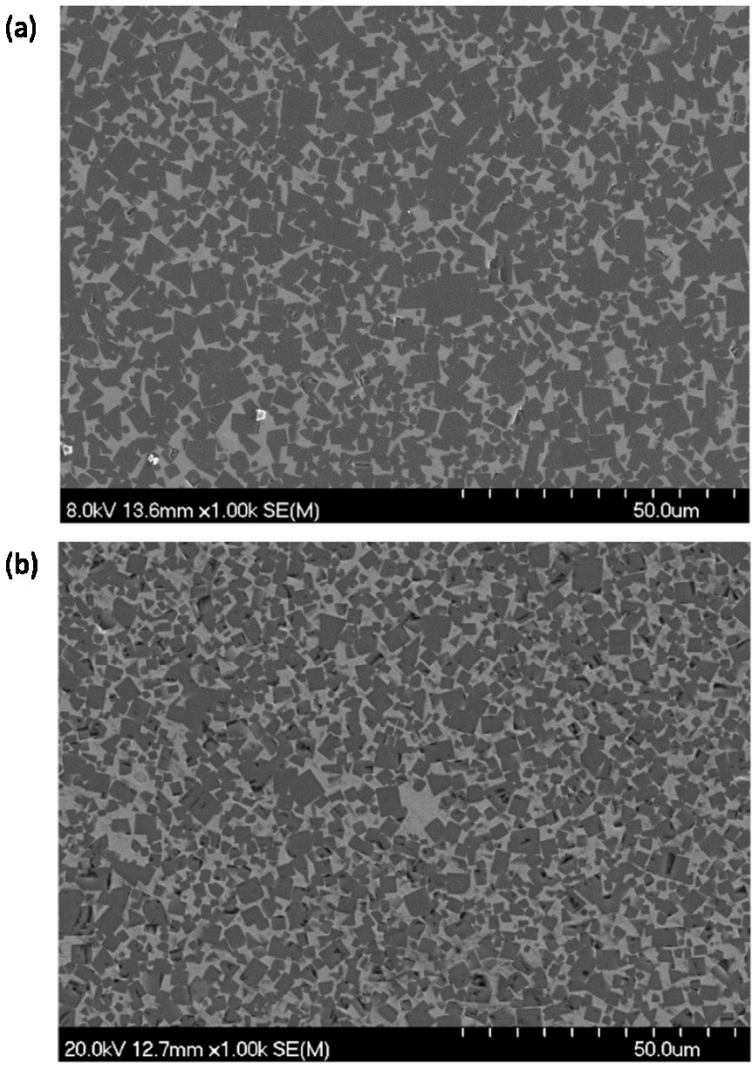

Figure 5.7 Representative FE-SEM images of the as-sintered and polished cermets prior to wear testing: (a) TiC-Ni_3Al and (b) TiC-Ni_3Al with 2.5 vol.% GNPs.

The phase formation and stability of the vacuum sintered TiC-Ni_3Al cermets, without and with GNP additions, was examined using XRD. Representative traces, after sintering at 1550°C for 120 minutes, are presented in Figure 5.8 for the TiC-Ni_3Al cermets with 0 and 2.5 vol.% GNP. The presence of the Ni_3Al intermetallic phase is detected through XRD, confirming that the reactive homogenisation of the Ni and Ni/Al mixture was successfully achieved. No significant changes in the peak positions, intensity or width was noted for the GNP additions, which indicates their stability during sintering, and the likely scenario that they do not dissolve and then re-precipitate during sintering.

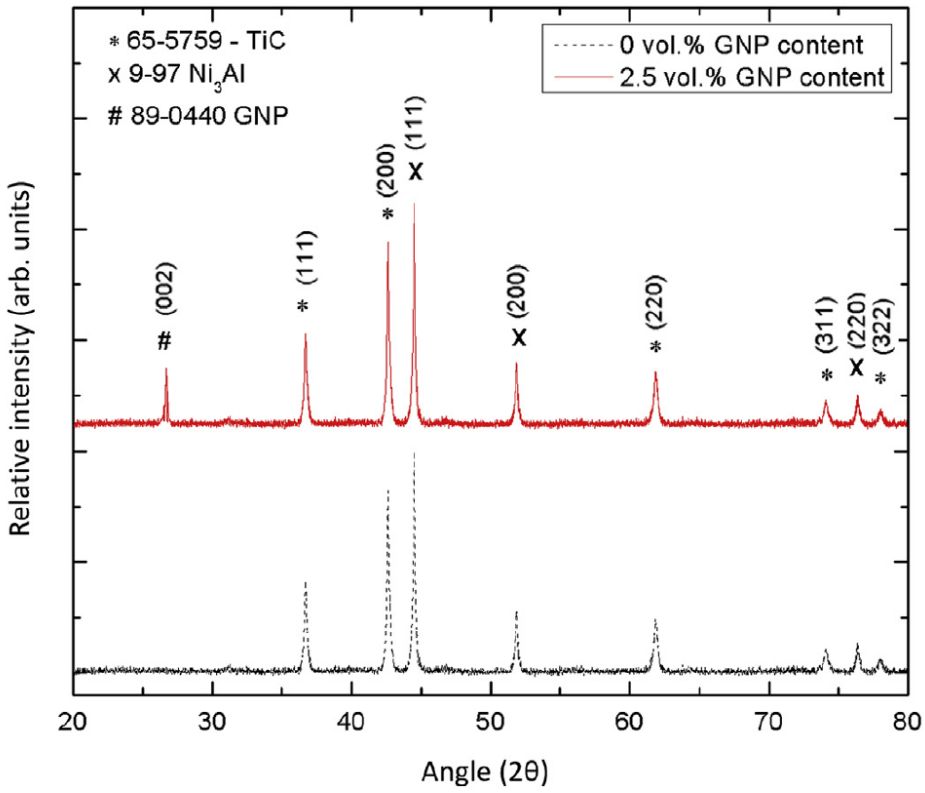

Figure 5.8 Typical, representative XRD diffraction traces for TiC-30 vol.% Ni_3Al cermets with GNP additions of 0 and 2.5 vol.%.

5.3.2 Mechanical Properties

The wear response of a material is typically affected by several parameters, notably the hardness and fracture toughness. Figure 5.9(a) demonstrates the influence of GNP content on the resultant

Vickers hardness (measured under a 1 kg load) for the various TiC-Ni_3Al cermet compositions. It is apparent that GNP additions have a moderately significant effect on the hardness, with an increase of ~16% for the maximum GNP addition of 2.5 vol.%, raised from ~1060 HV1 to ~1220 HV1. This can, at least in part, be related to the reduction of ductile Ni_3Al content and increasing addition of high modulus GNPs. It has been noted for some ceramic systems, for example Si_3N_4, that additions of more than 1 vol.% of GNPs tends to result in degraded final densification, with a resultant reduction of the hardness values [122]. Such a trend is not observed for the present TiC-Ni_3Al materials, as densification is largely unaffected by GNP additions up to 2.5 vol.%, while the hardness is noticeably improved. Fracture toughness is also an important parameter in determining the response of nominally wear resistant materials [72]. The application of indentation fracture resistance (IFR) testing, using a Vickers indenter, is a useful toughness-related parameter for characterising materials that will be subjected to analogous situations of impact by sharp particles [123], such as during abrasive or erosive wear. Figure 5.9(b) presents the IFR measured data for the present cermets, as a function of GNP addition. It is apparent that the overall IFR increases with added GNP content above 0.25 vol.%. Its was reported in the literature that pure TiC has a relatively low fracture resistance at ~2 $MPa•m^{1/2}$ [124], highlighting the benefits of metallic phase addition and development of the cermet-type microstructure. In comparison to TiC, pure Ni_3Al has a value of 14.6 to 18.2 $MPa•m^{1/2}$, depending on the grain size [125]. Simply assessing the composite constituents, GNPs are a relatively hard phase in comparison to the binder, which could be anticipated to lead to an increase the brittle characteristics of the binder phase, subsequently reducing the fracture resistance. However, a recent study of GNP additions to alumina ceramics has demonstrated that the most probable mechanism of the increase in IFR is a crack/deflection bridging effect [35]. It was proposed in that work that since the GNP dimensions are small, and they uniformly distributed within the composite, the flakes may concentrate at the grain boundaries, helping to reduce crack propagation between individual grains [126]. Hence, it is proposed that the GNPs will increase the fracture resistance through crack deflection and bridging mechanisms in the present cermet systems. However, in addition, there is an apparent TiC grain refinement with the GNP additions, as noted earlier, which likely also therefore reduces the Ni_3Al ligament dimensions, such that further strengthening through a Hall-Petch type mechanism cannot be discounted.

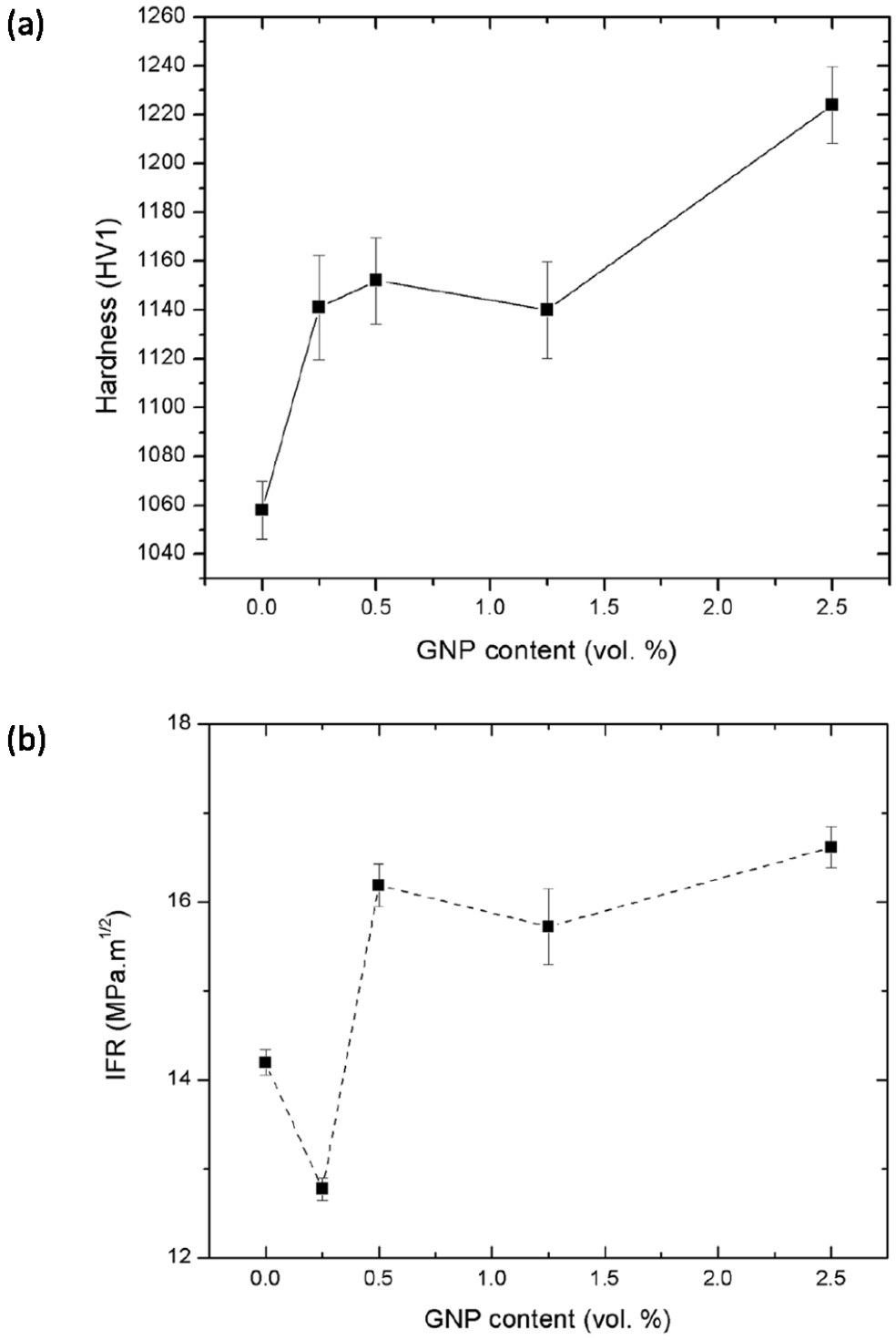

Figure 5.9 (a) Vickers hardness values for the TiC-30 vol.% Ni_3Al cermets as a function of GNP content. (b) Indentation fracture resistance (IFR) values for the TiC-30 vol.% Ni_3Al cermets as a function of GNP content.

5.3.3 Sliding Wear Behaviour

The wear performance of the TiC-30 vol.% Ni_3Al cermets and, particularly, the effects of GNP additions on the wear mechanism(s) was evaluated through a combination of scratch testing and sliding wear experiments. The scratch test is a relatively simple and precise method to evaluate the abrasive wear response, and allows determination of the true friction coefficient by elimination of the third-body effects, which are typically generated during more traditional dry sliding wear tests [127]. In the case of a single-pass scratch test, on bilinear elastic-plastic materials, the coefficient of friction (COF) is defined by the ratio between tangential force (F_T) to the normal force (F_N):

$$\mu = \frac{F_T}{F_N} \qquad \textbf{Equation 5.5}$$

The frictional force increases with surface roughness and the adhesion between the diamond indenter and the material being evaluated. In the present work, the 50-100 N load range was initially chosen in order to minimize any effects due to surfaces imperfections/roughness, and to identify the true COF of the composite material [128]. However, ultimately the lower load did not provide reproducible data, and only the higher 100 N was utilised. The resultant COF shows a tendency to decrease significantly as GNP additions are incorporated, from ~0.53 to ~0.15 when the 100 N applied load was used (Figure 5.10). Clearly, in this instance even small GNP additions are acting as an effective solid lubricant, as noted in prior studies using graphite rather than GNPs [13].

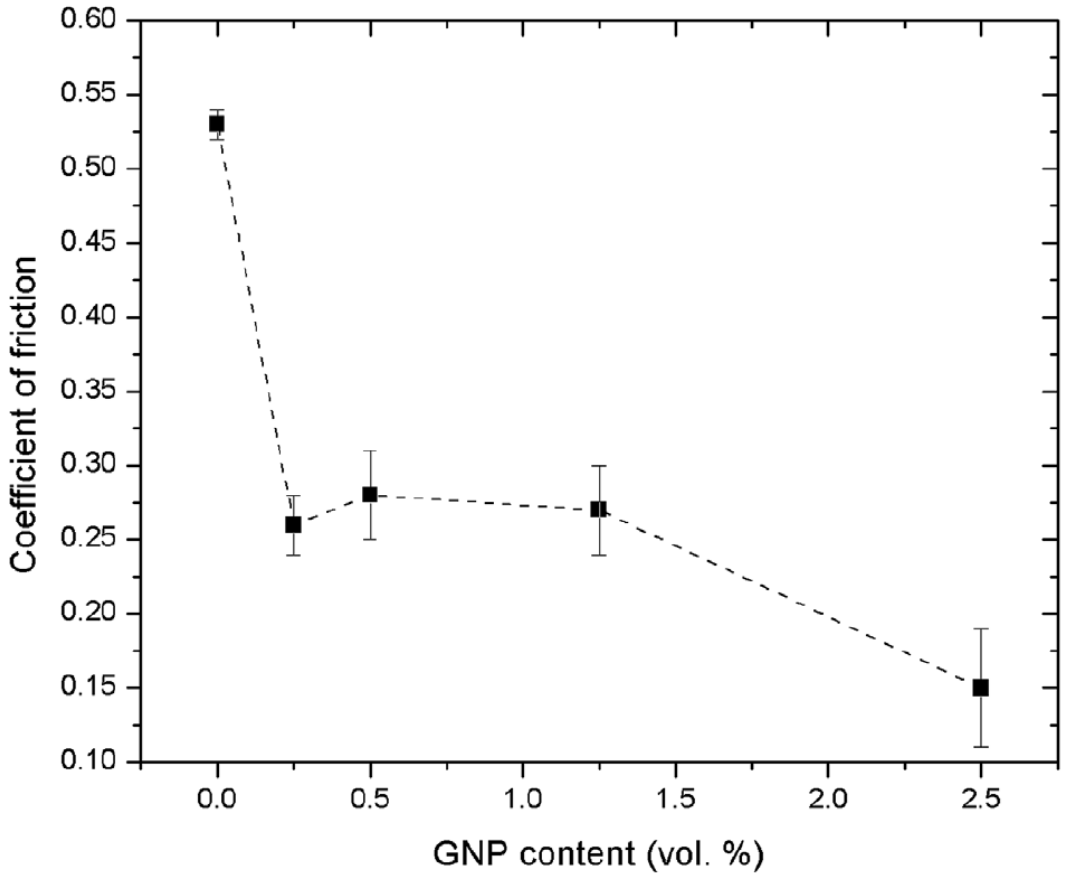

Figure 5.10 The coefficient of friction determined from scratch testing on the $TiCNi_3Al$ cermets as a function of GNP content. Tests were conducted with a 100 N applied load.

Figure 5.11 shows examples of the scratch damage examined using SEM, where the crack damage within the surface can be analysed. The 100 N load was chosen, as noted above, as a larger scratch width generated and the data was more reproducible. Due to the fixed indenter geometry, the wider the measured scratch track, the greater the penetration depth (and hence, in principle, the softer the material). For the present cermets, the scratch hardness number increases from ~13.8 to ~18.9 GPa with the GNP additions. The SEM images also shows a moderate amount of edge "chipping" in the samples prepared without GNP additions, while such damage is minimal for the example with 2.5 vol.% GNP incorporation.

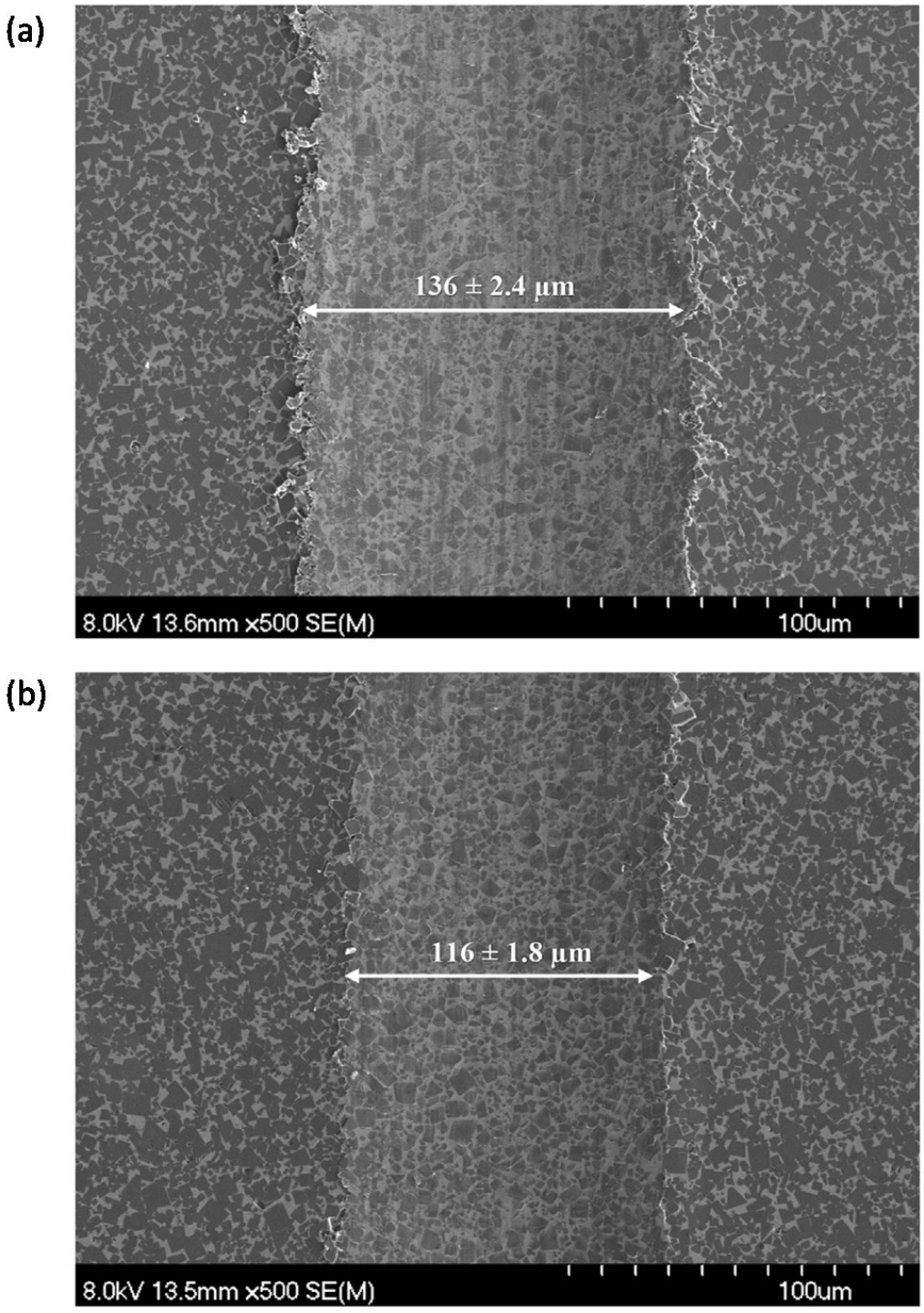

Figure 5.11 FE-SEM images of the scratch track surfaces, indicating the width of the tracks created using a Rockwell diamond indenter, with an applied load of 100 N: (a) TiC-30 vol.% Ni_3Al cermets with 0 vol.% GNPs, and (b) TiC-30 vol.% Ni_3Al cermets with 2.5 vol.% GNPs.

The dry sliding wear response was determined using a continuous sliding block-on-ring type geometry, which allows measurement of the material loss as a function of sliding distance, and subsequently calculation of the specific wear rate, following Eqn. 5.3. As would be anticipated, Figure 5.12 demonstrates that the material volume loss of the cermets during the sliding wear tests increases with increasing sliding distance (*i.e.*, increasing test duration). However, it is also clearly apparent that the extent of material loss *decreases* with an increasing GNP content, for a fixed time/distance, further highlighting the benefits of low volume fractions of GNP addition. All samples follow an initial transient stage of wear up to ~100 m in distance, typically referred to as the "running-in period" [107,129], after which the wear volume change is roughly linear with increasing sliding distance (*i.e.*, nominally 'steady state').

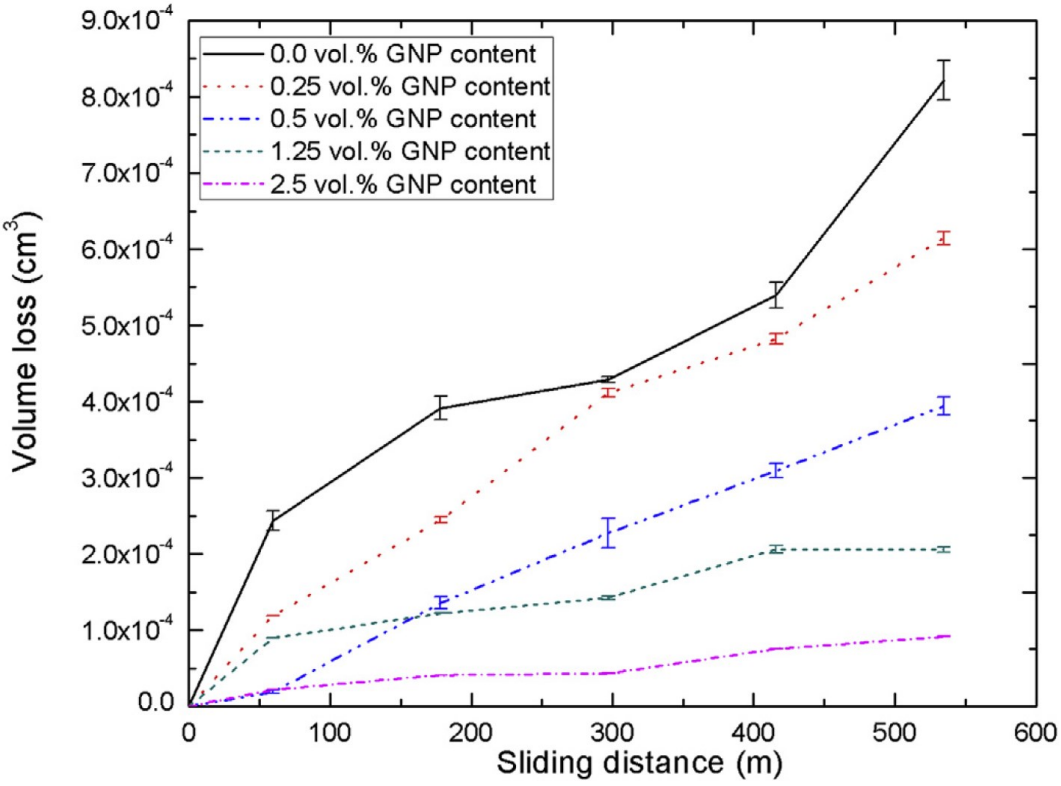

Figure 5.12 The calculated wear track volumes for the TiC-Ni_3Al cermets as a function of sliding distance and GNP contents.

Figure 5.13 presents the specific wear rate data for the present cermets, calculated based on weight loss at the end of the wear test period of 45 minutes (*i.e.*, a total sliding distance of 540 m). The specific wear rates are seen to decrease incrementally with increasing GNP content, with the lowest

wear rate (~1.7 x 10^{-6} mm^3/Nm) obtained for 2.5 vol.% GNP content, being essentially one order of magnitude lower than the baseline cermet without GNP additions. It should be stressed that these values are over one order of magnitude *higher* than observed for similar TiC-Ni_3Al materials when tested with a reciprocating, ball-on-flat test geometry [20], which can mostly be attributed to the test approach, although those materials also exhibited a subtle core-rim structure. In comparison, very similar wear rates were observed for Ti(C,N) cermets with graphite additions using a more comparable block-on-ring geometry [13].

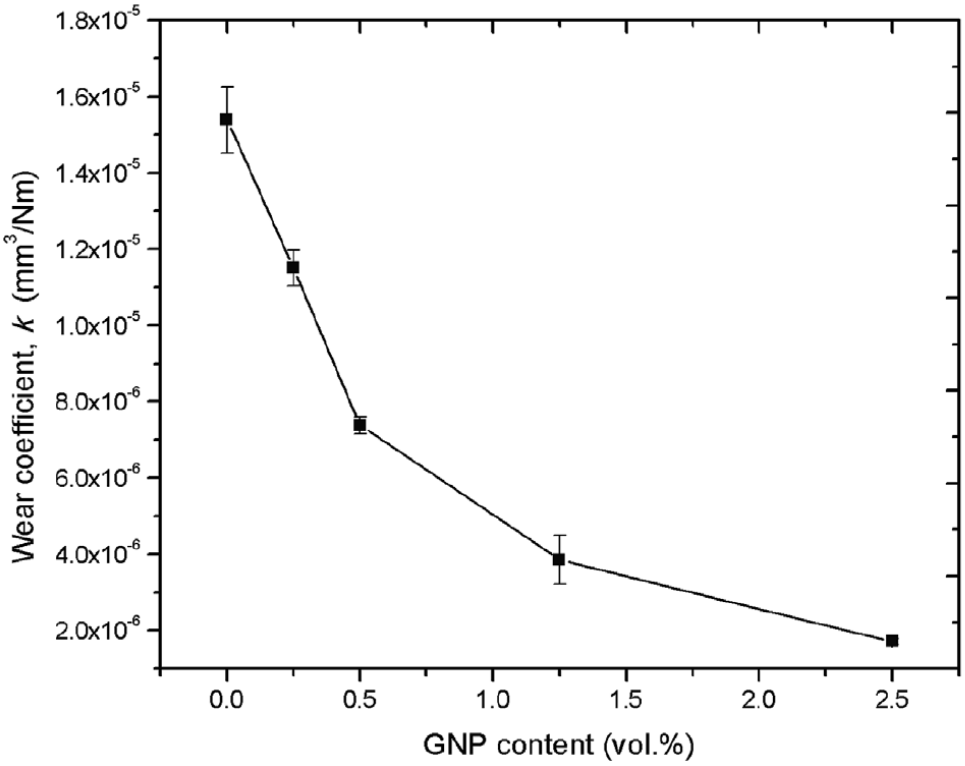

Figure 5.13 The calculated specific wear rates (k) for the TiC-30 vol.% Ni_3Al cermets as a function of GNP content.

It has previously been reported that graphite can act as a "soft" filler, which may be released during the sliding wear process, and can then be incorporated into a tribolayer between the contact surfaces [107]. Consequently, the graphite (or graphene) can act as a solid lubricant, which contributes to a reduction of the frictional sliding coefficient, which was shown previously in Figure 5.10. An apparently related behaviour can be seen from the trends in the present work, when utilising the GNP additions; here it can be hypothesised that the graphene flakes are extruded

from the grain boundary during Hertzian compressive loading, and these flakes subsequently contribute to the tribofilm. When two surfaces are in sliding contact, the temperature can rapidly rise, through frictional heating produced at the interface between the materials. In extreme situations, the surface and sub-surface temperature can cause material property change, and consequently having an effect on the wear performance, and as well deformation and friction of the surface [129]. Figure 5.14 demonstrates that there is an almost constant rate of temperature rise, up to ~90°C at the conclusion of the test. GNP additions slightly lower this thermal increase, by lowering the COF. It is important to stress that such temperatures are far below those needed for any significant oxide formation to arise on the exposed wear surface, aside from any formed through simple passivation of newly exposed surfaces. As shown in the present work, GNP additions significantly improve both the mechanical *and* tribological performance of the present TiC-Ni_3Al cermets, including a significant decrease of the COF and specific wear rate.

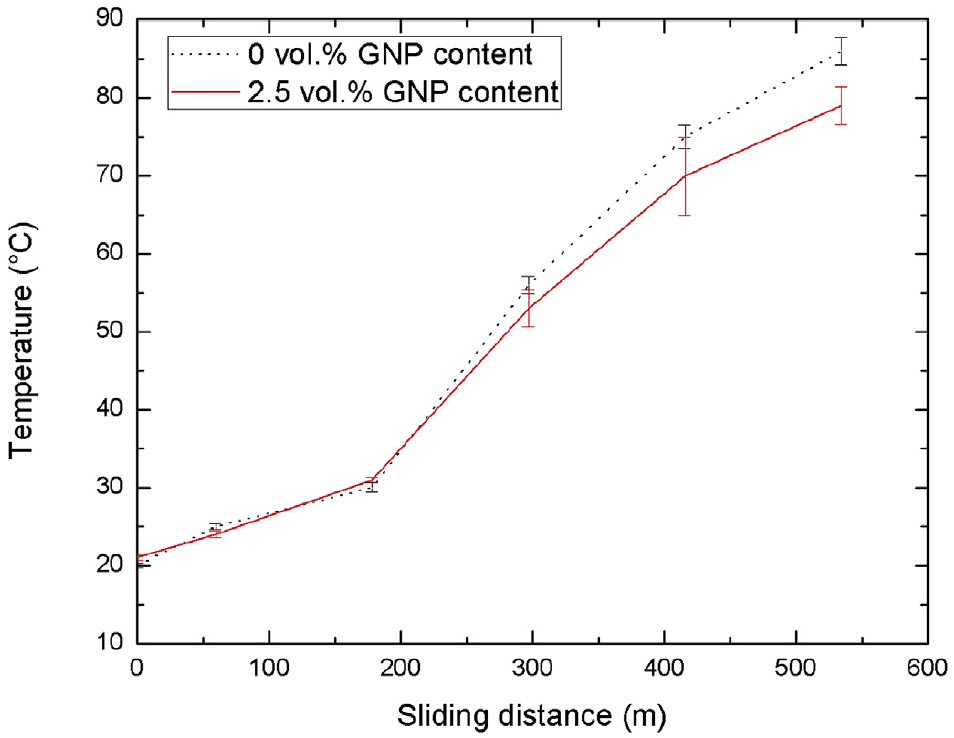

Figure 5.14 - The nominal measured temperature profile for the interface between the test sample and WC-Co counter-face material, as a function of total sliding distance and GNP content, for 0 and 2.5 vol.% GNPs.

Typical FE-SEM images of the worn surfaces of the TiC-Ni_3Al cermets, with various GNP contents, after continuous dry sliding wear, are presented in Figure 5.15. It is evident that the extent of wear on the surfaces of the cermet samples becomes progressively less severe with an increasing volume fraction of GNPs. At the highest GNP loading (*i.e.*, 2.5 vol.%), the original, nominally two-phase cermet surface microstructure is still largely visible. Previous studies have shown that additions up to 0.8 wt.% of graphite can enhance the sliding wear performance of Ti(C,N)-based cermets [108], while for higher graphite contents, the wear rate starts to increase again. For comparison, in the current work, additions of up to ~1 wt.% (*i.e.*, 2.5 vol.%) are used, and the wear resistance of the cermets continues to increase within the composition range examined; this may indicate a small benefit to using GNP additions over graphite particles, but also indicates the need to study an expanded composition range.

From Figure 5.15 (a,b), the surface appears to be quite rough, and there is a clear formation of a surface tribolayer or tribofilm; in this instance the original two-phase TiC-Ni_3Al microstructure (without GNP additions) cannot be clearly discerned. The formation of a tribofilm indicates the occurrence of adhesive wear, which usually follows abrasive wear. Here the surface damage initially arises from an abrasion process, mainly by material ploughing. This creates damaged material that is freed from the surface, often from both the test sample and the counter-face. Several prior studies have shown similar transitions, from abrasive wear, typically two- to three-body, and then to adhesive wear [1,130]. In the present case, it also appears that the combination of abrasive and then adhesive wear is more severe, as the specific wear rate for the GNP-free TiC-Ni_3Al cermets is higher that when compared to those with GNP additions (shown previously in Figure 5.13). It can be assumed that this increased wear is, at least in part, related to a higher coefficient of friction for the material prepared without GNP additions. This is further confirmed by scratch testing and the related COF data presented in Figure 5.10. Considering the two binder phase metals, for both the test sample(s) and the counter-face wheel, adherence between the Ni_3Al and Co may potentially arise through cold welding during plastic deformation of any asperities [123]. This mechanism favours further extrusion of the binder phases, while cracking and fragmentation of the hard phase ceramic particles will further increase the wear rate.

A previous study has shown that without solid lubricant, the formation of a tribofilm was limited while additions of a graphitic phase such as GNP or graphite was beneficial in creating a more uniform and homogenous tribolayer [131]. This is somewhat contrary to our own studies where,

for TiC-Ni_3Al based cermets, a tribolayer is typically observed (especially at higher applied loads) [1]. However, small additions of graphite can significantly improve the wear properties of cermets [107,109], due to the production of wear debris from the extruded binder phase(s) forming a lubricious tribofilm, thus protecting surfaces from further damage due to the reduction of the direct frictional contact between them. As with graphite additions [107,108], incremental increases in the GNP content most likely reduce the coefficient of friction and, in consequence, reduce the degree of abrasive and adhesive wear. When up to 1.25 vol.% of GNP particles (roughly 0.5 wt.%) is added, there is an indication of predominantly abrasive/erosive wear occurring on the worn surface (Fig. 5.15(c,d)). An overall smoother surface is observed, indicating that a stable and continuous solid lubricant film is likely formed between the tribo-pairing [131]. As can be seen from the specific wear rate data in Fig. 5.13, and the microstructural observations in Fig. 5.15(e,f), further additions of GNPs, in this case 2.5 vol.% (or roughly 1 wt.%) significantly increase the wear resistance of the composite. Here it can be seen that there is relatively minimal surface damage, which retains a smooth appearance. The original TiC grains and Ni_3Al binder matrix are still readily visible. In the present case, for moderate GNP additions, a considerable lubrication effect is seen, drastically reducing the extent of surface wear of the cermet.

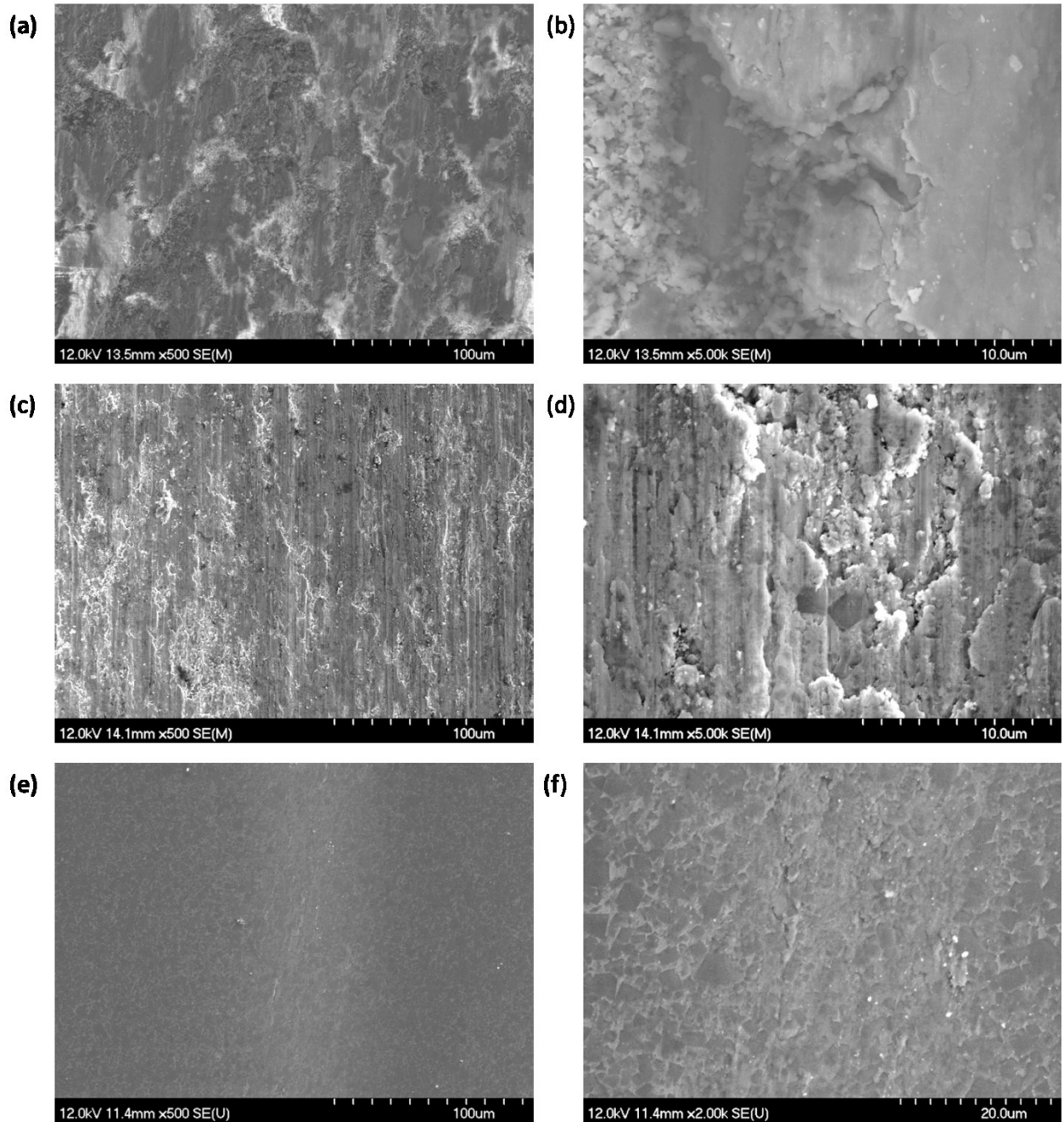

Figure 5.15 - FE-SEM images of the wear tracks for the TiC-Ni_3Al cermets at low and high magnifications. (a,b) TiC-Ni_3Al cermet without GNP additions (c,d) TiC-Ni_3Al cermet with 0.5 vol.% GNPs. (e,f) TiC-Ni_3Al cermet with 2.5 vol.% GNPs.

Observations from generated SEM/EDS shows an example of a worn surface in the Figure 5.16**,** with grooving arising from the sliding motion combined with surface asperities. Chemical analysis

shows that the composition was consistent after the test, relative to the starting surface, and showed no significant evidence of effects such as oxidation or associated chemical reactions.

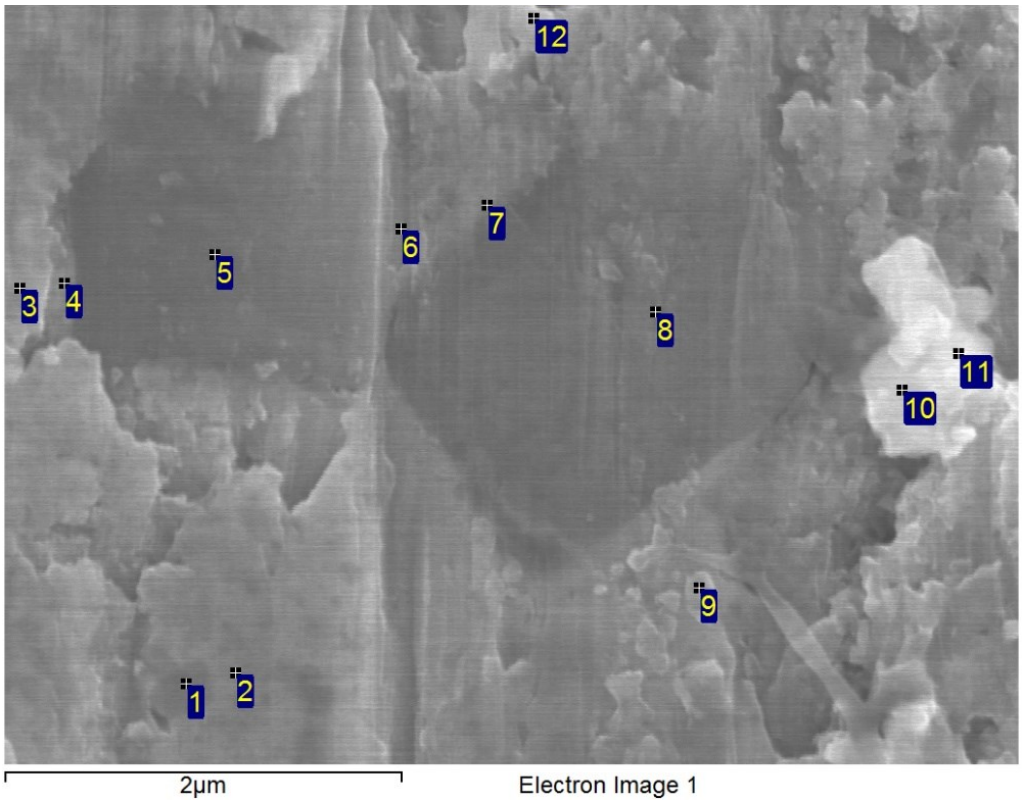

Figure 5.16 EDS analysis of the surface wear track from the TiC-30 vol.% Ni_3Al cermet with 2.5 vol.% GNP content. Spectra are recorded for the corresponding locations identified in the associated FE-SEM image (top).

Table 5.3 EDS analysis of the surface wear track from the TiC-30 vol.% Ni_3Al cermet with 2.5 vol.% GNP content corresponding to Figure 5.16

Spectrum	Ti	Ni	C	Al	Total
1	40.33	43.45	9.12	4.59	100
2	17.19	67.83	5.08	8.44	100
3	41.95	39.08	10.65	4.49	100
4	53.24	31.73	12.33	2.7	100
5	83.89	1.49	14.62	0	100
6	17.41	69.29	4.98	8.09	100
7	40.43	44.68	10.09	4.81	100
8	80.09	3.47	15.87	0.56	100
9	21.92	59.53	11.79	6.76	100
10	41.85	39.73	14.56	3.86	100
11	26.45	58.78	7.79	6.98	100
12	55.85	30.19	11.28	2.68	100

Rough surfaces tend to control the initial contact mechanics between solids, and hence the resulting early stage wear. Previous studies show that graphene coatings can be utilised as solid lubricants [126], decreasing friction and consequently enhancing the tribological performance of the materials [110,111]. From Fig. 5.15(a,b), it is possible to observe that there is significant abrasion wear and erosion arising from brittle fracture and binder extrusion wear mechanisms; these result in formation of third-body wear debris. As noted in previous tribological studies on cermets, these materials often tend to form large, plate-like wear debris [132]; this can be seen as tribolayer removal or spalling. These plate-like particles, and other generated debris, are then effectively 'milled' in between the two surfaces, acting as a solid lubricant during sliding wear.

Wear debris can be generated in a wide variety of sizes and shapes, which can provide some indication of the operating wear mechanism that generates the debris [123]. To further elucidate the wear mechanisms relating to the current TiC-Ni_3Al cermets, and the influence of GNP additions on their wear response, combined FE-SEM observation and EDS mapping were

conducted on selected samples of wear debris recovered from the tests. Typical FE-SEM images are presented in Fig. 5.17 of the wear debris generated under constant speed sliding, at an applied load of 100 N, for 0 and 2.5 vol.% GNP contents in the TiC-Ni_3Al cermets. The morphology of the wear debris is essentially irregular, with 'plate-like' shapes, and with a finer size distribution for the GNP-containing samples, with particles with ranging from 1-20 μm. The morphology of the wear debris in shown in Fig. 5.17(a,b) indicates a mechanism that includes a combination of ploughing and brittle fracture [133]. The individual particles are a composite of predominantly sub-micron grain fragments of WC and TiC, present within their respective metallic binder phases (or a mixture). The presence of plate-like particles in Fig. 5.17(a,b), indicates that samples without GNP additions are affected to a significant extent by an adhesive wear mechanism (predominantly spalled regions of the tribolayer), while small spherical wear debris particles are mostly likely caused by attrition under the high stress during the cyclic sliding movement and rolling-contact fatigue. The plate-like particles initiate by successive adhesion and transfer within the tribofilm, and then failure and spallation of the tribofilm. As wear progresses, the tribolayer thickness increases and failure leads to formation of plate-like sections of the film [134]. In analogy with the process within a high energy ball mill, there are highly stressed (in the ~3.5GPa range [73]) contact regions between the test specimen and the WC-Co counter-face, where any surface asperities will be the regions where the contact load is the highest. Under the high stress, particles are removed from both surfaces. These fine particles then interact with other debris and the tribo-pair surfaces, and through mechanical attrition generate still finer debris.

In contrast, Fig. 5.17(c,d) show the wear debris of samples with the highest GNP contents, which possess a finer and predominantly spherical morphology. In this instance, the degree of adhesive wear is dramatically reduced, and the amount of tribolayer that is generated or released into the debris is much lower. A majority of the debris particles are effectively fine, fragmented material from the original composite structure.

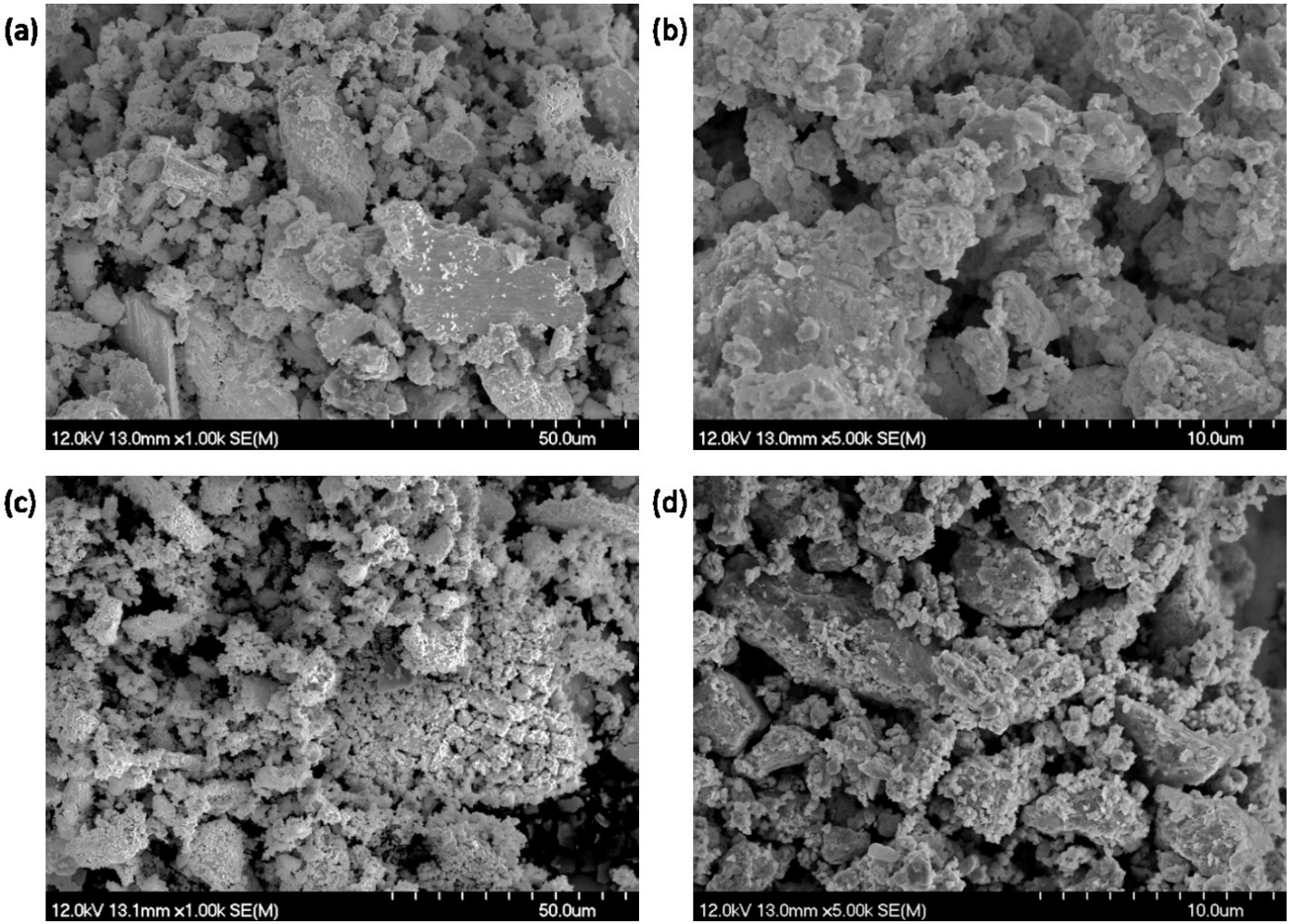

Figure 5.17 Wear debris from selected TiC-Ni_3Al samples: (a,b) TiC-Ni_3Al without GNP additions, and (c,d) TiCNi_3Al with 2.5 vol.% GNP additions. (a) and (c) show lower magnification images and overall debris structure, while (b) and (d) shows higher magnification images, where it is possible to observe individual "debris" morphology. Wear debris was generated with a 100 N applied load at 210 rpm.

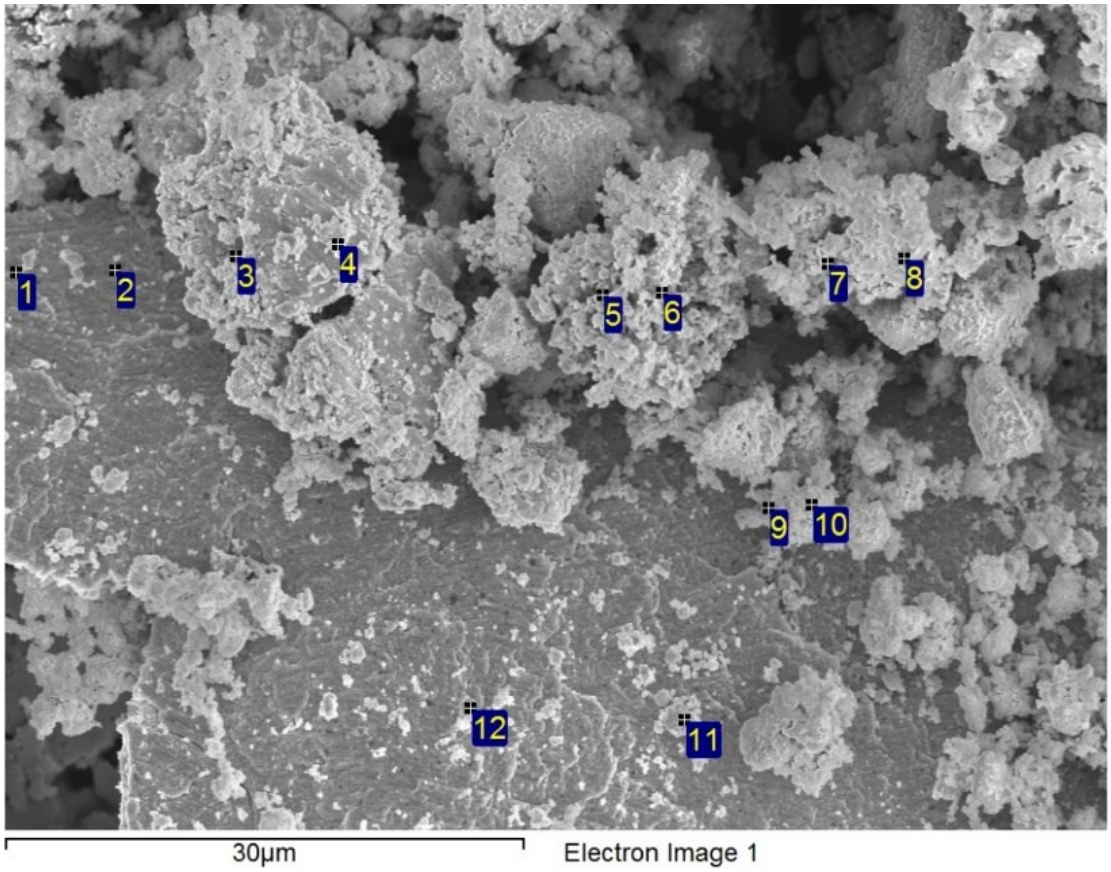

Figure 5.18 EDS analysis of the wear debris from the TiC-30 vol.% Ni_3Al cermet with 2.5 vol.% GNPs. Spectra are recorded for the corresponding locations identified in the associated FE-SEM image.

Table 5.4 EDS analysis of the wear debris from the TiC-30 vol.% Ni_3Al cermet with 2.5 vol.% GNPs corresponding Figure 5.18.

Spectrum	W	Co	Ti	C	O	Al	Total
1	56.52	12.32	15.51	7.9	6.98	0.77	100
2	69.71	8.2	12.12	5.62	3.8	0.55	100
3	87.82	6	2.01	3.03	1.14	0	100
4	71.26	12.59	5.86	8.07	2.22	0	100
5	75.71	13.84	0	8.23	2.22	0	100
6	68.3	7.39	14.09	5.94	4.28	0	100
7	89.21	5.01	1.24	3.33	1.21	0	100
8	71.46	10.13	0	11.69	5.03	1.69	100

9	77.5	8.97	4.43	5.91	3.19	0	100
10	69.52	14.93	6.19	6.45	2.91	0	100
11	63.49	16.78	7.16	8.27	4.3	0	100
12	68.01	15	8.07	6.27	2.65	0	100

5.3.4 Wear Model

Analysis of the wear sliding wear response, as a function of cermet composition, demonstrates that a clear transition in behaviour was observed. Aside from an improvement in the wear resistance, through additions of GNPs, differing wear mechanisms were also observed. Based on this, it is possible to propose a simple model of the main wear mechanisms observed (Fig 5.19). In the TiC-Ni_3Al samples without GNP additions (Figure 5.19(a)), the main observed wear mechanism is one of adhesion, which has followed an initial abrasive wear stage, which can be partly explained by the chemical affinity between the metallic phases of the sample and counter sphere [134,135]. As GNPs are added into the cermet microstructure, in the first instance up to 1.25 vol.% (Figure 5.19(b)), there is significantly less adhesive wear, due to the influence of GNPs in lowering the COF of the tribopair, as well as an increase in the fracture resistance [136,137]. In this instance, abrasive wear is starting to become the predominant wear mechanism. Also, intercrystallite fracture is more common resultant due to increase in the toughness of the binder phase [138,139]. The incorporation of further GNPs, up to 2.5 vol.%, results in a further increase in the cermet toughness, combined with a greater reduction of the COF for the tribo-pairing. Here the wear rate is significantly reduced, by roughly one order of magnitude over the GNP-free cermet. In this case, essentially only abrasive wear is observed, and cermet degradation is mainly caused by fatigue and brittle fracture of the ceramic grains and binder [50-52].

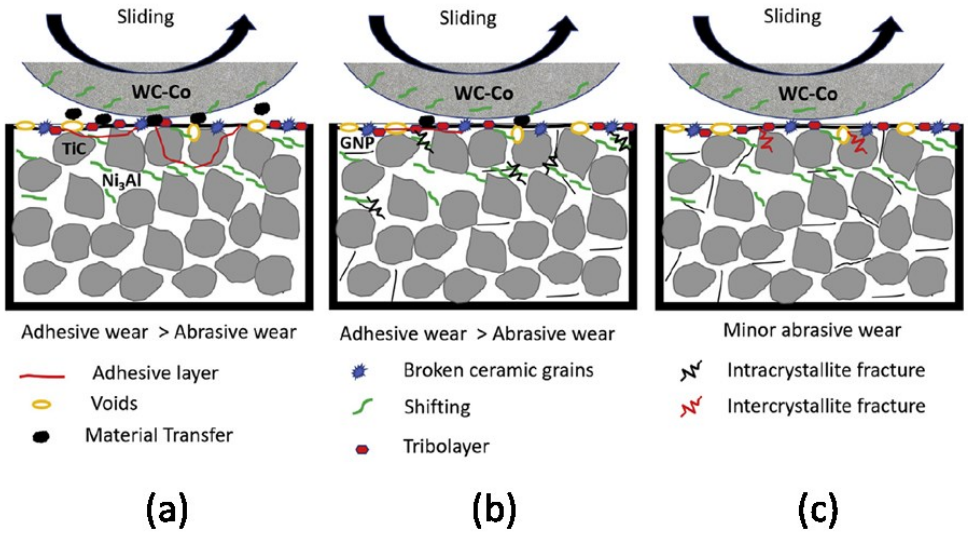

Figure 5.19 Schematic representation of the proposed wear mechanism transitions when GNPs are incorporated. TiC-Ni_3Al cermets with: (a) 0 vol.% GNPs, 0.5 vol.% GNPs, and 2.5 vol.% GNPs.

5.4 Conclusions

The following conclusions can be drawn in the present work:

- High density TiC-Ni_3Al based cermets can be readily prepared with GNP additions of up to 2.5 vol.%. It is shown that GNP additions do not significantly degrade the densification behaviour, for the composition range studied, with all materials sintered to greater than 99 % of theoretical density.
- The cermet hardness and IFR values are both significantly increased through GNP additions.
- The incorporation of up to 2.5 vol.% GNP into the binder phase also demonstrates a significant reduction in the cermet COF could be achieved.
- For TiC-Ni_3Al cermets fabricated with 2.5 vol.% GNPs, the specific wear rate was reduced by roughly one order of magnitude relative to the baseline composition prepared in the absence of GNPs.
- The addition of GNPs to the cermet microstructure results in a transition from a more severe adhesive wear mechanism, to one that is predominantly abrasive/erosive in nature, and far more minor in scale.

Acknowledgements

The Canada Foundation for Innovation, the Atlantic Innovation Fund, and other partners who helped fund the Facilities for Materials Characterisation, managed by the Dalhousie University Clean Technologies Research Institute, are gratefully acknowledged. The present work was also made possible with support from CAPES, Brazil, through the programme Coordination for the Improvement of Higher Level or Education Personnel. I would like to acknowledge my PhD supervisors Z.N. Farhat and K.P. Plucknett for their guidance on this work.

CHAPTER 6 THE INFLUENCE OF INTERMETALLIC ORDERING ON WEAR AND INDENTATION PROPERTIES OF TiC-Ni_3Al CERMETS

Status: *Published: Wear 426-427 (2019) 390-400.*

Abstract

Cermets based on titanium carbide with a nickel aluminide binder (TiC-Ni_3Al) offer potential substitutes for tungsten carbide (WC) based hardmetals due to their high wear and corrosion resistance at ambient and elevated temperatures. In the current work, the effects of post-sinter heat treatments (between 600 and 1340 °C) on atomic ordering of the Ni_3Al have been assessed through Vickers indentation, scratch testing and nano-indentation methods. Changes in the atomic structure are evidenced from X-ray diffraction by abrupt increases in the (111) and (200) peak intensities. An increase in Vickers hardness, from 1400 to 1530 HV, is observed as a result of heat treatment at 1200ºC. Furthermore, the scratch hardness value was improved from 11.89 to 18.12 GPa, with the main wear mechanisms being identified as TiC grain pull out and brittle fracture. Ordering transitions were subsequently related to the structural changes predicted through *ab-initio* modelling approaches.

Keywords: long range ordering; nanoindentation; scratch testing.

6.1 Introduction

'Cermets' are composite materials comprised of ceramic and metallic phases that have been developed to satisfy industry needs of high hardness, toughness and wear resistance [143]. Because of their characteristics, cermets are widely used in thermal spray coatings and, for applications in corrosive and/or erosive environments [1,143]. Tungsten carbide (WC) and titanium carbide (TiC) are the most common ceramic components in cermets, due to their high Young's modulus and hardness, chemical and thermal stability, and wear resistance. While both are utilised in aerospace applications, TiC has a significant advantage due to its low density (4.93 g/cm^3) when compared with WC (15.63 g/cm^3) [1,8,18].

It has been shown that TiC has good wettability by a variety of molten metals, including Ni, Cu, Al, Co, and Fe, along with a number of different alloys [40]. The intermetallic nickel aluminide (Ni_3Al) has been extensively studied as a metallic binder for TiC-based cermets [1,144,145], and on its own [26,146,147]. It has excellent properties at high temperature, high oxidation resistance up to 1100 ºC and elevated yield strength for temperatures up to 900 ºC [1,72]. Moreover, Ni_3Al shows high stress-corrosion cracking resistance when tested up to 700 ºC [147]. More recently, the reciprocating wear response of TiC-Ni_3Al cermets has been reported [1,98], showing the effects of binder content (20-40 vol.%) on the wear mechanisms and hardness. These studies have also confirmed optimal wear resistance for these materials with intermediate binder contents (25-30 vol.% Ni_3Al) [1].

Another fundamental property of Ni_3Al that has been studied, is the influence of crystal structure upon mechanic properties. Aoki and Izumi reported that single crystals of Ni_3Al have a predominantly ductile behaviour while, in contrast, polycrystalline Ni_3Al is very brittle [148]. The crystalline characteristics, such as long-range ordering (LRO), created by disordered-ordered phase transitions and their effects on the mechanical properties of Ni_3Al phase have been also reported [147,148].

As LRO is believed to increase properties such as hardness and toughness [149], the main objectives of the present work were to develop heat-treatments to obtain increasingly ordered phases of Ni_3Al within a TiC cermet structure, then study the effects of these treatments upon the wear and mechanical behaviour. Previous work has reported on the kinetics of formation of long-range-ordered structures through the migration of atoms within the crystal structure by vacancy ordering [26,150]. Ni_3Al was shown to form ordered structures close to the melting phase, at ~1350°C, however in many cases heat-treatments were only conducted up to 1000 °C [146,147,149]. The current work investigates the influence of ordering heat-treatments, within the temperature range of 600 to 1340 °C. The Vickers hardness, indentation fracture resistance (IFR), and scratch test resistance of TiC cermets prepared with 30 vol.% Ni_3Al intermetallic binder are tested.

6.2 Experimental Procedures

6.2.1 Raw Materials and Cermet Processing

The precursor powders used in this study for the synthesis of TiC-Ni_3Al cermets included fine, high purity TiC powder (lot #45693; particle size = 1-2 μm), supplied by Treibacher Industrie AG (Althofen, Austria), and both elemental Ni (lot # NAD71; particle size <45 μm) and Ni/Al 50/50 at.% (lot # D28X029; particle size <150 μm) from Alfa Aesar (Ward Hill, MA, SA). The bulk composition of TiC-30 vol.% Ni_3Al was produced through an *in-situ* reaction sintering step, from the initial blend of Ni and Ni/Al [1,151]. The blend of the Ni, Ni/Al and TiC powders was mixed with the goal to form a nominally stoichiometric Ni_3Al binder phase through a subsequent 'reaction' liquid phase sintering process. A volume ratio of 70:30 was selected for the TiC:Ni_3Al composition in the current study, as this nominally exhibits the best wear resistance, in comparison with other binder contents[1,98].

To synthesise the final compositions, the TiC, Ni and Ni/Al powders were mixed in ~50 g batches, with the addition of 0.5 wt.% polyvinyl butyral (PVB) wax to aid compaction and increase green strength. The powder blends were then ball milled in acetone for 24 hours at ~60 RPM, using yttria stabilized zirconia milling media (Ø = 10 mm), with a 10:1 mass ratio of media:powder. The milled powder mixture was subsequently dried in a fume hood, for a minimum of 24 hours, and then sieved through a -75 μm mesh to eliminate any large aggregates. The powders were then compacted within a hardened die using a uniaxial hand press, with an applied load of ~70 MPa, into 31.75 mm diameter x ~ 5 mm thick pellets. The disc-shaped samples were then sealed in polyethylene bags and further compacted using a cold isostatic press, at ~207 MPa, to achieve high green density and minimise possible pressing defects such as residual pores and density gradients.

The cermet samples were sintered in a vacuum furnace (Model Red Devil®; R.D. Webb Co., Natick, MA, USA), at a temperature of 1550 °C for 120 minutes. They were processed under a dynamic vacuum (<$5x10^{-4}$ Torr), with heating and cooling rates of 20 °C/min; below ~800 °C the furnace cools naturally at a lower rate. Post-sinter ordering heat treatments were subsequently performed on selected samples, using the same vacuum furnace, at 600°C, 800°C, 1000°C, 1200°C, and 1340°C for 120 minutes; vacuum level, and heating/cooling conditions were essentially the same as for the sintering cycle.

6.2.2 Materials Characterization

The immersion densities of the specimens were determined by applying Archimedes' principle in water (at ~24°C). The sample's weight was recorded on a scale, with 1 µg resolution, and the test is repeated 3 times for statistical purposes. The density is then calculated following:

$$p = \left(\frac{MA}{MA-Mw}\right) * p\,W \qquad \textbf{Equation 6.1}$$

where p is Archimedes density, MA = mass in air, MW = mass in water and pW = density of water at the specific test temperature. The specimens were subsequently diamond ground flat, and then polished down to a 0.25µm surface finish using diamond paste for microstructural examination and further testing.

Crystallographic analyses of the initial milled powders and the resultant sintered and heat-treated samples were performed using an X-ray diffraction (XRD) system (Model D-8 Advance; Bruker Corp., Billerica, MA, USA), using CuKα radiation, and operating at 40 kV and 40 mA. A scan angle range of 20 - 90° 2θ was used, with a scan rate of 0.5°/min at room temperature. Phase analysis was then conducted using the ICDD® PDF-4 database (International Centre for Diffraction Data®, Newton Square, PA, USA) for inorganic materials. In the context of the present study, the XRD technique is widely used to identify ordering effects through the relative increase in the intensity of selected diffraction lines. The microstructures of the raw powders and sintered/heat-treated materials were assessed using field emission scanning electron microscopy (FE-SEM) examination (Model S-4700, Hitachi High Technologies, Inc., Tokyo, Japan), and optical microscopy (Model Olympus BX-51, Olympus Corp., Tokyo, Japan).

The Vickers hardness of the polished surfaces was determined by applying a load of 1 kg, held for 15 seconds, following ASTM 1327-15. The mean indent sizes were then precisely measured using the above-mentioned optical microscope. The indentation fracture resistance (IFR) was also assessed with a related Vickers indentation method, using a 30 kg applied load. For the present materials, it was determined that Palmqvist-type cracks would likely be occurring, using the method of direct crack propagation, determined from the equation of Shetty and colleagues [44]:

$$K_{IC} = \frac{0.0319P}{(ac^{\frac{1}{2}})} \qquad \textbf{Equation 6.2}$$

where P is the applied load, a is the half the indent diagonal length (*i.e.*, the distance from the corner to the center of the indent), and c is the indentation crack length, measured using optical microscopy. To ensure the repeatability of the measurements of both hardness and the IFR, a minimum of 10 indentations was performed for each of the tests.

Assessment of the wear resistance was conducted using a (UMT-1; CETR, Campbell, CA, USA) system, using the scratch test, with a diamond indenter sliding in linear motion across the flat test sample surface. This is achieved with a single pass length of 5 mm, and a speed of 0.166 mm/s, with tests performed at room temperature (22 ± 2 °C) and a relative humidity of 40-50%. In the sliding scratch test, the load is applied downward against the surface on the sample with a Rockwell diamond indenter (with a tip radius of 200 μm). Loads of 30 N and 100 N were applied to generate the scratch tracks, where 30 N is used to determine the coefficient of friction (COF), the scratch depth and to assess the operative wear mechanisms. The 100 N load was applied to calculate the scratch hardness. To achieve this, the average width of the scratch track was subsequently measured using the FE-SEM, and the scratch hardness number, HS_p, was then determined using the following relationship [116]:

$$HS_p = \frac{8P}{\pi W^2} \qquad \textbf{Equation 6.3}$$

where P is the applied load and W the scratch width. The data was collected and processed using the UMT digital data-acquisition system and software.

6.2.3 Computational Modelling Approach

The first-principles calculations were performed using the VASP code (www.vasp.at), which performs density functional theory (DFT) calculations using the projector-augmented wave (PAW) formalism and a planewave basis. The exchange and correlation effects were treated in the framework of the generalized gradient approximation (GGA) using the Perdew-Burke-Ernzerhof (PBE) functional [152], and PAW data sets as supplied with the VASP code. To ensure sufficient accuracy, the energy cut-off was set to 320 eV. The special points sampling integration over the Brillouin zone was employed by using the Monkhorst-Pack method [153], with an 11 x 11 x 11 special k-point mesh. These parameters were sufficient to converge the cell stress to better than 0.1%. The metallic occupancy of the levels was treated by the Methfessel-Paxton scheme [154],

using a smearing parameter of 0.2, which was determined by minimising the total energy at the experimental cell volume of aluminum, and then used for the Ni_3Al variants as well. Each structure was fully optimized to better than 0.002 eV/Å in forces, and using ground state electronic convergence of 10-5 eV, together with a tolerance for the ionic relaxation convergence of 10-3 eV.

In this work, elastic properties of the optimized cubic and disordered-Ni_3Al structures were determined by using finite differences, combining both cell distortions and atomic displacements, thus yielding the elastic tensor including ionic relaxation. Using the computed single crystal elastic constants, elastic properties including the bulk modulus, shear modulus, Young's modulus, and Poisson ratio were obtained by applying a standard Voigt-Reuss-Hill averaging procedure [155].

The mcsqs code reports the best special quasirandom structures (SQS) found, the best match to the correlations computed in the first step. As the SQS model generated has only P1 symmetry, rather than the cubic symmetry, a projection technique was used to determine the elastic tensor of cubic symmetry closest to the elastic tensor determined for the SQS model [156–158].

6.3 Results and Discussions

6.3.1 Microstructure and Intermetallic Ordering of the Cermets

In the present work, fully dense sintered cermet compositions were heat-treated with the objective of altering the mechanical characteristics of the TiC-Ni_3Al cermets (and specifically the Ni_3Al binder phase), and therefore the material's wear resistance. The sintering mechanisms associated with production of high density cermet specimens are, predominantly, (i) liquid wetting and capillary driven particle rearrangement, and (ii) dissolution-reprecipitation of the ceramic phase (*e.g.*, TiC) within the molten metallic binder (e.g., Ni_3Al) phase [36]. These processes start to occur above roughly 1400 °C for the present cermets, once the Ni_3Al phase is melted[90], allowing accelerated mass transport mechanisms to occur in the presence of the liquid phase. Initially, capillary forces drive some degree of hard TiC particle rearrangement, and consequently densification. In addition, the dissolution of small TiC grains into larger grains occurs. For ie., as illustrated by the Figure 6.2 grains with less than ~1μ starts to be consumed when the samples are heat treated at 800 °C and larger grains grow as the sample is heat treated at higher temperatures. This allows grain shape accommodation and helps to eliminate porosity during sintering [159,160].

Figure 6.1 illustrates typical SEM micrographs obtained from the polished surfaces of the bulk cermet specimens, in this instance for the as-sintered material and the equivalent sample after secondary heat-treatment at 1200 °C for 120 minutes. The LRO heat treatments do not cause any effects on the respective phase compositions, although there is a small degree of TiC coarsening evident for the samples heat-treated at 1000–1340 °C (for 2 h), as observed in Figure 6.2(a). This observation highlights that even are relatively modest temperatures, sufficient diffusion is arising to coarsen the microstructure. The related subtle changes in the TiC grain size distribution are shown in Figure 6.2(b).

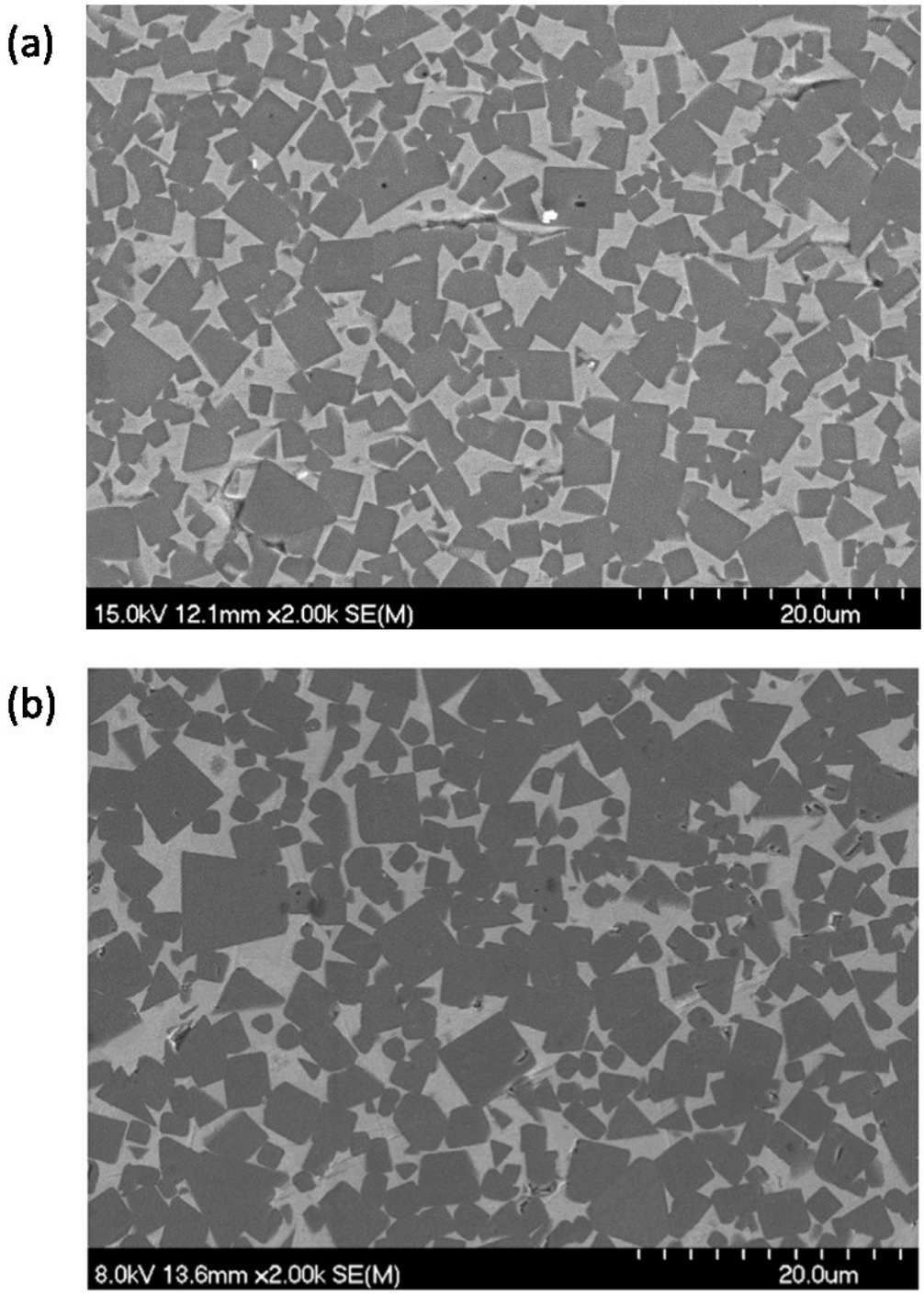

Figure 6.1 Representative SEM images obtained from the polished surfaces of the cermets: (a) as-sintered TiC-Ni_3Al, and (b) sintered TiC-Ni_3Al, subsequently heat-treated at 1200 °C (for 120 minutes). Note the TiC grains exhibit the darker contrast, with the continuous Ni_3Al being the lighter contrast phase.

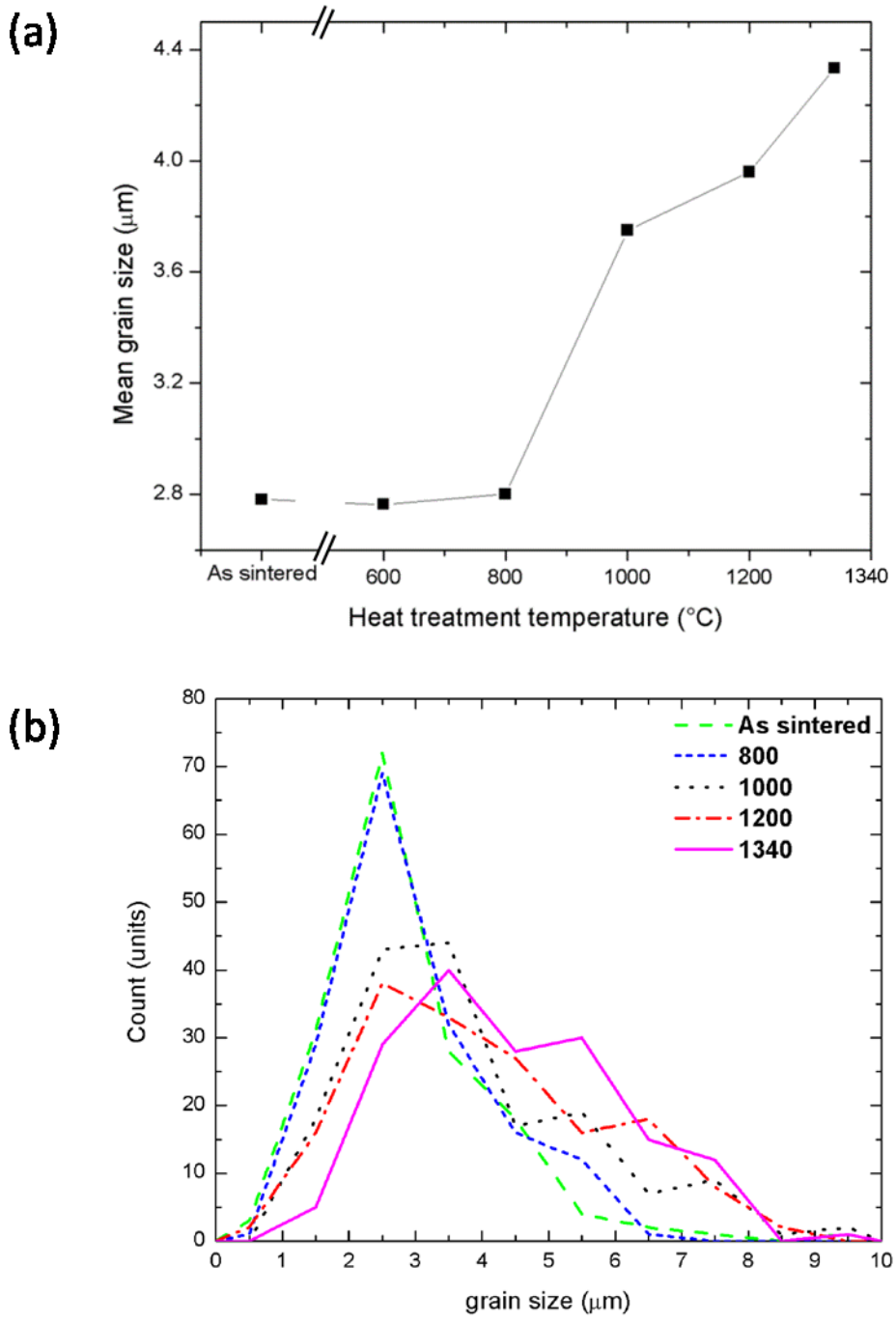

Figure 6.2 (a) Comparison of the measured TiC grain size for the as-sintered TiC-Ni_3Al cermets and those subjected to post-sinter heat-treatments at temperatures ranging from 600 to 1340 °C (held for 120 minutes). (b) The TiC grain size distributions for the as-sintered TiC-Ni_3Al cermets and those subjected to post-sinter heat-treatments at temperatures ranging from 800 to 1340 °C (held for 120 minutes); note that data for 600 °C was essentially identical to that observed for the as-sintered cermets and those subjected to 800 °C heat treatments.

Thermodynamic experiments, involving the study of the ordering kinetics in Ni_3Al $L1_2$-type superstructures, have previously been conducted by Kozubski [149]. It was shown that there is a correlation between the "order-order" reactions and the stability of long range ordered phases. Furthermore, it was reported that the ordering in Ni_3Al superstructures takes place due to "correlated atomic jumps" between the different sub-lattices and vacancies at specific temperatures. When this atomic jump takes place, a disordered structure (or a structure that may have a defect) could become ordered. The process is then facilitated by providing energy into the system (*e.g.*, heat), and can take place up to the melting temperature of Ni_3Al [149].

The phase formation and evidences of the LRO effects on Ni_3Al were initially examined using XRD analysis. Figure 6.3 shows representative XRD traces for the raw powder mixture, the as-sintered TiC-Ni_3Al cermet and a sintered specimen subsequently heat treated at 1200 °C for 120 minutes. An abrupt increase in the intensity of the (111) and (200) X-ray peaks of Ni_3Al and NiAl is shown on heat treated samples, which indicates the occurrence of ordering effects. In the traces representing the milled powder mixture, NiAl was understandably not detected. This is due to the use of a Ni/Al starting powder that has a 1:1 weight ratio, such that the overall composition of this precursor component is in the Al_3Ni-Al_3Ni_2 phase field of the Ni-Al system. The presence of TiC is clearly identified in each example, showing the stability of this phase when heat treated; the constancy of the 2θ angles of the TiC peaks confirms that there is no C loss, which would lead to a sub-stoichiometric TiC_x phase and a measurable peak shift.

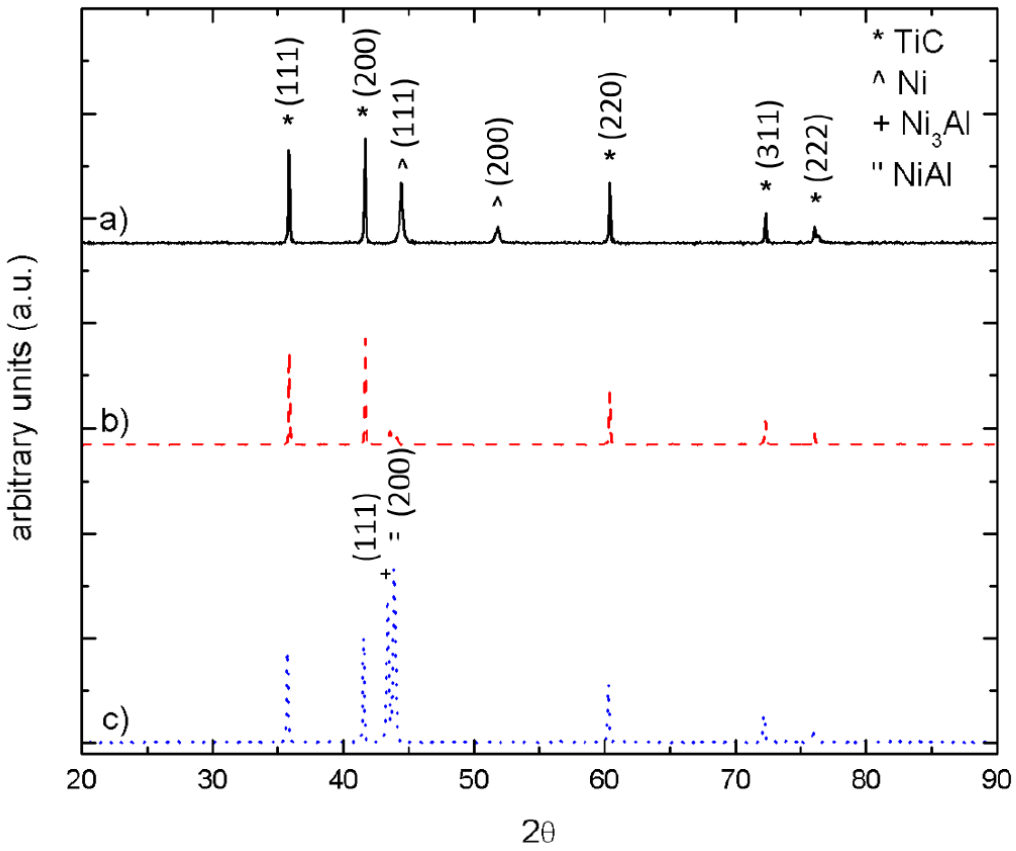

Figure 6.3 XRD traces obtained for: (a) the raw, as-milled TiC-Ni/Al-Ni powder mixture, (b) an assintered TiC-Ni_3Al cermet (sintered at 1550 °C for 60 min), and (c) the sintered and heat-treated TiCNi_3Al (with a post-sinter heat-treatment at 1200 °C, held for 120 minutes).

A previous studies has demonstrated that formation of LRO superstructures within Ni_3Al have an effect on various mechanical properties by changing the distribution of crystal defects [147]. A series of atomic migration events occurs through a vacancy-related mechanism, where atoms diffuse from their initial lattice sites and into an vacant neighbouring site, which is thermally activated [149]. When the atomic jumps take place, a scenario can arise where a non-equilibrium system is transformed into a new, lower energy configuration. This usually involves an increase in the LRO, which shows the minimum free enthalpy and most favorable energy state [149].

6.3.2 Micro-indentation Response

Cermets and hardmetals are invariably used in applications that require high wear and/or abrasion resistance. Typically, the Vickers hardness is viewed as being one of the most important factors relating to wear, while fracture toughness is also regularly considered. When thinking more specifically about abrasion and sharp particle impact (i.e., erosion), the indentation fracture response can also be considered to be an important parameter. With this in mind, in the present work both Vickers hardness and IFR tests have been applied to assess the effects of ordering heat-treatments on the Ni_3Al binder. It must be borne in mind that A large number of variables are likely to affect both the Vickers hardness and IFR These include factors such as the chemical and mechanical properties of the ceramic/metal interface, residual stresses between phases, the ductile binder content, the crystal structure of components, and both the size and shape of ceramic grains [20,77,161,162][20,77,161,162][30-34].

A comparison of the Vickers hardness of the as-sintered and heat-treated TiC-Ni_3Al cermets is presented in Figure 6.4. The as-sintered cermet exhibits a hardness of ~1385 HV1 (i.e., a 1 kg load), which is reduced through an intermediate temperature heat-treatment, to a minimum of ~1340 HV1 at 800 °C. This small reduction may be the result of stress relief between the phases, through the movement of dislocations during the stages of recovery and recrystallization [15,20,35]. The initial residual stress is caused by the mismatch between the thermal expansion coefficients of TiC ($\alpha = 7 \times 10^{-6}/K^{-1}$)[164] and Ni_3Al ($\alpha = 12.5 \times 10^{-6}/K^{-1}$) [165]. Recrystallization of the intermetallic Ni_3Al grains during the intermediate temperature heat treatment can then be seen to reduce the residual stress, as has been previously observed in the TiC-MoNi system [166]. Increasing the heat-treatment temperature from 800 °C to 1200 °C results in the opposite trend, that the Vickers hardness now increases, peaking at close to 1520 HV1, which is an increase of nearly 10 % over the as-sintered material. It is clear that at the higher heat-treatment temperatures the LRO effects overtake the recrystallisation response, and the rearrangement/ordering of the Ni_3Al crystal structure is believed to increase hardness.

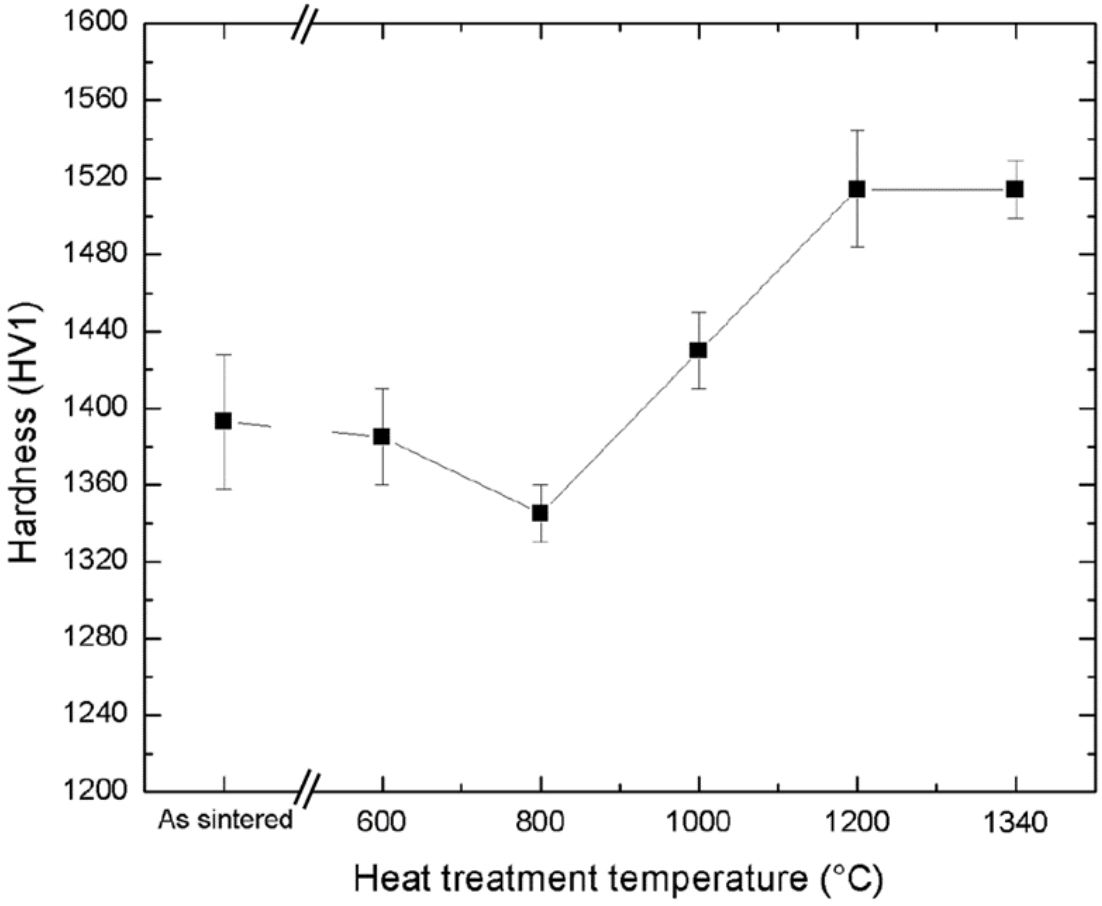

Figure 6.4 Comparison of the measured Vickers hardness (using a 1 kg load) for the as-sintered TiC-Ni_3Al cermets and those subjected to post-sinter heat-treatments at temperatures ranging from 600 to 1340 °C (held for 120 minutes).

According to previous publications [1,8], both the hardness and IFR of TiC-Ni_3Al cermets are strongly related to the Ni_3Al binder content (as is the Young's modulus). For binder contents below 20 vol.%, the hardness (and Young's modulus) increase, as there is a greater amount of the high modulus ceramic phase, while the IFR decreases as the material becomes more brittle. However, for these materials the best wear resistance typically occurs between 25 and 30 vol.% of binder, highlighting the importance of both hardness and toughness in terms of the tribological response. In the present study, the percentage of binder is constant, and it is therefore possible to observe the effects of the heat-treatment on the toughness response of this cermet composition. As shown in Figure 6.5, a transition to a tougher behavior is apparent following intermediate temperature heat-treatments (*i.e.*, at 800 °C), as evidenced by an increase in the IFR; this correlates well with the

decrease in hardness previously noted in Figure 6.4, and corresponds to a more ductile phase combination in the cermet. With further increase in the heat-treatment temperature (*i.e.*, 1000 °C, and above), it can be seen that the IFR now decreases, ultimately to a value below that of the as-sintered material. Under these conditions the binder phase, which is a barrier for crack growth, effectively becomes more brittle due to the heat-treatments [167,168].

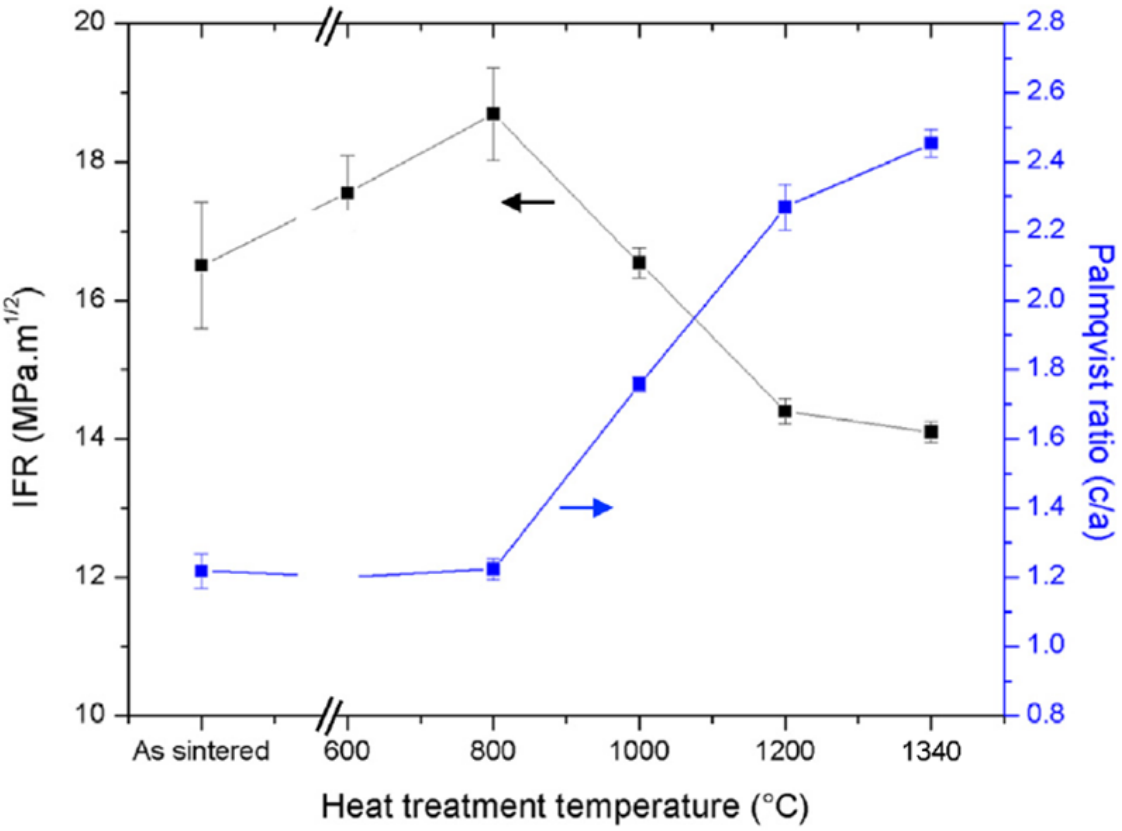

Figure 6.5 Calculated indentation fracture resistance of TiC-Ni_3Al cermets as-sintered and subjected to heat treatment for 120 min. All samples show a Palmqvist-type cracking behaviour, based on measurement of the c:a crack length:indent diagonal ratio.

An evaluation of a material's fracture toughness (K_{IC}) can be obtained in a diverse number of ways, which effectively reveal the crack resistance of a material. One approach that is both simple and directly applicable to sharp impact/abrasion scenarios is the Vickers indentation test, where the indent and associated crack lengths can give a measure of toughness (or IFR). However, there is significant conjecture regarding this approach [169], and a large number of equations have been

developed and applied. Two of the more widely used in the literature depend on the occurrence of either a median-radial or Palmqvist crack [45,74]. In particular, the ratio between the indent crack length (c) and indentation size (a) provides information regarding whether median-radial or Palmqvist cracking is more probable. In the present case, for both the as-sintered and 800°C heat-treated samples, the c:a ratios are less than 2.5 [43], at 1.21 and 1.22 respectively, which is indicative of a Palmqvist-type crack system. A significant IFR improvement, from ~16.5 to ~19 MPa.m$^{0.5}$, was calculated when comparing these two samples. However, when the TiC-Ni_3Al cermets were heat-treated at 1200 °C there is a transition to a more brittle behaviour, as evidenced by the decreased IFR. This is clearly shown by the increase in the c:a ratio, which has increased to 2.27, IFR, but also clearly by the the c:a ratio, which has increased to 2.27, although it is still in the Palmqvist-type crack range.

6.3.3 Scratch Testing Behaviour

The wear performance of the various TiC-Ni_3Al cermets, and the effects of applying the various heat treatments on wear mechanisms, was evaluated through the use of scratch testing, chosen due to its efficacy as a method to evaluate the abrasive wear behavior and the true coefficient of friction [127,170,171]. For elastic-plastic materials, the coefficient of friction (COF), μ, is defined by the ratio between the tangential force (F_T) and the normal force (F_N), represented by:

$$\mu = \frac{F_T}{F_N} \qquad \textbf{Equation 6.4}$$

The magnitude of the coefficient of friction is susceptible to effects arising from surface roughness and the adhesion between the (diamond) indenter, in the present work, and the tested material. Applied loads of 1, 10, 20, 30 and 100 N were initially evaluated. However 30 N was utilized to record data in order to minimize the effects due to the surface imperfections and identify the true COF of the composite material [128]. Fig. 6 presents examples of the recorded COF curves, following scratch testing, for the as-sintered and heat-treated cermets. Similarly, Figure 6.7 shows the resultant scratch depth for the same samples.

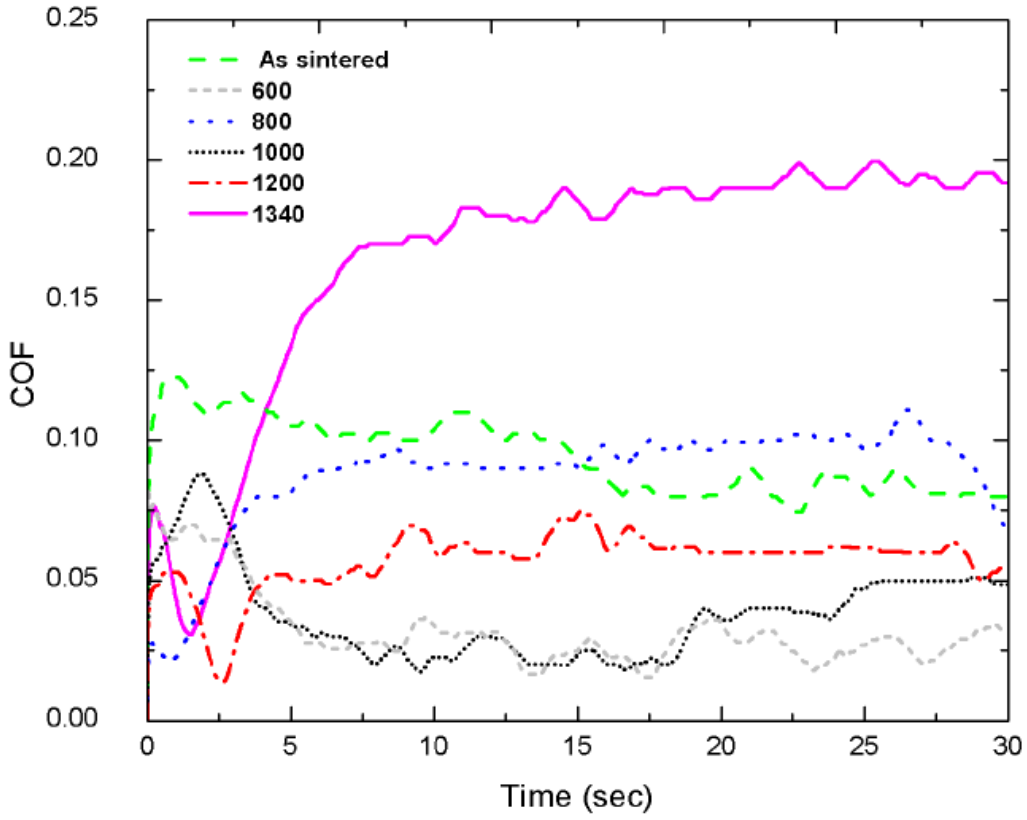

Figure 6.6 Representative coefficient of friction traces recorded from scratch tests on the as-sintered TiC-Ni_3Al cermets (as sintered), together with those heat treated at various temperatures. Tests were conducted with a 30 N applied load.

Previous investigations reported by Buckley [48] and Hutchings [173] show that elevated frictional forces are originated by plastic plowing under dry sliding conditions. The samples heat treated at 1340 ºC show the highest COF (Figure 6.6), which also leads to the second highest penetration depth of the Rockwell indenter (Figure 6.7). High adhesive force is directly related with a high tangential force, which will result from a high COF between the tribo-pairing, and consequently high wear rates can be anticipated[50]. As might be anticipated from the previous discussion relating to the cermet hardness values and indentation fracture resistance, the TiC-Ni_3Al samples heat treated at 800ºC and 1200ºC show the best scratch resistance, with penetration depths of 15 and 4 µm (Figure 6.7), respectively, combined with the lowest COFs (Fig. 6). The depth results of this samples could be directly compared with WC-Co, where a similar study showed a scratch depth of ~4 µm when subjected to 30N load [51].

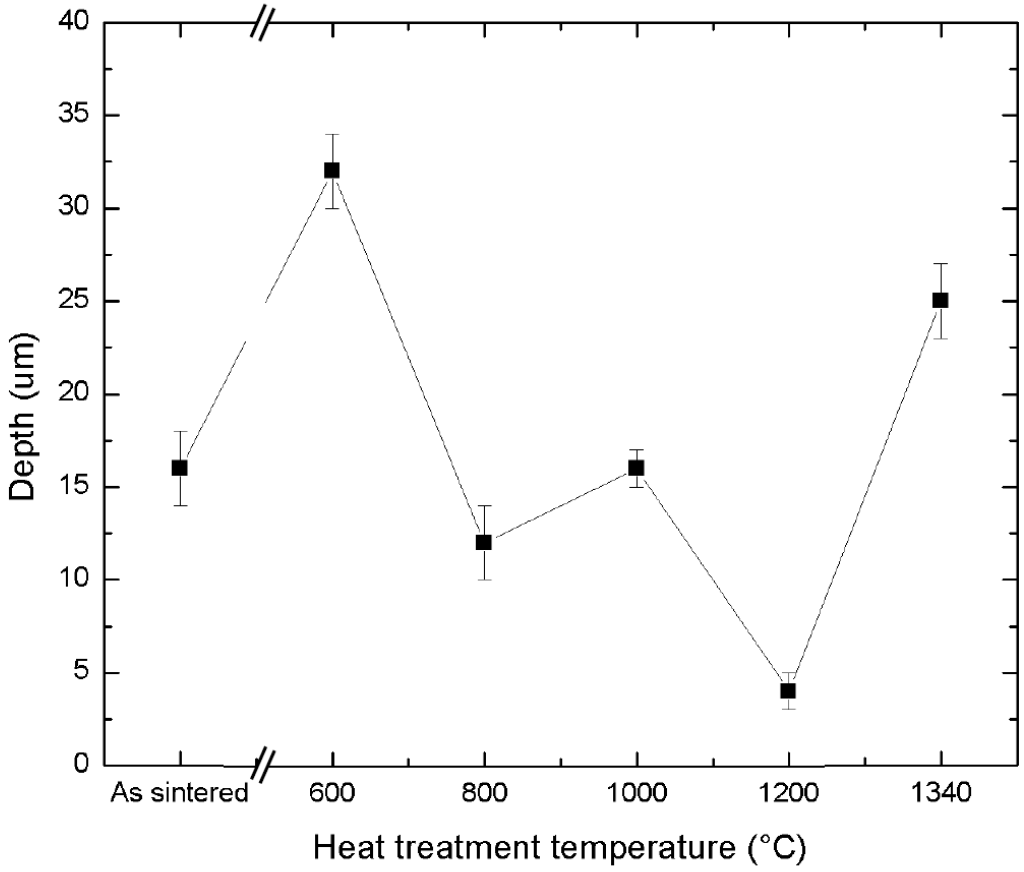

Figure 6.7 Measured scratch depths (with associated standard deviation errors) as a function of the $TiCNi_3Al$ cermet processing condition (as-sintered or heat-treated at a temperature between 600 and 1340 °C). Tests were conducted with a 30 N applied load.

Representative cermet microstructural damage, after scratch testing of the surfaces, are presented in Figure 6.8, for the as-sintered and 1200 °C heat-treated samples, respectively. Significant grooving surface damage is generated on the as-sintered samples (Figure 6.8 (a) and (b)), which is reduced measurably for the 1200 °C heat treated samples (Figure 6.8 (c) and (d)). A resultant improvement in the scratch hardness number, from 11.89 to 18.12 GPa, was calculated when comparing these samples, based on the mean scratch widths (for example, as shown in Figures 6.8(b) and (d), respectively). The presence of several wear mechanisms, such as plastic deformation of the binder phase, micro-cutting, micro-grooving, and grain fracture, are all observed in the tested cermets during scratch testing. The microstructural damage evolution indicates that the heat-treated binder phase in the $TiC\text{-}Ni_3Al$ cermets provides a more robust matrix

for the containment of the ceramic grains, especially after processing at 1200 °C, with (qualitatively) a lower degree of plastic deformation than is seen for the as-sintered samples.

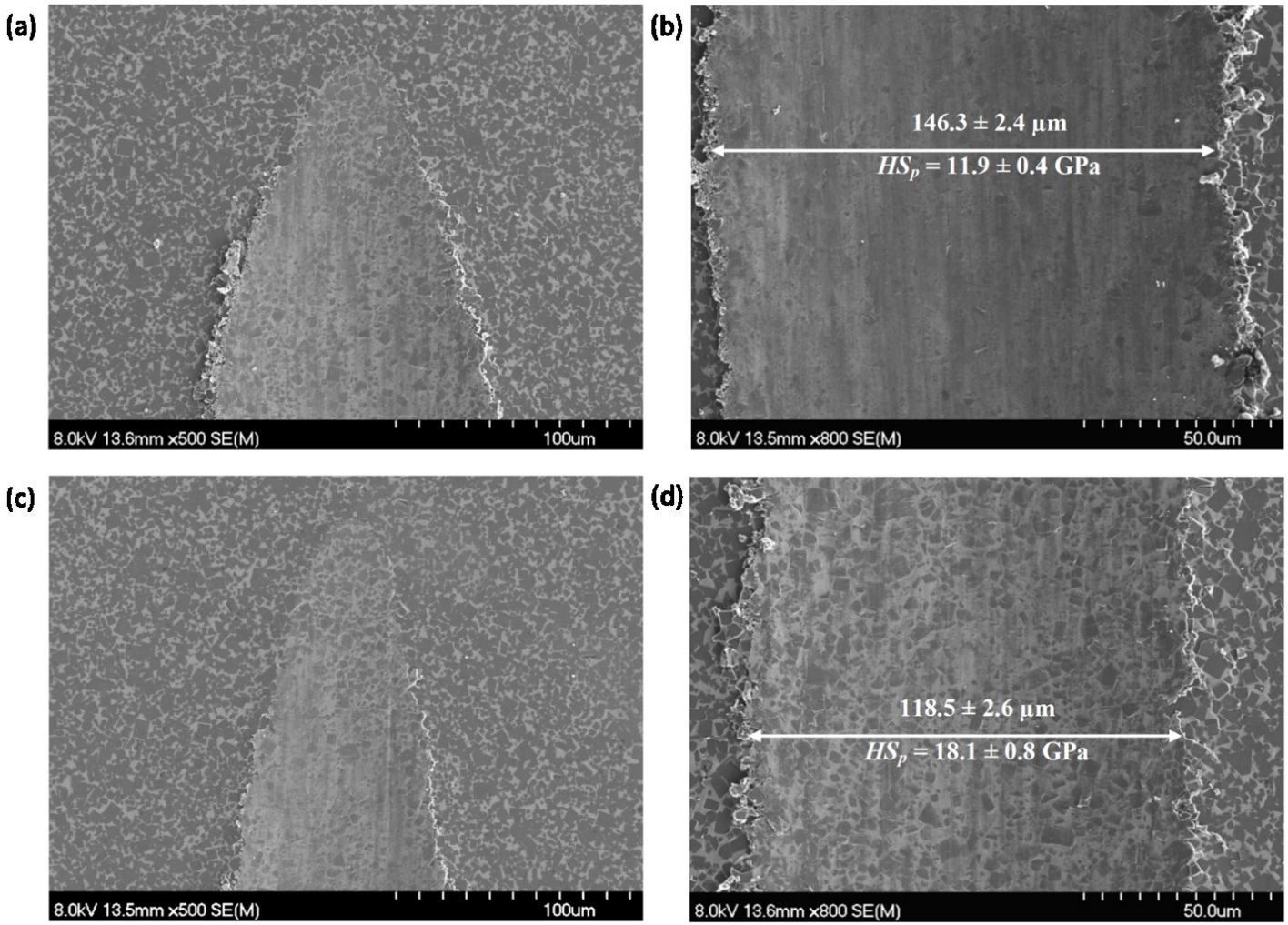

Figure 6.8 Representative FE-SEM images of a scratch test conducted on the as-sintered TiC-Ni_3Al cermet using a 100 N applied load. (a) The scratch initiation point. (b) Higher magnification image showing the mean scratch width (and standard deviation error) and associated damage. Representative FE-SEM images of a scratch test conducted on the sintered and heat-treated (1200 °C for 120 minutes) TiCNi_3Al cermet using a 100 N applied load. (c) The scratch initiation point. (d) Higher magnification image showing the mean scratch width (and standard deviation error) and associated damage.

The various damage mechanisms are better highlighted by examining the samples at higher magnifications within the FE-SEM. The response following intermediate temperature heat-treatments, at either 600 or 800 °C, is presented in Figure 6.9. The presence of partial TiC grain pull out is shown in Figure 6.9(a) [indicated with arrow 1], together with intra-granular cracks within TiC grains [indicated with arrow 2]. Brittle fracture is a common wear mechanism observed when the locally applied load causes a (nominally compressive) stress that exceeds the maximum ultimate strength of the brittle ceramic grains [50,52]. It has been shown in related work on TiC-stainless steel cermets that the Hertzian contact stresses under such applied loads are well into the GPa range [53], which will be even higher when using the smaller radius Rockwell indenter in the present work. The grain/grain fragment pull-out mechanism is characteristic of cermets, linked to the relatively weak bond ultimate strengths of the grain boundaries between the ceramic and binder phases, which can result in complete removal of the ceramic particles [54]. Figure 6.9(b) shows the presence of extensive plastic deformation, which ultimately can lead to 'chip' debris formation [55]. Due to the stress caused by the diamond indenter, the binder deforms (*i.e.*, is extruded) and is lifted by the indenter, a process that is often called 'buckling' [as indicated with arrow 3 in this figure] [56]. Eventually, this whole region of material might be removed as a 'chip'. Extensive, localized deformation in the region inside the scratch track is apparent, where carbide grains are pushed against each other, causing impingement wear and binder extrusion [indicated with arrows 4 and 5, respectively]; Larser-Basse first described this process of removal of the binder phase from between hard particles, where the binder phase is extruded away from the surface and carbide grains are retain in the matrix [57]. In the case of reciprocating sliding wear, the formed wear debris tends to be retained more between the sliding tribo-pair, and the particles are eventually 'crushed', due to the cyclic back-and-forth movement, resulting in a form of 'fretting' wear. This process eventually tends to generate a somewhat protective tribolayer on the surface of the sample, as the third-body debris is constantly refined through attrition; this also tends to result in high oxygen content within the tribolayer [2,3]. In the case of a single pass scratch test no oxygen content was observed using the SEM-EDS analysis, such a tribolayer will not be generated, and it is therefore possible to observe the generation of debris by removal of individual grains [58]. An example of this is presented in Figure 6.9 (c), where a single exposed carbide grain is apparent, that has been severely fractured into multiple parts due to sufficient contact stress to overcome its ultimate strength.

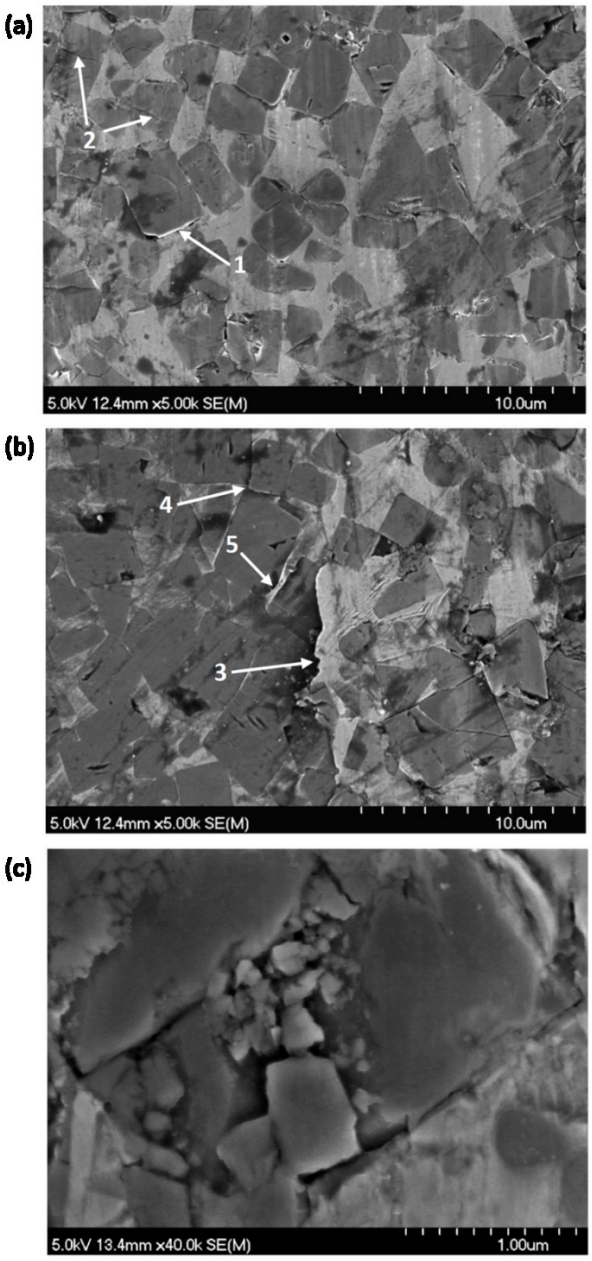

Figure 6.9 (a) Representative FE-SEM image demonstrating the microstructural characteristics relating to the various wear mechanisms for TiC-Ni_3Al, heat-treated at 600 ºC, after scratch testing, showing: (1) grain pull-out, and (2) intra-granular cracks. (b) Typical FE-SEM image showing the start of chip formation on a TiC-Ni_3Al cermet, heat-treated at 600 ºC. (c) A FE-SEM image demonstrating brittle fracture of a single TiC grain (which occupies most of the field of view) in a TiC-Ni_3Al cermet heat treated at 800 ºC. All samples were tested with a 30 N applied load. Note that arrowed regions correspond to discussion within the main text.

When heat-treating at higher temperatures, from 1000 to 1340 ºC, a transition to a more brittle failure mechanism becomes apparent during wear testing. It should be stressed that cermets are

excellent wear resistant materials due to a variety of factors. One of these relates to the properties of the metallic phase, which can still hold the ceramic particles and protect the surface even once the ceramic phase particles might be damaged [58]. For reciprocating sliding wear scenarios, surface and sub-surface cracks are typically the initiation points for grain pull-out mechanisms, which can also arise in other forms of erosive and abrasive wear [59]. In the case of scratch testing, the initiation of this cracks can be readily observed at high magnifications (Figure 6.10(a)), in this instance for a sample heat-treated at 1000 °C. Moreover, the binder extrusion and removal process are lessened, and the carbide grains maintain a high degree of their original separation, indicating that the ordering heat-treatments significantly increase the strength of the binder phase. The extent of sub-surface damage can be viewed by using FIB microscope, as this allows precision cutting through the near surface zone to reveal the microstructure immediately adjacent to the surface. An example of the sub-surface damage and cracking for the same sample shown in Figure 6.10(a) is presented in Figure 6.10(b). Here it can be seen that the sub-surface damage depth is quite limited (less than 3 μm), and cracking is mostly retained within the brittle TiC grain. Figure 6.10(c) demonstrate fracture within a TiC grain that has propagated into the adjacent region of the Ni_3Al intermetallic phase [indicated with arrow 6], which shows relatively minimal ductility in this heat-treatment condition (1000 °C for 120 minutes). This observation correlates well with the previous IFR calculations, where the heat-treatment at 1000 °C decreases the toughness of the binder (and hence the composite).

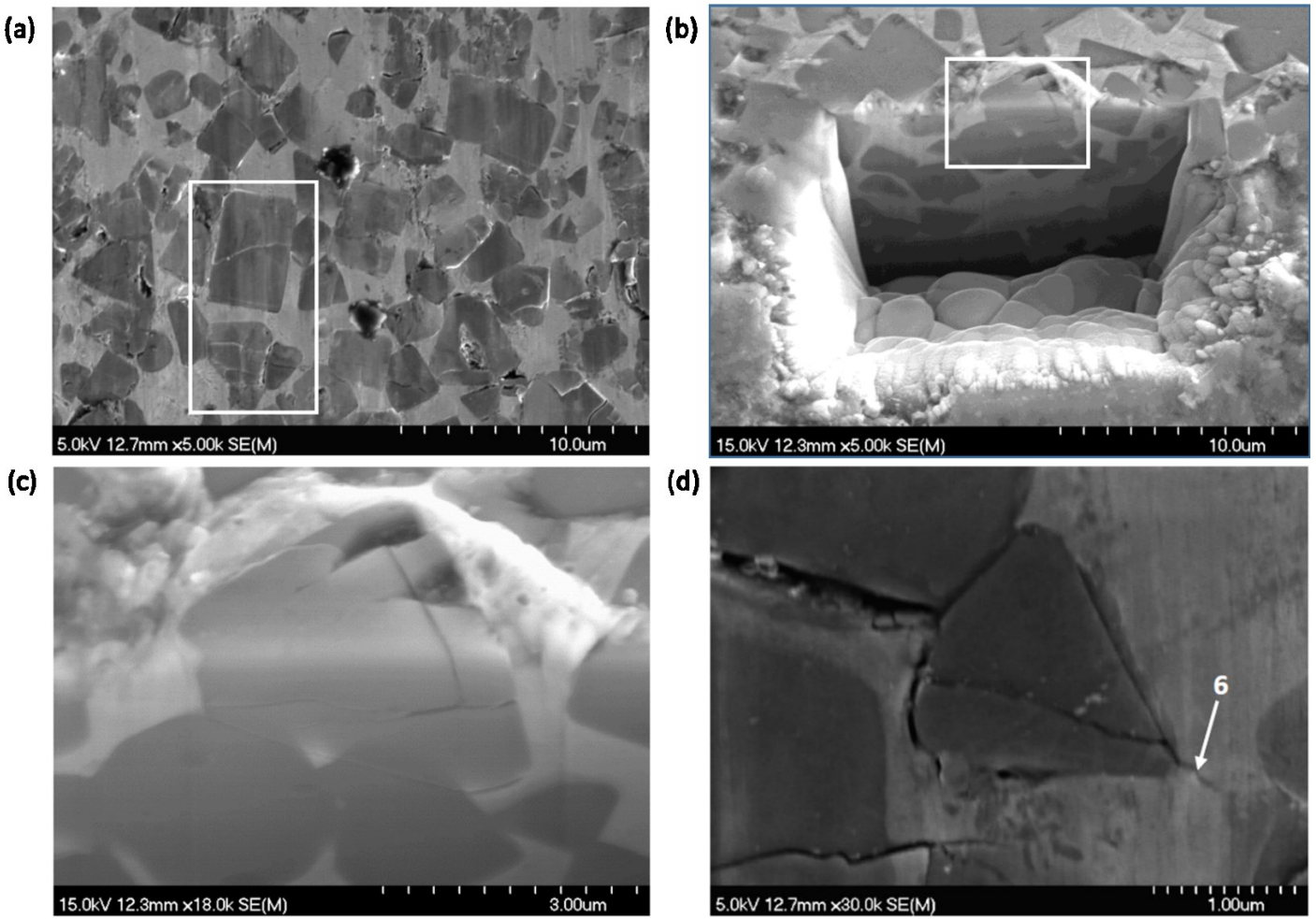

Figure 6.10 Damage mechanisms in a TiC-Ni_3Al sample heat-treated at 1000 ºC. (a) A FE-SEM image highlighting the retention of TiC grains within the binder phase, even though they are heavily cracked (e.g., as highlighted in the boxed region). (b) Example FE-SEM image of a FIB-milled cross-section highlighting sub-surface damage in a TiC grain that is still retained within the binder phase (c) Closeup FE-SEM image of the inset region from (b) demonstrating that sub-surface crack formation is limited to a few microns depth. (d) A typical FE-SEM image showing cracking within a TiC grain that has passed through into the now (more) brittle Ni_3Al binder (arrowed). All samples were tested under a 30 N applied load.

Further confirmation of the apparent embrittlement of the Ni_3Al binder phase can be observed in Figure 6.11(a), for a sample heat-treated at 1340 ºC. Here it can be seen that a large crack extends through several TiC grains and the Ni_3Al binder phase without any change in trajectory. A significant increase in the number and length of the cracks is observed for this heat-treatment, combined with a larger scratch depth (Figure 6.7). The FE-SEM image in Figure 6.11(b) shows an example of the extrusion-micro cutting mechanism, which proceeds though a cracking-extraction of the TiC phase. In this case, the contact stress was sufficient to yield the Ni_3Al binder, which results in the TiC grain being partially lifted above the worn surface, while adjacent TiC grains are slightly recessed relative to the original planar surface.

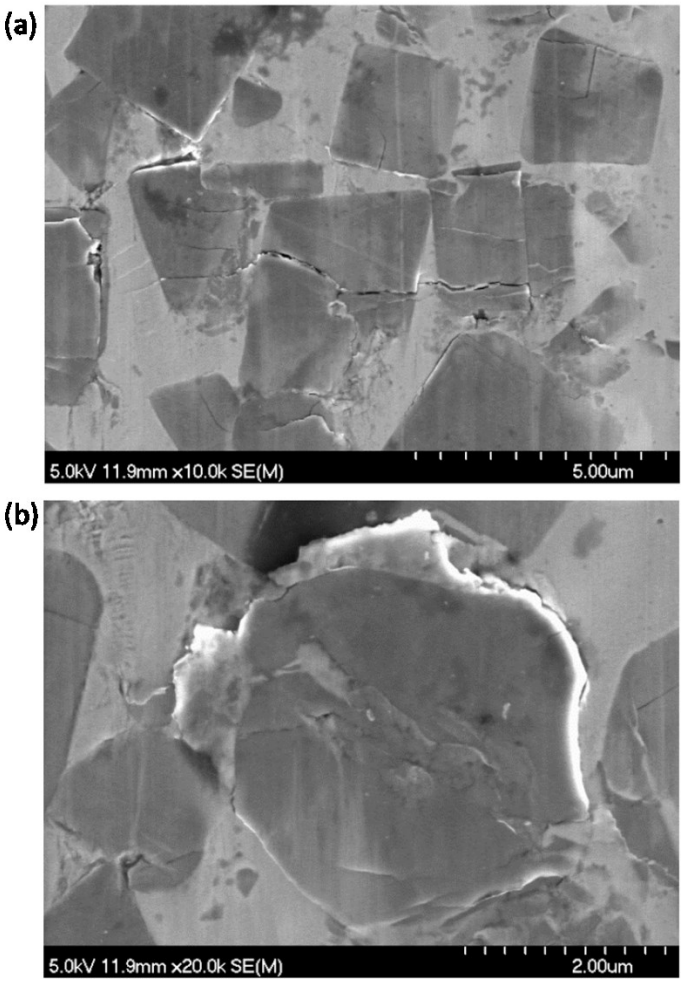

Figure 6.11 Example FE-SEM images of the damage mechanisms in a TiC-Ni_3Al sample heat-treated at 1340 ºC. (a) Brittle fracture within the binder phase. (b) A partially lifted out TiC grain, showing extensive debonding. All tests conducted with a 30 N applied load.

In terms of comparison between the present materials and industrial standard hardmetals, as outlined earlier, the scratch depth tests highlighted comparable scratch depths between the present materials heat treated at intermediate temperatures and WC-Co [51]. In prior work, a further direct comparison was made through reciprocating wear tests [2,4], assessing the present materials with varying binder contents to commercial WC-Co. Optimized TiC-Ni_3Al cermets, with 25 or 30 vol% stoichiometric Ni_3Al binder, exhibited slightly lower specific wear rates ($0.3–0.7\times10^{-7}mm^3/Nm$) when compared to the WC-Co ($\sim 1\times10^{-7}mm^3/Nm$) [2,4].

6.3.4 Computational Modelling

The special quasirandom structures (SQS) method [60] was used to generate the Ni_3Al random model (Figure 6.12(a)), with minimal periodicity error. To construct the disordered Ni_3Al, an experimental lattice constant of 3.5718 Å [61] was used. In the SQS approach, models are constructed whose particle-particle correlations are optimized to meet a given criterion, extended out to some pre-determined range, under the assumption that the total energetics are insensitive to long-range correlations. In this way, a periodic model of moderate size can be constructed whose properties closely mimic those of a truly random model. The SQS model studied here is generated by the *mcsqs* code based on a recently described Monte Carlo method [62]. The SQS model is presented in Figure 6.12(b), which shows the triclinic cell generated for the disordered-Ni_3Al alloy with 32 atoms supercell.

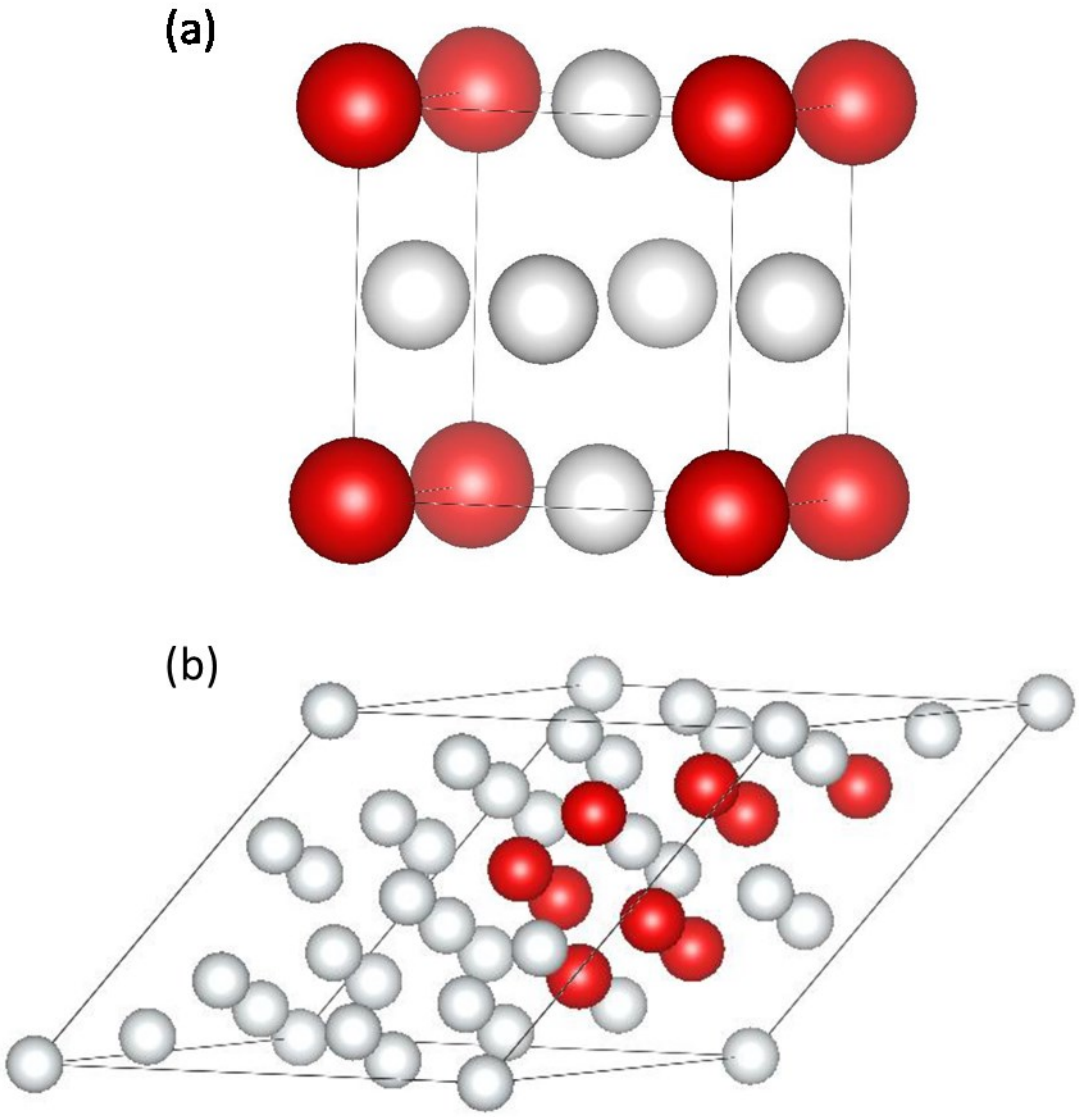

Figure 6.12 (a) Unit cell representation of ordered Ni_3Al (a). The ordered Ni_3Al has Cu_3Au-type structure, with Ni atoms at the face centers and Al atoms at the corners of the cube, with a cell constant of a = 3.571 Å. (b) The SQS structure has P1 symmetry, and cell parameters a = 16.5158, b = 15.0768, c = 11.6784 Å, and α = 104.96°, β = 18.13°, γ = 56.79°. Ni: small grey spheres; and Al: large red spheres.

The calculated elastic tensor elements of the systems of interest are shown in Table 6.1. Based on these results the elastic moduli are calculated. The first-principles calculations are in excellent agreement with the existing experimental measurements [63] and other theoretical data [64]. The calculated elastic modulus of the ordered $L1_2$ phase shows higher values than the one of the disordered Ni_3Al and overlaps with the experimental measurements where these alloys have been

made. The higher value of the C_{12} in case of the disordered-Ni_3Al shows more directional bonding, and a more resistant transverse displacement in response to longitudinal strain is expected.

Table 6.1 Calculated elastic stiffness coefficients of ordered-disordered Ni_3Al (in black colour), together with other experimental* and theoretical# results.

Structure	**Stiffness coefficient**			**Modulus parameter (GPa)**			**Source**
	C_{11}	C_{12}	C_{44}	*B*	*G*	*E*	
$L1_2$-Ni_3Al*	224	149	125	171	-	-	[64]
$L1_2$-$Ni_3Al^{\#}$	239	151	123	-	-	-	[64]
$L1_2$-Ni_3Al	233.2	153.8	125.2	180	79	207	This work
Disordered-Ni_3Al	208.8	162.8	91.7	177	54	146	This work

The response of the materials to strain beyond their elastic limits is related to ductility and brittleness, and there are several empirical correlations between polycrystalline elastic coefficients and the ductile versus brittle behaviour. One is the Poisson ratio, for which in polycrystalline metals the threshold for brittle to ductile behaviour occurs at $v \approx 0.25$. Another, is the ratio of bulk to shear moduli, B:G, whereby B:$G > 1.75$ suggests ductile behaviour. These criteria are not a definitive predictor of ductility, as they do not capture all the complexity of the ductile to brittle transition. However, they do provide guidelines for the likely trends in ductility of the material. In accordance to the Poisson's ratio (Table 6.2), in the both the ordered and disordered phases of Ni_3Al, the interatomic forces are not central, and it is expected that a ductile response is observed in the alloys. However, as mentioned above, the ductility of an alloy depends strongly and on the presence of impurities, cracks, dislocations and other factors.

Table 6.2 Calculated ratios of the bulk to shear moduli B=G, and Poisson's ratio v, together with the available experimental values*. Both data sets are based on the Voigt – Reuss - Hill averaging scheme.

Structure	**B:G**	v	**Source**
$L1_2$-Ni_3Al*	-	0.4	[64]
$L1_2$-Ni_3Al	2.27	0.309	This work
Disordered-Ni_3Al	3.32	0.363	This work

6.4 Conclusions

The following conclusions can be drawn from the present work:

1. A suitable heat-treatment is proposed with the goal to create a long-range ordered Ni_3Al intermetallic. To achieve this, heat-treatment temperatures from 600 ºC to close to the melting point (1340 ºC) were used, with each held for 120 minutes. Optimal results were obtained at 1200 ºC, with the measured Vickers hardness increasing from 1400 HV1 to approximately 1530 HV1.
2. A reduction of the Vickers hardness was noticed in the heat treatments performed at 600 and 800 °C. This behaviour is attributed to an annealing stress relief mechanism within the cermet composition.
3. The results of wear measurements, conducted by scratch testing at 30 N applied load, revealed that the scratch depth was reduced from ~15 to less than 5 μm when the cermets were heat-treated at 1200 °C, in contrast to the as-sintered compositions.
4. The main wear mechanisms were identified as grain pull-out and brittle fracture of the TiC grains in all as-sintered and heat-treated samples. Plastic deformation-chip formation was also observed for samples heat-treated at 800 °C.
5. In terms of applying the LRO process, heat treatment at 1200 °C exhibited the overall best wear performance, as well the highest micro-hardness values.

6. The first-principles elastic modulus results are in excellent agreement with the experimental findings, as a decrease in the values of the disordered-Ni_3Al is observed. As shown, the higher value of the C12 in case of the disordered-Ni_3Al indicates more directional bonding, and a more resistant transverse displacement in response to longitudinal strain is expected.

Acknowledgements

The Canada Foundation for Innovation, the Atlantic Innovation Fund, and other partners who helped fund the Facilities for Materials Characterisation, managed by the Dalhousie University Clean Technologies Research Institute, are gratefully acknowledged. The present work was also made possible with support from CAPES, Brazil, through the programme Coordination for the Improvement of Higher Level or Education Personnel. I would like to acknowledge, T. Z. Todorova and J.W. Zwanziger for the Computational Modelling section of this work, Z. Russell for her support on the experimental part of this work, as well my PhD supervisors Z.N. Farhat and K.P. Plucknett for their guidance.

CHAPTER 7 UNDERSTANDING THE ELASTIC AND THERMAL RESPONSE IN TiC-BASED CERAMIC-METAL COMPOSITE SYSTEMS: FIRST-PRINCIPLES AND MECHANICAL STUDIES

Status: *Published: Journal of Alloys and Compounds 789 (2019) 712-719.*

Abstract

First-principles and experimental studies of fundamental mechanical (elastic moduli, Poisson ratio and hardness) and thermal (expansion coefficient) properties were compared to assess the responses in titanium carbide (TiC) based ceramic-metal (cermet) composite systems, and evaluate the potential for predictive modelling of cermet behaviour. The TiC cermets were prepared with 30 vol-% of stoichiometric nickel aluminide (Ni_3Al) binder using a liquid phase sintering process, performed at 1500 °C for 60 minutes. Densities greater than 99% of theoretical were achieved under these conditions. The experimental elastic moduli were determined using a pulse-echo method, while hardness was assessed using the Vickers indentation test. The volumetric thermal expansion of the sample was studied using dilatometry.

Keywords: cermets; elastic modulus; thermal expansion coefficient; density functional theory;

7.1 Introduction

Two-phase ceramic-metal composites, or cermets, are an important class of material for applications in a variety of industries, including aerospace, biomedical, mining, petrochemicals, etc. [175,176]**.** Strength and light weight are key characteristics of a material for many applications, and it is always of interest to find ways to increase mechanical properties while keeping weight and cost down. In terms of aerospace applications, that goal may be achieved if the material holds a few key features: high wear and corrosion resistance; good hardness and toughness; high strength; high performance at extreme temperatures; and ideally for it to be environmentally friendly. The interest in a variety of cermet systems is due to a combination of the unique mechanical properties possessed by the ceramic and

metallic binder phases, namely high elastic and hardness, and ductility and toughness, respectively. In combination, these attributes can provide excellent wear and/or erosion resistance for cermets and related hardmetals.

Carbide-based ceramics, such as titanium carbide (TiC), are common components in many hard, wear resistant cermets. These materials have excellent properties such as high hardness, chemical inertness, high thermal conductivity, and a high melting temperature [95,177,178]. The desired properties of the cermets are also controlled through the addition of ductile metallic binders, such as elemental or alloyed Ni, Fe, or Co, and more recently nickel aluminide intermetallics (Ni_3Al) [1,7,165,179].

The interest in nickel aluminides is substantial, due to their simple structure, moderately low density (comparable to steels), high yield stress and ductility, high-temperature creep resistance, good corrosion resistance at elevated temperatures, and anomalous yielding response (whereby the yield stress actually increases with increasing temperature, up to some maximum) [179,180]. Several studies have shown the rapid infiltration of molten Ni_3Al through a TiC powder preform, which results in high density TiC/Ni_3Al composites [1,181,182], and confirms good wettability in this system. Different experimental techniques exist for optimal TiC/Ni_3Al preparation, including vacuum sintering, vacuum melt-infiltration and conventional hot-pressing [179,183]. As a result of the Ni_3Al incorporation, the strength of the material was shown increase at elevated temperature, up to ~1000°C [181], verifying transfer of the Ni_3Al anomalous yielding phenomenon to the composite systems.

However, for a number of reasons, many studies have an incomplete understanding of the influence of the atomic structure of these composites in relation to the roles of the constituents, the optimal ceramic-binder ratios, and their ultimate mechanical and thermal characteristics. The present study benchmarks the recent progress in experimental improvements of TiC-Ni_3Al composites with *first-principles* calculations in an effort to predict selected fundamental mechanical and thermal properties of these composites, as originated in atomic composition and structure. Based on both new and previously obtained experimental results [1], the current work compares the promising mechanical and thermal properties of TiC-based cermets with Ni_3Al 30 vol-% binder content, as well as pure TiC and Ni_3Al bulk properties.

7.2 Methods

7.2.1 Experimental Procedures

7.2.1.1 Sample preparation and microstructure characterization

High-density samples of TiC-Ni_3Al with 30 vol-% binder content were prepared using commercial TiC powder (lot no. 45693; particle size = 1-2 μm), supplied by Treibacher Industrie AG (Althofen, Austria), with a blend of elemental Ni powder (lot no. L10W013: particle size 2.2-3 μm) and Ni/Al powder (50/50 at-%; lot no. D28X029; D50<150 μm), both sourced from Alfa Aesar, MA, SA. The cermet powders were prepared with 0.5 wt-% of polyvinyl butyral binder, which is added to the powder blend through ball milling in acetone for 24 hours. Conventional disc-shaped pellets were produced by using ~6 g of the powder blend, followed by uniaxial compaction in a 31.75 mm diameter hardened steel die, at a pressure of ~69 MPa. The disc samples are then vacuum bagged, and further compacted by cold isostatic pressing at ~207 MPa. For sintering, the samples were placed into graphite crucibles on a thin layer of 'bubble alumina' to avoid direct contact with the graphite. The loaded crucibles were then placed into a graphite resistance vacuum furnace (R.D. Webb Red Devil®), and sintering was conducted under dynamic vacuum of 5 x 10^{-4} Torr atmosphere at 1500 °C for 60 minutes, with heating and initial cooling rates of 20 °C min^{-1}, and a natural furnace cooling rate for temperatures below ~800 °C.

The TiC-Ni_3Al cermets were also densified within a dilatometer (Model 401 C, Netzsch Instruments, Germany). In this instance, cylindrical samples were used for dilatometry, and were fabricated by uniaxial compaction in a 4.76 mm die at a pressure of ~50 MPa. The dilatometer was evacuated down to 1 x 10^{-5} mbar and then purged with argon for the heating/cooling period. The samples were heated at a rate of 20 °C/min to 1500 °C. Cooling was conducted at a nominal rate of 20 °C/min. During dilatometry measurements, the TiC-Ni_3Al samples were placed on an alumina (Al_2O_3) cradle, and supported with two Al_2O_3 discs in contact with the Al_2O_3 pushrods of the dilatometer to prevent any potential reaction with the pushrods. The cradle and plates were also coated in advance with a protective yttria (Y_2O_3) layer to prevent any bonding with the samples.

The sintered sample densities were measured following the Archimedes method, by immersion in absolute ethanol at room temperature**.** Scanning electron microscopy (SEM; Model S-4700,

Hitachi High Technologies, Tokyo, Japan), energy dispersive X-ray spectroscopy (EDS; Model Inca X-MaxN, Oxford Instruments, Abingdon, UK) and X-ray diffractometry (XRD; Model D-8 Advance, Bruker Corp., Billerica, MA, USA) techniques were used for investigation of the sample microstructures, phase mixtures and indentation damage mechanisms. Polished cross sections were examined via SEM, coupled with EDS for chemical microanalysis. The resultant digital images were analysed to determine the Ni_3Al-TiC grain growth, phase distribution and degree of densification. XRD was used to detect the crystalline phases in the sintered samples and to confirm the *in-situ* intermetallic formation.

7.2.1.2 Mechanical properties measurements

Information relating to the elastic and plastic deformation responses of the samples were assessed through calculations of elastic modulus and hardness indentation tests. Stiffness, together with hardness, are among the most important mechanical properties of materials. As the hardness is a material's resistance to permanent deformation following some form of indentation, it depends strongly on the balance of elastic and plastic deformation, while the stiffness is effectively a material's resistance to volume/dimension change.

In this work, the cermet hardness was determined using the Vickers hardness (VH) test, with an applied load of 1 kgf. The values were obtained using the standard ASTM procedure [184], with data averaged for six indentations, with the full load applied for a duration of 10 seconds. The Young's modulus, *E*, of the samples was confirmed through measurement of the transverse, v_T (shear), and longitudinal, v_L (compressional), wave velocities using the ultrasonic pulse-echo method [185]. A Panametrics NDT 25DL ultrasonic thickness gage was used for these measurements, where ultrasonic pulses were passed through the cermet, reflected off the back surface, and then received at the transducer in the form of an echo. The Poisson's ratio, μ, and Young's and shear modulus, G, are then related to the longitudinal and transverse velocities as follows [185]:

$$\mu = (\rho v_L^2 - 2\rho v_T^2)/(2\rho v_L^2 - 2\rho v_T^2) = (v_L^2 - 2v_T^2)/\left(2(v_l^2 - v_T^2)\right) \qquad \textbf{Equation 7.1}$$

where ρ is the sample density. Once Poisson's ratio is known, Young's modulus can be calculated from the equation:

$$E = v_L^2 \rho(1+\mu)(1-2\mu)/(1-\mu) \quad \textbf{Equation 7.2}$$

The shear modulus of a material is related to the transverse wave velocities through the relationship:

$$G = v_T^2/\rho \quad \textbf{Equation 7.3}$$

The bulk modulus, B, can then be found from the relationship between B and the calculated Young's modulus or Poisson's ratios:

$$Y = (3B-2G)/2(3B+G), \text{ or } \mu = (9BG)/(3B+G) \quad \textbf{Equation 7.4}$$

7.2.1.3 Thermal expansion coefficient measurements

The coefficients of thermal expansion of the samples were determined through dilatometry studies, using the same system outlined above. As with sintering, the dilatometer was evacuated down to 1 x 10^{-5} mbar and was subsequently purged with argon during the heating/cooling period. The samples were then heated at a rate of 20 °C/min to 800 °C, with cooling at a nominal rate of 20 °C/min, while placed on an Al_2O_3 cradle, and supported with two thin Al_2O_3 discs that are in contact with the Al_2O_3 pushrods. The cradle and plates were again coated with a thin protective Y_2O_3 layer, to prevent any reaction with the samples.

7.2.2 First-principles methods

The first-principles calculations were performed using the VASP code (www.vasp.at). This code performs density functional theory (DFT) calculations, using the projector-augmented wave (PAW) formalism and a planewave basis. The VASP version 5.4 PAW atomic data sets were used, with the Perdew-Burke-Ernzerhof (PBE) exchange and correlation functional [186]. A number of convergence studies were conducted and an appropriate planewave cut-off energy and *k*-point mesh were used. These parameters were sufficient to converge the cell stress to better than 0.1%. The metallic occupancy of the levels was treated by the Methfessel-Paxton scheme [154], using a smearing parameter of 0.2 Ha, which was determined by minimizing the total energy at the experimental cell volume of aluminium, and then used for the other compounds as well.

7.2.2.1 Elastic Modulus and ductility

The theoretical elastic moduli in the present work were determined by using finite differences, combining both cell distortions and atomic displacements, thus yielding the elastic tensor, including ionic relaxation. Each structure was fully relaxed as described above. Using the computed single crystal elastic constants, elastic properties including the bulk modulus, shear modulus, Young's modulus, and Poisson ratio were obtained by applying a Voigt-Reuss-Hill averaging procedure [187]. The response of the materials to strain beyond their elastic limits is related to ductility and brittleness, and there are several empirical correlations between polycrystalline elastic coefficients and 'ductile versus brittle' behaviour. One is the Poisson ratio, for which in polycrystalline metals the threshold for brittle to ductile behaviour occurs at $\nu \approx 0.25$ [188]. This criterion is not a definitive predictor of ductility, as it does not capture all the complexity of the ductile to brittle transition. However, the Poisson ratio provides guidelines for the trends in ductility of the material.

7.2.2.2 Thermal expansion

The most frequently examined thermodynamic properties in an ab initio calculation are the equilibrium atomic volume, isothermal bulk modulus, and the linear thermal expansion coefficient under ambient conditions. In our calculations, the contributions to the free energy from the lattice vibrations are calculated using the phonon densities of states, derived by means of the density functional perturbation theory (DFPT), as implemented in VASP and interfaced with Phonopy code [189]. The volumetric coefficient of thermal expansion, $\alpha_V = \partial ln\, V / \partial\, T$, has been calculated for the compounds studied here, by computing the phonon modes and frequencies at a range of cell volumes generated by varying the lattice parameters from -2.5 % to + 2.5 % around the zero Kelvin relaxed value, in steps of 0.5%. Using these calculations, the free energy is constructed as a function of both temperature and cell volume, by the standard expression [156]:

$$F(V,T) = U_0(V) + \tfrac{1}{2}\sum_{q,v} \hbar(q,v|V) + k_B T \sum_{q,v} log\left(1 - exp\left(\frac{-\hbar(q,v|V)}{k_B T}\right)\right) \qquad \textbf{Equation 7.5}$$

Subsequently, at each temperature, the free energy as a function of volume is fitted to the Birch-Murnaghan equation of state, in order to extract the temperature-dependent cell volume [190], and the obtained volume is then differentiated as a function of temperature to obtain the thermal expansion coefficient.

7.3 Results and Discussion

7.3.1 Sintering, microstructural characterization, and hardness of TiC/30vol-% Ni_3Al cermets

An example of the typical TiC/30 vol-% Ni_3Al dilatometry results, obtained during the sintering step, are presented in Figure 7.1. The main expansion peak occurs between 69 - 72 minutes, and corresponds to sintering temperatures in the range of 1318 - 1369 °C. After the complete melting and formation of the liquid Ni_3Al intermetallic phase, there is a significant increase in the sample shrinkage, due to the accelerated diffusion rates that are available when liquid phase sintering. This can be seen by the peak in the first derivative plot. After this, densification up to 14% occurs in the material, generating a final sintered cermet with densities >99 % of theoretical (when completing an isothermal hold at 1500 °C for 60 minutes).The characteristics of TiC-based cermets are highly dependent on the matrix properties and the binder phase behaviour. Their mechanical behaviour is also sensitive to the TiC particle shape and spatial distribution in the final densified structure.

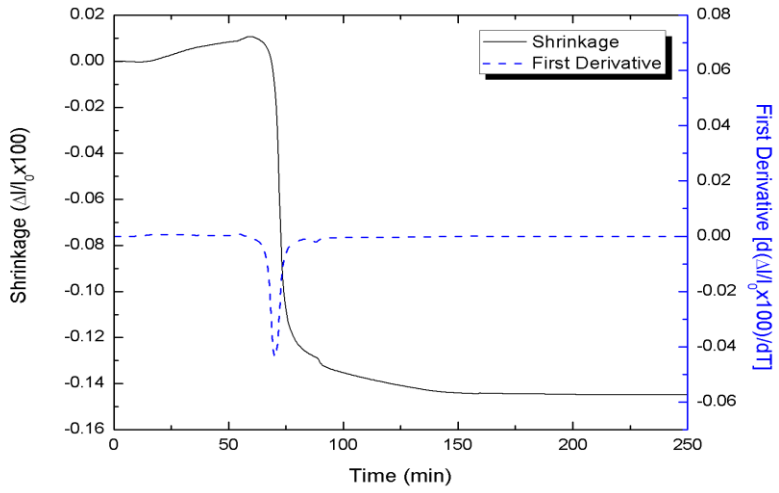

Figure 7.1 Representative dilatometry curve during sintering, for a TiC/30 vol-% Ni_3Al cermet showing, the extent of densification as a function of temperature. Samples heated/cooled to 1500 °C at a rate of 20 °C/min.

Figure 7.2 demonstrates a typical SEM image example of the microstructure of the sintered TiC-30 vol-% Ni_3Al cermet. With an initial, mean TiC powder particle size of 1.25 μm [191], a moderate degree of coarsening can be seen following sintering, with TiC grains present from 2 to 8 μm in size (dark grey contrast phase). The densification of the sample occurs via a dissolution/re-precipitation mechanism, where the reduction of free energy drives densification and Ostwald ripening, causing small grains to dissolve, and then precipitation of the dissolved material onto the (statistically) larger grains.

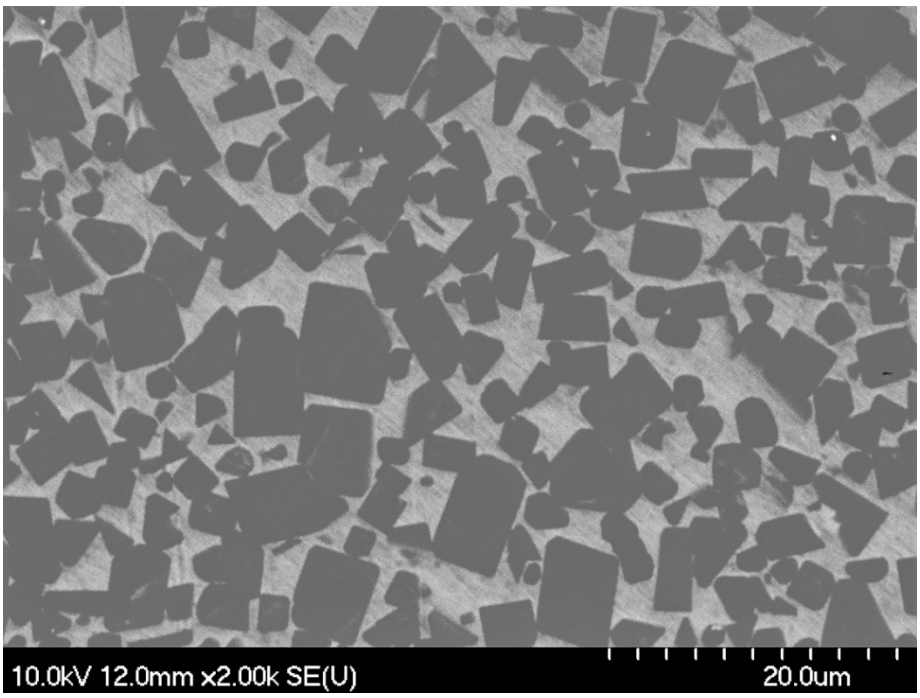

Figure 7.2 Representative SEM image obtained from the polished surface of the sintered TiC-30 vol-% Ni_3Al cermet. Note that TiC grains are the darker contrast phase, while the continuous Ni_3Al binder is the lighter contrast phase.

Associated EDS maps of the Ti-C and Ni-Al phases are presented in Figure 7.3 (a). It is notable that upon cooling, the TiC phase completely segregates from the Ni_3Al, and there is no evidence of any significant reaction or alloying between the two components. Further confirmation of the complete chemical reaction of the Ni/Al and Ni mixture to Ni_3Al is observed, where regions of Ni concentration and Al are connected in the points 1, 2, 3 and 15 in Figure 7.3 (b). Negligible phase

“overlapping” is observed, on the points 4 and 14, highlighting a sharp, discrete interface at the scale evident from SEM imaging.

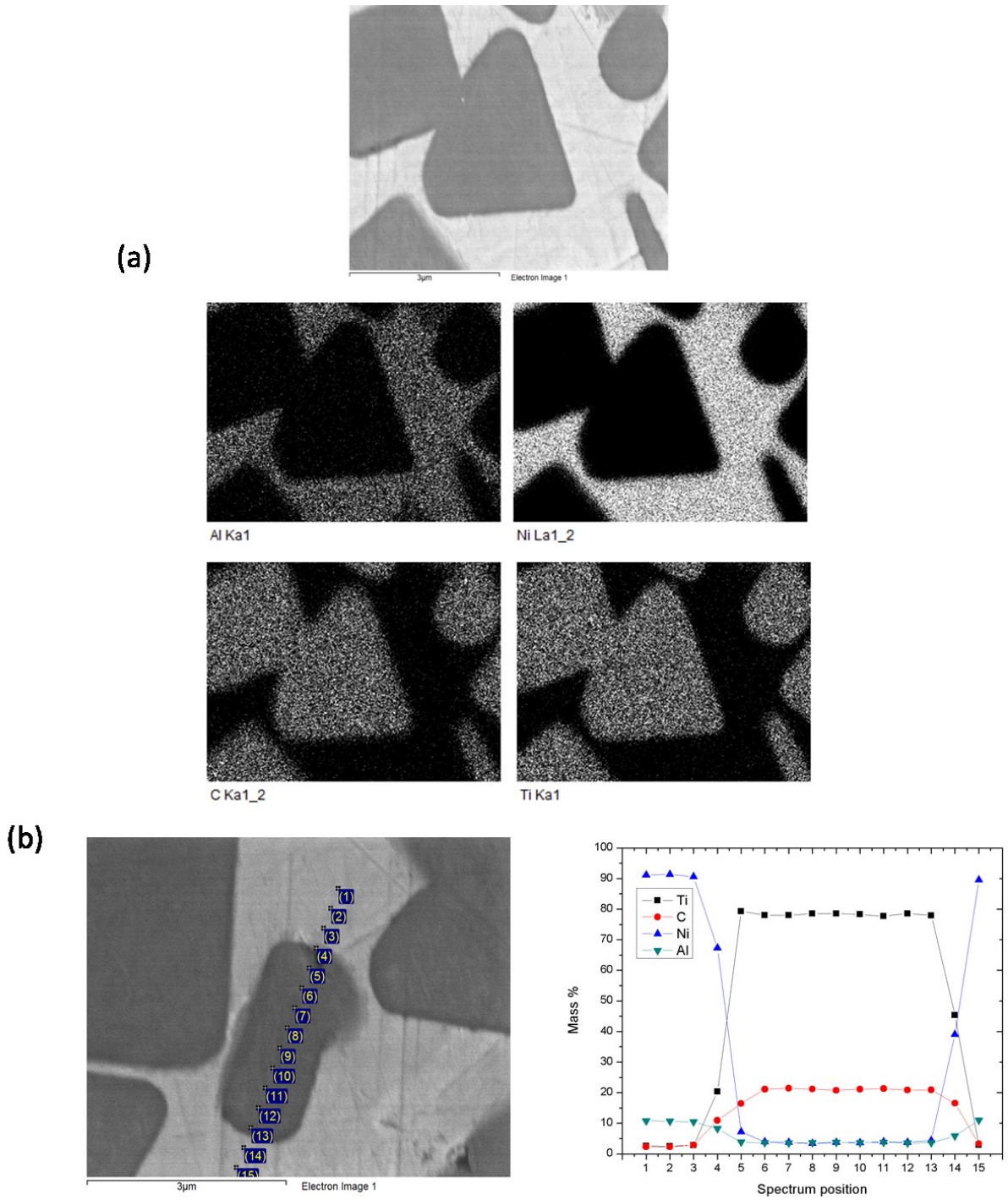

Figure 7.3 Representative microstructure and chemical composition of the sintered sample. (a) EDS map across an isolated grain of TiC within the 30vol-% Ni_3Al binder. The TiC phase is denoted in dark grey colour, while the Ni_3Al phase is in light grey colour. (b) SEM-EDS point analysis showing the degree of chemical composition between phases.

The Ni_3Al intermetallic phase formation is also confirmed by XRD, as shown in Figure 7.4, demonstrating completion of the *in-situ* reaction process with Ni and Ni/Al, with confirmation of the retention of the TiC phase and the transition from pre-alloyed Ni/Al and Ni powders to the Ni_3Al cubic $L1_2$ intermetallic phase.

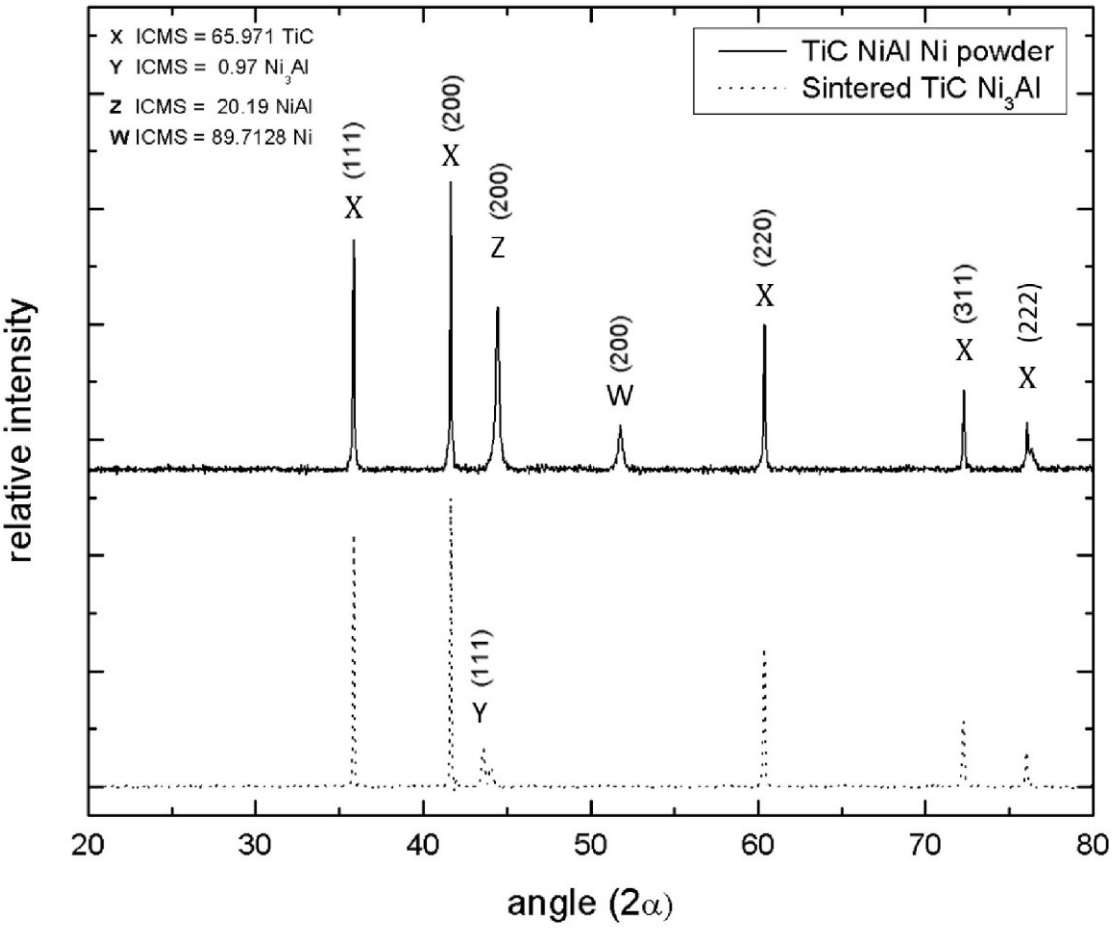

Figure 7.4 XRD analysis of TiC, Ni/Al and Ni powder mixture before sintering (solid line) and the sintered TiC/ 30 vol-% Ni_3Al cermet (dotted line).

Figure 7.5 shows an example of a Vickers hardness test for the TiC-Ni_3Al 30 vol-% cermet. A Vickers hardness value of 1318.7 ± 53.3 VH1 (12.93 GPa) was measured for this sample, at an applied load of 1 kgf. As reported previously [192], cermets with 80 - 90 vol-% TiC show higher hardness than in the cases with lower ceramic contents, as would be expected based on the relative elastic moduli of the phases. It is important to emphasise that for the present cermet system the 30

vol-% concentration of Ni_3Al still contributes significantly to the overall hardness of the composite.

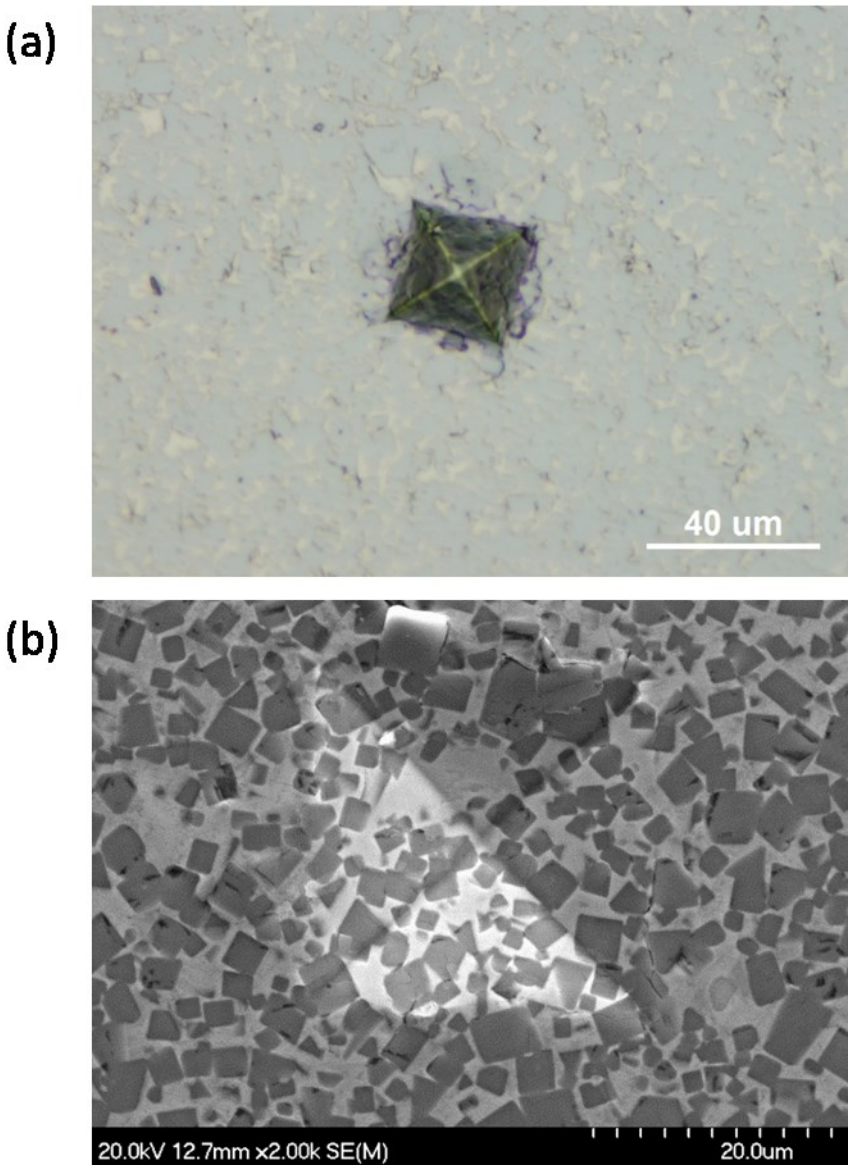

Figure 7.5 (a) Optical microscopy and (b) SEM images following a Vickers hardness test on a TiC-30 vol-% Ni_3Al cermet, using a 1 kgf indentation.

7.3.2 Bulk properties

As a first step, the *ab initio* calculated bulk properties of the elemental constituents were assessed, specifically face centred cubic (FCC) Al, FCC - Ni, hexagonal closed packed (HCP) α–Ti and

HCP - C (graphite). Subsequent to this, the formation energies of the cubic $L1_2$ -Ni_3Al and $L1_2$ - TiC components of the composite system were assessed.

The choice of HCP - Ti and HCP - C structures in the theoretical work is nominally based on the potential for forming TiC via a mechanical alloying process [193], as well as the more common carbothermal reduction route. Although in nature graphite exists in two type of stacking sequences – ABCABC (β - rhombohedral) and ABAB (α - hexagonal (HCP)), it is shown that the only experimentally stable phase is the HCP-form [194–196]. In the current work we consider only HCP-C and the van der Waals (vdW) interlayer interactions were taken into account through the use of the PBE/DFT-D2 method of Grimme [197], which previously has shown calculated HCP-C values in good agreement with experimentally measured elastic stiffness coefficients (C33), equilibrium interlayer distance and binding energies [196].

The calculated lattice parameters and formation energies are presented in Table 7.1, along with experimental [195,198–202] and other theoretically [203] calculated data, where available. Overall, the calculated lattice parameters in the present work are in good agreement with both experimental and prior theoretical data, showing the typical slight dilation due to the use of the PBE exchange and correlation functional.

Table 7.1 Computed lattice constants and formation energies of all the elements and compounds studied in the present work, together with comparison (where possible) to experimental (in bold) and other theoretical studies (in italics).

Compound	**Lattice parameter (Å)**	**Cell volume ($Å^3$)**	**ΔH_{form} (kJ/mol)**	***m*** **(μ_B) per unit cell**
Al - FCC	4.04975 [29]	66.42 [29]		
	4.041	66.00		
Ni - FCC	3.5157 [30]	43.45 [30]		*0.44 - 0.58* [33]
	3.5135	43.36		0.5678

Compound	Lattice parameter (Å)	Cell volume (Å^3)	ΔH_{form} (kJ/mol)	m (μ_B) per unit cell
Ti - HCP	a_0 = 2.9506 [31]	35.28 [31]		
	c_0 = 4.6788 [31]			
	a_0 = 2.94452			
	c_0 = 4.69813	35.28		
C - HCP (graphite) + vdW	a_0 = 2.464 [32]	35.29 [32]		
	c_0 = 6.711 [32]			
	a_0 = 2.456			
	c_0= 6.71	35.05		
Ni_3Al ($L1_2$)	3.568 [32]	45.42 [32]	-46.00 [32]	0.24 [32],
	3.5664	45.36	-42.22	*0.6 - 0.71* [33]
				0.70613
TiC ($L1_2$)	4.328 [*34]*	81.07 [*34]*	-131, -190,	
	4.3228	80.80	184.1 [*34]*	
			-152.8	

At Tc = 41 K, Ni_3Al possesses weak itinerant ferromagnetism and strong exchange-enhanced paramagnetic properties for 73.5–74.5 at. % Ni concentrations [204]. As shown in Table 7.1 the calculated total magnetizations of Ni and L_{12}-Ni_3Al in the present work are in a good agreement with the existing theoretical and experimental data

The stabilities of the Ni_3Al and TiC systems are also shown in Table 7.1. These values represent the formation energy for the corresponding chemical reaction and were obtained from the total

energy from the DFT calculation for each phase in its ground state, together with the energies for the pure elements, also obtained from DFT. It can been seen that the formation energies of Ni_3Al and TiC from PAW-GGA are -42.22 kJ/mol and -152.8 kJ/mol, respectively, which are both in good agreement with the experimental values of -46 kJ/mol (Ni_3Al) [200] and in the reported range of -130 to -190 kJ/mol in the case of TiC [202]. These results show that both materials are stable relative to their constituent elements.

7.3.3 Elastic and plastic properties

The calculated elastic tensor elements of the systems of interest are shown in Table 7.2. Based on these tensor results, the elastic moduli were calculated. Because such alloys are typically used in a bulk polycrystalline form, rather than as single crystals, reporting their moduli based on a polycrystalline averaging procedure provides a more realistic representation of the material properties. Our first-principles calculations are in good agreement with the existing experimental values [205–210] and other theoretical [211–214] data.

Table 7.2 Calculated elastic stiffness coefficients and elastic moduli of the studied systems, together with other experimental (in bold red colour) and theoretical (in italics blue colour) results.

	C_{11}	**C_{12}**	**C_{44}**	**C_{13}**	**C_{33}**	**B [GPa]**	**G[GPa]**	**E[GPa]**	ν
Al - FCC	107/ 116 [36]	61/ 65 [36]	28/ 27 [36]	-	-	76 [36]	26 [36]	70 [36]	0.35 [36]
						77.8 [42]	*24.8* [42]	*67.35* [42]	*0.355* [42]
									0.356
						77.65	24.66	66.91	
	102.05	65.44	30.11						
Ni - FCC	246 [37]	147 [37]	124.7 [37]	-	-	180 [37]	76 [37]	200 [37]	0.31 [37]
	268.7 [43]	*150.9* [43]	*129.9* [43]			*190.2* [43]			
						196.67		200.2	0.33
Ti - HCP (α)	248.77	170.62	116.48				75.25		
	160 [38]	73/ 110 [38]	20.7/ 46.5 [38]	66 [38]	181 [38]	110 [38]	44 [38]	116 [38]	0.32 [38]
					181.76			113.8	0.31
	167.48	82.16	42.65	71.47		102	43.26		

	C_{11}	C_{12}	C_{44}	C_{13}	C_{33}	**B [GPa]**	**G[GPa]**	**E[GPa]**	ν
C - HCP	1109/+-16 [39]	175 [39]	4.8 [39]	-3/ -2.5 [39]	42 [39]	15.3 [39]	11.5 [39]	27 [39]	0.23 [39]
					42.44 [44]	*34* [44]	*9.7* [44]	*25* [44]	*0.31* [44]
									0.31
					43.47	34.09	14.26		
		191.34	4.32	-3.85				37.56	
	1057.74								
	224 [40]	149 [40]	125 [40]			171 [40]			
Ni_3Al ($L1_2$)	*239* [45]	*151* [45]	*123* [45]	-	-				
	233.23	153.84	125.15			180	79.10	207	0.30
	500 [41]	106 [41]	175 [41]			223 [41]	182 [41]	449 [41]	
TiC ($L1_2$)	*510* [41]		*168* [41]	-	-	*250* [41]	*179* [41]		
								447.5	
	558.6	132.83	163.08			274.75	182.12		0.228

Figure 7.6 compares the calculated *ab initio* and experimental data obtained for the elastic moduli (Young's, shear and bulk) of the TiC-30 vol-% Ni_3Al cermets. The theoretical elastic moduli of the TiC-30 vol-% Ni_3Al in this work are evaluated by the use of a 'rule of mixtures' (ROM) method [215].

The ROM approach is one of the simplest empirical methods permitting to estimate a property of a composite material, composed by two (or more) different components with different physical characteristics. With the ROM method, the only parameters considered are the amount of each component in the composite and the property of interest for each pure component; typically, no other parameters that play an important role on the composite properties are considered, with the occasional exception of residual porosity. Therefore, it should be noted that the cermet's final elastic and thermal properties depend on its chemical composition and microstructure, but also on the magnitude and type of residual stresses [216]. These residual stresses arise as a result of the superposition of macroscopic (thermal-residual stresses), with microscopic stresses due to the mismatch between the thermal and elastic properties of the carbide and binder phases [217,218]. While the effect of the thermal-residual stress on the cermet performance can even be largely eliminated by slow cooling and/or subsequent annealing, the microscopic stress is an intrinsic characteristic of the composite due to its multiphase nature [219]. By using the ROM in our *ab initio* calculations, to estimate the elastic moduli of the TiC-30 vol-% Ni_3Al cermet, the magnitude of residual stresses is not taken in account, and nor are the effects of microstructure parameters considered (i.e. size of the particles and their orientation, the presence of porosity/defects, *etc.*). Consequently, the obtained theoretical value of Young's modulus, at 375 GPa, somewhat overestimates the present experimental finding of 332 GPa. The same trend is observed in the case of shear modulus, with an experimental value of 130 GPa, while the theoretical one is 151 GPa. The calculated value of the Poisson ratio is above 0.25, which indicates ductile behaviour in the cermet.

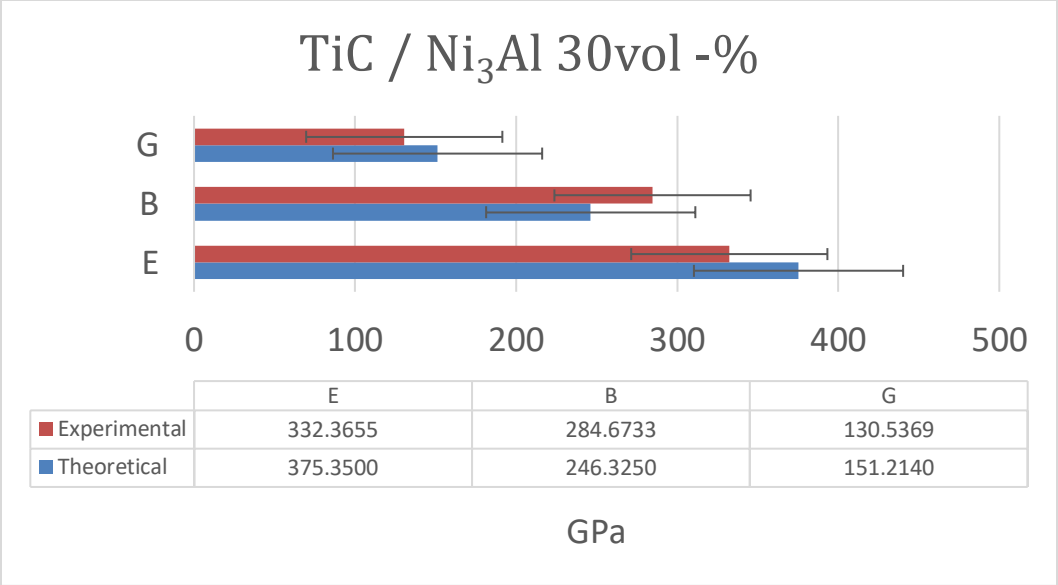

Figure 7.6 Experimental and first-principles elastic modulus of the TiC/30 vol-% Ni_3Al sample.

7.3.4 Thermal expansion (ab initio and experiment)

The presently calculated thermodynamics data of the studied systems, together with the available experimental [220–223] and theoretical results, are presented in Table 7.3. The calculated equilibrium thermal volumes (V_T) in Table 7.3 overestimates by approximately 2% the other available theoretical and experimental results. However, overall, the present calculations in the cases of Al and Ni are in good agreement with the experimental and other theoretical data. In this work the calculated thermal expansion of Al and Ni are compared to previously published results [220]. These two sets of data are sufficiently accurate to be viewed as an experimental standard for comparisons. The agreements between our *ab initio* results of the predicted thermal expansion coefficients and available experimental data for Ni_3Al appeared to be as good, as are the cases for Al and Ni. It should be noted that the Ni_3Al thermal expansion values in [220] have larger uncertainties, due to the limited experimental data. For example, in [224] is reported an averaged $\alpha = 17.3 \times 10^{-6}$/°C, between 26.85 and 726.85 °C for Ni_3Al. The calculated values of $\alpha = 6.4 \times 10^{-6}$ /°C for the TiC example are in good agreement with the available experimental data [221].

Table 7.3 Calculated thermodynamic properties of the studied systems at ambient conditions (T = 26.85 °C (300K) and P = 0 GPa), along with experimental (in bold) and other theoretical (in italics) data where available.

Material	**V_T (Å ^{3} / per atom)**	**B_T (GPa)**	**α (10^{-6}/K)**
Al - FCC	16.60 [47]	72.20 [47]	22.30 / 23.1 [47]
	16.82 [47]	*68.06* [47]	*24.88* [47]
	16.88	68.73	24.24
Ni - FCC	10.94 [47]	186 [47]	13.10 [47]
	11.09 [47]	*191.6* [47]	*12.68* [47]
	11	185.08	12.99
Ti - HCP (α)	17.56	107.45	8.06 [48] 8.46
C - HCP (graphite) + vdW contribution	8.92	226.84	0.6 - 5.2 [50] 4.69
Ni_3Al ($L1_2$)	11.32 [47]		12.5 [47]
	11.32 [47]	*182.4* [47]	*12.17* [47]
	11.45	170.98	12.33
TiC ($L1_2$)	10.31	253.83	4.1-7.7 [48] 6.43

Figure 7.7 shows a typical example of the experimentally obtained volumetric thermal expansion data for TiC/30 vol-% Ni_3Al, which is in the range of ~2.5 x 10-6/°C at 76.85 °C, increasing up to 18 x 10-6/°C at the temperature of 500 °C. Using the ROM and the theoretical values in Table 7.3, the calculated volumetric thermal expansion coefficient of the sample at 26.85 °C is 8.2 x 10-6/°C. From an experimental point of view, the obtained results at 26.85 °C are not definitive, due

to the limitations on accuracy that can be achieved by the dilatometer at such temperature. The use of the ROM approach to estimate the theoretical values of the thermal expansion coefficients also contributes to the difference between experimental and computed results, due to the reasons mentioned in the previous section.

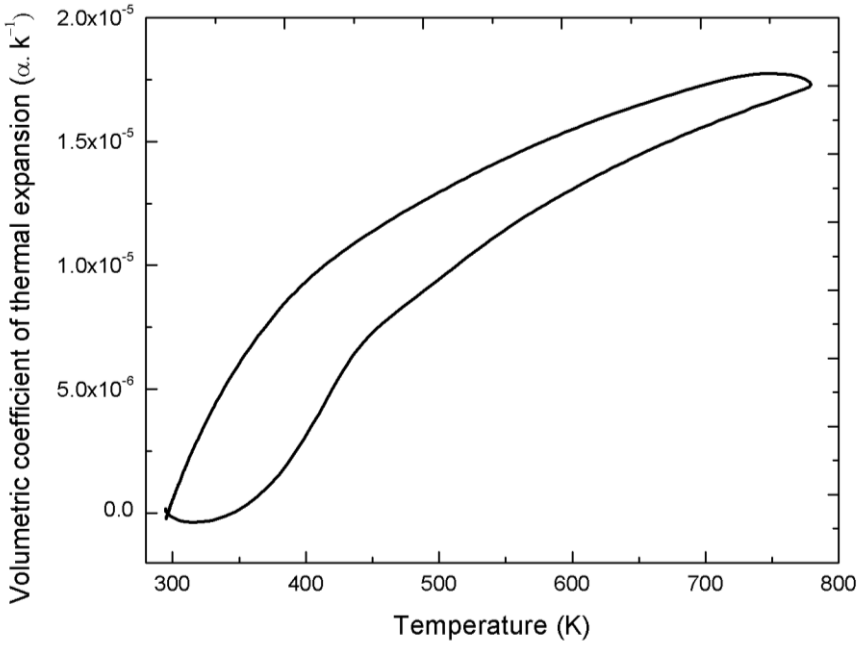

Figure 7.7 Volumetric thermal expansion coefficient measurements for a TiC-30 vol-% Ni_3Al sample previously densified at 1500 °C. The heating rate is 5 °C /min., in a flowing Ar atmosphere (10 ml/min), from room temperature up to 500 °C, and back to room temperature.

7.4 Conclusions

In the present work we have considered selected mechanical and thermal properties of TiC-Ni_3Al cermets, compared to pure TiC and Ni_3Al (as well as their elemental constituents), based on both experimental and first-principles studies. It is shown that, for the pure TiC and Ni_3Al, the theoretical calculations were in good agreement with the measured experimental data for the many different parameters examined and calculated, notably elastic properties, thermal expansion coefficients, and selected structural properties.

For the TiC/30 vol-% Ni_3Al cermet system, the theoretical *ab initio* results differ from the experimental findings, which is likely due to the lack of considering major atomistic characteristic

by the rule of mixture and the precision that can be obtained at room temperature by the dilatometry measurements. However, significant enhancement of the sample stiffness is observed at 30 vol-% Ni_3Al binder content compared to TiC-Ni_3Al cermets previously reported [1]. Moreover, the high plastic resistance of the sample was confirmed by the Vickers hardness, which was found to be 1318.68 ± 53.3 (12.93 GPa).

Acknowledgements

The present work was also made possible with support from CAPES, Brazil, through the programme Coordination for the Improvement of Higher Level or Education Personnel, and from the Natural Sciences and Engineering Research Council, through the Discovery Grants programme. The Canada Foundation for Innovation, the Atlantic Innovation Fund, and other partners who helped fund the Facilities for Materials Characterisation, managed by the Dalhousie University Clean Technologies Research Institute, are also gratefully acknowledged. I would like to acknowledge T. Z. Todorova and J. W. Zwanziger for their support on the *First-principles* calculations part of this work, as well my PhD supervisor K.P. Plucknett for his guidance.

CHAPTER 8 – PRECIPITATION HARDENABLE TiC-BASED CERMETS

Abstract

Titanium carbide-steel cermets are composites with a good combination of wear and corrosive performance at ambient temperature. Stainless steel alloys have been applied in many industrial applications, with a large variety of heat treatment procedures that have been developed for some of these steels. The current work stu dies the effects of heat treatments on precipitation hardenable steels (grade 17-4 PH) in comparison with a non-heat treatable steel (316L) when used in a cermet structure combined with TiC. Martensitic Cu-rich precipitates were identified by X-ray diffraction analysis when the TiC-17-4 PH cermets were heat treated. A significant increase in Vickers hardness, from 1160 to 2342 HV1, was observed as a result of a 1150 °C heat treatment for this system. Moreover, the scratch resistance was significantly improved, with a scratch depth reduced from 1.74 to 0.8 μm under an applied load of 30 N.

Keywords: Vickers hardness, scratch testing, scanning electron microscopy, confocal laser scanning microscopy.

8.1 Introduction

Cermets based on titanium carbide (TiC) with steel binders are promising structural materials due to the ability to synthesize high-density composites with excellent interfacial cohesion between the metallic binder and the carbide phase [225]. A further advantage can potentially be achieved when using a precipitation hardening steel as a binder phase, as such a material can be heat treatable using a wide variety of temperature/time regimes to obtain the desired final properties, in comparison with other grades of stainless steel (such as 316) that cannot be heat treated.

Some limited solubility of the ceramic phase within the metallic matrix is necessary to obtain fully densified cermet with suitable mechanical and wear performance [8]. On occasions, there is potential partial solubility of components within the binder phase into the TiC grains [73], although this is arguably undesirable. TiC and tungsten carbide (WC) are the most common materials used

as the ceramic phase(s) in cermets due to their superior hardness, remarkably high young modulus, chemical-thermal stability, and high wear resistance. While both are appropriated for use in applications that have challenging environments, such as aircraft landing gear and wing flap tracks, TiC has a significant advantage due to its much lower density (4.93 g/cm^3) when compared with WC(15.63 g/cm^3) [1,8,18].

One of the most commonly used methods for fabricating cermets is the press-and-sinter approach [226]. However, other methodologies such as melt-infiltration sintering and impregnation of pressed and sintered briquettes from titanium carbide with molten steel are also used by industry [72,225]. Post heat treatment process, such as hardening and tempering heat treatments have been studied previously using carbon steel as a binder [225]. In this work, it was demonstrated that it is possible to successfully significantly affect the properties of the final composite. Prior work by Kim *et al*. shows an increase from 1280 HV to 1320HV when an austenitization treatment was applied to an SKD11 tool steel, showing that the heat treatments at temperatures below 1,010°C are favorable to supress the retention of austenite with minimal loss in hardness [227].

Grade 17-4 PH (AISI Type 630) alloy is the most common precipitation hardening martensitic stainless steel, containing 3–4 wt.% Cu content. When heat treated, this alloy forms a fine, copper-rich precipitate phase that is evenly distributed in the matrix of the steel, and which is responsible for increasing the mechanical performance mostly affecting the hardness and UTS [228]. Due to a combination of mechanical and corrosion resistance properties, this alloy has been extensively used for applications in power plants, as well as the marine and chemical processing industries. The mechanical properties of 17-4 PH steel are usually improved by aging heat treatment, however other properties such as the wear resistance and fatigue performance are still somewhat limiting. The aging treatments vary from 480-620 °C, with a peak hardness (48 HRC) achieved when aging at 496 °C for 240 minutes (termed H925 condition, as in 925 °F) and at 621 °C (H1150, as in 1150 °F) for 240 minutes, which also showed the highest elongation (8%). The addition of hard particles such as TiC is therefore expected to increase the wear resistance properties in the final composite [228,229]

In the current study, an appropriate precipitation hardening heat treatment is applied to increase the mechanical properties and consequently, improve the wear resistance of two families of TiC–stainless steel cermets. These TiC cermet compositions were based on either a non-hardening 316L

binder or a hardenable 17-4 PH binder, where 5-30 vol% of binder phase was evaluated in each case comparison. The presented study therefore investigates the influence of the binder phase content and subsequent heat treatments upon the mechanical and densification behaviour, as well as the basic tribological properties of these materials, which is evaluated by scratch testing.

8.2 Materials and Methods

8.2.1 Raw Materials and Processing

The cermets samples in this research were produced using TiC powder (lot no.:45693; particle size = 1-2 μm) from Treibacher Industrie AG (Althofen, Austria), and pre-alloyed 17-4 PH powder (batch: 18D0775; particle size D_{80}: ~5 μm) and 316L powder (batch: 18D0788; particle size D_{80}: ~5 μm), both obtained from Sandvik Osprey Powders (Neath, England). The bulk composition of TiC–steel specimens were produced through a vacuum liquid phase sintering process. Chemical composition analysis of the as-received TiC and steel powders were determined using inductively coupled plasma optical emission spectroscopy (ICP-OES; Model Varian Vista Pro, CA, USA). The results are shown in Table 8.1.

Table 8.1 ICP-OES chemical analysis of the TiC and steel powders used in the present work (in wt.%). C was not measured.

Powder/Elements	**Ti**	**Co**	**Cu**	**Cr**	**Mo**	**V**	**W**	**Nb**	**Mn**	**Ni**	**Fe**
TiC	78.13										
316L		0.10	0.25	17.05	2.30	0.04	0.04	0.02	15.90	10.70	67.98
17-4 PH		0.04	4.30	15.80	0.17	0.04	0.01	0.15	0.80	4.70	71.87

The powder blends, including the TiC and one of the two types of stainless steel (varied from 5 to 30 vol.%), were mixed in 50 g batches with the addition of 0.5 wt.% polyvinyl butyral (PVB) wax, They were then ball milled in acetone for 24 hours at 60 RPM, using yttria stabilized zirconia milling media (Ø = 10 mm), with a 10:1 ratio of mass media/powder. The powder batches were then dried in a fume hood, for a period of 24 hours, and sieved through a -75 μm mesh to eliminate

any large aggregates. The volume ratios of 95-70:5-30 TiC: steel was used for both 316L and 17-4PH based compositions to study the effect of the binder phase volume fractions, and achieve most desirable wear properties following a similar methodology to previous publications [72,73]. The dry sieved powders were subsequently compacted in a uniaxial press with an applied load of 69 MPa (10,000 psi) into discs with 20 mm diameter and 5 mm thick. The compacted discs were then further densified by cold isostatic pressing (CIP) at 207 MPa (30,000 psi), with the pressure held for 30 seconds.

Vacuum sintering was then performed at 1550°C for 60 minutes under a vacuum of 5 x 10^{-4} Torr (model R.D. Webb Red Devil®), with a heating and cooling rate of 20 °C/min. Once the furnace cooled below ~800°C a natural furnace cool arose. The vacuum sintered samples prepared with the 17-4 PH steel binder were than subjected to a solution heat treatment. This was conducted in an air atmosphere box furnace (Thermo Scientific Lindberg/Blue M), at 1040 °C for 30 minutes, in steel heat treatment bags, followed by oil quenching. The samples were then subjected to aging heat treatments, at either 496 °C for 240 minutes (H925 condition) or 621 °C for 240 minutes (H1150 condition), followed by air cooling.

8.2.2 Materials Characterization

The crystallographic characteristics of the initially milled powders and the resultant heat-treated samples were assessed using X-ray diffraction (XRD; Bruker D-8 Advance, Bruker Corp., Billerica, MA, USA). CuKα radiation was used at 40 kV and 40 mA, with 2theta scan angles from 20 - 90°, at 1°/min.

The density of the specimens was determined using Archimedes' principle, in water at 24°C. The weight is recorded on a scale with 1 μg resolution and measurements were repeated three times per sample for accurate statistical value; three samples were tested for each composition. The density of the disks is then calculated following Equation 7.1:

$$p = \left(\frac{MA}{MA-Mw}\right) * p\,W \qquad \textbf{Equation 8.1}$$

where p is Archimedes density, MA is the mass in air, MW is the mass in water and pW is the density of water calculated for a specific temperature.

A series of polishing procedures was used for microstructure analysis, polishing to a mirror like finish down to 0.25μm diamond paste. Initial microstructure evaluation, assessment of the main wear mechanisms, and phase characterization were then performed using optical microscopy (OM; model Olympus BX-51, Tokyo, Japan), scanning electron microscopy (SEM; Model S-4700, Hitachi High Technologies, Inc., Tokyo, Japan) and energy dispersive X-ray spectroscopy (EDS; Inca X-max, Oxford Instruments, Concord, MA, USA), and XRD. The Vickers hardness of the cermets was measured through indenting with a load of 1 kg, as suggested in ASTM 1327 – 15 - Standard Test Method for Vickers Indentation Hardness of Advanced Ceramics and 30kg for comparison. The mean indentation size is then determined using OM. The extent of crack propagation was measured using 30 kg indentation load following the approaches of both Shetty [10] and Anstis [11] using OM.

Measurement of the wear resistance was conducted by scratch testing, using a Universal Micro Tribometer (UMT-1; CETR, Campbell, CA, USA), with a diamond indenter sliding in a linear motion across the polished surface under a known load. To achieve this, a single pass of 5 mm length is undertaken, with speed of 0.166 mm/s; test environment conditions were room temperature (23°C) and a relative humidity from 40-50%. In the scratch test, the load is applied normal to the surface of the sample with a Rockwell diamond indenter, with tip radius of 200 μm. Applied loads of 10, 20 and 30 N were used to generate the scratch tracks. Related data was simultaneously obtained from the UMT through software that provides dynamic numerical values for the depth of the indenter versus the applied force. Moreover, the coefficient of friction can also be extracted through the digital data-acquisition system obtained from UMT equipment. The wear tracks were then evaluated using SEM and a confocal laser scanning microscope (CLSM; Keyence VK-X100K; Keyence Company, Osaka, Japan) to observe the damaged area. The average width of the scratch track, *W*, was subsequently measured using the SEM, and the scratch hardness number, *HSp*, was then determined using the relationship:

$$HS_p = \frac{8P}{\pi W^2} \qquad \textbf{Equation 8.2}$$

where *P* is the applied load and *W* is the scratch width, as noted previously.

8.3 Results and Discussion

8.3.1 Characterization of Cermets

Figure 8.1 shows the as-received and milled powder mixtures used for the preparation of the green compact bodies. It is noted that the TiC particles shown in Figure 8.1(a) are mostly small (in the 1-2 μm range), and with an irregular, angular shape from the milling production process. Conversely, Figure 8.1(b,c) demonstrate that the pre-alloyed 316L and 17-4PH steel powders are largely spherical, ranging from 0.5-5 microns in range due to the production method of gas atomization. It is appropriate to mention that for the objective of this paper, a fine and homogeneous distribution of the steel particles should allow for a high sintered density, without the presence of large voids caused by melting and capillary removal. At the same time, the possibility arises to obtain a fine-scale sintered structure, that favours mechanical properties such as yield, fatigue strength and impact toughness [32].

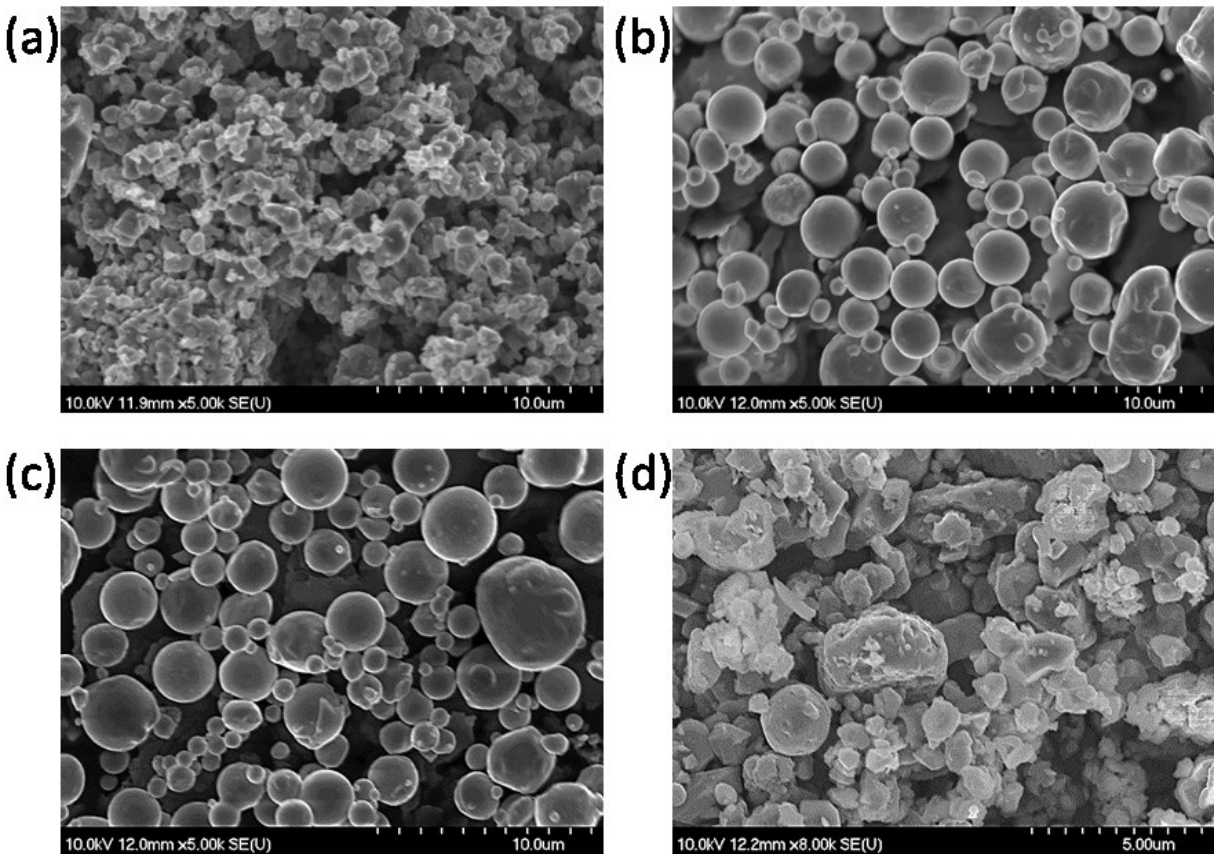

Figure 8.1 Representative SEM of the individual powders (a) TiC (b) pre-alloyed 316L (c) pre-alloyed precipitation hardening 17-4 and (d) as-milled TiC – 316L powder blend.

The mass transfer and densification behaviour of these materials are mostly associated with high diffusion rates, due to melting of the metallic binder phase, which occurs at 1390-1440°C for the 316L and 1404-1440°C for 17-4 PH [231]. At these temperatures, liquid phase sintering arises via partial dissolution-reprecipitation of the TiC phase within the microstructure, which allows densities to be achieved that are close to theoretical [36]. This mechanism of sintering usually causes slight coarsening of the microstructure. In the present case the TiC grains start with a mean particle size of ~1.25 μm [232]. Coarsening during sintering then leads to final TiC grains with a mean size of 3.14 (± 0.89 μm) for the 316L steel and ~3.27 (± 1.14 μm) for the 17-4 PH steel.

The degree of densification of the samples, according to the binder composition and volume content, is presented in the Figure 8.2. The reduction in free-energy acts as a driving force for sintering, causing the transition of small grains into larger ones and elimination of porosity [233]. For both binder compositions, a significant amount of residual porosity was present when only 5 vol.% of the binder is used; this resulted in ~10 vol.% porosity for the 17-4 PH steel, compared with ~4 vol.% porosity for the 316L stainless steel binder. This result is also confirmed by the correspondent microstructures shown in Figures 8.3(a) and 8.4(a). Conversely, a significant improvement in the densification is observed for the samples with 10 vol.% of binder (and higher) for both steel grades (Figure 8.2). In these cases, the sintered densities achieved >99% of the theoretical values.

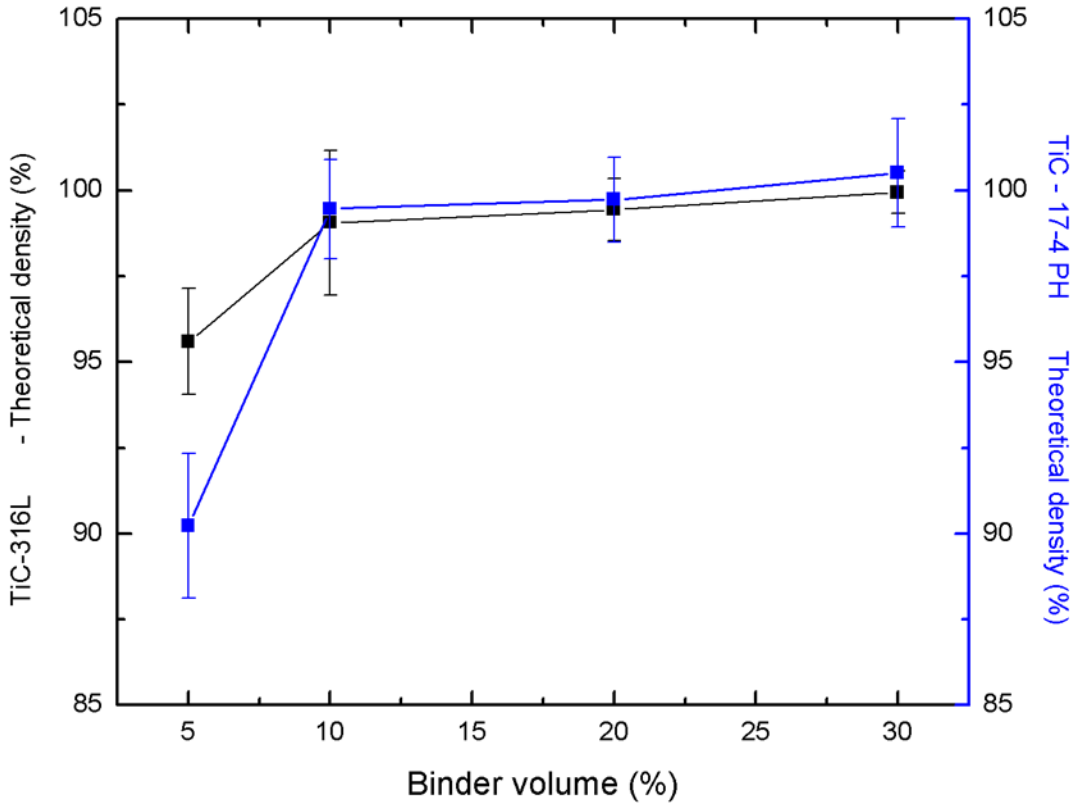

Figure 8.2 The densification behaviour of the sintered samples as a function of the binder volume content of 316L and 17-4PH.

Figure 8.3 and 8.4 show the resultant microstructures for the sintered samples using the two respective steel binders, 316L and 17-4 PH, varied from 5-30 vol%. The light gray phase highlights the steel metallic phase in each case, while the dark gray particles show the TiC phase. For both samples prepared with 5 vol.% steel binder, it is possible to observe localized porosity, which is ~5 μm in size. Significant densification is observed for samples with the higher binder contents, with less than 0.1 vol.% porosity.

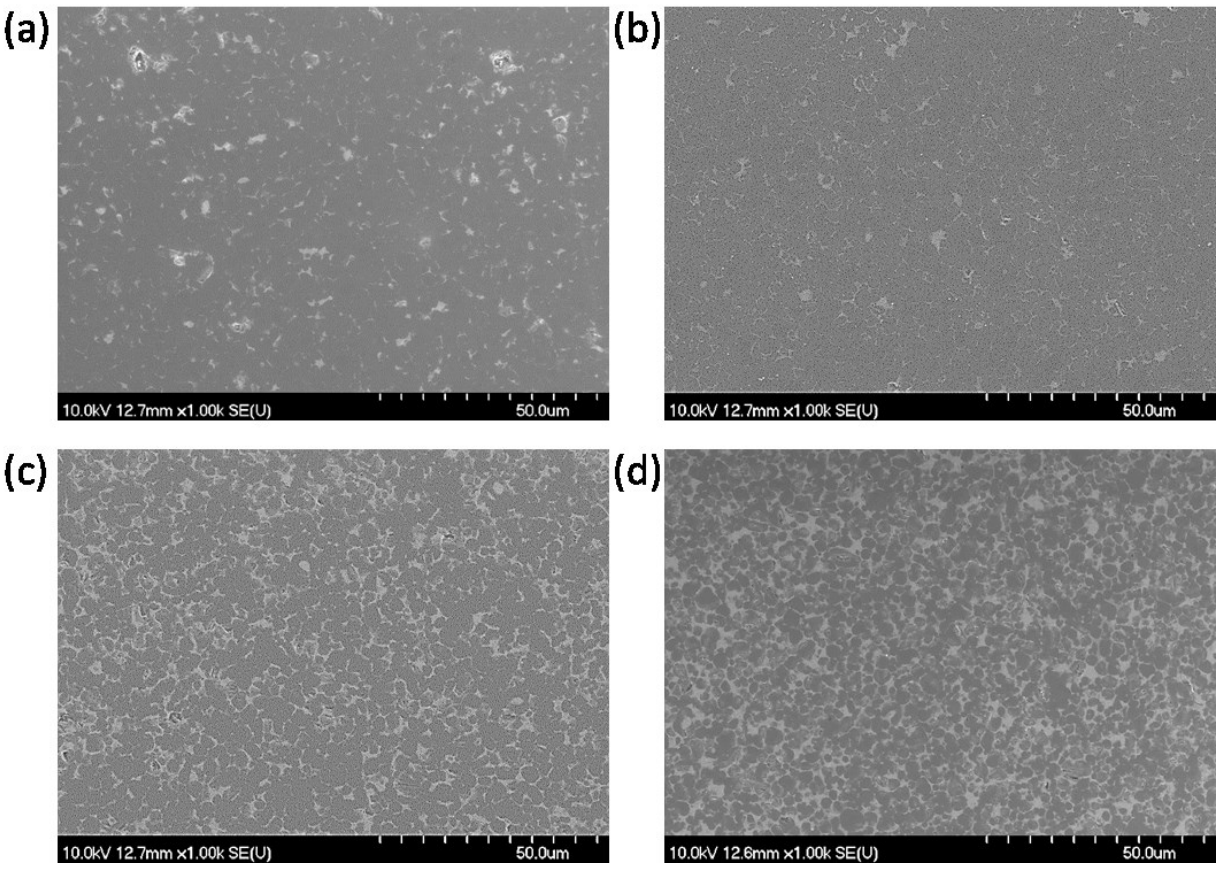

Figure 8.3 Representative SEM of sintered samples (a) TiC 5 vol% 316L (b) TiC 10 vol% 316L (c) TiC 20 vol% 316L and (d) TiC 30 vol% 316L.

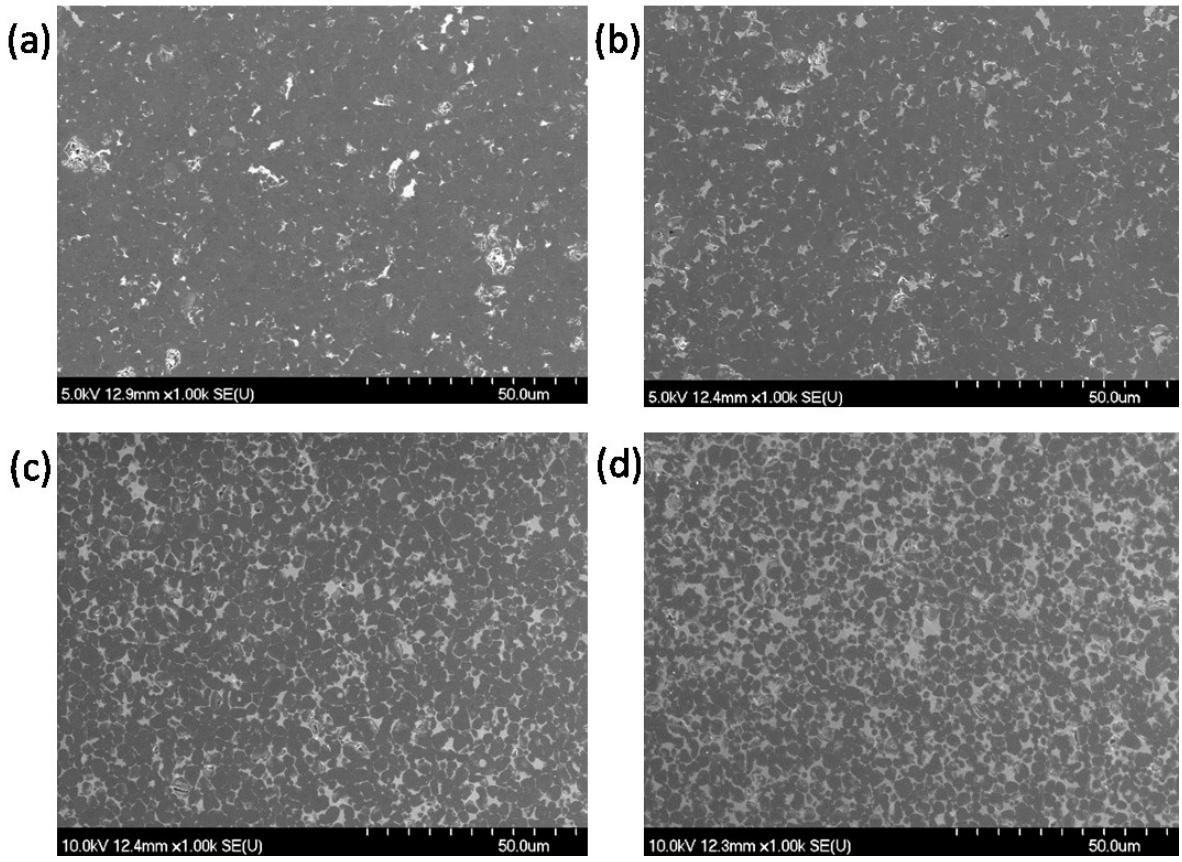

Figure 8.4 Representative SEM of TiC 17-4 PH sintered samples with varying steel contents: (a) 5 vol.%, (b) 10 vol.%, (c) 20 vol.%, and (d) 30 vol.%.

For the TiC-316L samples, as has been observed in previous studies [73,234], the formation of a "core-rim" structure occurs during the sintering treatment, with a dark-gray contrast "core" of TiC surrounded by light-gray "rim" that is shown in the Figure 8.5. The EDS line scan crossing a TiC grain can be seen in Table 8.2, with the respective chemical composition in the following table. No presence of any core-rim was observed for the samples using 17-4 PH steel as the binder.

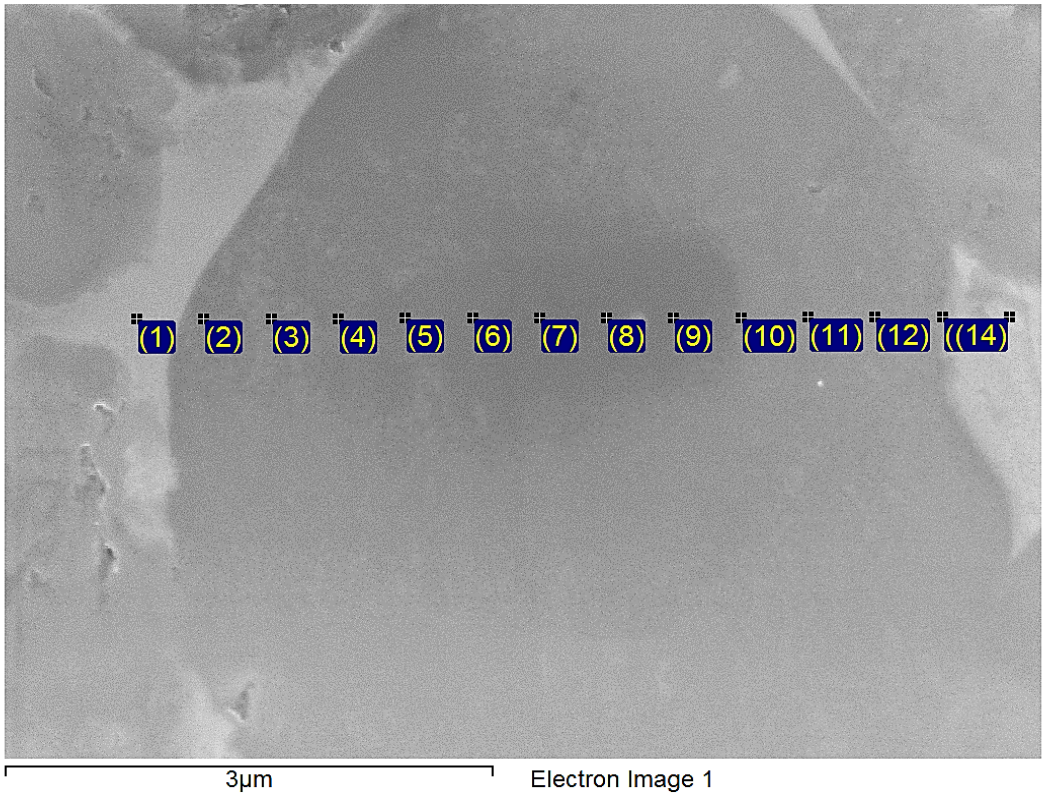

Figure 8.5 Representative SEM of TiC 17-4 PH sintered sample with 30 vol.%. Observe the core-rim structure. Table 8.2 has the spectrum the corresponds to this figure.

Table 8.2 Results of EDS analysis of the core-rim structure shown on Figure 8.5.

Spectrum	C	Ti	Cr	Mn	Fe	Ni	Mo
1	16.83	20.18	42.14	0.76	19.07	0.38	0.64
2	18.55	24.29	39.06		18.1		
3	24.43	68.48	4.81		2.29		
4	24.91	75.09					
5	25.15	74.85					
6	25.57	74.43					
7	25.72	74.28					
8	24.97	75.03					
9	25.1	74.9					
10	25.11	74.89					
11	24.65	75.35					
12	25.44	74.56					
13	26.27	73.73					
14	17.55	25.74	3.98		45.52	6.14	1.07

XRD-based phase identification for the powders and reacted phases following sintering are presented in Figure 8.6. The resultant peaks relating to (nominally) stoichiometric TiC powders are observed on the diffraction patterns, namely (111), (200), (220), (311) and (222). Both as-received steel powders show quite dissimilar peaks, with the 17-4PH powders showing the presence of two α-Fe (ferrite) peaks at (110) and (200). On the other hand, 316L shows both (α)-ferrites peaks and (γ)-austenite phases at (111), (200) and (220). When sintered, the same phases are present according to the X-ray diffraction spectrum, only changing in terms of the peak intensity.

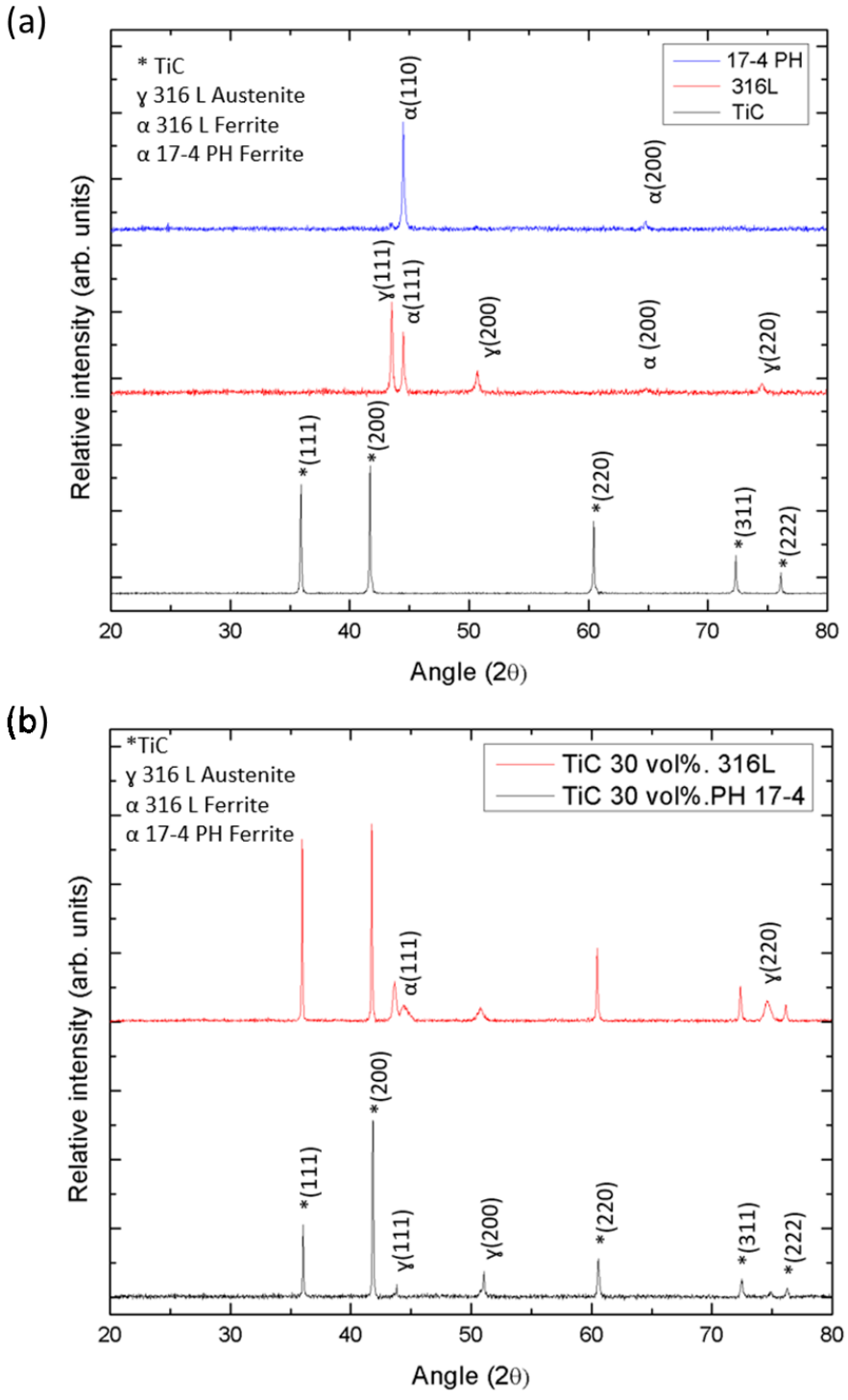

Figure 8.6 XRD spectrum related to: (a) the individual as-received powders; (b) the sintered TiC - 30 vol.%316L and TiC - 30 vol.% 17-4 PH cermets.

The solution heat treatment was performed at 1040 °C and quenched into oil followed, by an aging heat treatment under one of two conditions: (i) 4 hours at 496 °C (H925), and (ii) 4 hours at 621 °C (H1150). The H925 and H1150 precipitation conditions allow the steel binder to have a fine structure, with BCC Cu-rich precipitates, which are observed in conjunction with the increase of the γ-austenite phase according to the XRD diffraction patterns in Figure 8.7 [235]. The H1150 condition shows a higher γ-austenite peak intensity, allowing the austenite grains to increase in their mean size. Based on the literature, the H925 condition gives the highest hardness and strength due to a finer scale microstructure, when compared to H1150 condition, where the energy and time given by the heat treatment allow the further growth of the precipitates and transition of the lattices to an α-FCC structure [229,235].

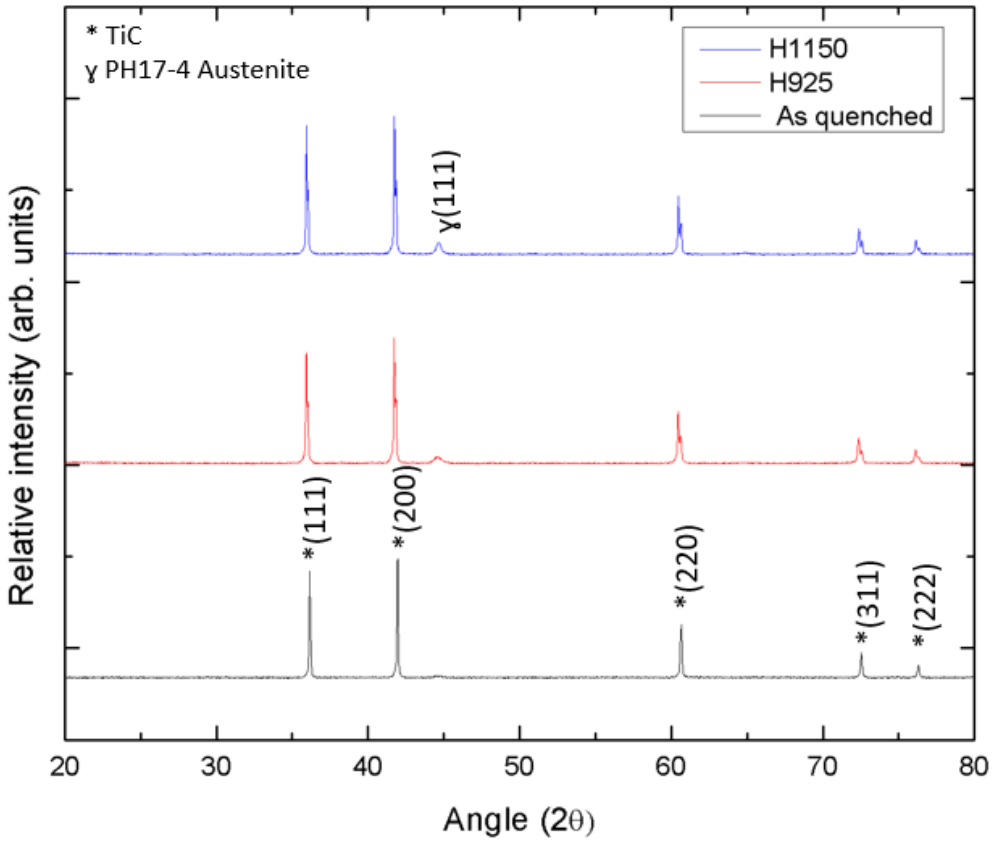

Figure 8.7 XRD spectrum related to TiC-30vol%. PH 17-4 for samples "as quenched", conditioned at H925 and H1150.

8.3.2 Mechanical and Wear Response

When measuring the Vickers hardness of cermets, it is important to undertake a few considerations about these materials [163]. Cermets tend to be hard and brittle materials, so at high loads the energy is going to be dissipated by the generation of cracks, reducing the overall measured hardness value (as a portion of the imparted energy is consumed in generating the cracks). The series of hardness experiments shows aspects of the properties of both the binder and carbide phases, which can be significantly affected by factors such as the chemical and mechanical properties of the sintered carbide/metal interface, residual stresses between phases, crystal structure, and the size and shape of carbide grains [20,77,161,162]. In the case of the "quenched" samples, the residual stress is going to be a significant variable, due to the high cooling rate and the high degree of thermal coefficient mismatch of TiC (α = 7 x $10^{-6}/K^{-1}$) and steel (α = 13 x $10^{-6}/K^{-1}$).

The measured Vickers hardness using 1 and 30 kg loads, as a function of the differing volume fractions of 316L or 17-4 PH steel, are shown in Figure 8.8. As noted in previous publications [1,236], the Vickers hardness decreases in a nominally linear manner as the volume content of the binder phase is increased up to some upper limit. In the case of the present TiC-316L cermets, the measured hardness decreases from 2600 HV1 at 5 vol.% binder down to 1600 HV1 at 30 vol.% binder. The same behaviour and trend are observed with the 17-4 PH steel, however starting with a slightly lower hardness, at 2500 HV1 at 5 vol% binder and decreasing to 1200 HV1 at 30 vol%. The minor difference in hardness between the 316L and 17-4 PH arises from the difference in alloying elements, where the 316L has 14 wt.% Ni when compared to 4 wt.% in the 17-4 PH, which is a common additive to increase strength and hardness without sacrificing ductility and toughness [237]. The higher molybdenum content is also responsible for the higher as sintered hardness of 316L when compared to 17-4 PH [235,237].

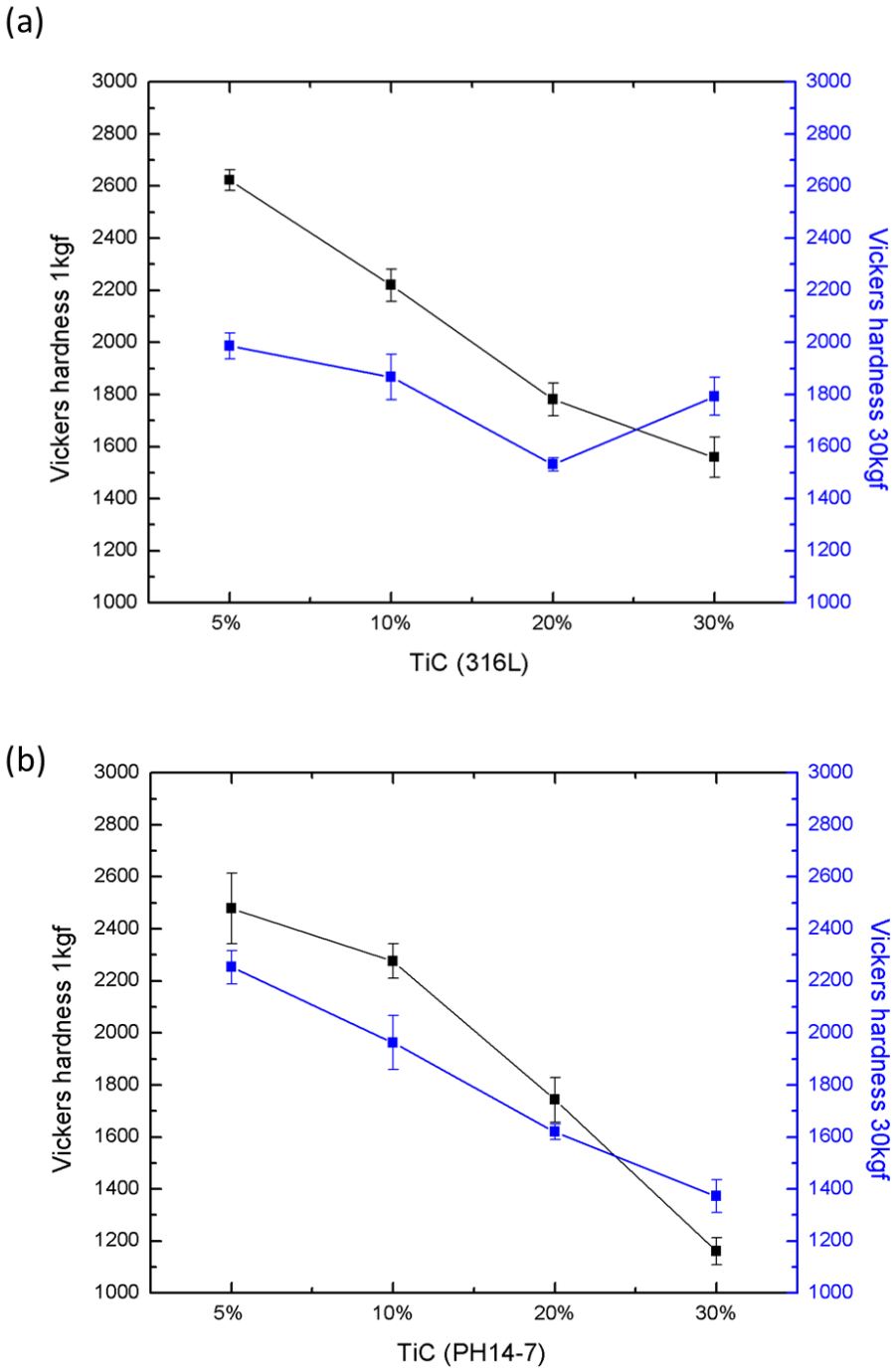

Figure 8.8 Vickers hardness measurements related to as-sintered (a) TiC-316L and (b) TiC-PH17-4 cermets.

The resultant Vickers hardness and the effect of the heat treatments on the TiC-17-4 PH cermets is shown in Figure 8.9. Samples with less than 20 vol.% of binder exhibited catastrophic thermal shock during the oil quenching treatment (OQ), so it was not possible to measure the hardness. Figure 8.8 shows that, when the samples with 20 vol.% were submitted to the various heat treatments, a small change in hardness was observed, from 1740 HV1 to 1765 HV1 when conditioned at H925. On the other hand, the sample with 30 vol.% showed a significant increase in hardness during the quenching heat treatment, due to the carbon trapped inside the austenite lattice [238], resulting in a significantly harder and more brittle material.

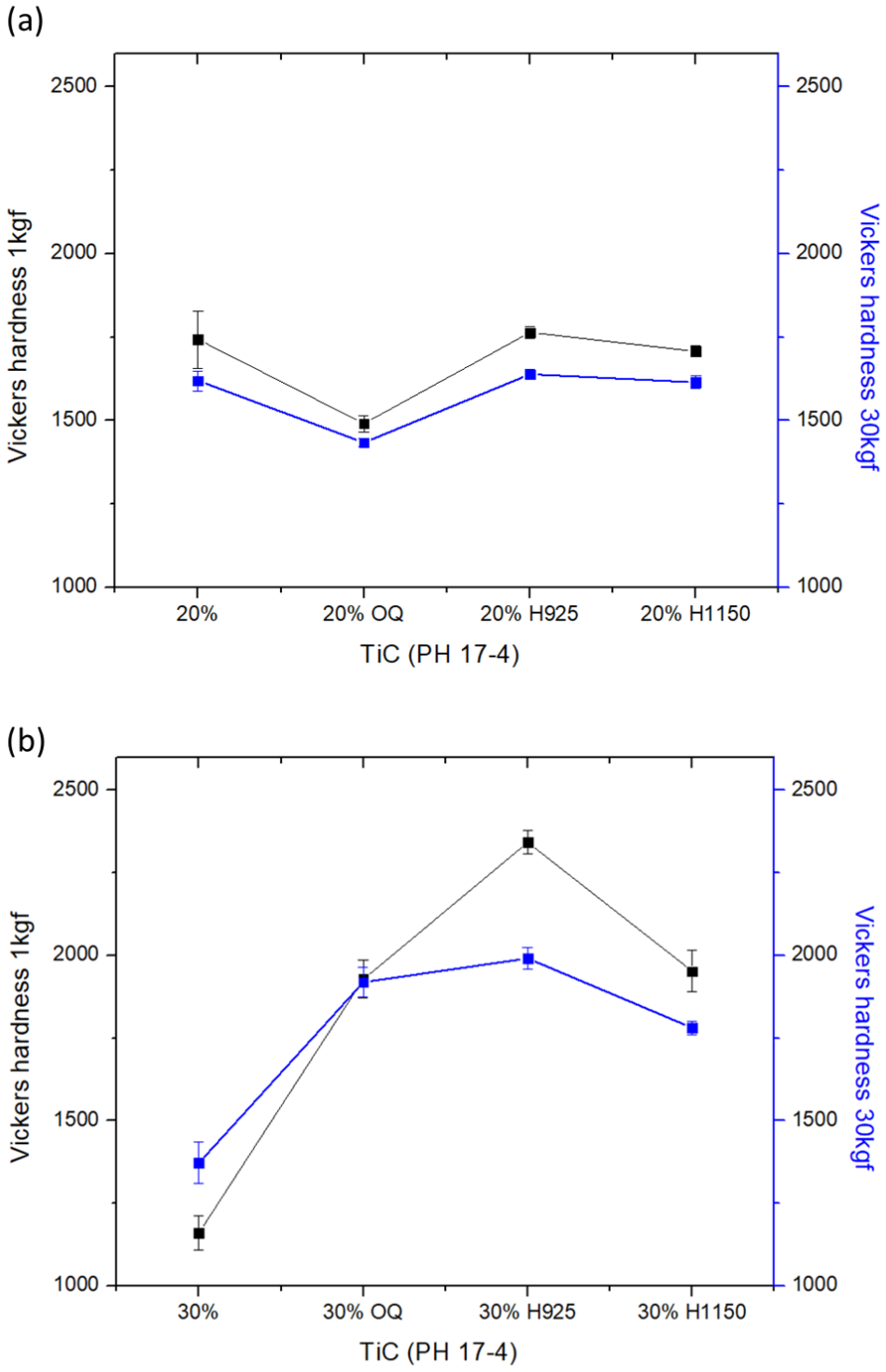

Figure 8.9 Vickers hardness measurements related to the heat-treated TiC-17-4 PH with (a) 20 vol.% and (b) 30 vol.% binder.

As can be observed in Figure 8.10, there is also a measurable reduction in the indentation fracture resistance as a secondary effect of the heat treatment, however based on the c:a ratio, cracking response is still in the Shetty region [115], particularly for the samples with higher binder content. Although yet to be evaluated, it is expected that the as-quenched samples would present a larger component of residual stress between the TiC and steel phases when heat treated. For instance, comparable cermet consituents, such as TiC and Ni_3Al has shown up to 1.6 GPa of residual stress for both TiC under compression and Ni_3Al under tension [239]. Close values might be expected for the TiC-steel composite when "as-sintered", due to its broadly similar thermal expansion coefficient ($\alpha = 13 \times 10^{-6}/K^{-1}$) when compared to ($\alpha = 12.5 \times 10^{-6}/K^{-1}$) for Ni_3Al. The magnitude of the residual stress reaches its peak in the quenched samples, where the cooling rates are approximately 50 °C/s [240]. This is due to martensite formation, which is a brittle phase, resulting in the lowest fracture resistance.

The elastic modulus and hardness of the TiC based cermets are strongly related to the binder volume content [1,8]. As the volume binder content increases, there is a tendency for the cermet to become less hard and more tough. Moreover, the best wear resistance can often found be between 25-40 vol.% of binder [168], highlighting the subtle complexity of projecting wear response solely on hardness. A transition to a more brittle behavior, in conjunction with a decrease in IFR, is noted at low binder content for the non-heat-treated samples. The transition from median/radial cracking to Palmqvist cracks is shown when the binder volume is increased from 5-10 vol% steel content for all the compositions.

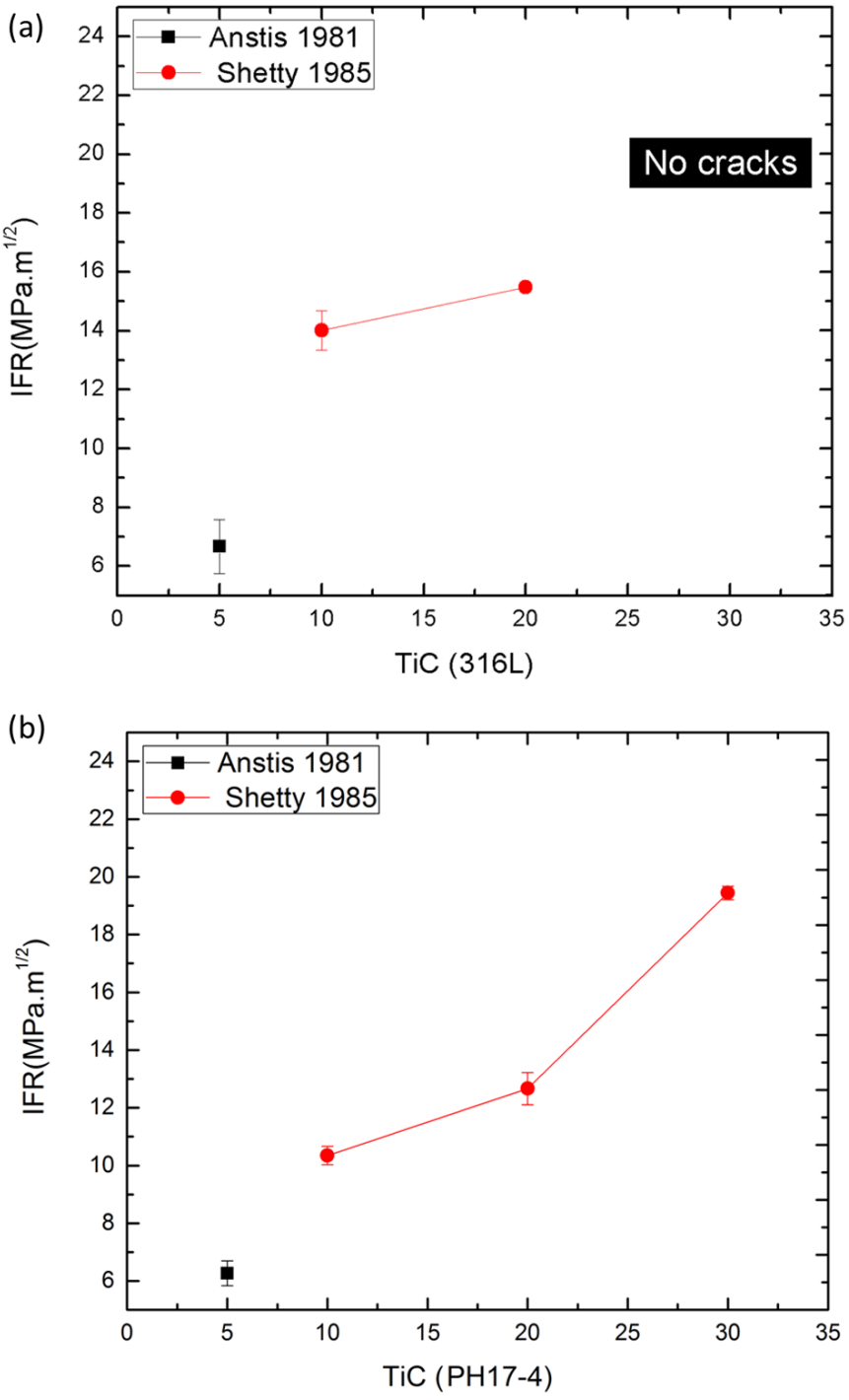

Figure 8.10 Calculated Indentation fracture resistance of TiC-stainless steel cermets as-sintered. Samples show a transition from median/radial to Palmqvist cracking behaviour. (a) TiC with 5-30 vol.% 316L binder and (b) TiC with 5-30 vol.% 17-4 PH steel binder.

The extent of the effects heat-treatment on the hardness and toughness of the TiC cermets behave in a similar matter, where the mechanical properties are minimally affected for 20 vol. % steel binder, however when the binder volume is >20% vol there is a significant effect. A slight reduction in toughness from ~13 to 12 MPa.$m^{-1/2}$ is observed in 20 vol. % steel binder specimens after heat treatment when compared to the as-sintered condition. As for the specimens with 30 vol%, the embrittlement effect is more significant when the sample is quenched; this is attributed to the formation of martensite in the binder. The minimum toughness is coincident with the maximum hardness, which shows an almost stable condition when heat treated at H925, and some recovery from 13.5 to 15 MPa.$m^{-1/2}$ when processed under the H1150 condition [227,241].

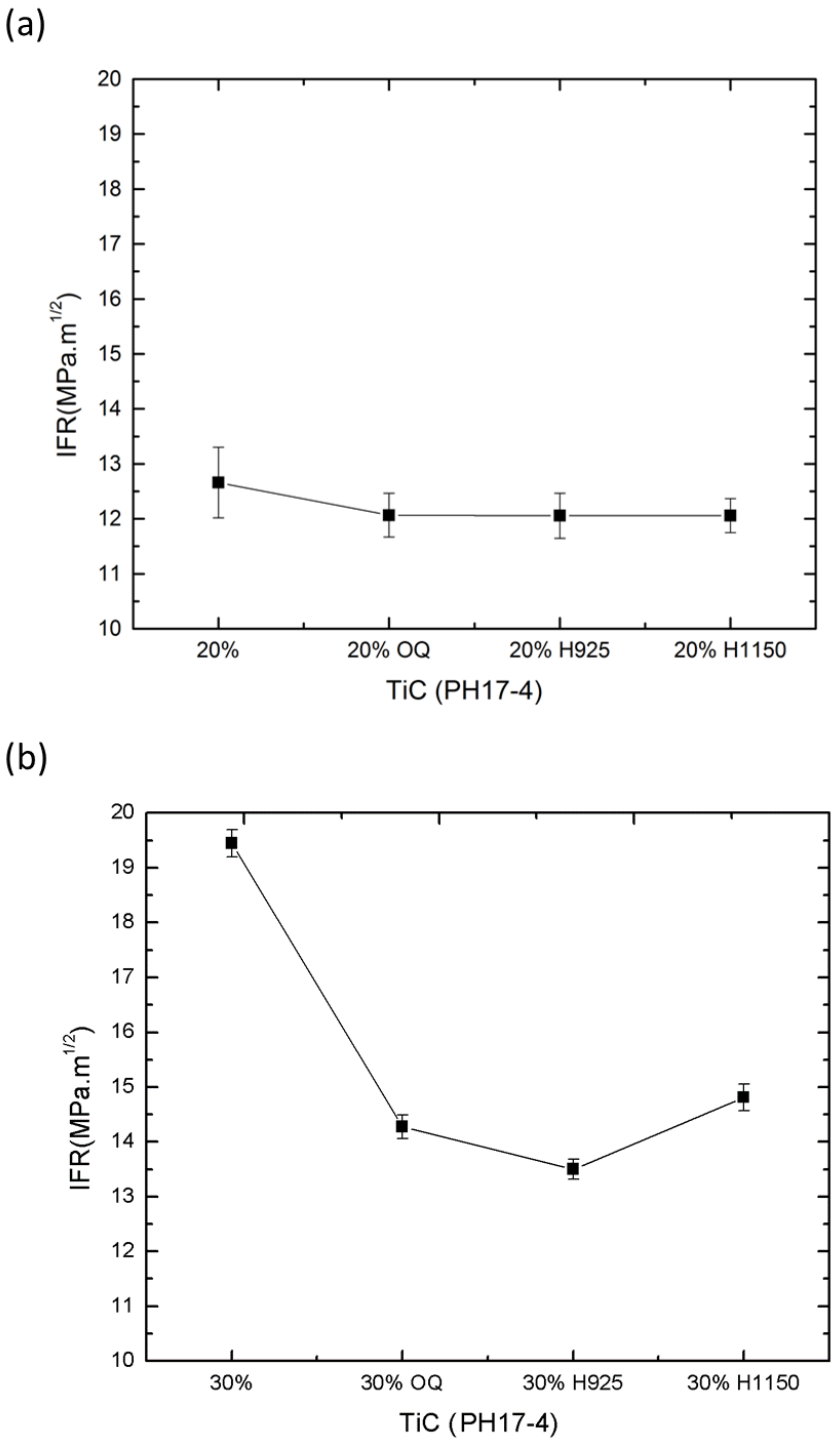

Figure 8.11 The calculated IFR for TiC-17-4 PH following precipitation hardening when heat treated. Samples show a transition from Palmqvist to Median/Radial cracks behaviour. (a) TiC 20 vol.% 17-4 PH and (b) TiC with 30 vol.% 17-4 PH.

8.3.3 Wear Behaviour

The scratch depth of the evaluated TiC cermet samples is shown in Table 8.3 as a function of composition and the applied load. The corresponding 3D CLSM images and cross-section profiles of selected samples are shown in Figure 8.11-16. It is possible to observe a linear trend; as the applied load increases, the scratch penetration is deeper and wider, in combination with a larger scratch 'edge build up'. It can be observed that for 20 and 30 vol.% 17-4 PH steel binder, even though the peak hardness occurs with the H925 heat treatment, the H1150 shows better scratch resistance possibly due to a more favourable combination of hardness and fracture resistance [242,243].

Table 8.3 Scratch depth according to different compositions and applied load (SD is the standard deviation).

Composition/Loads	10N	SD	20N	SD	30N	SD
TiC-316L						
5 vol.%	0.66	0.13	0.69	0.14	0.77	0.12
10 vol.%	0.444	0.18	0.839	0.12	1.109	0.17
20 vol.%	0.934	0.21	1.194	0.08	1.786	0.09
30 vol.%	1.36	0.17	1.961	0.18	2.722	0.12
TiC-PH17-4						
5 vol.%	0.737	0.15	0.988	0.12	1.08	0.12
10 vol.%	0.392	0.12	0.461	0.15	0.999	0.14
20 vol.%	0.556	0.19	0.711	0.18	1.296	0.19
30 vol.%	0.96	0.14	1.3	0.09	1.74	0.21
TiC-PH17-4 Heat treated						
20 vol.%	0.556	0.15	0.711	0.17	1.296	0.12
20 vol.% OQ	0.672	0.21	0.874	0.09	1.15	0.19
20 vol.% H925	0.697	0.24	0.812	0.12	1.372	0.13
20 vol.% H1150	0.881	0.12	1.071	0.14	1.513	0.15
TiC-PH17-4 Heat treated						
30 vol.%	0.96	0.13	1.3	0.12	1.74	0.14
30 vol.% OQ	0.352	0.1	0.647	0.16	0.82	0.16
30 vol.% H925	0.499	0.14	0.742	0.1	0.932	0.18
30 vol.% H1150	0.321	0.19	0.617	0.19	0.806	0.12

A smaller edge build up is observed outside of the scratch zone for samples with the lower binder contents, due to the lower degree of plasticity. In Figure 8.12, it is possible to observe only up to

0.3 µm of edge buildup on the scratched sample at 30 N with 5% binder when compared to 1.3 µm when submitted to the same load with 30 vol% binder.

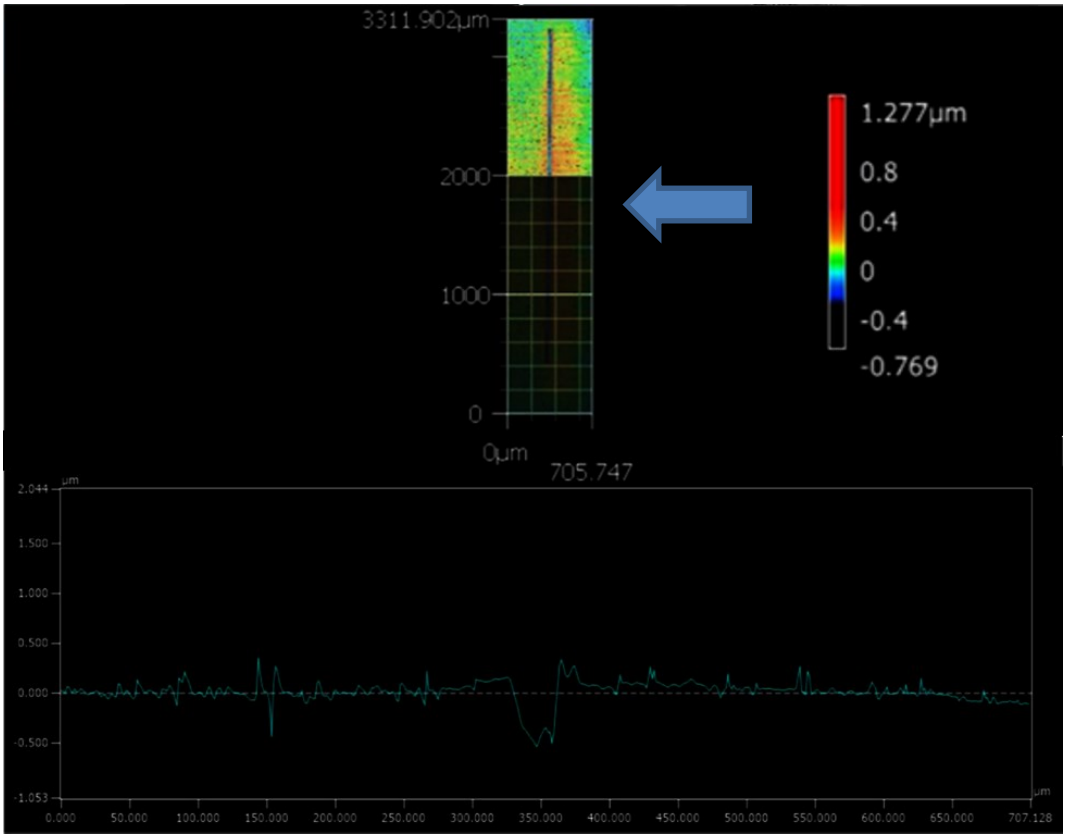

Figure 8.12 CLSM image of a representative scratched surface of the TiC-5 vol.% 316L binder under 30 N applied load. The 3D image is represented on the top with the respective scratched 2D profile on the bottom of the image representing the center line highlighted by the blue arrow.

When the cross-sectional shape of the scratch track is observed for the sample TiC-5vol%316L (Figure 8.12), high angles and "spikes" are seen inside the scratch track in the samples with higher carbide contents, suggesting a brittle fracture mechanism is dominant. In comparison, a more "rounded" scratch cross-section arises when the binder content is 30 vol.% as shown in the Figure 8.13. The increasingly smooth and more "spherical" shape indicates that the material has a significant capacity for plastic deformation due to the higher binder phase content [244]. The changes in width and depth of the wear track are also clearly visible, changing from the mean value of 2.72 of scratch depth to 0.77 µm, with a width reduction from 60 to 45 µm, on average, as the binder content was decreased from 30 to 5 vol.%.

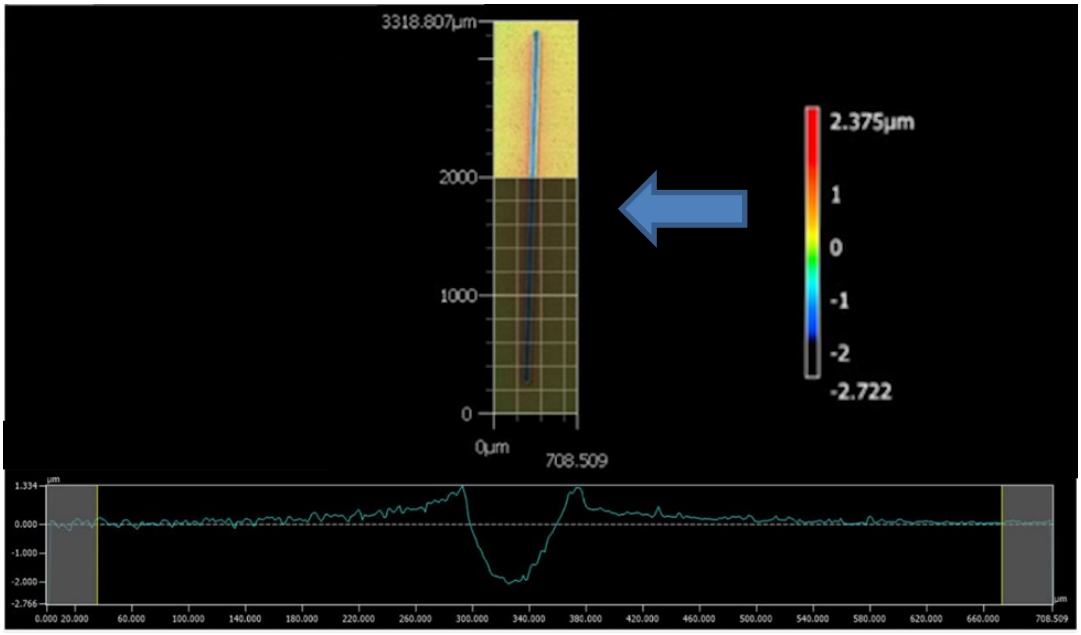

Figure 8.13 CLSM images of a representative scratched surface of a TiC - 30 vol.% 316L binder, with 30 N applied load. The 3D image is represented on the top with the respective scratched 2D profile on the bottom of the image representing the center line highlighted by the blue arrow. Note the edge build up around the scratch track.

Similar behaviour is seen on the samples as sintered samples using 17-4 PH (Figure 8.14), however with the lower binder content (5 vol.%) arguably shows a slightly more rounded profile compared to Figure 8.12, and there is then a further transition to a more rounded/angular scratch profile with higher binder contents (Figure 8.14). For the TiC-17-4 PH cermets, the width and depth of the wear track change from a mean value of 1.74 of scratch depth at 30 vol.% binder down to 1.08 µm at 5 vol.% binder, with a similar width reduction from average values of 66 to 45 µm for the same samples.

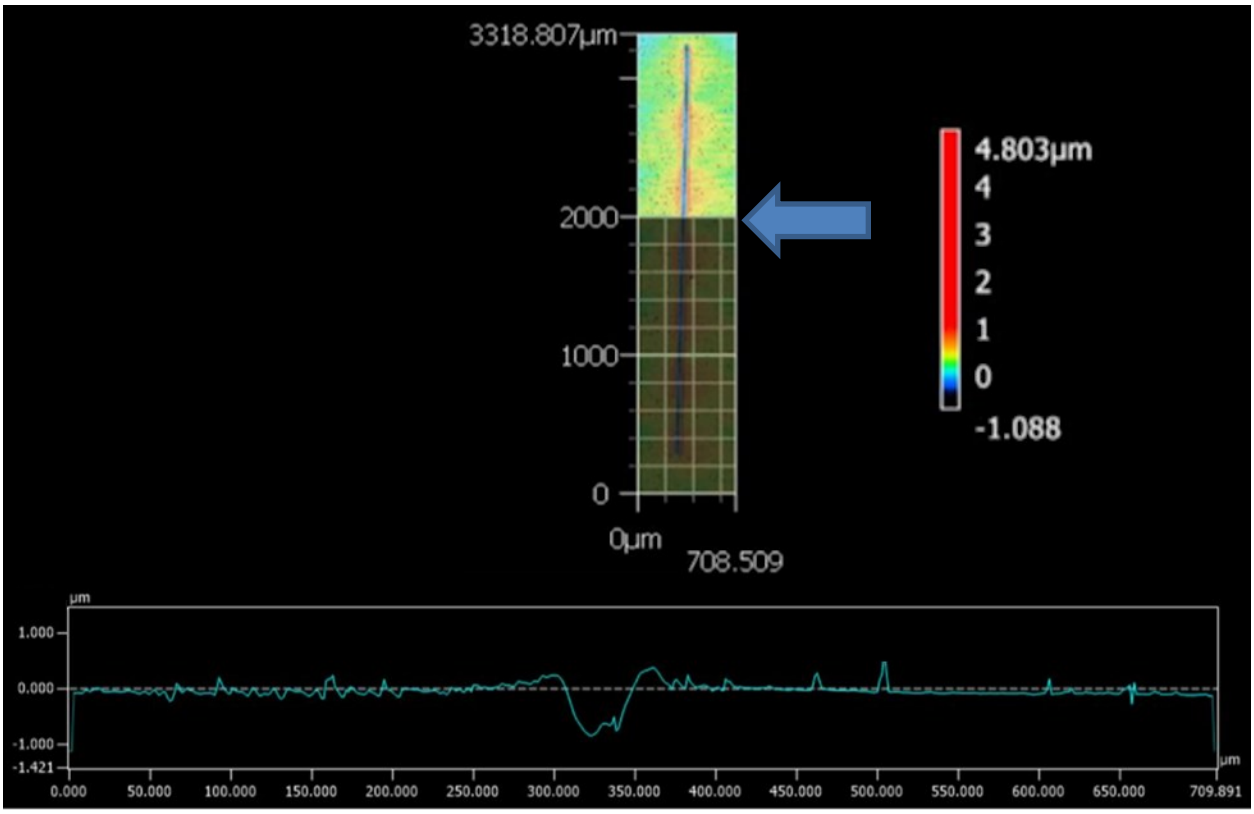

Figure 8.14 CLSM images of a representative scratched surface of the as sintered TiC-5 vol.% 17-4 PH binder cermet, with 30 N applied load. The 3D image is represented on the top with the respective scratched 2D profile on the bottom of the image representing the center line highlighted by the blue arrow.

A direct comparison between the 'as-sintered' 316L and 17-4 PH steel binders shows that, for the 'as-sintered' materials, the TiC-316L cermet showed a better scratch resistance at a fixed binder content. However, a larger extent of brittle fracture occurred when compared to the samples with the 17-4 PH steel binder.

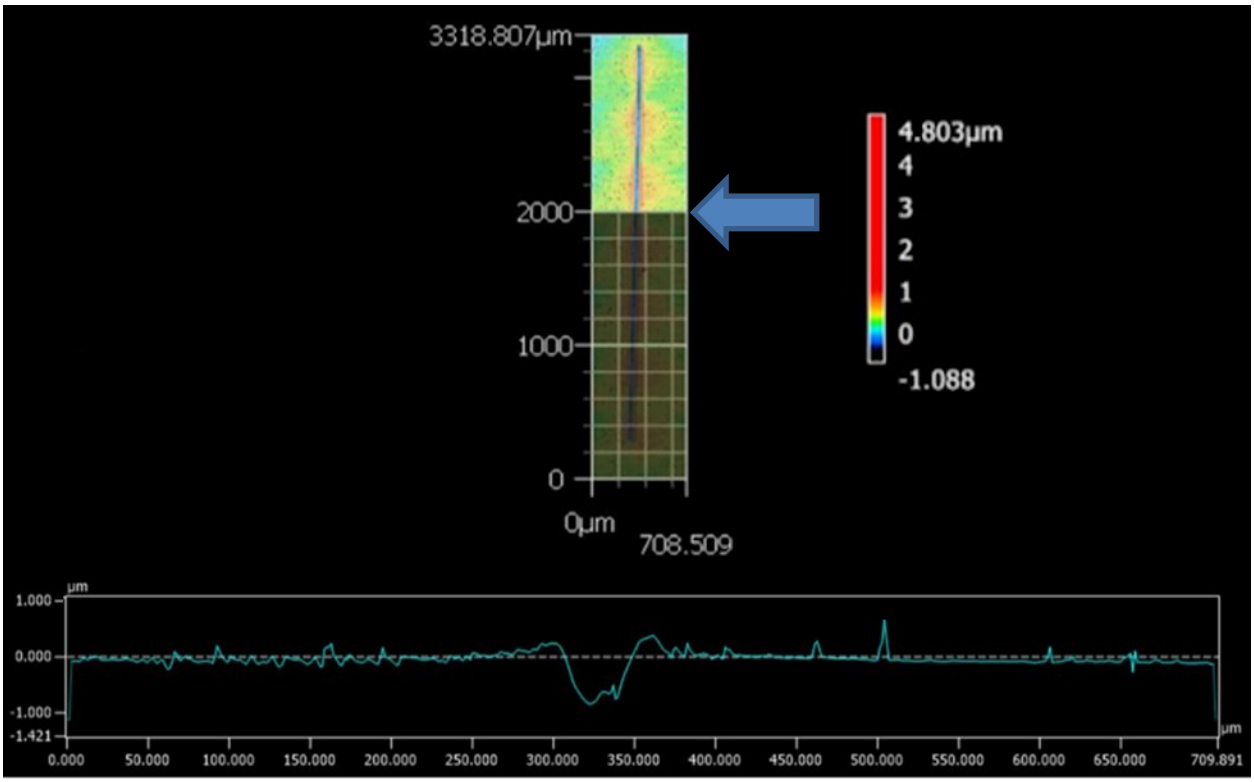

Figure 8.15 CLSM images of a representative scratched surface of the TiC cermet with 30 vol.% 17-4 PH steel binder, using 30 N applied load.

The overall highest scratch resistance, and therefore nominal wear resistance, was obtained from the sample containing 30 vol% 17-4 PH steel, when heat treated under the H1150 condition. As can be observed in Figure 8.16 and Table 8.3, this sample shows an average 0.80 µm scratch depth, with a scratch width of 35 µm. A low level of edge build up is noted for these scratches, being 0.3 µm on average.

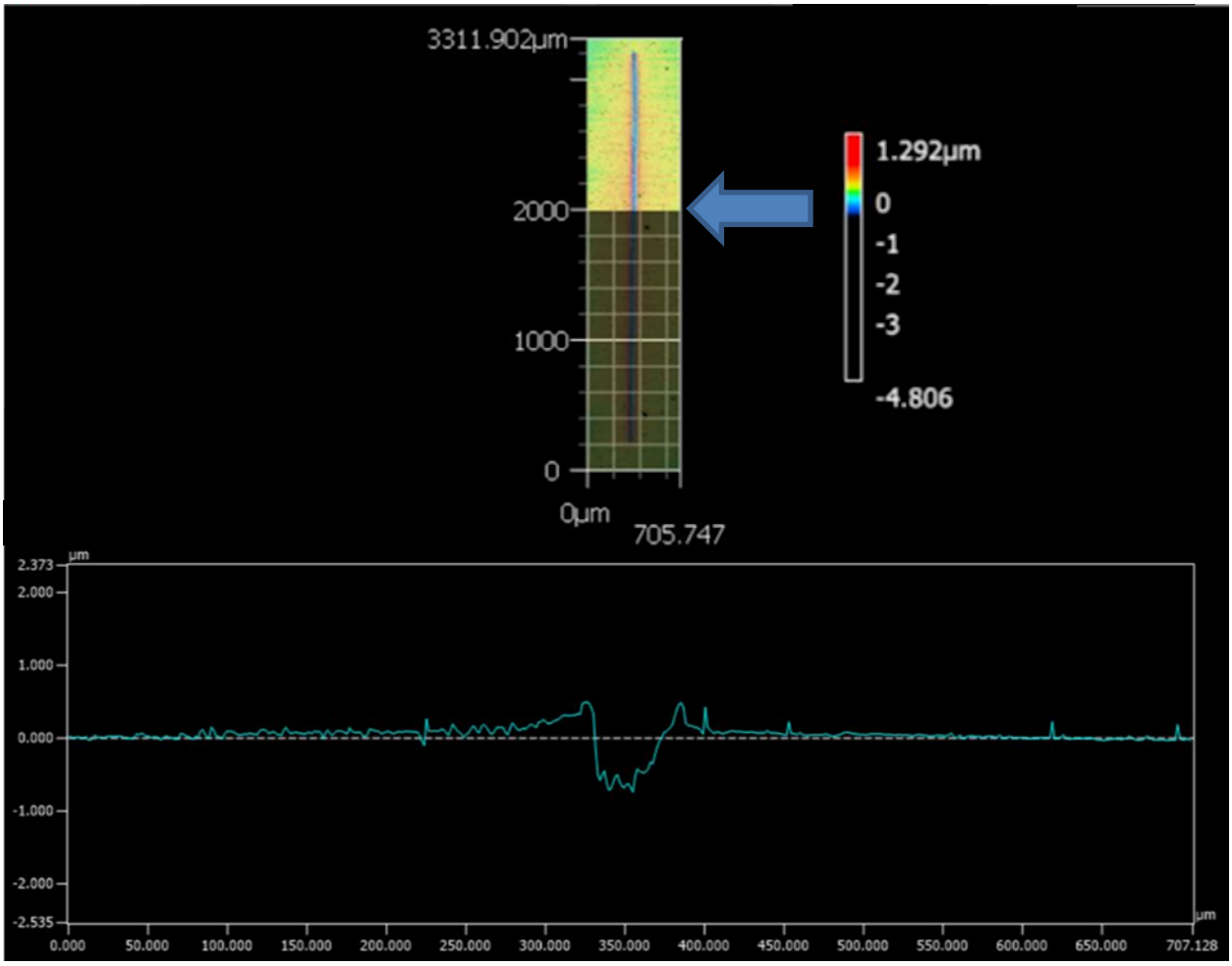

Figure 8.16 CLSM images of a representative scratched surface of the TiC cermet with 30 vol.% 17-4 PH steel binder, after a final heat-treatment at H1150 with 30 N applied load. The 3D image is represented on the top left and the scratched 2D profile is shown on the bottom of the image (upper right-hand side), representing the centerline highlighted by the arrow.

Example SEM images that demonstrate the extent of microstructural damage induced after scratch testing in various samples, using a 30 N indentation force, are shown in Figures 8.17-19. The images confirm the previously presented results obtained by CLSM. Figure 8.17 (a) shows the scratch width and corresponding scratch hardness measured for the TiC-30 vol.%316L steel cermet specimens. A "micro-cutting" line and ploughing wear mechanisms are observed in the center of the scratch track, possibly where the *"tip"* of the diamond indenter was located. Some plastic deformation is also shown in the center of the wear track, confirming that the material shows a high fracture resistance when submitted to a dynamic load test [68,245].

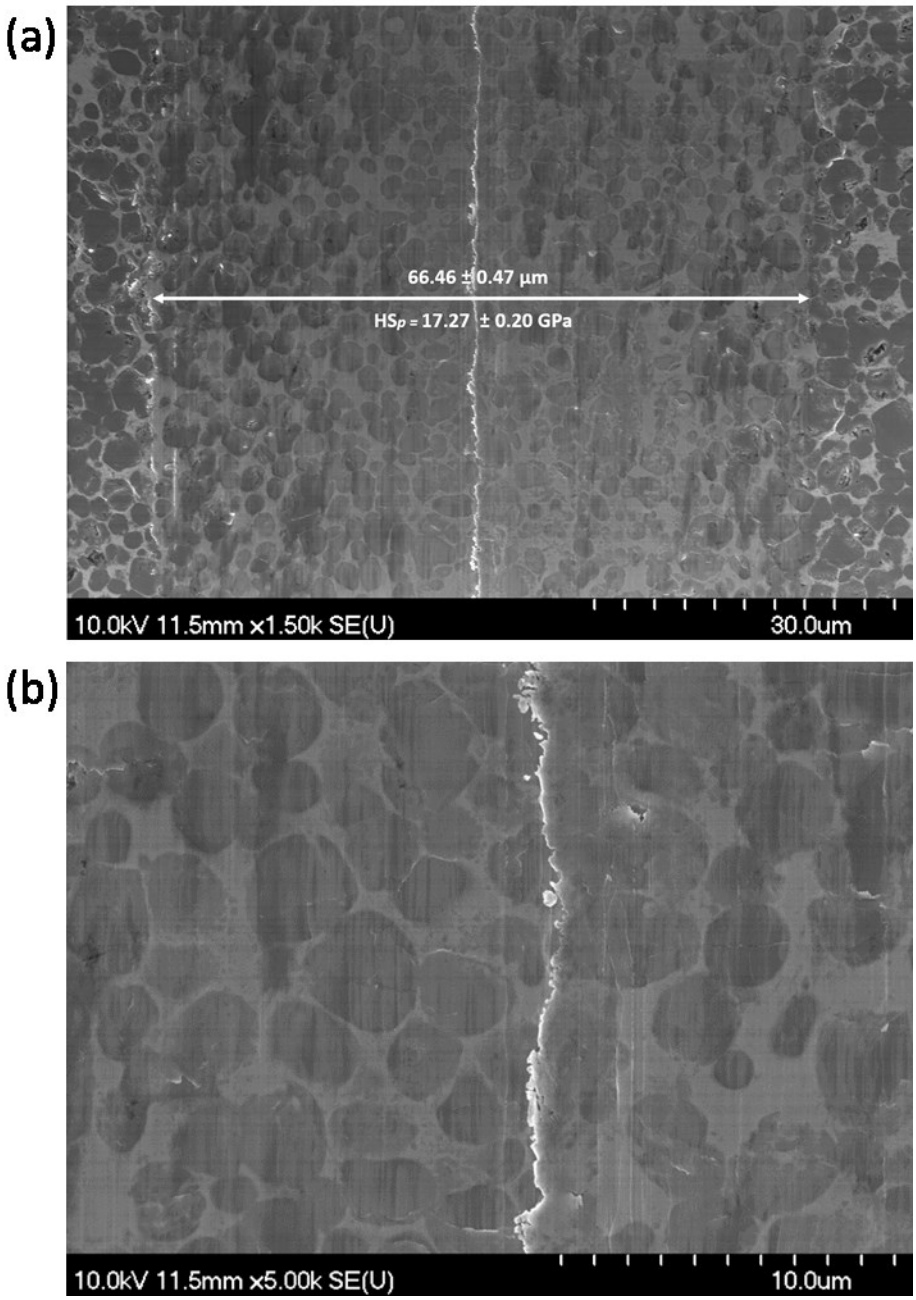

Figure 8.17 SEM images of the scratch track surfaces, indicating the width and scratch hardness of the tracks created using a Rockwell diamond indenter, with an applied load of 30 N: (a) TiC-30 vol.% 316L steel cermet showing the mean scratch width (and associated standard deviation error) and damaged surface and (b) Higher magnification image of the same sample.

For the specimens using 17-4 PH steel as the binder phase, a higher degree of micro-cutting and micro-grooving is present, as shown in Figure 8.18. No grain fracture or grain pullout was observed

for any of the steel-based cermet compositions, although this is a common wear mechanism for cermets, which is indicative of a strong interfacial bond between the TiC grains and steel binder [246]. A slight increase in scratch resistance is observed when 17-4 PH steel is used as a binder phase when compared with 316L, which supports the theory that the wear resistance is not directly proportional to the hardness since the TiC-30 vol.% 316L cermet shows a better Vickers hardness (1600 HV1) when compared with TiC 30 vol.% 17-4 PH steel cermet (1200 HV1).

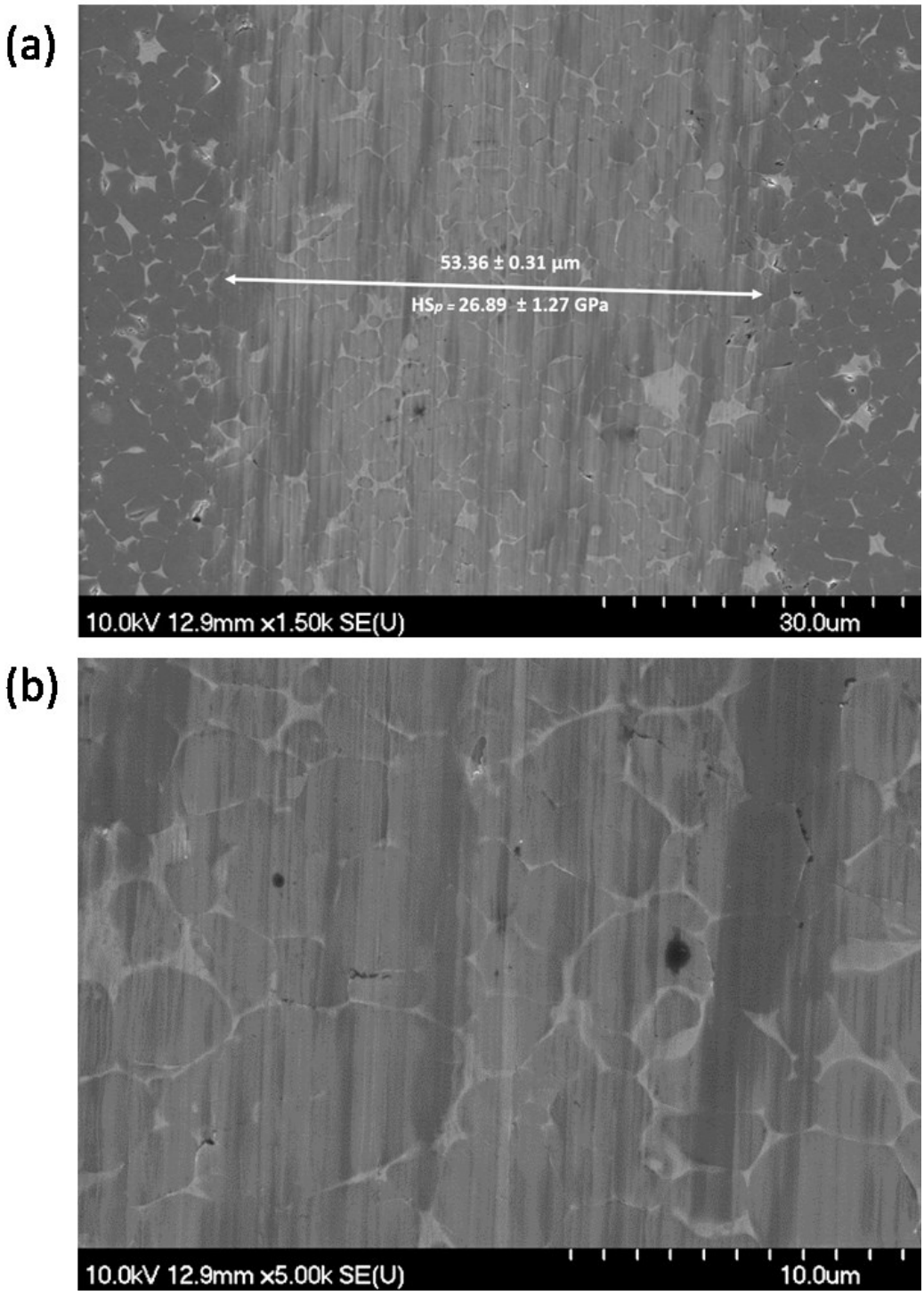

Figure 8.18 FE-SEM images of the scratch track surfaces, indicating the width and scratch hardness of the tracks created using a Rockwell diamond indenter, with an applied load of 30 N: (a) TiC-30 vol.17-4 PH showing the mean scratch width (and associated deviation error) and damaged surface and (b) Higher magnification of the same image.

In terms of the heat-treated samples, as anticipated from previous results in relation to the fracture resistance and hardness values, the TiC-30 vol.% 17-4 PH steel sample heat-treated at 621 °C (H1150) shows the best scratch resistance, with a scratch width of 31.87 μm and an associated scratch hardness of 75.55 GPa (Figure 8.19 (a)) after testing at 30 N applied load. The experiments in this work confirm that the minimum scratch depth is achieved with a combination of high hardness-IFR, highlighting the importance of both parameters in terms of wear resistance, not simply hardness.

The extent of strengthening by formation of Cu-based precipitates in the TiC-17-4 PH steel cermets, when the specimen is subjected to heat-treatment, depends upon various factors. The predominant contributor relates to the strain field formed around the precipitates, according to Bhambroo and colleagues [247]. In the initial stages of the ageing treatment, the Cu-based precipitates are coherent with the surrounding martensitic matrix and provide an effective resistance to the motion of dislocations during deformation, thereby strengthening the material to a moderate extent. As either the ageing time or temperature increases, the copper precipitates grow and lose their coherency, with the matrix, increasing somewhat in size and spacing, thus reducing their efficiency at pinning dislocation. In the present case, the toughness of the material shows a small increase with the heat-treatment temperature, with an expected slight associated decrease in the strength of the PH-grade steel[229]. As a result, the extent of the strengthening decreases with an increase in ageing duration or temperature. In this work, the peak hardness is attained after ageing at the H925 condition (496 °C for 4 hours), which is well-described in the literature based on the formation of coherent fine (Cu-based) precipitates [229,247]. These precipitates grow on subsequent ageing at the higher temperature (H1150, or 621 °C for 4 hours) leading to a loss of precipitate coherency with the matrix, and increased precipitate spacing. This then allows more easy passage of dislocations between the precipitates and a corresponding decrease in the strength of the material, subsequently increasing the ductility/toughness. It is under this condition that the cermet shows the best overall wear resistance among the tested cermet compositions.

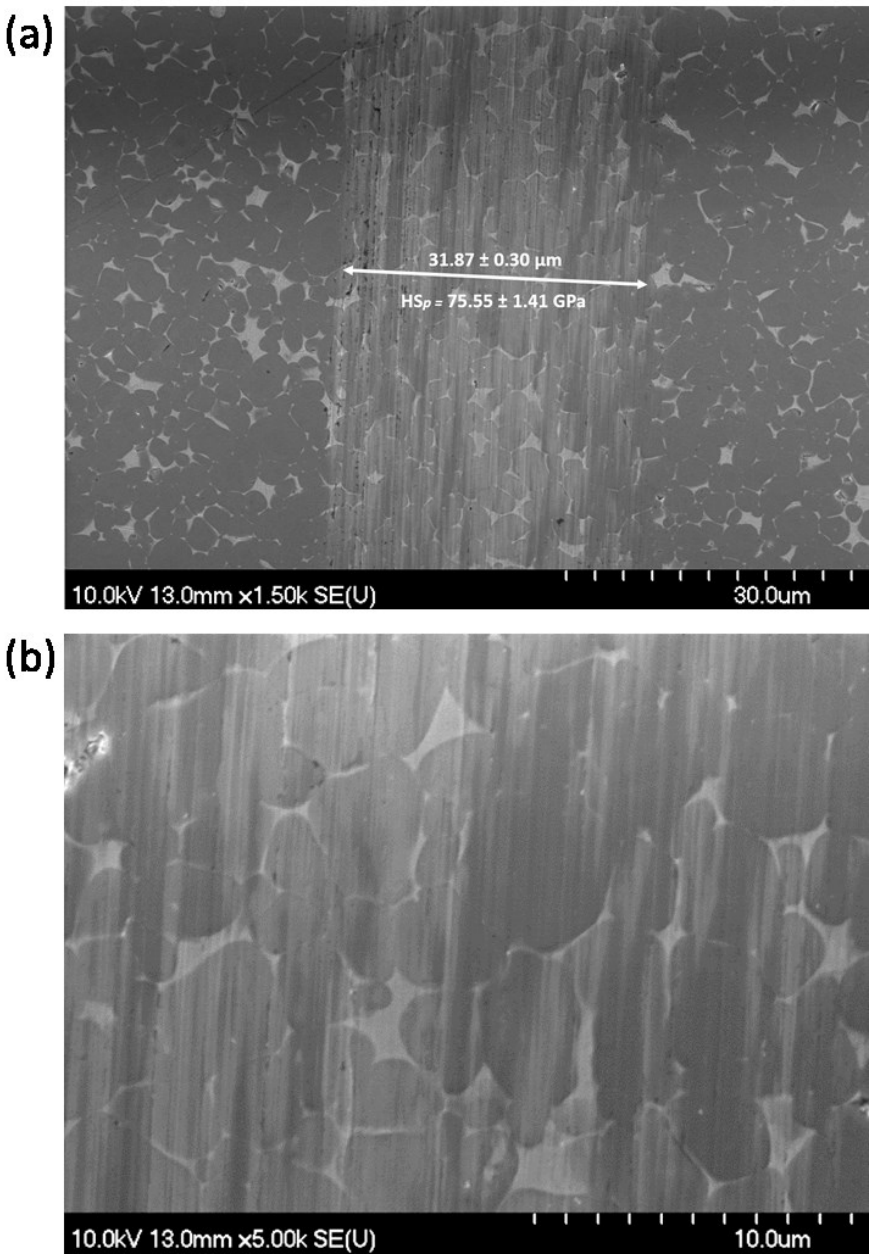

Figure 8.19 FE-SEM images of the scratch track surfaces, indicating the width and scratch hardness of the tracks created using a Rockwell diamond indenter, with an applied load of 30 N: (a) TiC-30 vol.% 17-4 PH steel cermet H1150 conditioned sample showing the mean scratch width (and associated deviation error) and damaged surface and (b) Higher magnification image of the same.

8.3 Conclusions

1. Steel based cermets were successfully manufactured using a vacuum liquid phase sintering methodology;
2. A comparison between selected mechanical characteristics of the TiC-316L and TiC-17-4 PH steel has been undertaken;
3. A high Vickers hardness of 2600 HV1 occurs for the TiC-316L steel cermets with 5 vol.% binder, which decreases down to 1600 HV1 at 30 vol.% binder. The same trend is observed with the TiC-17-4 PH steel cermets, however with a slight lower hardness of 2500 HV1 at 5 vol.% binder, decreasing down to 1200 HV1 at 30 vol.% of the steel. This difference is proposed to arise from the differences in Ni contents between the two steels, as Ni imparts strengthening; 14% Ni for 316L when compared to 4% for 17-4 PH;
4. A readily applicable heat treatment schedule was examined for the TiC cermets with the precipitation hardened steel. This sequence included an austenitization step, followed by an oil quench, and then an elevated temperature heat-treatment. Samples with less than 20 vol.% 17-4 PH steel binder cracked and fragmented during the oil quenched heat treatment, while samples with 30 vol. % binder, heat treated at 496 °C for 4 hours (condition H925) showed the highest hardness of ~2300 HV1.
5. Conversely, samples heat-treated at 621 °C for 4 hours (condition H1150) showed the highest scratch resistance, due to a combination of good hardness and indentation fracture resistance.
6. The scratched surfaces were subsequently analysed by SEM and, in 3D, using CLSM. This showed the degree of damage and the operating mechanism(s) generated by the Rockwell diamond indenter during scratch loading.
7. The tested samples show both micro-cutting and grooving as the main abrasive wear mechanisms.

Acknowledgements

The Canada Foundation for Innovation, the Atlantic Innovation Fund, and other partners who helped fund the Facilities for Materials Characterisation, managed by the Dalhousie University

Clean Technologies Research Institute, are gratefully acknowledged. The present work was also made possible with support from CAPES, Brazil, through the programme Coordination for the Improvement of Higher Level or Education Personnel.

CHAPTER 9 CONCLUSION

9.1 Conclusions

This novel work has extensively studied several compositions using TiC and TiN as base ceramics for use in cermets for challenging wear applications. Both base materials were selected because of their combination of excellent mechanical, wear and thermal properties, combined with low density. The TiC-Ni_3Al cermet systems have achieved extremely high wear resistance properties, with specific wear rates down as low as 1 x 10^{-7} mm^3/Nm when applied in continuous sliding wear applications with moderate applied loads, while stainless steel-based TiC cermets are in the range from 5-20 x 10^{-7} mm^3/Nm in previous work [73,74].

Several approaches were examined to understand the wear mechanism(s) involved when these materials, along with novel variants, are being subjected to tribological damage scenarios. Alternative heat treatment methodologies and/or addition of secondary phase materials (such as graphene nano-platelets, or GNPs) were successfully applied in the synthesis processes of these novel cermets. Firstly, suitable heat treatments and different binder compositions were successfully employed, obtaining sintered cermets with high density. Secondly, the mechanical and tribological properties of these materials have been assessed, with a primary focus upon the operative wear mechanisms.

For the TiN-based cermets, prepared with a nominally stoichiometric Ni_3Al intermetallic binder, a study of the changes in thermal characteristics, through differential scanning calorimetry and dilatometry, was undertaken using various amounts of Mo_2C additions. Micro- and macro-segregation phenomena were observed in the pure TiN-Ni_3Al system, due to poor wetting of the molten Ni_3Al on TiN, resulting in high porosity and binder de-wetting (observed as exudation, or 'sweating', from the cermet structure). This high porosity compromises the application of this material due to poor mechanical properties. This work showed that the incorporation of up to 10 vol.% of Mo_2C into the cermet improves the wettability during liquid phase sintering, considerably reducing porosity in the final specimens. A simple microstructural model was developed, based on the use of evidence from EDS chemical mapping. This model demonstrates that during sintering/cooling the Mo_2C first dissolves into the liquid phase, then reprecipitates directly onto

the individual TiN particles, creating an enveloping Mo_2C 'shell' structure. This shell can be anticipated to lead to a reduction of the contact angle between the molten Ni_3Al intermetallic binder phase and the TiN. This study highlights the beneficial effects of Mo_2C additions in processing TiN cermets and helps in providing a simple methodology than can be applied by industry to further increase densification in such difficult to sinter cermet systems, therefore likely improving the mechanical and wear properties of such materials.

Besides having achieved wear rates on the scale of 1 x 10^{-7} mm^3/Nm, TiC cermets prepared with 30 vol-% Ni_3Al maintain a moderately high coefficient of friction of ~0.25 when dry sliding against standard WC-Co counter-face surfaces. To further increase the wear resistance, several compositional variants of this baseline cermet were produced using GNPs. In comparison to carbon nanotubes, GNPs are a relatively cheap material, and well known to increase mechanical properties in many composite systems, which also have been a strategic choice for manufacturing of selflubricant cermets. For the current work, high density TiC-Ni_3Al based cermets were sintered containing GNP additions of up to 2.5 vol.%. It is shown that these GNP additions do not significantly degrade the densification behavior, for the composition range studied, with all materials sintered to greater than 99% of theoretical density. The composite hardness and indentation fracture resistance (IFR) were both significantly increased due to the additions of GNPs. The reduction of the coefficient of friction for the TiC-Ni_3Al cermets promoted a further increase in the wear resistance of these material by roughly one order of magnitude when tested using an aggressive "block on ring" tribological geometry. It is important to note a transition from an aggressive adhesion wear mechanism (without GNPs) to a less severe abrasive/erosive wear for both the damaged surface and the analysed wear debris, once GNPs were incorporated.

To further evaluate parameters affecting the wear performance of the TiC cermets, again with 30 vol-% Ni_3Al, a suitable heat-treatment for achieving a long range ordered Ni_3Al intermetallic structure was investigated. In terms of the balance of wear and mechanical characteristics, optimal results were obtained when this composite system was heat treated at 1200 °C for 120 minutes. Under such conditions, the Vickers hardness increased by ~10%, while the scratch resistance was increased by a factor of three when tested under an applied load of 30 N, when compared with the 'as-sintered' condition. As an effect of the heat treatment, the Ni_3Al intermetallic binder is ordered, showing a transition from a ductile to a more brittle behavior. The main wear mechanisms

were characterized as grain pull-out and brittle fracture of the TiC grains in both the as-sintered and heat-treated cermet samples. Plastic deformation-chip formation was a dominant mechanism for samples heat-treated at 800 °C.

Finally, a novel precipitation hardening heat treatment was implemented for TiC-based cermets with steel-based binders, with the goal to evaluate and study the impacts on its mechanical and wear properties. With this in mind, comparison has been made between the physical and mechanical characteristics of two cermet systems, namely TiC prepared with a non-hardenable 316L stainless steel binder and also TiC with a 17-4 PH steel, precipitation hardenable binder. Successful aging heat treatments were applied to the cermets using the 17-4 precipitation hardenable steel, when using a binder content higher than 20 vol. % (below this amount the cermets suffered too severe thermal shock, and fractured into smaller pieces); the complete heat-treatment cycle for these cermats involved austenitization, quenching and then the precipitation heat treatment. The highest 'as-sintered' Vickers hardness occurs for the TiC-316L cermets, at 2600 HV1 when using 5 vol.% binder, which decreases down to 1600 HV1 at 30 vol% binder. The same trend is observed for TiC with the 17-4 PH steel, however starting with a slight lower hardness at 2500 HV1 at 5 vol.% binder, which decreases to 1200 HV1 with 30 vol.%. 17-4 PH steel binder. These differences are proposed to arise from differences in the Ni content of the two binders, being 14 wt.% Ni for the 316L steel, compared to just 4 wt.% Ni for 17-4 PH.

When the TiC-based specimens with 17-4 PH steel binders were oil quenched from the austenitizing temperature, the components with a TiC content greater than 80 vol.% suffered thermal shock. Cermets with 20 and 30 vol.% 17-4 PH binder were successfully heat treated under two different conditions, at 496 °C for 4 hours or 621 °C for 4 hours (termed H925 and H1150, respectively). The highest Vickers hardness values are obtained for the samples heat treated under the H925 condition, with a value of ~2300 HV1. While heat treating under the H925 conditions provides the higher hardness, applying the H1150 heat-treatment conditions demonstrated the best wear resistance when evaluated using scratch testing, which is proposed to be due to a combination of good hardness and the retention of high indentation fracture resistance.

9.2 Recommendations for Future Work

This work has studied several ways to further increase the wear performance of advanced cermets, either by applying heat treatments that affect the binder phase properties, such as ordering or precipitation hardening, or though incorporating GNPs into the structure. In each case, it is shown that it is possible to further increase wear resistance by increasing the hardness and/or toughness or reducing the coefficient of friction.

In terms of the binder volume content, it will be desirable to observe the effects of heat treatments on higher binder contents of cermets prepared with hardenable binders, such as 35 and 40 vol.%, to further increase the significance of the binder volume on the heat-treated cermets wear response. In particular, such binder levels are employed in thermal spray coatings and laser cladding coatings. As a complementary study, to fully understand these materials when synthesized and heat treated, the residual stress between the ceramic and the metallic phase must be measured due to its potentially large effects upon the hardness and toughness of the cermets. The residual stress due to the thermal coefficient mismatch between the ceramic and metallic phase, when quenched, is expected to be of the order of several GPa, however it is then decreased by the coarsening of the microstructure during aging heat treatments.

Other important aspect yet to be explored is the addition of larger amounts of GNPs (currently added up to a maximum of 2.5 vol.%), and the subsequent impact of this upon the densification behaviour, and mechanical and wear performance. From this work, the wear resistance is continuously increased up to 2.5 vol.% GNPs. However, higher quantities were not yet tested due to the limitation of work scope. It is also suggested that the use of other types of functionalized graphene (e.g. graphene oxide) are explored, that have been shown to have better processability, due to their being more easily dispersed in an aqueous suspension medium. Other types of carbon-based additives are also promising, such as carbon nanotubes, carbon black, single and few-layer graphene.

To further develop these materials, additions of industrial diamonds with different coarse and fine particles sizes are also recommended. It should be noted that in this present work, preliminary trials of industrial diamond incorporation were undertaken, with the materials processed via liquid phase sintering. However, the industrial diamond particles were transformed into graphite due to

its unstable nature at high temperatures. Spark plasma sintering is recommended to test the effects of additions of industrial diamond into the cermet compositions, due to its short processing time compared to conventional vacuum sintering, minimizing the time for the diamond-graphite phase transition to occur.

Another important aspect of these materials that is yet to be studied a the tribo-corrosion properties of these cermets, and the effect of the carbon additive additions, such as GNPs. In many usage scenarios, combined tribo-corrosion environments are encountered. In these instances, carbon additives may play a significant role in improving the mechanical and chemical resistance of advanced cermets.

REFERENCES

[1] T.L. Stewart, K.P. Plucknett, The sliding wear of TiC and Ti(C,N) cermets prepared with a stoichiometric Ni_3Al binder, Wear. 318 (2014) 153–167. doi:10.1016/j.wear.2014.06.025.

[2] S. Kang, Stability of N in Ti(CN) Solid Solutions for Cermet Applications, Powder Metall. 40 (1997) 139–142. doi:10.1179/pom.1997.40.2.139.

[3] S. Cardinal, A. Malchère, V. Garnier, G. Fantozzi, Microstructure and mechanical properties of TiC-TiN based cermets for tools application, Int. J. Refract. Met. Hard Mater. 27 (2009) 521–527. doi:10.1016/j.ijrmhm.2008.10.006.

[4] P. Xiao, B. Derby, Wetting of titanium nitride and titanium carbide by liquid metals, Acta Mater. 44 (1996) 307–314. doi:10.1016/1359-6454(95)00165-0.

[5] H.O. Andrén, Microstructure development during sintering and heat-treatment of cemented carbides and cermets, Mater. Chem. Phys. 67 (2001) 209–213. doi:10.1016/S0254-0584(00)00441-7.

[6] G.S. Upadhyaya, Production of Metal and Carbide Powders, Cem. Tungsten Carbides. (1998) 55–88. doi:http://dx.doi.org/10.1016/B978-081551417-6.50004-6.

[7] A. Lasalmonie, Intermetallics: Why is it so difficult to introduce them in gas turbine engines, Intermetallics. 14 (2006) 1123–1129. doi:10.1016/j.intermet.2006.01.064.

[8] T.L. Stewart, K.P. Plucknett, The effects of Mo_2C additions on the microstructure and sliding wear of TiC0.3N0.7-Ni_3Al cermets, Int. J. Refract. Met. Hard Mater. 50 (2015) 227–239. doi:10.1016/j.ijrmhm.2015.01.013.

[9] L. Chen, W. Lengauer, P. Ettmayer, K. Dreyer, H.W. Daub, D. Kassel, Fundamentals of liquid phase sintering for modern cermets and functionally graded cemented carbonitrides (FGCC), Int. J. Refract. Met. Hard Mater. 18 (2000) 307–322. doi:10.1016/S0263-4368(00)00041-X.

[10] J. Gu, G. Barber, S. Tung, R.-J. Gu, Tool life and wear mechanism of uncoated and coated milling inserts, Wear. 225–229 (1999) 273–284. doi:10.1016/S0043-1648(99)00074-5.

[11] J.K. Park, S.T. Park, Densification of TiN-Ni cermets by improving wettability of liquid nickel on TiN grain surface with addition of Mo_2C, Int. J. Refract. Met. Hard Mater. 17 (1999) 295–298. doi:10.1016/S0263-4368(99)00016-5.

[12] R.M. German, P. Suri, S.J. Park, Review: liquid phase sintering, J. Mater. Sci. 44 (2009) 1–39, http://dx.doi.org/10.1007/s10853-008-3008-0.

[13] P. Ettmayer, Hardmetals and Cermets, Annu. Rev. Mater. Sci. 19 (1989) 145–164. doi:10.1146/annurev.ms.19.080189.001045.

[14] J. García, V.C. Ciprés, A. Blomqvist, B. Kaplan, Cemented carbide microstructures: A review, Int. J. Refract. Met. Hard Mater. 80 (2018) 40–68. doi:10.1016/j.ijrmhm.2018.12.004.

[15] P. Fauchais, G. Montavon, G. Bertrand, From powders to thermally sprayed coatings, J. Therm. Spray Technol. 19 (2010) 56–80. doi:10.1007/s11666-009-9435-x.

[16] H.O. Pierson,. The Refractory Carbides, Academic Press, New York ;London, 1996. https://doi.org/10.1016/B978-081551392-6.50003-9.

[17] H.O. Pierson, The Refractory Nitrides, Handb. Refract. Carbides Nitrides. (1996) 156–162. https://doi.org/10.1016/B978-081551392-6.50010-6.

[18] A. Rajabi, M.J. Ghazali, J. Syarif, A.R. Daud, Development and application of tool wear: A review of the characterization of TiC-based cermets with different binders, Chem. Eng. J. 255 (2014) 445–452. doi:10.1016/j.cej.2014.06.078.

[19] J.J. Gangler, Some Physical Properties of Eight Refractory Oxides and Carbides, J. Am. Ceram. Soc. 33 (1950) 367–374. https://doi.org/10.1111/j.1151-2916.1950.tb14155.x.

[20] A. Rajabi, M.J.G. et al., Chemical composition, microstructure and sintering temperature modifications on mechanical properties of TiC-based cermet-A review, Mater. Des. 67 (2015) 95–106.

[21] G. V. White, K.J.D. Mackenzie, I.W.M. Brown, J.H. Johnston, Carbothermal synthesis of titanium nitride - Part III Kinetics and mechanism, J. Mater. Sci. 27 (1992) 4300–4304. doi:10.1007/BF00541556.

[22] B.J. Aylett, The Chemistry of Transition Metal Carbides and Nitrides, Springer Netherlands, Dordrecht, 1996. https://doi.org/10.1007/978-94-009-1565-7.

[23] A. Ilbagi, P. Delshad Khatibi, I.P. Swainson, G. Reinhart, H. Henein, Microstructural analysis of rapidly solidified aluminium-nickel alloys, Can. Metall. Q. 50 (2011) 295–302. https://doi.org/10.1179/1879139511Y.0000000006.

[24] M.H. Yoo, J.A. Horton, C.T. Liu, Micromechanisms of yield and flow in ordered intermetallic alloys, Acta Metall. 36 (1988) 2935–2946. https://doi.org/10.1016/0001-6160(88)90176-9.

[25] K. Morsi, Review: reaction synthesis processing of Ni–Al intermetallic materials, Mater. Sci. Eng. A. 299 (2001) 1–15. https://doi.org/10.1016/S0921-5093(00)01407-6.

[26] C. Abromeit, S. Matsumura, Kinetics of antiphase domain boundaries during an $L1_2$ order-disorder phase transformation: A Monte Carlo simulation, Philos. Mag. A. 82 (2002) 2287–2302. https://doi.org/10.1080/01418610208235739.

[27] G.K. Dey, Physical metallurgy of nickel aluminides, Sadhana. 28 (2003) 247–262. https://doi.org/10.1007/BF02717135.

[28] P. V. Badiger, V. Desai, M.R. Ramesh, Development and Characterization of Ti/TiC/TiN Coatings by Cathodic Arc Evaporation Technique, Trans. Indian Inst. Met. 70 (2017) 2459–2464. https://doi.org/10.1007/s12666-017-1107-9.

[29] P. Jozwik, W. Polkowski, Z. Bojar, Applications of Ni_3Al Based Intermetallic Alloys—Current Stage and Potential Perceptivities, Materials (Basel). 8 (2015) 2537–2568. doi:10.3390/ma8052537.

[30] ISO/TS 80004-13:2017(en), Nanotechnologies — Vocabulary — Part 13: Graphene and related two-dimensional (2D) materials, (n.d.). https://www.iso.org/obp/ui/#iso:std:iso:ts:80004:-13:ed-1:v1:en (accessed September 2, 2019).

[31] R.M. German, Powder metallurgy science, 1984.

[32] R.M. German, Sintering theory and practice, 1996.

[33] W.D. Kingery, M.D. Narasimhan, Densification during sintering in the presence of a liquid phase. II. Experimental, J. Appl. Phys. 30 (1959) 307–310. doi:10.1063/1.1735156.

[34] H. Tanaka, A. Yamamoto, J. Shimoyama, H. Ogino, K. Kishio, Strongly connected *ex situ* MgB_2 polycrystalline bulks fabricated by solid-state self-sintering, Supercond. Sci. Technol. 25 (2012) 115022. https://doi.org/10.1088/0953-2048/25/11/115022.

[35] J. Zackrisson, Development of cermet microstructures during sintering and heat-treatment, Doktorsavhandlingar Vid Chalmers Tek. Hogsk. 32 (1999) 1–48. https://doi.org/10.1007/s11661-001-0104-z.

[36] R.M. German, P. Suri, S.J. Park, Review: Liquid phase sintering, J. Mater. Sci. 44 (2009) 1–39. https://doi.org/10.1007/s10853-008-3008-0.

[37] N. Frage, N. Froumin, M.P. Dariel, Wetting of TiC by non-reactive liquid metals, Acta Mater. 50 (2002) 237–245. https://doi.org/10.1016/S1359-6454(01)00349-4.

[38] D. Chatain, L. Coudurier, N. Eustathopoulos, Wetting and interfacial bonding in ionocovalent oxide-liquid metal systems, Rev. Phys. Appliquée. 23 (1988) 1055–1064. https://doi.org/10.1051/rphysap:019880023060105500.

[39] N.M. Parikh, M. Humenik, Cermets: {II}. Wettability and Microstructure Studies in Liquid-Phase Sintering, J. Am. Ceram. Soc. 40 (1957) 315–320. https://doi.org/10.1111/j.1151-2916.1957.tb12628.x.

[40] S. V. Dudiy, B.I. Lundqvist, Wetting of TiC and TiN by metals, Phys. Rev. B. 69 (2004) 125421. https://doi.org/10.1103/PhysRevB.69.125421.

[41] G. Oteborg, Microscopic Theory of Wetting and Adhesion in Metal-Carbonitride Systems, 2002.

[42] G.W. Stachowiak, A.W. Batchelor, Future Directions in Tribology, Eng. Tribol. (2006) 705–717. https://doi.org/10.1016/B978-075067836-0/50018-3.

[43] J.E. Ingvaldsen, J.A. Gulla, Context-aware user-driven news recommendation, CEUR Workshop Proc. 1542 (2015) 33–36. doi:10.1017/CBO9781107415324.00.

[44] D.K. Shetty, I.G. Wright, P.N. Mincer, A.H. Clauer, Indentation fracture of WC-Co cermets, J. Mater. Sci. 20 (1985) 1873–1882.

[45] K. Niihara, R. Morena, D.P.H. Hasselman, Evaluation of K-Ic of brittle solids by the indentation method with low crack-to-indent ratios, J. Mater. Sci. Lett. 1 (1982) 13–16. https://doi.org/10.1007/BF00724706.

[46] A. Nastic, A. Merati, M. Bielawski, M. Bolduc, O. Fakolujo, M. Nganbe, Instrumented and Vickers Indentation for the Characterization of Stiffness, Hardness and Toughness of Zirconia Toughened Al_2O_3 and SiC Armor, J. Mater. Sci. Technol. 31 (2015) 773–783. doi:10.1016/J.JMST.2015.06.005.

[47] J.M. Challen, P.L.B. Oxley, An explanation of the different regimes of friction and wear using asperity deformation models, Wear. 53 (1979) 229–243. https://doi.org/10.1016/0043-1648(79)90080-2.

[48] S.F. Moustafa, Wear and wear mechanisms of Al-22%Si/$A1_2O_3$ composite, Wear. 185 (1995) 189–195. doi:10.1016/0043-1648(95)06607-1.

[49] F.P. Bowden, D. Tabor, The friction and lubrication of solids: Part II, Volume 2, 1964.

[50] G.W. Stachowiak, A.W. Batchelor, G.W. Stachowiak, A.W. Batchelor, 12 – Adhesion and Adhesive Wear, in: Eng. Tribol., 2006: pp. 553–572. https://doi.org/10.1016/B978-075067836-0/50013-4.

[51] T. Sasada, M. Oike, N. Emori, Effect of Abrasive Grain Size on the Transition Between Abrasive and Adhesive Wear., Wear. 97 (1984) 291–302. https://doi.org/10.1016/0043-1648(84)90155-8.

[52] G.W. Stachowiak, A.W. Batchelor, G.W. Stachowiak, A.W. Batchelor, 11 – Abrasive, Erosive and Cavitation Wear, in: Eng. Tribol., 2006: pp. 501–551. https://doi.org/10.1016/B978-075067836-0/50012-2.

[53] R. Norling, I. Olefjord, Erosion-corrosionof Fe- and Ni-based alloys at 550ºC, Wear. 254 (2003) 173–184. https://doi.org/10.1016/S0043-1648(02)00299-5.

[54] G.W. Stachowiak, A.W. Batchelor, Abrasive, Erosive and Cavitation Wear, in: Eng. Tribol., 2006. https://doi.org/10.1016/b978-075067836-0/50012-2.

[55] S. Huth, Metallic materials for tribocorrosion systems, 2011. https://doi.org/10.1016/B978-1-84569-966-6.50010-5.

[56] G.W. Stachowiak, A.W. Batchelor, G.W. Stachowiak, A.W. Batchelor, 13 – Corrosive and Oxidative Wear, in: Eng. Tribol., 2006: pp. 573–593. https://doi.org/10.1016/B978-075067836-0/50014-6.

[57] I. García, D. Drees, J.P. Celis, Corrosion-wear of passivating materials in sliding contacts based on a concept of active wear track area, Wear. 249 (2001) 452–460. https://doi.org/10.1016/S0043-1648(01)00577-4.

[58] P.A. Dearnley, G. Aldrich-Smith, Corrosion-wear mechanisms of hard coated austenitic 316L stainless steels, Wear. 256 (2004) 491–499. https://doi.org/10.1016/S0043-1648(03)00559-3.

[59] G.W. Stachowiak, A.W. Batchelor, G.W. Stachowiak, A.W. Batchelor, 3 – Lubricants and Their Composition, in: Eng. Tribol., 2006: pp. 51–101. https://doi.org/10.1016/B978-075067836-0/50004-3.

[60] G.W. Stachowiak, A.W. Batchelor, G.W. Stachowiak, A.W. Batchelor, 9 – Solid Lubrication and Surface Treatments, in: Eng. Tribol., 2006: pp. 419–459. https://doi.org/10.1016/B978-075067836-0/50010-9.

[61] S. Bull, Materials Degradation and its Control by Surface Engineering;, Imperial College Press, 2000. https://doi.org/10.1016/S0301-679X(00)00017-7.

[62] Y. Yahagi, Y. Mizutani, 13 Corrosive and Oxidative Wear, Tribol. Ser. 24 (1993) 637–656. https://doi.org/10.1016/S0167-8922(08)70587-X.

[63] A.W. Batchelor, G.W. Stachowiak, Predicting synergism between corrosion and abrasive wear, Wear. 123 (1988) 281–291. https://doi.org/10.1016/0043-1648(88)90144-5.

[64] A. Sáez, F. Arenas, E. Vidal, Microstructure development of WCoB-TiC based hard materials, Int. J. Refract. Met. Hard Mater. 21 (2003) 13–18. https://doi.org/10.1016/S0263-4368(02)00104-X.

[65] J.C. LaSalvia, D.K. Kim, M.A. Meyers, Effect of Mo on microstructure and mechanical properties of TiC-Ni-based cermets produced by combustion synthesis - Impact forging technique, Mater. Sci. Eng. A. 206 (1996) 71–80. https://doi.org/10.1016/0921-5093(95)09994-8.

[66] S. Sabatello, N. Frage, M.. Dariel, Graded TiC-based cermets, Mater. Sci. Eng. A. 288 (2000) 12–18. https://doi.org/10.1016/S0921-5093(00)00889-3.

[67] C. Jin, M. Gaier, Z. Memarrashidi, C. Onouha, Z. Farhat, Using Combined Microscopy Techniques to Assess Sliding Wear Damage in High Performance Cermets, Microscopy7.Org. (n.d.). http://www.microscopy7.org/book/490-499.pdf (accessed September 11, 2017).

[68] M. Gaier, Z.N. Farhat, K.P. Plucknett, The effects of graphene nano-platelet additions on the sliding wear of TiC-Ni_3Al cermets, Tribol. Int. 130 (2019) 119–132.

doi:10.1016/j.triboint.2018.09.015.

[69] I.J. Shon, I.K. Jeong, I.Y. Ko, J.M. Doh, K. Do Woo, Sintering behavior and mechanical properties of WC-10Co, WC-10Ni and WC-10Fe hard materials produced by high-frequency induction heated sintering, Ceram. Int. 35 (2009) 339–344. https://doi.org/10.1016/j.ceramint.2007.11.003.

[70] M.F. Zawrah, Synthesis and characterization of WC-Co nanocomposites by novel chemical method, Ceram. Int. 33 (2007) 155–161. https://doi.org/10.1016/j.ceramint.2005.09.010.

[71] J. Wang, Y. Wang, Y. Ding, W. Gong, Microstructure and wear-resistance of Fe-(Ti,V)C composite, Mater. Des. 28 (2007) 2207–2209. https://doi.org/10.1016/j.matdes.2006.06.019.

[72] C.C. Onuoha, G.J. Kipouros, Z.N. Farhat, K.P. Plucknett, The reciprocating wear behaviour of TiC-304L stainless steel composites prepared by melt infiltration, Wear. 303 (2013) 321–333. https://doi.org/10.1016/j.wear.2013.03.040.

[73] C. Jin, C.C. Onuoha, Z.N. Farhat, G.J. Kipouros, K.P. Plucknett, Reciprocating wear behaviour of TiC-stainless steel cermets, (2016). https://doi.org/10.1016/j.triboint.2016.10.012.

[74] G.R. Anstis, P. Chantikul, B.R. Lawn, D.B. Marshall, A critical evaluation of indentation techniques for measuring fracture toughness: I Direct crack measurements, J. Am. Ceram. Soc. 46 (1981) 533–538. https://doi.org/10.1111/j.1151-2916.1981.tb10320.x.

[75] A. Nieto, J. Kim, O. V. Penkov, D.-E. Kim, J.M. Schoenung, Elevated temperature wear behavior of thermally sprayed WC-Co/nanodiamond composite coatings, Surf. Coatings Technol. 315 (2017) 283–293. https://doi.org/10.1016/j.surfcoat.2017.02.048.

[76] P.L. Fauchais, J.V.R. Heberlein, M.I. Boulos, Thermal Spray Fundamentals, Springer US, Boston, MA, 2014. https://doi.org/10.1007/978-0-387-68991-3.

[77] J. Pirso, M. Viljus, S. Letunovitš, K. Juhani, R. Joost, Three-body abrasive wear of cermets, Wear. 271 (2011) 2868–2878. https://doi.org/10.1016/j.wear.2011.06.005.

[78] A.H. Dent, S. Depalo, S. Sampath, Examination of the Wear Properties of HVOF Sprayed Nanostructured and Conventional WC-Co Cermets With Different Binder Phase Contents, J. Therm. Spray Technol. 11 (2002) 551–558. https://doi.org/10.1361/105996302770348691.

[79] J.A. Picas, M. Punset, M. Teresa Baile, E. Martín, A. Forn, Properties of WC-CoCr based coatings deposited by different HVOF thermal spray processes, Plasma Process. Polym. 6 (2009) 948–953. https://doi.org/10.1002/ppap.200932402.

[80] R.M. Genga, L.A. Cornish, G. Akdogan, Effect of Mo_2C additions on the properties of SPS manufactured WC-TiC-Ni cemented carbides, Int. J. Refract. Met. Hard Mater. 41 (2013) 12–21, http://dx.doi.org/10.1016/j.ijrmhm.2013.01.008.

[81] N. V. Novikov, V.P. Bondarenko, V.T. Golovchan, High-temperature mechanical properties of WC-Co hard metals (Review), J. Superhard Mater. 29 (2007) 261–280. https://doi.org/10.3103/S1063457607050012.

[82] Y. Kasukabe, A. Ito, S. Nagata, S.-C. Chen, H. Tamura, T. Hara, A.L. Ramirez-Ledesma, M.A. Aguilar-Mendez, R.A. Rodriguez-Diaz, A.A. Sivkov, Y. Gerasimov, A.A. Evdokimov, Ceramics based on titanium nitride and silicon nitride sintered by SPS-method, Mater. Sci. Eng. 93 (n.d.). https://doi.org/10.1088/1757-899X/93/1/012030.

[83] W. Zeng, X. Gan, Z. Li, K. Zhou, Effect of TiC addition on the microstructure and mechanical properties of TiN-based cermets, Ceram. Int. 43 (2017) 1092–1097. https://doi.org/10.1016/j.ceramint.2016.10.046.

[84] R. Tu, P. Zhu, S. Zhang, P. Xu, L. Zhang, H. Hanekawa, T. Goto, ScienceDirect Comparison of CVD-deposited Ni and dry-blended Ni powder as sintering aids for TiN powder, J. Eur. Ceram. Soc. 34 (2014) 1955–1961. https://doi.org/10.1016/j.jeurceramsoc.2013.12.050.

[85] C. Liu, A. Leyland, Q. Bi, A. Matthews, Corrosion resistance of multi-layered plasma-assisted physical vapour deposition TiN and CrN coatings, Surf. Coatings Technol. 141 (2001) 164–173. https://doi.org/10.1016/S0257-8972(01)01267-1.

[86] D. Zou, D. Yan, L. Xiao, Y. Dong, Characterization of nanostructured TiN coatings fabricated by reactive plasma spraying, Surf. Coatings Technol. 202 (2008) 1928–1934. https://doi.org/10.1016/j.surfcoat.2007.08.022.

[87] Z. Mao, J. Ma, J. Wang, B. Sun, Properties of TiN-matrix coating deposited by reactive HVOF spraying, J. Coatings Technol. Res. 6 (2009) 243–250. https://doi.org/10.1007/s11998-008-9105-9.

[88] K.K.P. Plucknett, T.T.N. Tiegs, K.K.B. Alexander, P.P.F. Becher, J.H. Schneibel, S.B. Waters, P.A. Menchhofer, Intermetallic bonded ceramic matrix composites, Oak Ridge National Laboratory, Oak Ridge, TN, 1995. https://doi.org/10.2172/102180.

[89] Q. Shen, L. Zhang, R. Tu, Effect of Mo addition on the wettability between Ni_3Al and TiC, Key Eng. Mater. 226 (2002) 501–504, http://dx.doi.org/10.4028/www.scientific.net/kem.224-226.501.

[90] W.A. Sparling, K.P. Plucknett, The effects of Mo_2C additions on the sintering response of TiC0.3N0.7-Ni_3Al cermets, Int. J. Refract. Met. Hard Mater. 61 (2016) 98–106, http://dx.doi.org/10.1016/j.ijrmhm.2016.08.013.

[91] Y. Li, N. Liu, X. Zhang, C. Rong, Effect of Mo addition on the microstructure and mechanical properties of ultra-fine grade TiC–TiN–WC–Mo_2C–Co cermets, Int. J. Refract. Met. Hard Mater. 26 (2008) 190–196. https://doi.org/10.1016/j.ijrmhm.2007.05.005.

[92] J. Long, Z. Zhang, T. Xu, W. Peng, X. Wei, B. Lu, R. Li, WC–Ni_3Al–B composites prepared through Ni+Al elemental powder route, Trans. Nonferrous Met. Soc. China. 22 (2012) 847–

852. https://doi.org/10.1016/S1003-6326(11)61255-7.

[93] H. Okamoto, Al-Ni (aluminum-nickel), J. Phase Equilibria Diffus. 25 (2004) 394–394. https://doi.org/10.1007/s11669-004-0163-0.

[94] C.A.L. Patino, Infiltration Processing of Metal Matrix Composites Using Coated Ceramic Particulates, National Library of Canada = Bibliothèque nationale du Canada, 2000. https://doi.org/10.16953/deusbed.74839.

[95] S. Zhang, Titanium carbonitride-based cermets: processes and properties, Mater. Sci. Eng. A. 163 (1993) 141–148. https://doi.org/10.1016/0921-5093(93)90588-6.

[96] Y. Zhao, Y. Zheng, W. Zhou, X. Lv, Characterization of functionally gradient Ti(C, N)-based cermets fabricated by vacuum liquid phase sintering and nitriding treatment during cooling, Int. J. Refract. Met. Hard Mater. 46 (2014) 20–23. https://doi.org/10.1016/j.ijrmhm.2014.05.003.

[97] J. Vaci, K. Plucknett, Melt-Infiltration and Wetting Transitions of Ni_3Al Alloy Infiltrated Into TiC-Al_2O_3 Preforms, in: John Wiley & Sons, Inc., n.d.: pp. 447–455. https://doi.org/10.1002/9780470291313.ch43.

[98] S. Buchholz, Z.N. Farhat, G.J. Kipouros, K.P. Plucknett, The reciprocating wear behaviour of TiC-Ni_3Al cermets, Int. J. Refract. Met. Hard Mater. 33 (2012) 44–52. https://doi.org/10.1016/j.ijrmhm.2012.02.008.

[99] M. Guo-zheng, X. Bin-shi, W. Hai-dou, S. Hong-juan, Y. Da-xiang, Effect of surface nanocrystallization on the tribological properties of 1Cr18Ni9Ti stainless steel, Mater. Lett. (2011).

[100] Y. Zheng, W.J. Liu, Q. Yuan, L. Wen, W.H. Xiong, Effect of Grain Growth Inhibitor on the Microstructure and Mechanical Properties of Ti(C,N)-Based Cermet, Key Eng. Mater. 280–283 (2005) 1413–1416. https://doi.org/10.4028/www.scientific.net/KEM.280-283.1413.

[101] V.a.d. Souza, A. Neville, Using In Situ Atomic Force Microscopy to Investigate the Kinetics of Corrosion of WC–Co–Cr Cermet Coatings Applied by High-Velocity Oxy-Fuel, J. Eng. Mater. Technol. 129 (2007) 55. https://doi.org/10.1115/1.2400258.

[102] N.S. Stoloff, C.T. Liu, The Physical and Mechanical Metallurgy of Ni_3Al and Its Alloys, Phys. Metall. Process. Intermet. Compd. 34 (1996) 159–211. https://doi.org/10.1007/978-1-4613-1215-4_6.

[103] Y. Peng, H. Miao, Z. Peng, Development of TiCN-based cermets: Mechanical properties and wear mechanism, Int. J. Refract. Met. Hard Mater. 39 (2013) 78–89. https://doi.org/10.1016/j.ijrmhm.2012.07.001.

[104] X.Y.Y. Dong, Y.L.L. Qiao, Y. Zang, Q.S.S. Cui, Effect of ultrasonic vibration on the behavior of antifriction and wear resistance of Al_2o_3/Al_2o_3 ceramic friction pairs under oil

lubrication, Phys. Procedia. 50 (2013) 449–452. https://doi.org/10.1016/j.phpro.2013.11.070.

[105] W. Chen, D. Zhang, Z. Lv, H. Li, Self-lubricating mechanisms via the in situ formed tribo-film of sintered ceramics with hBN addition in a high humidity environment, Int. J. Refract. Met. Hard Mater. 66 (2017) 163–173. https://doi.org/10.1016/j.ijrmhm.2017.03.014.

[106] X. Huang, J. Wang, H. Zhang, J. Ren, Q. Zan, Q. Gong, B. Wu, WC-Ni-Cr-based self-lubricating composites fabricated by pulsed electric current sintering with addition of WS2 solid lubricant, 2017. https://doi.org/10.1016/j.ijrmhm.2017.03.013.

[107] J. Liu, J. Xiong, Z. Guo, T. Yang, W. Wan, L. Zhou, J. Ye, T. Li, S. Li, Effect of graphite size on the tribological behavior of Ti (C, N)-based cermets self-mated wear pairs, Int. J. Refract. Met. Hard Mater. 64 (2017) 83–89. https://doi.org/10.1016/j.ijrmhm.2017.01.014.

[108] L. Zhou, J. Xiong, Z. Guo, J. Ye, J. Liu, Tribological performances of Ti(C,N)-based cermets with different graphite contents in dry sliding condition, Int. J. Refract. Met. Hard Mater. 68 (2017) 113–120. https://doi.org/10.1016/j.ijrmhm.2017.07.001.

[109] P.K. Rohatgi, S. Ray, Y. Liu, Tribological Properties of Metal Matrix Graphite Particle Composites, Int. Mater. Rev. 37 (1992) 129–149.

[110] X. Liu, J. Li, X. Yu, H. Fan, Q. Wang, S. Yan, L. Wang, W. Jiang, Graphene nanosheet/titanium carbide composites of a fine-grained structure and improved mechanical properties, Ceram. Int. 42 (2015) 165–172. https://doi.org/10.1016/j.ceramint.2015.08.071.

[111] W. Zhai, X. Shi, J. Yao, A.M.M. Ibrahim, Z. Xu, Q. Zhu, Y. Xiao, L. Chen, Q. Zhang, Investigation of mechanical and tribological behaviors of multilayer graphene reinforced Ni_3Al matrix composites, Compos. Part B Eng. 70 (2015) 149–155. https://doi.org/10.1016/j.compositesb.2014.10.052.

[112] K. Zhang, Z. Zhang, X. Lu, K. Li, Y. Du, J. Long, T. Xu, H. Zhang, L. Chen, Y. Kong, Microstructure and composition of the grain/binder interface in WC-Ni_3Al composites, Int. J. Refract. Met. Hard Mater. 44 (2014) 88–93. https://doi.org/10.1016/j.ijrmhm.2014.01.015.

[113] Z. Memarrashidi, The Aqueous Corrosion Response of Ti(C,N), TiC and WC Based Ceramic-Metal Composites, (2015). https://doi.org/10.1007/BF00555296.

[114] K. Plucknett, T.N. Tiegs, P.F. Becher, P.F.B. Kevin Plucknett, Terry N. Tiegs, Method of making sintered ductile intermetallic-bonded ceramic composites, n.d. https://patents.google.com/patent/US5905937A/en (accessed January 29, 2018).

[115] D.K. Shetty, I.G. Wright, P.N. Mincer, A.H. Clauer, Indentation fracture of WC-Co cermets, J. Mater. Sci. 20 (1985) 1873–1882. https://doi.org/10.1007/BF00555296.

[116] J.A. Williams, Analytical models of scratch hardness, Tribol. Int. 29 (1996) 675–694. https://doi.org/10.1016/0301-679X(96)00014-X.

[117] J.K. Lancaster, The influence of substrate hardness on the formation and endurance of molybdenum disulphide films, Wear. 10 (1967) 103–117. https://doi.org/10.1016/0043-1648(67)90082-8.

[118] P. Kun, F. Wéber, C. Balázsi, K. Parvez, Z. Wu, R. Li, X. Liu, R. Graf, Preparation and examination of multilayer graphene nanosheets by exfoliation of graphite in high efficient attritor mill, Sup Info. 9 (2011) 47–51. https://doi.org/10.1021/ja5017156.

[119] F.T.L. Muniz, M.A.R. Miranda, C. Morilla dos Santos, J.M. Sasaki, The Scherrer equation and the dynamical theory of X-ray diffraction, Acta Crystallogr. Sect. A Found. Adv. 72 (2016) 385–390. https://doi.org/10.1107/S205327331600365X.

[120] M. Yi, Z. Shen, Kitchen blender for producing high-quality few-layer graphene, Carbon N. Y. 78 (2014) 622–626. https://doi.org/10.1016/j.carbon.2014.07.035.

[121] A.C. Ferrari, Raman spectroscopy of graphene and graphite: Disorder, electron–phonon coupling, doping and nonadiabatic effects, Solid State Commun. 143 (2007) 47–57. https://doi.org/10.1016/J.SSC.2007.03.052.

[122] E. Bódis, O. Tapasztó, Z. Károly, P. Fazekas, S. Klébert, A.M. Keszler, K. Balázsi, J. Szépvölgyi, Spark plasma sintering of Si_3N_4/multilayer graphene composites, Open Chem. 13 (2014) 484–489. https://doi.org/10.1515/chem-2015-0064.

[123] G.W. Stachowiak, A.W. Batchelor, G.W. Stachowiak, A.W. Batchelor, 16 – Wear of Non-Metallic Materials, in: Eng. Tribol., 2006: pp. 651–704. https://doi.org/10.1016/B978-075067836-0/50017-1.

[124] E. Rocha-Rangel, Fracture Toughness Determinations by Means of Indentation Fracture, in: Nanocomposites with Unique Prop. Appl. Med. Ind., InTech, 2011. https://doi.org/10.5772/18127.

[125] A. V. Laptev, A.I. Tolochin, M.S. Kovalchenko, Y.I. Evich, I.Y. Okun', Structure and Properties of Ni_3Al Intermetallic Under Vacuum Impact Sintering, Powder Metall. Met. Ceram. 54 (2016) 554–567. https://doi.org/10.1007/s11106-016-9749-4.

[126] H.J. Kim, S.M. Lee, Y.S. Oh, Y.-H. Yang, Y.S. Lim, D.H. Yoon, C. Lee, J.-Y. Kim, R.S. Ruoff, Unoxidized Graphene/Alumina Nanocomposite: Fracture- and Wear-Resistance Effects of Graphene on Alumina Matrix, Sci. Rep. 4 (2015) 5176. https://doi.org/10.1038/srep05176.

[127] A. Vencl, N. Manić, V. Popovic, M. Mrdak, Possibility of the abrasive wear resistance determination with scratch tester, Tribol. Lett. 37 (2010) 591–604. https://doi.org/10.1007/s11249-009-9556-x.

[128] A.K. Basak, J.P. Celis, M. Vardavoulias, P. Matteazzi, Coefficient of friction measured from nano- to macro-normal loads on plasma sprayed nanostructured cermet coatings, Metall. Mater. Trans. A Phys. Metall. Mater. Sci. 45 (2014) 1049–1056. https://doi.org/10.1007/s11661-013-2033-z.

[129] J. Pirso, S. Letunovitš, M. Viljus, Friction and wear behaviour of cemented carbides, Wear. 257 (2004) 257–265. https://doi.org/10.1016/j.wear.2003.12.014.

[130] T.W. Scharf, S.V. Prasad, P.G. Kotula, J.R. Michael, C.V. Robino, Elevated temperature tribology of cobalt and tantalum-based alloys, Wear. 330–331 (2015) 199–208. https://doi.org/10.1016/j.wear.2014.12.051.

[131] J. Ye, J. Xiong, Z. Guo, T. Yang, L. Zhou, J. Liu, S. Li, T. Li, Preparation of self-lubricating Ti(C,N)-based cermets by solid carburization and wear behavior, Int. J. Refract. Met. Hard Mater. 67 (2017) 68–73. https://doi.org/10.1016/j.ijrmhm.2017.05.010.

[132] C. Jin, C.C. Onuoha, Z.N. Farhat, G.J. Kipouros, K.P. Plucknett, Microstructural damage following reciprocating wear of TiC-stainless steel cermets, (2016). https://doi.org/10.1016/j.triboint.2016.10.011.

[133] J.A. Williams, Wear and wear particles - Some fundamentals, Tribol. Int. 38 (2005) 863–870. https://doi.org/10.1016/j.triboint.2005.03.007.

[134] H. Klaasen, J. Kübarsepp, T. Roosaar, M. Viljus, R. Traksmaa, J. Kbarsepp, T. Roosaar, M. Viljus, R. Traksmaa, Adhesive wear performance of hardmetals and cermets, Wear. 268 (2010) 1122–1128. https://doi.org/10.1016/j.wear.2010.01.006.

[135] A. Hase, H. Mishina, Wear elements generated in the elementary process of wear, Tribol. Int. 42 (2009) 1684–1690. https://doi.org/10.1016/j.triboint.2009.02.006.

[136] J. Chen, J. Li, D. Xiong, Y. He, Y. Ji, Y. Qin, Preparation and tribological behavior of Ni-graphene composite coating under room temperature, Appl. Surf. Sci. 361 (2016) 49–56. https://doi.org/10.1016/j.apsusc.2015.11.094.

[137] F. Mao, U. Wiklund, A.M. Andersson, U. Jansson, Graphene as a lubricant on Ag for electrical contact applications, J. Mater. Sci. 50 (2015) 6518–6525. https://doi.org/10.1007/s10853-015-9212-9.

[138] Y.-F. Chen, J.-Q. Bi, C.-L. Yin, G.-L. You, Microstructure and fracture toughness of graphene nanosheets/alumina composites, Ceram. Int. 40 (2014) 13883–13889. https://doi.org/10.1016/j.ceramint.2014.05.107.

[139] J. Dusza, J. Morgiel, A. Duszová, L. Kvetková, M. Nosko, P. Kun, C. Balázsi, Microstructure and fracture toughness of Si_3N_4 graphene platelet composites, J. Eur. Ceram. Soc. 32 (2012) 3389–3397. https://doi.org/10.1016/j.jeurceramsoc.2012.04.022.

[140] Tribological performance evaluation of tungsten carbide-based cermets and development of a fracture mechanics wear model, Wear. 201 (1996) 233–243. https://doi.org/10.1016/S0043-1648(96)07252-3.

[141] L. he, Y. tan, H. tan, C. zhou, L. Gao, Tribological properties of nanostructured Al_2O_3-40%TiO_2 multiphase ceramic particles reinforced Ni-based alloy composite coatings, Trans. Nonferrous Met. Soc. China. 23 (2013) 2618–2627. https://doi.org/10.1016/S1003-

6326(13)62776-4.

[142] H. Klaasen, J. Kübarsepp, A. Tšinjan, F. Sergejev, Performance of carbide composites in cyclic loading wear conditions, Wear. 271 (2011) 837–841. https://doi.org/10.1016/j.wear.2011.03.005.

[143] Z. Guo, J. Xiong, M. Yang, C. Jiang, WC-TiC-Ni cemented carbide with enhanced properties, J. Alloys Compd. 465 (2008) 157–162. https://doi.org/10.1016/j.jallcom.2007.10.132.

[144] P.J. Blau, C.E. DeVore, Sliding friction and wear behaviour of several nickel aluminide alloys under dry and lubricated conditions, Tribol. Int. 23 (1990) 226–234. https://doi.org/10.1016/0301-679X(90)90027-M.

[145] P.J. Blau, Friction and Wear of Ordered Intermetallic Alloys of Ni_3AI, Vol. 18, ASM International, Materials Park, Ohio, 1992. https://doi.org/10.1361/asmhba00.

[146] Y.v.r.k.r.k. Prasad, S. Sasidhara, V.K. Sikka, Characterization of mechanisms of hot deformation of as-cast nickel aluminide alloy, Intermetallics. 8 (2000) 987–995. https://doi.org/10.1016/S0966-9795(00)00048-0.

[147] N.S. Stoloff, Physical and mechanical metallurgy of Ni_3Al and its alloys, Int. Mater. Rev. 34 (1989) 153–184. https://doi.org/10.1007/978-1-4613-1215-4_6.

[148] K. Aoki, O. Izumi, Flow and fracture behaviour of $Ni_3(AlTi)$ single crystals tested in tension, J. Mater. Sci. 14 (1979) 1800–1806. https://doi.org/10.1007/BF00551018.

[149] R. Kozubski, J. Sołtys, M.C. Cadeville, V. Pierron-Bohnes, T.H. Kim, P. Schwander, J.P. Hahn, G. Kostorz, J. Morgiel, Long-range ordering kinetics and ordering energy in Ni_3Al-based γ' alloys, Intermetallics. (1993). https://doi.org/10.1016/0966-9795(93)90009-K.

[150] S. Institution of Corrosion Science and Technology (Great Britain), Y. Mueller, C. Latkoczy, S. Virtanen, P. Schmutz, Corrosion science., Pergamon Press, 1961. http://www.academia.edu/23404339/Analytical_characterization_of_the_corrosion_mechanisms_of_WC_Co_by_electrochemical_methods_and_inductively_coupled_plasma_mass_spectroscopy (accessed December 4, 2017).

[151] S.L. Shang, Y. Wang, D.E. Kim, Z.K. Liu, First-principles thermodynamics from phonon and Debye model: Application to Ni and Ni_3Al, Comput. Mater. Sci. (2010). https://doi.org/10.1016/j.commatsci.2009.12.006..

[152] J.P. Perdew, K. Burke, M. Ernzerhof, Generalized Gradient Approximation Made Simple [Phys. Rev. Lett. 77, 3865 (1996)], Phys. Rev. Lett. 78 (1997) 1396–1396. https://doi.org/10.1103/PhysRevLett.78.1396.

[153] H.J. Monkhorst, J.D. Pack, Special points for Brillouin-zone integrations, Phys. Rev. B. 13 (1976) 5188–5192. https://doi.org/10.1103/PhysRevB.13.5188.

[154] M. Methfessel, A.T. Paxton, High-precision sampling for Brillouin-zone integration in metals, Phys. Rev. B. 40 (1989) 3616–3621. https://doi.org/10.1103/PhysRevB.40.3616.

[155] R. Hill, The Elastic Behaviour of a Crystalline Aggregate, Proc. Phys. Soc. Sect. A. 65 (1952) 349–354. https://doi.org/10.1088/0370-1298/65/5/307.

[156] S. Saha, J.W. Zwanziger, Elastic properties of ternary (Alx,Mg1−x)Sc random alloys from first principles methods, J. Alloys Compd. 610 (2014) 138–142. https://doi.org/10.1016/j.jallcom.2014.04.102.

[157] M. Moakher, A.N. Norris, The Closest Elastic Tensor of Arbitrary Symmetry to an Elasticity Tensor of Lower Symmetry, J. Elast. 85 (2006) 215–263. https://doi.org/10.1007/s10659-006-9082-0.

[158] F. Tasnádi, M. Odén, I.A. Abrikosov, Ab initio elastic tensor of cubic $Ti_{0.5}Al_{0.5}N$ alloys: Dependence of elastic constants on size and shape of the supercell model and their convergence, Phys. Rev. B. 85 (2012) 144112. https://doi.org/10.1103/PhysRevB.85.144112.

[159] M. Gaier, W.A. Sparling, Z. Memarrashidi, Z.N. Farhat, K.P. Plucknett, The influence of Mo_2C additions on the microstructural development and sintering response of TiN-Ni_3Al cermets, Int. J. Refract. Met. Hard Mater. 71 (2018) 262–272. https://doi.org/10.1016/j.ijrmhm.2017.11.025.

[160] G. Xiao, Q. Fan, M. Gu, Z. Wang, Z. Jin, Dissolution-precipitation mechanism of self-propagating high-temperature synthesis of TiC-Ni cermet, Mater. Sci. Eng. A. 382 (2004) 132–140. https://doi.org/10.1016/j.msea.2004.04.052.

[161] Y. Wan, J. Gong, Influence of TiC particle size on the load-independent hardness of Al2O3-TiC composites, Mater. Lett. 57 (2003) 3439–3443. https://doi.org/10.1016/S0167-577X(03)00096-X.

[162] K.P. Plucknett, P.F. Becher, S.B. Waters, Titanium Carbide / Nickel Aluminide Composites, Ceram. Soc. 44 (1998) 1839–1844. https://doi.org/10.1111/j.1151-2916.1998.tb02555.x.

[163] P. Hvizdoš, J. Balko, J.M. Córdoba, E. Chicardi, Nanoindentation of (Ti,Ta)(C,N)–Co cermets prepared by methods of mechanochemistry, Int. J. Refract. Met. Hard Mater. 49 (2015) 219–224. https://doi.org/10.1016/j.ijrmhm.2014.07.038.

[164] H.W. Newkirk, H.H. Sisler, Determination of Residual Stresses in Titanium Carbide-Base Cermets by High-Temperature X-Ray Diffraction, J. Am. Ceram. Soc. 41 (1958) 93–103. https://doi.org/10.1111/j.1151-2916.1958.tb15449.x.

[165] P.F. Becher, K.P. Plucknett, Properties of Ni_3Al-bonded Titanium Carbide Ceramics, J. Eur. Ceram. Soc. 18 (1998) 395–400. https://doi.org/10.1016/S0955-2219(97)00124-6.

[166] S.R. Agnew, J.I. Keene, L. Dong, M. Shamsujjoha, M.R. O'Masta, H.N.G. Wadley,

Microstructure characterization of large TiC-Mo-Ni cermet tiles, Int. J. Refract. Met. Hard Mater. 68 (2017) 84–95. https://doi.org/10.1016/J.IJRMHM.2017.07.004.

[167] K. Jia, T.E. Fischer, Sliding wear of conventional and nanostructured cemented carbides, Wear. (1997). https://doi.org/10.1016/S0043-1648(96)07423-6.

[168] L.S. Sigl, H.E. Exner, The flow stress and hardness of metal-reinforced brittle composites, Mater. Sci. Eng. A. 108 (1989) 121–129. https://doi.org/10.1016/0921-5093(89)90413-9.

[169] G.D. Quinn, R.C. Bradt, On the vickers indentation fracture toughness Test, J. Am. Ceram. Soc. 90 (2007) 673–680. https://doi.org/10.1111/j.1551-2916.2006.01482.x.

[170] G. Subhash, W. Zhang, Investigation of the overall friction coefficient in single-pass scratch test, Wear. 252 (2002) 123–134. https://doi.org/10.1016/S0043-1648(01)00852-3.

[171] T. Kayaba, K. Hokkirigawa, K. Kato, Analysis of the abrasive wear mechanism by successive observations of wear processes in a scanning electron microscope, Wear. 110 (1986) 419–430. https://doi.org/10.1016/0043-1648(86)90115-8.

[172] D. Tabor, Surface effects in adhesion, friction, wear and lubrication, Tribol. Int. (1981). https://doi.org/10.1016/0301-679x(81)90112-2.

[173] I. Hutchings, P. Shipway, Tribology: Friction and wear of engineering materials: Second Edition, 2017.

[174] D. Anderson, A. Warkentin, R. Bauer, Experimental and numerical investigations of single abrasive-grain cutting, Int. J. Mach. Tools Manuf. (2011). https://doi.org/10.1016/j.ijmachtools.2011.08.006.

[175] P. Jozwik, W. Polkowski, Z. Bojar, Applications of {Ni_3Al} Based Intermetallic Alloys-Current Stage and Potential Perceptivities, Materials (Basel). https://doi.org/10.1016/0301-679x(81)90112-2.

[176] V.L.. Toth, Transition Metal Carbides and Nitrides., Angew. Chemie. 84 (1971) 960–960. https://doi.org/10.1002/ange.19720841920.

[177] H.Y. Liu, J.H. Huang, C.F. Yin, J.G. Zhang, G.B. Lin, Microstructure and properties of TiC-Fe cermet coatings by reactive flame spraying using asphalt as carbonaceous precursor, Ceram. Int. 33 (2007) 827–835. https://doi.org/10.1016/j.ceramint.2006.01.020.

[178] S. Zhang, Material development of titanium carbonitride-based cermets for machining application, Key Eng. Mater. 138 (1998) 521–543.

[179] K.P. Plucknett, T.N. Tiegs, P.A. Menchhofer, P.F. Becher, S.B. Waters, Ductile Intermetallic Toughened Carbide Matrix Composites, Ceram. Eng. Sci. Proc. 17 (1996) 314–321.

[180] T.N. Tiegs, K.B. Alexander, K.P. Plucknett, P.A. Menchhofer, P.F. Becher, S.B. Waters,

Ceramic composites with a ductile Ni_3Al binder phase, Mater. Sci. Eng. A. 209 (1996) 243–247. https://doi.org/http://dx.doi.org/10.1016/0921-5093(95)10128-4.

[181] K.P. Plucknett, P.E. Becher, S.B. Waters, Flexure strength of melt-infiltration -processed titanium carbide/nickel aluminide composites, J. Am. Ceram. Soc. 81 (1998) 1839–1844.

[182] B.L. He, Y.F. Zhu, Microstructure and properties of TiC/Ni_3Al composites prepared by pressureless melt infiltration with porous TiC/Ni_3Al preforms, Mater. Manuf. Process. 26 (2011) 586–591. https://doi.org/10.1080/10426910903229339.

[183] T.N. Tiegs, J.L. Schroeder, P.A. Menchhofer, F.C. Montgomery, D.L. Barker, F. Goranson, D.E. Wittmer, Processing and Properties of TiC-Ni_3Al Composites, in: Proc. 3rd Int. Symp. Struct. Intermet. 23-27 Sept. 2001, 2001: p. 811.

[184] W. Conshohocken, Standard Test Method for Vickers Indentation Hardness of Advanced Ceramics 1, Test. (2003) 1–10. https://doi.org/10.1520/C1327-08.2.

[185] S. Siva Shashidhara Reddy, K. Balasubramaniam, C. V. Krishnamurthy, M. Shankar, Ultrasonic goniometry immersion techniques for the measurement of elastic moduli, Compos. Struct. 67 (2005) 3–17. https://doi.org/10.1016/j.compstruct.2004.01.008.

[186] J.P. Perdew, M. Ernzerhof, K. Burke, Generalized gradient approximation made simple, Phys. Rev. Lett. 77 (1996) 3865–3868. https://doi.org/10.1103/PhysRevLett.77.3865.

[187] E.R. Newnham, Properties of Materials: Anisotropy, Symmetry, Structure, 2013. https://doi.org/10.1017/CBO9781107415324.004.

[188] S. Timoshenko, J.N. Goodier, Theory of Elasticity, J. Elast. (1986). https://doi.org/10.1007/BF00046464.

[189] A. Togo, I. Tanaka, First principles phonon calculations in materials science, Scr. Mater. 108 (2015) 1–5. https://doi.org/10.1016/j.scriptamat.2015.07.021.

[190] F. Birch, Finite elastic strain of cubic crystals, Phys. Rev. 71 (1947) 809–824. https://doi.org/10.1103/PhysRev.71.809.

[191] H. Hosokawa, K. Shimojima, A. Matsumoto, K. Kato, H. Matsubara, Wettability of Ni/(Ti x Me 1 - X)(CuNv) System (Me = Mo, W), Int. J. Refract. Met. Hard Mater. (2012). https://doi.org/10.1016/j.ijrmhm.2012.01.005.

[192] C. Zhang, Y. Du, S. Zhou, Y. Peng, J. Wang, Grain growth and hardness of TiC-based cermets: Experimental investigation and thermodynamic calculations, Ceram. Int. 42 (2016) 19289–19295. https://doi.org/10.1016/J.Ceramint.2016.09.096.

[193] M.B. Rahaei, R. Yazdani rad, A. Kazemzadeh, T. Ebadzadeh, Mechanochemical synthesis of nano TiC powder by mechanical milling of titanium and graphite powders, Powder Technol. 217 (2012) 369–376. https://doi.org/10.1016/j.powtec.2011.10.050.

[194] J.D. Bernal, The Structure of Graphite, Proc. R. Soc. A Math. Phys. Eng. Sci. (1924). https://doi.org/10.1098/rspa.1924.0101.

[195] P. Trucano, R. Chen, Structure of graphite by neutron diffraction, Nature. 258 (1975) 136–137. https://doi.org/10.1038/258136a0.

[196] X. Chen, F. Tian, C. Persson, W. Duan, N.X. Chen, Interlayer interactions in graphites, Sci. Rep. 3 (2013). https://doi.org/10.1038/srep03046.

[197] S. Grimme, Semiempirical GGA-type density functional constructed with a long-range dispersion correction, J. Comput. Chem. 27 (2006) 1787–1799. https://doi.org/10.1002/jcc.20495.

[198] A.S. Cooper, Precise lattice constants of germanium, aluminum, gallium arsenide, uranium, sulphur, quartz and sapphire, Acta Crystallogr. 15 (1962) 578–582. https://doi.org/10.1107/S0365110X62001474.

[199] V.S. Kogan, Isotope effects in the structural properties of solids, Uspekhi Fiz. Nauk. (1962). https://doi.org/10.3367/ufnr.0078.196212b.0579.

[200] R.M. Wood, The lattice constants of high purity alpha titanium, Proc. Phys. Soc. 80 (1962) 783–786. https://doi.org/10.1088/0370-1328/80/3/323.

[201] M.P. Arbuzov, I.A. Zelenkov, Thermal expansion of Ni_3Al with additions of a third element, Fiz. Met. Met. 16 (1963) 236–240.

[202] D.L. Vrel, J.M. Lihrmann, J.P. Petitet, Synthesis of Titanium Carbide by Self-Propagating Powder Reactions. 1. Enthalpy of Formation of TiC, J. Chem. Eng. Data. 40 (1995) 280–282. https://doi.org/10.1021/je00017a062.

[203] J.H. Xu, B.I. Min, A.J. Freeman, T. Oguchi, Phase stability and magnetism of Ni_3Al, Phys. Rev. B. 41 (1990) 5010–5016. https://doi.org/10.1103/PhysRevB.41.5010.

[204] J.Y. Rhee, Y. V. Kudryavtsev, Y.P. Lee, Optical property and electronic structures of Ni_2MnAl alloy, in: J. Magn. Magn. Mater., 2004. https://doi.org/10.1016/j.jmmm.2003.12.497.

[205] J. Vallin, M. Mongy, K. Salama, O. Beckman, Elastic constants of aluminum, J. Appl. Phys. (1964). https://doi.org/10.1063/1.1713749.

[206] Y. Mishin, M.J. Mehl, D.A. Papaconstantopoulos, Phase stability in the Fe-Ni system: Investigation by first-principles calculations and atomistic simulations, Acta Mater. (2005). https://doi.org/10.1016/j.actamat.2005.05.001.

[207] D. Tromans, Elastic Anisotropy of HCP Metal Crystals and Polycrystals, Ijrras. (2011).

[208] G. Savini, Y.J. Dappe, S. Öberg, J.C. Charlier, M.I. Katsnelson, A. Fasolino, Bending modes, elastic constants and mechanical stability of graphitic systems, Carbon N. Y. (2011).

https://doi.org/10.1016/j.carbon.2010.08.042.

[209] S.V. Prikhodko, J.D. Carnes, D.G. Isaak, H. Yang, A.J. Ardell, Temperature and composition dependence of the elastic constants of Ni_3Al, Metall. Mater. Trans. A Phys. Metall. Mater. Sci. 30 (1999).

[210] Y. Li, W. Wang, B. Zhu, M. Xu, J. Zhu, Y. Hao, W. Li, X. Long, Elastic and thermodynamic properties of TiC from first-principles calculations, Sci. China Physics, Mech. Astron. (2011). https://doi.org/10.1007/s11433-011-4500-0.

[211] H.H. Pham, M.E. Williams, P. Mahaffey, M. Radovic, R. Arroyave, T. Cagin, Finite-temperature elasticity of fcc Al: Atomistic simulations and ultrasonic measurements, Phys. Rev. B - Condens. Matter Mater. Phys. (2011). https://doi.org/10.1103/PhysRevB.84.064101.

[212] H. Lu, Z. Liu, X. Yan, D. Li, L. Parent, H. Tian, Electron work function-a promising guiding parameter for material design, Sci. Rep. (2016). https://doi.org/10.1038/srep24366.

[213] J.R. Cost, K.R. Janowski, R.C. Rossi, Elastic properties of isotropic graphite, Philos. Mag. (1968). https://doi.org/10.1080/14786436808223035.

[214] C. Wang, J. Xu, X. Hu, D. Chen, H. Sun, B. Yu, Elastic and thermodynamic properties of NiAl and Ni_3Al from first-principles calculations, Int. J. Mod. Phys. B. 25 (2011) 3623–3631. https://doi.org/10.1142/S0217979211101685.

[215] D.R. Askeland, P.P. Fulay, W.J. Wright, The science and engineering of materials, Stamford, CT Cengage Learn. C2011. (2011) 944. https://doi.org/10.2172/15009526.

[216] A. Krawitz, E. Drake, Residual stresses in cemented carbides - An overview, Int. J. Refract. Met. Hard Mater. (2015). https://doi.org/10.1016/j.ijrmhm.2014.07.018.

[217] F. Sergejev, E. Kimmari, M. Viljus, Residual stresses in TiC-based cermets measured by indentation, Procedia Eng. 10 (2011) 2873–2881. https://doi.org/10.1016/j.proeng.2011.04.477.

[218] J.W. Zwanziger, U. Werner-Zwanziger, E.D. Zanotto, E. Rotari, L.N. Glebova, L.B. Glebov, J.F. Schneider, Residual internal stress in partially crystallized photothermorefractive glass: Evaluation by nuclear magnetic resonance spectroscopy and first principles calculations, J. Appl. Phys. (2006). https://doi.org/10.1063/1.2191731.

[219] H. Pinto, L. Ito, M. Crovace, E.B. Ferreira, F. Fauth, T. Wroblewski, E.D. Zanotto, a. R. Pyzalla, Surface and bulk residual stresses in $Li_2O{\cdot}2SiO_2$ glass–ceramics, J. Non. Cryst. Solids. (2007). https://doi.org/10.1016/j.jnoncrysol.2007.04.007.

[220] Y. Wang, Z.-K. Liu, L.-Q. Chen, Thermodynamic properties of Al, Ni, NiAl, and Ni_3Al from first-principles calculations, Acta Mater. 52 (2004) 2665–2671. https://doi.org/10.1016/j.actamat.2004.02.014.

[221] C.R. Houska, Thermal expansion and atomic vibration amplitudes for TiC, TiN, ZrC, ZrN, and pure tungsten, J. Phys. Chem. Solids. 25 (1964) 359–366. https://doi.org/10.1016/0022-3697(64)90001-0.

[222] C. Kittel, Introduction to Solid State Physics, 2004. https://doi.org/citeulike-article-id:4202357.

[223] J.B. Nelson, D.P. Riley, The thermal expansion of graphite from 15°C. to 800°C.: Part I. Experimental, Proc. Phys. Soc. 57 (1945) 477–486. https://doi.org/10.1088/0959-5309/57/6/303.

[224] M. V. Nathal, R.A. Mackay, R.G. Garlick, Temperature dependence of γ-γ' lattice mismatch in Nickel-base superalloys, Mater. Sci. Eng. 75 (1985) 195–205. https://doi.org/10.1016/0025-5416(85)90189-2.

[225] N. Frage, L.M. Kaputkina, V.G. Prokoshkina, D.E. Kaputkin, N.R. Sverdlova, Changes in the phase composition, structure, and hardness of "titanium carbide-high-carbon steel" cermets under heat treatment, Met. Sci. Heat Treat. 49 (2007) 167–171. https://doi.org/10.1007/s11041-007-0030-9.

[226] M.N. Rahaman, Sintering of ceramics, 2007. https://doi.org/10.1016/B978-012654640-8/50006-7.

[227] S. Hoon Kim, D. Ha Kim, K.-C. Hwang, S.-B. Lee, S.-K. Lee, H. Uk Hong, D.-W. Suh, Heat Treatment Response of TiC-Reinforced Steel Matrix Composite, Met. Mater. Int. 22 (2016) 935–941. https://doi.org/10.1007/s12540-016-6176-5.

[228] H. Riazi, F. Ashra, S. Rahman, R. Ghomashchi, Influence of simultaneous aging and plasma nitriding on fatigue performance of 17-4 PH stainless steel, 703 (2017) 262–269. https://doi.org/10.1016/j.msea.2017.07.070.

[229] U.K. Viswanathan, S. Banerjee, R. Krishnan, Effects of aging on the microstructure of 17-4 PH stainless steel, Mater. Sci. Eng. A. 104 (1988) 181–189. https://doi.org/10.1016/0025-5416(88)90420-X.

[230] G.R. Anstis, P. Chantikul, B.R. Lawn, D.B. Marshall, A Critical Evaluation of Indentation Techniques for Measuring Fracture Toughness: I, Direct Crack Measurements, J. Am. Ceram. Soc. 64 (1981) 533–538. https://doi.org/10.1111/j.1151-2916.1981.tb10320.x.

[231] A. Szewczyk-Nykiel, R. Bogucki, Sinter-Bonding of AISI 316L and 17-4 PH Stainless Steels, J. Mater. Eng. Perform. 27 (2018) 5271–5279. https://doi.org/10.1007/s11665-018-3590-5.

[232] R.B. Collier, K.P. Plucknett, Spherical indentation damage in TiC-Ni_3Al composites, Int. J. Refract. Met. Hard Mater. 30 (2012) 188–195. https://doi.org/10.1016/j.ijrmhm.2011.08.008.

[233] R.M. German, The contiguity of liquid phase sintered microstructures, Metall. Trans. A. 16

(1985) 1247–1252. https://doi.org/10.1007/BF02670329.

[234] P. Li, J. Ye, Y. Liu, D. Yang, H. Yu, Study on the formation of core–rim structure in Ti(CN)-based cermets, Int. J. Refract. Met. Hard Mater. 35 (2012) 27–31. https://doi.org/10.1016/J.IJRMHM.2012.03.012.

[235] P. Kochmanski, J. Nowacki, Influence of initial heat treatment of 17-4 PH stainless steel on gas nitriding kinetics, Surf. Coatings Technol. 202 (2008) 4834–4838. https://doi.org/10.1016/j.surfcoat.2008.04.058.

[236] S. Buchholz, Z.N. Farhat, G.J. Kipouros, K.P. Plucknett, The reciprocating wear behaviour of TiC–Ni_3Al cermets, Int. J. Refract. Met. Hard Mater. 33 (2012) 44–52. https://doi.org/10.1016/j.ijrmhm.2012.02.008.

[237] A. Szewczyk-Nykiel, R. Bogucki, Sinter-Bonding of AISI 316L and 17-4 PH Stainless Steels, J. Mater. Eng. Perform. 27 (2018) 5271–5279. https://doi.org/10.1007/s11665-018-3590-5.

[238] G. Sahu, P.K. Sen, R. Sharma, S. Bohidar, A Review on Effect of Heat Treatment Process on Micrograin Structure of Steel, Int. J. Eng. Sci. Invent. 3 (2014) 46–52.

[239] J. Wall, H. Choo, T.N. Tiegs, P.K. Liaw, Thermal residual stress evolution in a TiC–50 vol.% Ni_3Al cermet, Mater. Sci. Eng. A. 421 (2006) 40–45. https://doi.org/10.1016/J.MSEA.2005.10.002.

[240] S. Ojha, N.S. Mishra, B.K. Jha, Effect of cooling rate on the microstructure and mechanical properties of a C-Mn-Cr-B steel, 2015. https://doi.org/10.1007/s12034-015-0862-7.

[241] G.F. Da Silva, S.S.M. Tavares, J.M. Pardal, M.R. Silva, H.F.G. De Abreu, Influence of heat treatments on toughness and sensitization of a Ti-alloyed supermartensitic stainless steel, J. Mater. Sci. 46 (2011) 7737–7744. https://doi.org/10.1007/s10853-011-5753-8.

[242] A. Ghabchi, S. Sampath, K. Holmberg, T. Varis, Damage mechanisms and cracking behavior of thermal sprayed WC-CoCr coating under scratch testing, Wear. 313 (2014) 97–105. https://doi.org/10.1016/j.wear.2014.02.017.

[243] K. Bonny, P. De Baets, W. Ost, S. Huang, J. Vleugels, W. Liu, B. Lauwers, Influence of electrical discharge machining on the reciprocating sliding friction and wear response of WC-Co cemented carbides, Int. J. Refract. Met. Hard Mater. 27 (2009) 350–359. https://doi.org/10.1016/j.ijrmhm.2008.09.002.

[244] X. Xu, S. van der Zwaag, W. Xu, The scratch and abrasive wear behaviour of a tempered martensitic construction steel and its dual phase variants, Wear. 358–359 (2016) 80–88. https://doi.org/10.1016/j.wear.2016.04.005.

[245] M. Gaier, T.Z. Todorova, Z. Russell, Z.N. Farhat, J.W. Zwanziger, K.P. Plucknett, The influence of intermetallic ordering on wear and indentation properties of TiC-Ni_3Al cermets, Wear. (2018). https://doi.org/10.1016/j.wear.2018.12.034.

[246] J. Smolik, K. Zdunek, B. Larisch, Investigation of adhesion between component layers of a multi-layer coating TiC/Ti(Cx, N1-x)/TiN by the scratch-test method, Vacuum. 55 (1999) 45–50. https://doi.org/10.1016/S0042-207X(99)00122-0.

[247] R. Bhambroo, S. Roychowdhury, V. Kain, V.S. Raja, Effect of reverted austenite on mechanical properties of precipitation hardenable 17-4 stainlesssteel, Mater. Sci. Eng. A. 568 (2013) 127–133. https://doi.org/10.1016/j.msea.2013.01.011.

[248] N. Liu, S. Chao, X. Huang, Effects of TiC/TiN addition on the microstructure and mechanical properties of ultra-fine grade Ti (C, N)-Ni cermets, J. Eur. Ceram. Soc. (2006). https://doi.org/10.1016/j.jeurceramsoc.2005.12.010.

Appendix A: The influence of Mo_2C additions on the microstructural development and sintering response of TiN-$N_{i2}Al$ cermets Copyright Letter

Appendix B: The effects of graphene nano-platelet additions on the sliding wear of TiC-Ni_3Al Copyright Letter

Appendix C: The influence of intermetallic ordering on wear and indentation properties of TiC-Ni_3Al Copyright Letter

Appendix D: Understanding the elastic and thermal response in TiC-based ceramic-metal composite systems: First-principles and mechanical studies Copyright Letter

Copyright Clearance Center RightsLink®

Home | Help | Email Support | Sign in | Create Account

Understanding the elastic and thermal response in TiC-based ceramic-metal composite systems: First-principles and mechanical studies

Author: T.Z. Todorova,M. Gaier,J.W. Zwanziger,K.P. Plucknett

Publication: Journal of Alloys and Compounds

Publisher: Elsevier

Date: 15 June 2019

© 2019 Elsevier B.V. All rights reserved.

Please note that, as the author of this Elsevier article, you retain the right to include it in a thesis or dissertation, provided it is not published commercially. Permission is not required, but please ensure that you reference the journal as the original source. For more information on this and on your other retained rights, please visit: https://www.elsevier.com/about/our-business/policies/copyright#Author-rights

BACK CLOSE WINDOW

© 2019 Copyright - All Rights Reserved | Copyright Clearance Center, Inc. | Privacy statement | Terms and Conditions

Comments? We would like to hear from you. E-mail us at customercare@copyright.com

Appendix E: 17-4PH Powder particle size distribution.

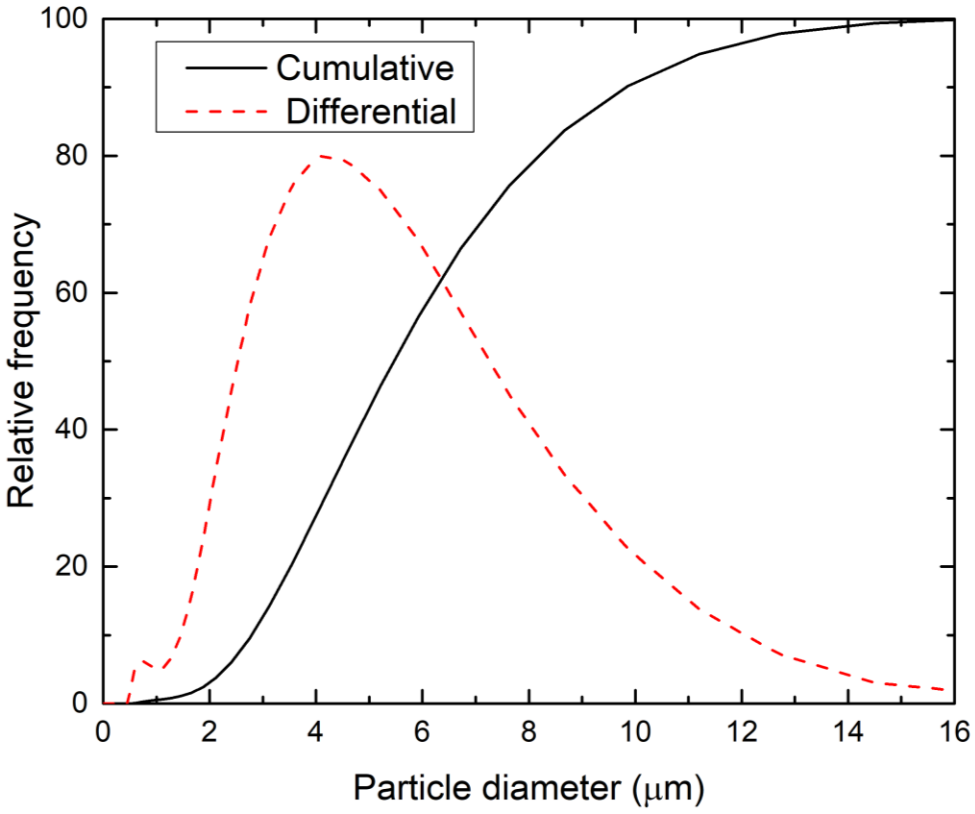

Appendix F: Powder particle size distribution.

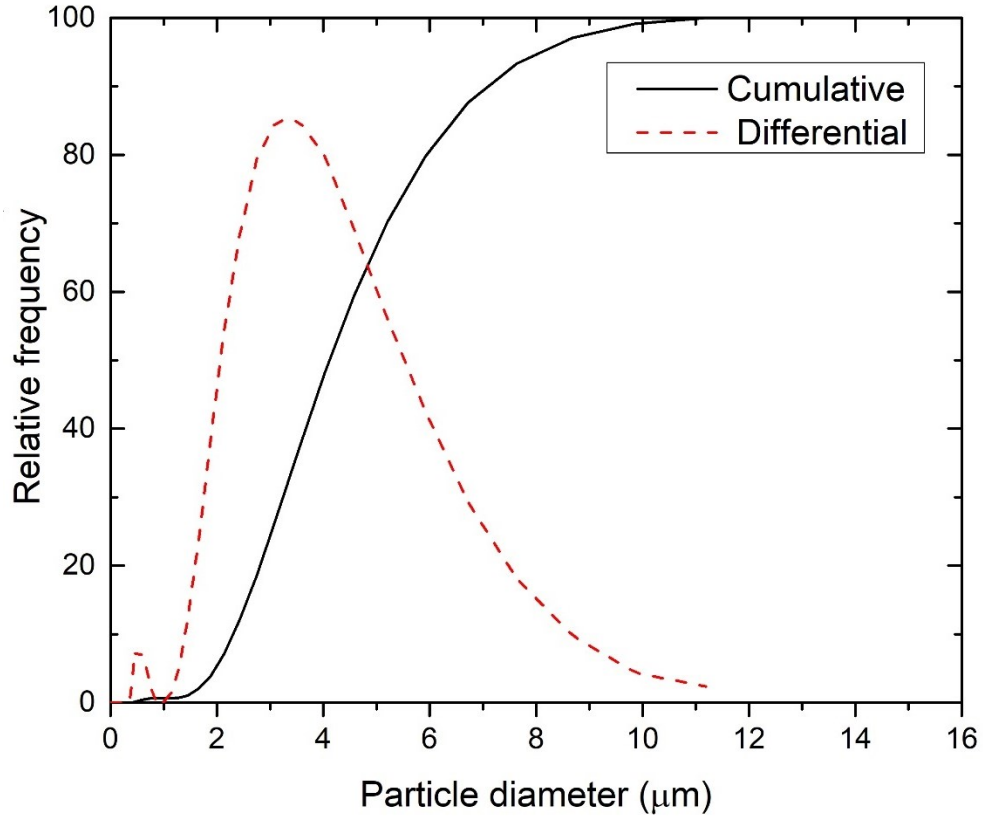

Appendix G: Representative dilatometry curves for TiC with 0 to 30 vol% 316L, showing the extent of densification as a function of temperature. Samples heated/cooled to 1500 °C at a rate of 20 °C/min.

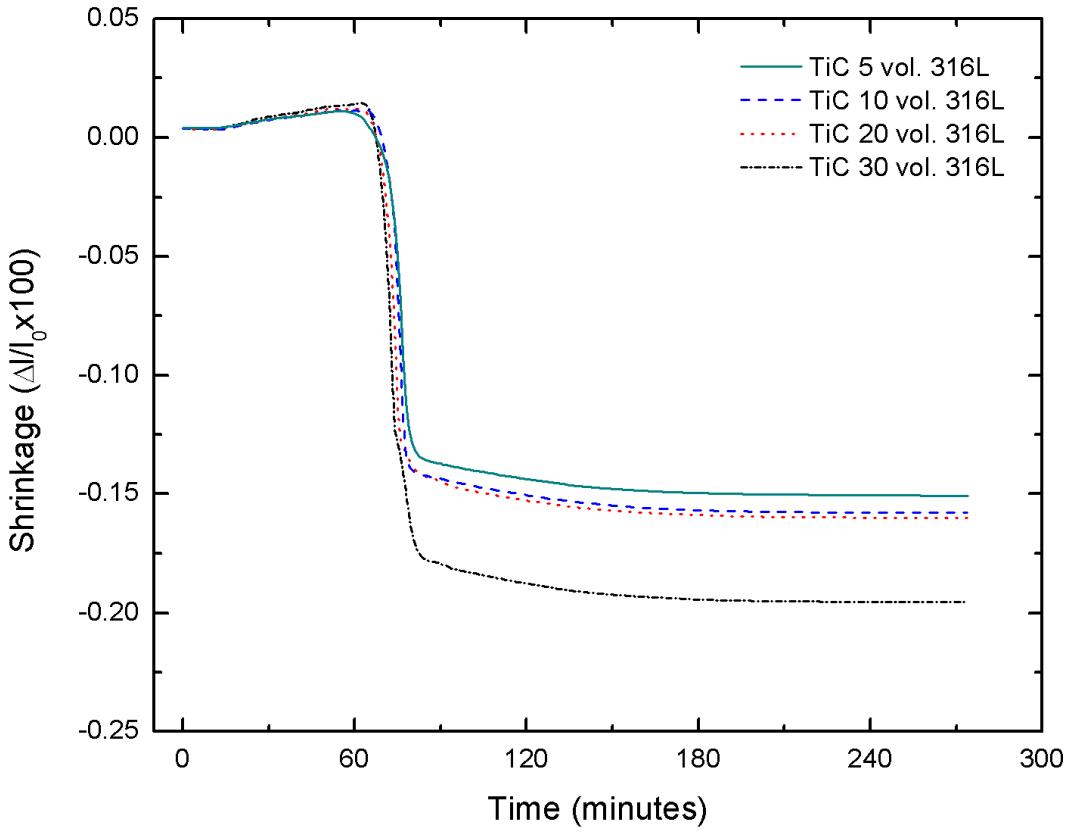

Appendix H: Representative dilatometry curves for TiC with 0 to 30 vol% 17-4PH, showing the extent of densification as a function of temperature. Samples heated/cooled to 1500 °C at a rate of 20 °C/min.

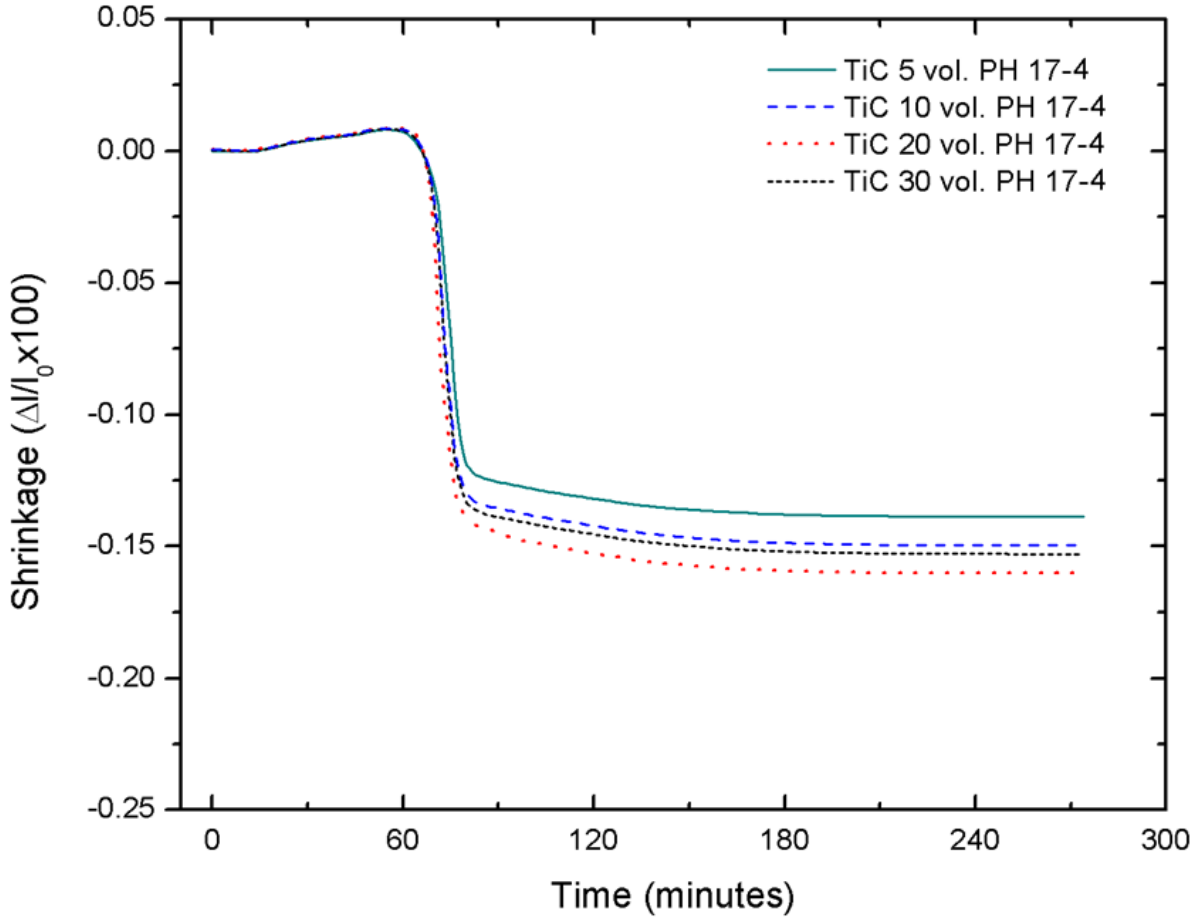

Appendix I: Temperature profile used on the dilatometry experiments.